Non-linear Bayesian inversion of controlled source electromagnetic data offshore Vancouver Island, Canada, and in the German North Sea

by

Romina Gehrmann
Dipl.-Geoph., University of Leipzig, 2008

A Dissertation Submitted in Partial Fulfillment of the
Requirements for the Degree of

DOCTOR OF PHILOSOPHY

in the School of Earth and Ocean Sciences

Non-linear Bayesian inversion of controlled source electromagnetic data offshore Vancouver Island, Canada, and in the German North Sea

by

Romina Gehrmann
Dipl.-Geoph., University of Leipzig, 2008

Supervisory Committee

Dr. Michael Riedel, Co-Supervisor
(School of Earth and Ocean Sciences)

Prof. Stan E. Dosso, Co-Supervisor
(School of Earth and Ocean Sciences)

Prof. emer. George D. Spence, Departmental Member
(School of Earth and Ocean Sciences)

Assoc. Prof. Maycira Costa, Outside Member
(Department of Geography)

Supervisory Committee

Dr. Michael Riedel, Co-Supervisor
(School of Earth and Ocean Sciences)

Prof. Stan E. Dosso, Co-Supervisor
(School of Earth and Ocean Sciences)

Prof. emer. George D. Spence, Departmental Member
(School of Earth and Ocean Sciences)

Assoc. Prof. Maycira Costa, Outside Member
(Department of Geography)

ABSTRACT

This thesis examines the sensitivity of the marine controlled source electromagnetic (CSEM) method to sub-seafloor resistivity structure, with a focus on gas hydrate and free gas occurrences. Different analysis techniques are applied with progressive sophistication to a series of studies based on simulated and measured data sets. CSEM data are modelled in time domain for one-dimensional models with gas hydrate, free gas and/or permafrost occurrences. Linearized and non-linear inversion methods are considered to infer subsurface models from CSEM data.

One study applies forward modelling and singular value decomposition to estimate uncertainties for permafrost models of the Beaufort Sea. This simulation study analyzes the resolution of the CSEM data for shallow water depth which is a challenging case because the electromagnetic signature of the air-water boundary may mask the sub-seafloor response. The results reveal a blind window as a function of water depth in which the CSEM data are insensitive to the sub-seafloor structure. However, the

CSEM data are sensitive to the top and the bottom of the permafrost with increasing uncertainties with depth.

The next study applies non-linear Bayesian inversion to CSEM data acquired in 2005/2006 on the Northern Cascadia margin to investigate sub-seafloor resistivity structure related to gas hydrate deposits and cold vents. Bayesian inversion provides a rigorous approach to estimate model parameters and uncertainties by probabilistically sampling of the parameter space. The resulting probability density function is interpreted here in terms of posterior median models, marginal and joint marginal probability densities for model parameters and credibility intervals. The Bayesian information criterion is applied to determine the amount of structure (number of layers) that can be resolved by the data. The parameter space is sampled with the Metropolis-Hastings algorithm in principal-component space. Non-linear, probabilistic inversion allows the analysis of unknown acquisition parameters such as time delays between receiver and transmitter clocks or unknown source amplitude. The estimated posterior median models and credibility intervals from Bayesian CSEM inversion are compared to reflection seismic data to provide a more complete geological interpretation. The CSEM data on the Northern Cascadia margin generally reveal a 1 to 3 layer sediment structure. Inversion results at the landward edge of the gas hydrate stability zone indicate a sediment unconformity as well as several potential cold vents which were previously unknown. The resistivities generally increase upslope due to sediment erosion along the slope. Inversion results on the middle slope infer several vent systems close to well-known Bullseye vent in agreement with ongoing interdisciplinary observations.

Finally, a trans-dimensional (trans-D) Bayesian inversion is applied to CSEM data acquired in 2012 in the German North Sea to investigate possible free gas occurrences. Trans-D inversion treats the number of layers as an additional unknown sampled probabilistically in the inversion. Parallel tempering is applied to increase sampling efficiency and completeness. Inversion results for the German North Sea yield resistivities at the seafloor which are typical for marine deposits, while resistivities at greater depth increase slightly and can be correlated with a transition from fine-grained marine deposits (Holocene age) to coarse-grained, glacial sediments (Pleistocene age), which is observed in a sediment core. The depths of layer interfaces estimated from CSEM inversion match the seismic reflector related to the contrast between the two depositional environments. The CSEM survey targeted a strong, phase-reversed, inclined seismic reflector within the glacial sediments, potentially indicating free gas.

While interface-depth estimates from CSEM inversion do not correlate closely with this reflector, resistivities are generally elevated above the strong seismic amplitudes and the thickness of the resistive layer follows the trend of the inclined reflector. However, the uncertainties of deeper interface depth estimates increase significantly and overlap with the targeted reflector at some of the measurement sites. Relatively low resistivities of a third layer correlate with sediments of late-Miocene origin with a high gamma-ray count indicating an increased amount of fine-grained sediments with organic material. The interface at the bottom of the third layer has wide uncertainties which relates to the penetration limit of the CSEM array.

Contents

List of Tables

List of Figures

Acronyms

AC	alternating current
AR	auto-regressive
ASSA	adaptive simplex simulated annealing
AUV	autonomous underwater vehicle
BGR	German Federal Institute for Geosciences and Natural Resources
BIC	Bayesian information criterion
CCGS	Canadian Coast Guard Ship
CF	calibration factor
CI	credibility intervals
CMP	common midpoint
CSEM	controlled source electromagnetics
CTD	conductivity, temperature, depth sounding
DC	direct current
DHS	downhill simplex
GHOZ	gas hydrate occurrence zone
GHSC	gas hydrate stability curve
GHSZ	gas hydrate stability zone
GR	gamma-ray
HED	horizontal electric dipole
IODP	Integrated Ocean Drilling Program
KS	Kolmogorov-Smirnov
MAP	maximum *a posteriori*
MARTIN	marine transient electromagnetic inversion program
mbsf	metres below seafloor
MCMC	Markov chain Monte Carlo
MCS	multi-channel seismic
MHS	Metropolis-Hastings sampling
MMU	Mid Miocene Unconformity
PPD	posterior probability density
RV	research vessel
Rx	receiver
SA	simulated annealing
SCS	single channel seismic

SVD	singular value decomposition
twt	two-way travel time
Tx	transmitter
wd	water depth
WP	way point

ACKNOWLEDGEMENTS

I would like to thank deeply:

My Supervisor Michael Riedel for supporting my research at the University of Victoria, for sharing his knowledge on gas hydrates and seismic processing, and for encouragement and patience.

My Co-supervisor Stan E. Dosso for introducing me to Bayesian inversion, for spending many hours on developing the CSEM inversion codes and deriving formulas together, and for revising the thesis in detail. Many thanks for being an amazingly approachable, knowledgeable and engaging supervisor.

Committee member George D. Spence for critical questions to diffusion theory and my geological interpretation of the inversion results, and for sharing his extensive knowledge on the Northern Cascadia margin and gas hydrates.

Committee member Maycira Costa for helping to make the contents of the thesis accessible to a broad audience.

Katrin Schwalenberg and Martin Engels for introducing me to time-domain CSEM, for supplying the CSEM data presented in this thesis, for hosting me at the Federal Institute for Geosciences and Natural Resources in Hanover and for teaching me to process CSEM data.

Nigel Edwards and Reza Mir for hosting me at the University of Toronto and teaching me about time-domain CSEM methods.

Andrei Swidinsky for answering my questions related to CSEM theory with enthusiasm and detail and revising parts of this thesis.

Carsten Scholl for supplying the 1-D forward and linearized inversion codes and answering my questions related to them.

Jan Dettmer for handing the trans-dimensional technique to me, together with great explanations and help to develop the code for CSEM inversion, and for discussing the results.

Volkhard Spiess, Hanno Keil and Asli Özmaral for supplying the high-frequency seismic lines GeoB00-142 on the Northern Cascadia margin and GeoB13-170 in the German North Sea and for discussing the geological interpretation with me.

Friends and colleagues, among others, Angela Schlesinger and Subbarao Yelisetti for sharing the office space, successes and doubts.

My parents, Ulrich and Leona Gehrmann, for financially and mentally supporting me from very young age to my adult life to pursue the education and life style I choose without questioning.

Jess-C and Oona Hall for loving support, patience and uplifting cheerfulness.

"I ought to know by this time that
when a fact appears to be opposed to a long train of deductions
it invariably proves to be capable of bearing some other interpretation."
Sherlock Holmes
(*A Study in Scarlet* by Sir Arthur Conan Doyle)

Chapter 1

Introduction

The marine controlled source electromagnetic (CSEM) method is an exploration technique to investigate the electrical resistivity of the sub-seafloor [*e.g.,* Cheesman et al., 1987]. In this thesis, marine CSEM is applied to study gas hydrate and shallow gas occurrences which are electrically resistive. Gas hydrate research is relevant for slope stability hazard assessment at continental margins, for evaluation of the global climate response to methane gas released into the atmosphere, and for estimating energy resources [*e.g.,* Sloan and Koh, 2008]. In terms of sub-seafloor gas hydrate deposits (or hydrocarbons in general), estimating the sub-seafloor resistivity complements more-commonly applied seismic methods which provide high structural resolution [*e.g.,* Hyndman and Spence, 1992]. However, estimating a sub-seafloor resistivity model from CSEM data requires sophisticated inversion algorithms. Common schemes to infer the resistivity structure are linearized inversion methods [*e.g.,* Constable et al., 1987]. In recent years, non-linear methods have become more popular and Bayesian methods, which provide quantitative uncertainty analysis (at higher computational costs), have been developed to analyze frequency-domain CSEM data [*e.g.,* Hoversten et al., 2006]. As a contribution to this developing field, the goal of this thesis is to rigorously estimate sub-seafloor resistivity models and uncertainties by applying non-linear Bayesian inversion to time-domain CSEM data, and compare the results to reflection seismic data to provide a more complete geological interpretation.

The marine CSEM method is based on electromagnetic fields, generated by an electric or magnetic source close to or on the seafloor, which propagate through the sub-seafloor and seawater. The electrical resistivity of marine sediments is mainly controlled by the conductance of pore fluids. Resistive material like hydrocarbons (in this study particularly free gas and gas hydrate) increases the sediment resistivity, and

can be targeted with the CSEM method. The electromagnetic field diffuses through a medium similar to the way heat diffuses along a temperature gradient. Diffusion time and field strength of the electromagnetic signal depend on the electrical resistivity of the volume between source and receiver, but direct interpretation in terms of a model of the resistivity structure is difficult, except for halfspace models [*e.g.,* Edwards, 2005].

The most common geophysical method for studying crustal structure and sediment lithology, as well as hydrocarbon reservoirs, is the active-source seismic method, where the source signal is a seismic wave, which travels through the medium [*e.g.,* Yilmaz, 2001]. The reflection seismic method is known for a high vertical resolution, depending on the frequency content of the seismic signal and the seismic velocity of the subsurface, and resolution reduces more slowly with depth than for CSEM. Seismic waves are reflected and transmitted at impedance (product of seismic velocity and density) contrasts. The time the seismic wave needs to travel to a reflector, reflect and travel to surface receivers at increasing offsets can be directly related to the velocity-depth profile. In marine environments, for example, seismic methods can image thin sediment lithology that corresponds to variations in sedimentation due to climatic changes [*e.g.*, Scholz and Rosendahl, 1988].

CSEM and seismic methods have very different resolution, are sensitive to different physical parameters, and potentially complement each other. How sub-seafloor structure from reflection seismic data and reflection amplitudes relate to bulk resistivities is particularly relevant for hydrocarbon exploration. A hydrocarbon reservoir is typically localized with seismic methods, but the amount of hydrocarbon in the volume beneath the reflector is estimated with electromagnetic and seismic methods in combination, as small amounts of hydrocarbon can lead to a prominent reflector, but a large amount of hydrocarbon is required to produce a strong increase in resistivity [*e.g.*, Ellingsrud et al., 2002; MacGregor et al., 2006].

To estimate a model of the sub-seafloor resistivity distribution for CSEM data requires sophisticated inversion algorithms. Solutions to inversion problems for finite data samples with noise are unfortunately non-unique [*e.g.*, Constable et al., 1987]. Therefore, it is important to estimate not only model parameter values but also uncertainties before comparing the results with those from other methods. Linearized and non-linear approaches can be applied to estimate uncertainties. The linearized approach can estimate local uncertainties about a specific sub-surface model, while non-linear approaches provide global uncertainty estimates. In this thesis, a linearized

approach by Edwards [1997] is carried out for permafrost models in the Beaufort Sea. Considering CSEM implementation, the Beaufort Sea is a challenging target area, due to the shallow water depth, and the effect of the air-water boundary on the electromagnetic signal [*e.g.*, Weiss, 2007]. Therefore, the uncertainty analysis is carried out for different water depths and seawater resistivities.

The non-linear approach to estimate uncertainties implemented in this thesis is a Bayesian inversion. A numerical implementation provides a rigorous probabilistic estimate for the model parameters by sampling the posterior probability density using Markov-chain Monte Carlo methods. The model parametrization (here, the number of subsurface layers) is an additional unknown in the problem and, in this study, it is estimated with the Bayesian information criterion or by including the parametrization as an unknown in the sampling procedure. The latter is referred to as trans-dimensional inversion, where transitions between dimensions (numbers of layers) result in a probability density for the model parameters as well as for the parametrization [*e.g.,* Gelman et al., 2000; Dettmer et al., 2009; Sambridge et al., 2006]. In this thesis, trans-dimensional inversion after Dettmer et al. [2010] is applied to investigating uncertainties of a shallow resistivity model in the German North Sea to evaluate possible lithological units and shallow gas occurrences.

The CSEM instrument considered in this thesis is a seafloor-towed horizontal electric array with one transmitter dipole and several receiver dipoles in line. The measured data are treated in the time domain. The instrument was designed to detect gas hydrate accumulations in continental margin sediments [Yuan and Edwards, 2000; Schwalenberg et al., 2005]. Gas hydrates are solid compounds containing water and gas molecules, and are also known as "the ice that burns" as their appearance is similar to ice, but gas molecules like methane burn easily when ignited. Gas hydrates are stable under certain pressure and temperature conditions as found in continental margins or below permafrost regions and are distributed world wide in great abundance [*e.g.*, Kvenvolden, 1993; Collett et al., 2009].

Gas hydrates in accretionary complexes are often considered for their effect on slope stability. Indications for gas hydrate-related sediment slumps and slides have been observed on several continental margins [*e.g.,* McIver, 1982; Mienert et al., 2005; Collett et al., 2009]. Large scale slumps and slides may generate tsunamis, which are dangerous for coastal communities [Micallef et al., 2008]. While this study does not discuss slope failure related to gas hydrate, it does evaluate gas hydrate occurrences on the Northern Cascadia continental margin offshore Vancouver Island,

Canada, where slope failures have been observed [*e.g.,* Lopez et al., 2010]. This study analyzes CSEM data acquired at the Northern Cascadia margin at the landward edge of the gas hydrate stability zone and at cold vent sites, ecosystems surrounding a rich supply of methane gas that forms massive gas hydrate deposits close to the seafloor.

Massive methane release from gas hydrates may have a strong impact on global climate [*e.g.,* Kennett et al., 2003]. Therefore, the potential of massive release of methane gas from gas hydrates is studied for marine and permafrost environments. In Arctic regions permafrost degradation has been observed [*e.g.,* Shakhova and Semiletov, 2007; Hughes-Clarke et al., 2009] and changes in the thermal regime may lead to gas hydrate dissociation within and beneath the permafrost realm. This thesis contains a CSEM modelling study on the Beaufort Sea shelf offshore the Northwest Territories where massive gas hydrates are found beneath permafrost regions. The sensitivity of the CSEM data to possible permafrost structures with depth is analyzed to evaluate if CSEM surveys can monitor the permafrost degradation.

Gas hydrate accumulations are categorized as unconventional gas reservoirs and estimates of total natural gas bound in gas hydrates world-wide exceed those of all other conventional hydrocarbon reserves, and so hydrates may represent a possible energy source of the future [Grace et al., 2008]. A gas hydrate production test at the Mallik site in the MacKenzie Delta, Canada, in 2007/2008 resulted in successful extraction of methane gas [Dallimore et al., 2008], and the first offshore production test was carried out successfully in 2013 in the Eastern Nankai Trough [*e.g.,* Yamamoto et al., 2014]. Another production test is intended for the Ulleung Basin offshore South Korea [Ryu et al., 2013a]. This thesis contains a modelling study of the sensitivity of CSEM to a gas hydrate reservoir in a sand layer in the Ulleung Basin. The uncertainty analysis is carried out with a non-linear Bayesian inversion.

1.1 Introduction to controlled source electromagnetic methods

The controlled source electromagnetic (CSEM) method is sensitive to the electrical resistivity of subsurface structure. Electromagnetic (EM) methods are relevant to detect conductive targets (*e.g.*, mineral deposits) or study areas where commonly applied seismic methods do not yield information. For example, seismic signals have difficulty penetrating geological units such as evaporites, carbonate reefs, permafrost

and igneous rocks as almost all the seismic energy is backscattered, while EM methods may be sensitive to material below those units. Another example involves gradual changes of physical properties in the subsurface where no seismic signature is observed, such as oil to water transitions in reservoirs. The amount of hydrocarbons increases the resistivity in the whole volume and may be detected with EM methods [*e.g.,* Edwards, 2005].

Marine CSEM instruments were first developed to study the electrical signature of the oceanic lithosphere [*e.g.,* Cox et al., 1986] and mid-ocean ridges [*e.g.,* Evans et al., 1994]. They are often applied in combination with the passive magnetotelluric methods, which lack natural-source high-frequency electromagnetic signals and corresponding near-surface information, due to attenuation in the water column [*e.g.,* Constable, 2010]. In the last 20 years, marine CSEM has become a popular tool for hydrocarbon exploration [*e.g.,* Ellingsrud et al., 2002] and gas hydrate detection [*e.g.,* Yuan and Edwards, 2000; Schwalenberg et al., 2005; Weitemeyer et al., 2011].

A time-domain marine CSEM system was developed by the EM group around Edwards and Chave [1986] at the University of Toronto. The instrument involves the use of a horizontal electric dipole (HED) transmitter (Tx) and receivers (Rx) towed by a cable on the seafloor behind a ship as shown in Fig. 1.1. In parallel, the EM group at Scripps Institution of Oceanography developed a frequency-domain system [Constable and Cox, 1996] with a deep-towed transmitter dipole. Receivers are deployed on the ocean floor and measure the electric and magnetic field components. This thesis focuses on the HED time-domain system with inline receiver dipoles measuring the electric field response developed by Yuan and Edwards [2000] and recently developed systems by Schwalenberg and Engels [2012a]. A more detailed description of the system and the theory behind it is provided in Chapter 2 and the individual instrumentation used to acquire data for this thesis are presented in Sec. 6.2 and Sec. 7.1.

1.2 Gas hydrates

Gas hydrates are clathrates composed of a host lattice of water molecules and guest molecules that interact through van der Waals (nonpolar) forces. Guest molecules are in a gaseous state and free to rotate within the lattice [*e.g.,* Gutt et al., 1999]. The molecular shape and size of the host lattice depends on the size of the guest molecule [Bohrmann and Torres, 2006]. While gas hydrates can contain any gas molecule

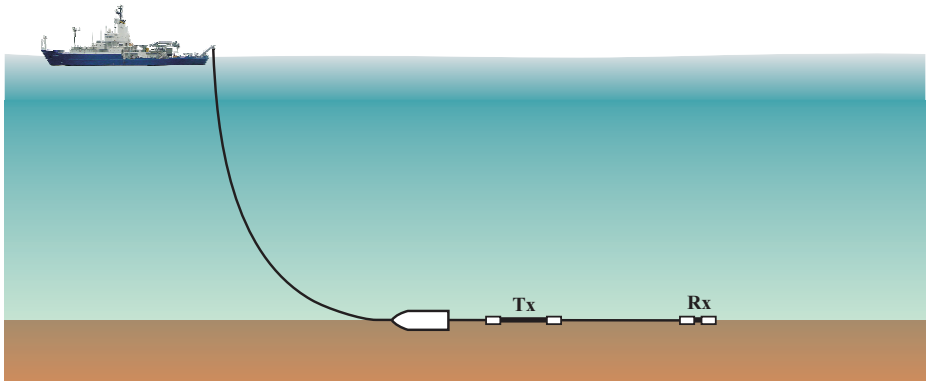

Figure 1.1: Configuration of the horizontal electric dipole-dipole system, after Schwalenberg et al. [2005]. Transmitter (Tx) dipole and inline receiver (Rx) dipole(s) are pulled behind heavy weight on the seafloor.

from noble gases to halogens with heavy molecular weight, in continental margins and below permafrost regions, gas hydrates usually contain hydrocarbons that are produced in the sediments from organic matter, and the most abundant is methane gas [Demirbas, 2010].

Gas hydrates were first discovered and synthesized in 1810 [Davy, 1811]. Naturally forming gas hydrates were observed in the 1930's clogging hydrocarbon transmission pipelines [Hammerschmidt, 1934] and in the permafrost regions of Russia [Makogon et al., 1971] and Canada [Bily and Dick, 1974], and subsequently in continental margins all over the world [*e.g.,* Markl et al., 1970; Kvenvolden, 1993]. Figure 1.2 illustrates the worldwide gas hydrate occurrences after Collett et al. [2009].

Gas hydrate formation depends on the abundance of water and free gas molecules, as well as on temperature, pressure, and the composition of the pore water and gas [*e.g.,* Sloan and Koh, 2008]. The organic carbon in shallow sediments is decomposed by microorganisms to produce biogenic gases such as methane. Fluid advection, diffusion and the solubility of methane in pore water control the physical transport and the availability of methane out of solution to form gas hydrates. The sedimentation rate, the sediment thickness, water depth and heat flow control gas hydrate stability [*e.g.,* Wallmann et al., 2006]. Gas hydrate stability curves (GHSC) for marine and permafrost environments are shown in Fig. 1.3.

Gas hydrate is stable on the left of the GHSC and between the two intersections of the temperature curve and the GHSC. Gas hydrates may exist above the seafloor, but pieces of gas hydrate and gas bubbles with a gas hydrate coating have a lower density

than water, rise and ultimately leave the gas hydrate stability zone (GHSZ). Molecules like carbon dioxide or ethane in the water-methane mixture shift the stability curve to higher temperatures and stabilize the formation, while dissolved ions in the pore water from salts like sodium chloride shift the stability curve to lower temperatures and degrade the stability [*e.g.,* Sloan and Koh, 2008; Bohrmann and Torres, 2006; Wright et al., 2005].

Gas hydrates in accretionary complexes are often discussed in terms of slope stability [*e.g.,* Hance, 2003]. They are known to stabilize the sediment matrix. However, when gas hydrates in sediments dissolve they create a gas- and water-rich mud, which, due to low density and increased pressure, may lift overlying sediments. In such cases, the stability of the slope can be degraded and the gas-water mixture may even rise to the surface [McIver, 1982]. Another issue is that changes in sedimentation rate and tectonic activity may trigger slope failure as well as sudden release of gas from gas hydrate. Slope failures are hazardous for underwater installations and may result in tsunamis damaging coastal regions [*e.g.,* Brown et al., 2006]; hazard assessment

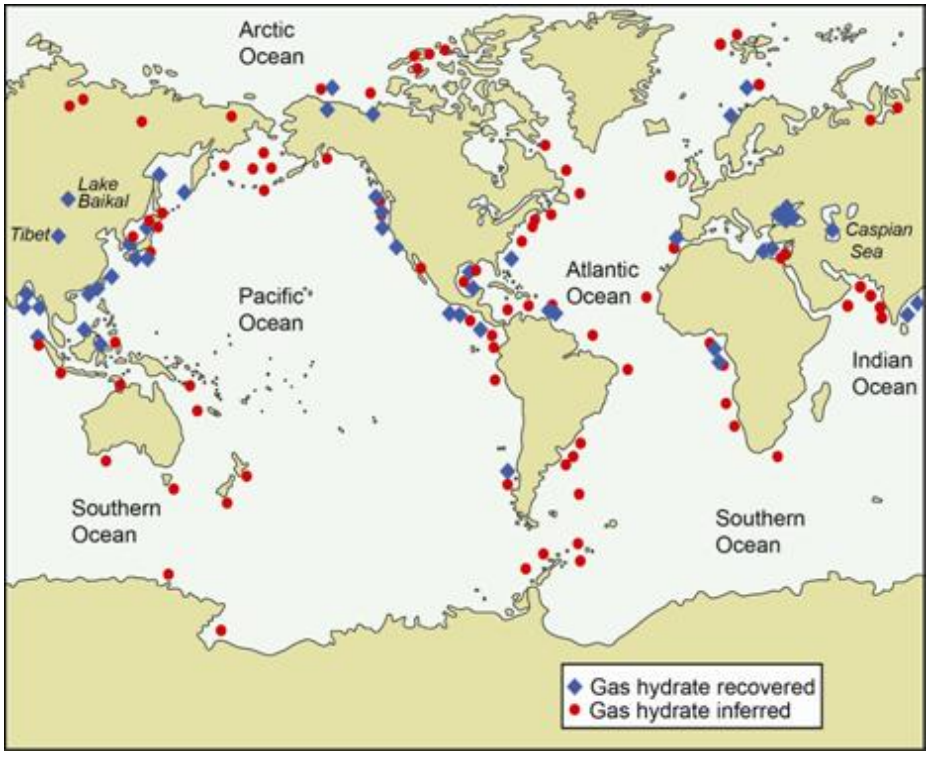

Figure 1.2: Gas hydrate occurrences world wide in continental margins and permafrost regions which were either recovered or inferred (courtesy of the USGS [Collett et al., 2009]).

requires the knowledge of the gas hydrate distribution.

Large scale dissociation of gas hydrate also needs to be analyzed in terms of climate feedback as methane, the dominant molecule in naturally occurring gas hydrates [Kvenvolden, 1993], absorbs radiation at a specific wavelength and is a 72-times stronger green house gas than carbon dioxide over a 20 year period. Even though its life span in the atmosphere is only about 12 years, methane oxidizes into carbon dioxide with a life span of thousands of years [*e.g.,* Forster et al., 2007; Archer et al., 2009]. Kennett et al. [2003] suggest a strong impact of rapid methane hydrate dissociation on climate change in the past and predict the same for the future. For example, Westbrook et al. [2009] have observed gas plumes along the landward edge of the GHSZ off of Svalbard and suggest the relationship to decomposing gas hydrates due to sea temperature increase which might affect all Arctic continental margins. Buffett and Archer [2004] have estimated a general reduction of hydrates at continental margins of about 15 % for a 3° C warming. Permafrost regions are most sensitive to climate change, because a general temperature rise is most pronounced

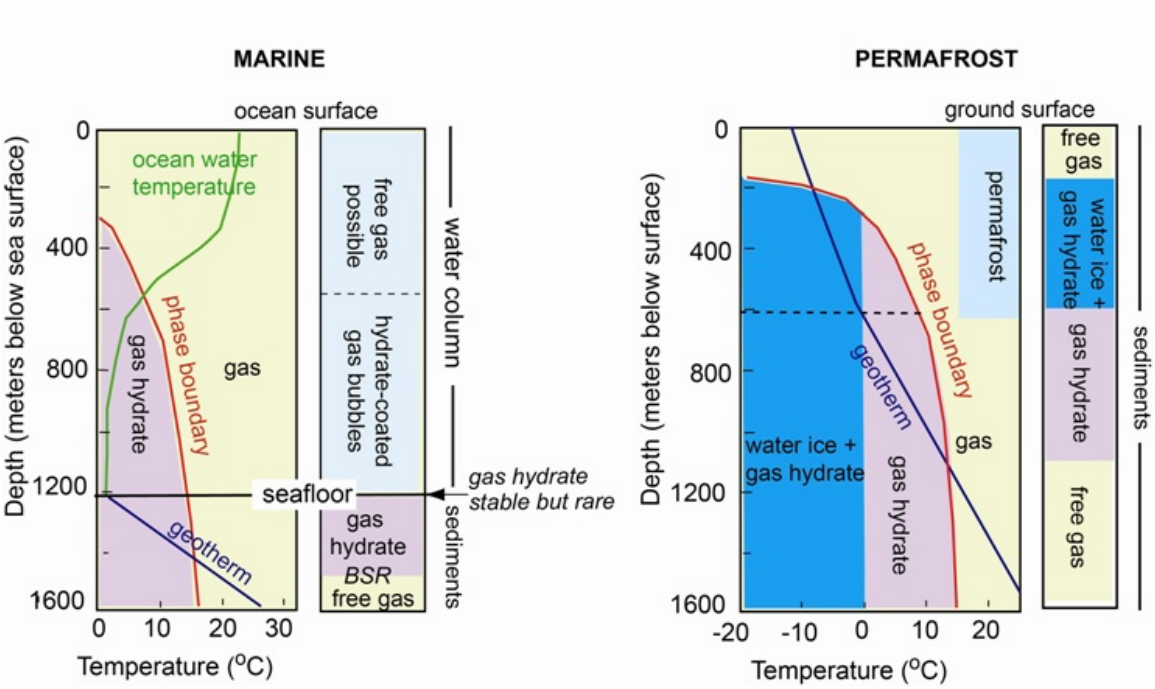

Figure 1.3: Gas hydrate stability curve (phase boundary in red) in marine and permafrost environments (after Ruppel [2007], courtesy of the USGS). The temperature in the environment is given by the ocean water temperature (green) and the geotherm (blue) in the sediments. Pressure to depth conversion assumes hydrostatic pressure.

at high latitudes [Schuur et al., 2008; Shakhova et al., 2010] and because sea level rise produces a rapid temperature increase. While marine methane hydrates may play a less significant role as dissociated methane is dissolved in the water column, releases from shallow water depth (< 100 m) and from permafrost regions may reach the atmosphere [McGinnis et al., 2006], and Archer et al. [2009] point out that slow releases of methane from oceanic methane hydrates and high-latitude wet lands will have a long-term impact on Earth's climate.

Another motivation to study gas hydrates is the energy resource they represent. The volume amount of methane at standard conditions is estimated to be $\sim$164 times the volume of methane bound in gas hydrates *in situ* [Kvenvolden, 1993]. However, most gas hydrate occurrences are heterogeneously distributed in fine-grained marine sediments and only a few reservoirs world wide in sand layers favour lucrative methane extraction. Gas hydrate production was tested in the MacKenzie Delta at the Mallik drill site [Dallimore and Collett, 2005], and 3000 m^3/day were extracted over a short period using reservoir depressurization. Dallimore et al. [2008] observed significant changes in physical properties of the sediment following gas hydrate dissociation, resulting in unconsolidated sands to gasified slurries. In the Alaskan North Slope, gas hydrate production is stimulated by fracturing and injecting carbon dioxide to replace methane in the hydrate lattice [Schoderbek and Boswell, 2011]. The first offshore production test for marine gas hydrates in the Nankai Trough offshore Japan has been successfully implemented with the depressurization method [*e.g.,* Yamamoto et al., 2014] and 20000 m^3/day of gas were recovered for six days. However, feasible production rates were not reached. Gas hydrate dissociation during petroleum production also implies risks due to gas blow outs and sediment collapse [*e.g.,* Dallimore et al., 2008].

1.2.1 Detecting gas hydrates with geophysical methods

Seismic methods are sensitive to the contrasts in seismic impedance at the base of the GHSZ, where the geotherm intersects with the GHSC (see Fig. 1.3). Solid gas hydrate in the sediments above the GHSZ increases the compressional velocity, and free gas below the GHSZ decreases it, resulting in a phase reversal of the seismic wave compared to the seafloor reflection. The reflector at the base of the GHSZ crosscuts strata and mimics the seafloor, and is therefore named the bottom simulating reflector (BSR) [Shipley et al., 1979; Hyndman and Spence, 1992]. While the presence of a BSR

does not require hydrate, it does require free gas below the GHSZ, because even small amounts of free gas reduce the compressional velocity sufficiently [Sloan and Koh, 2008]. BSRs are often the first indication of gas hydrate occurrences, although their presence may say little about the gas hydrate distribution in the sediment column above.

Several theories explain gas hydrate and free gas accumulation at the base of the GHSZ. For example, gas hydrate recycling [*e.g.,* Kvenvolden, 1993] occurs when sedimentation, sea level or temperature changes and tectonic uplift shift the base of the GHSZ. If the base of the GHSZ is shifted upwards, gas hydrates underneath dissolve and gas diffuses upwards to the new base of the GHSZ, where it may form gas hydrates which are more concentrated than before. Another theory is the fluid-expulsion model [*e.g.,* Hyndman and Davis, 1992], where upward migrating pore fluids increase the methane content in the GHSZ and gas hydrate builds up with a gradational top, which explains the common absence of seismic signatures within the GHSZ. The solubility-curvature mechanism of Haacke et al. [2007] suggests downward diffusion of methane to produce a thick free gas zone below the GHSZ, but the model is debated and restricted to specific regions.

Other seismic signatures of interest in addition to the BSR include bright spots (strong amplitudes) and seismic blanking (weak amplitudes), which can be related to massive gas hydrate accumulations [*e.g.,* Hornback et al., 2003]. Riedel [2007] relates intensified seismic blanking between sequential data acquisitions at the same site to recent gas hydrate formation and new subsurface fluid pathways. However, gas hydrates also exist when seismic signatures are absent [Sloan and Koh, 2008]. Accumulations of hydrate can be explained by fault systems or chimneys transporting free gas, which results in disruption and/or blurring of the seismic image of the sediment layering and bright spots [Holbrook et al., 2002]. Gas hydrate distributions can be estimated using elastic property inversion and rock physical modelling [*e.g.,* Dai et al., 2004]. However, gas hydrate are often heterogeneously distributed in the sediment matrix and form as cement between grain contacts, coat grains or fill pore spaces. Gas hydrates may grow as fracture-filling veins or can be uniformly distributed which depends on the distribution and amount of gas and the sediment type. Different models predict different seismic velocities and require calibration at drill sites [*e.g.,* Dai et al., 2008].

Downhole or well logging offers the best resolution for local gas hydrate characterization. Chlorinity, infrared imagery, sonic log velocities and resistivity logs are

all sensitive to gas hydrate occurrences [*e.g.,* Collett and Ladd, 2000; Riedel et al., 2006a]. Although logging is needed to verify and calibrate remote sensing methods, it is costly and invasive. The CSEM method offers an additional non-invasive approach to study the physical properties of gas hydrate-bearing sediments. It does not have the structural resolution of the seismic method, but it is sensitive to changes in the formation resistivity of a large volume instead of to the contrast alone. CSEM can indicate gas hydrate when no BSR is present [Yuan and Edwards, 2000] and support the existence of gas hydrate or free gas in seismic blank zones [Schwalenberg et al., 2005]. The offshore hydrocarbon industry has recently discovered the strengths of the electromagnetic methods to supplement the results from seismic methods. Some companies have developed their own electromagnetic systems and inversion algorithms [*e.g.,* Ellingsrud et al., 2002; Hu et al., 2009].

1.2.2 Relationship between resistivity and hydrate concentration

Archie's law is an empirical relationship that relates the resistivity of the formation ρ_0 and of the pore water ρ_w of fully saturated sediments as

$$\frac{\rho_0}{\rho_w} = a\phi^{-m}, \tag{1.1}$$

where ϕ is the porosity and m is a formation specific coefficient [Archie, 1942]. Winsauer and Shearin [1952] added the coefficient a to Eq. (1.1), which theoretically should be 1 as the ratio of the resistivities becomes 1 when $\phi = 1$. However, in practice non-unity values determined from calibration produce better results. Small values of m and a are linked to well-interconnected pore spaces. Hearst et al. [2000] implemented a saturation-dependent term

$$\frac{\rho_0}{\rho_w} = a\phi^{-m}S_w^n, \tag{1.2}$$

where S_w is the water saturation and n the saturation coefficient that depends on pore shape, connectivity, and the distribution of the conducting phase [Spangenberg, 2001]. If n is large, pore connectivity is assumed to be low [Riedel et al., 2006a]. The gas hydrate saturation S_h can be inferred from Eq. (1.2) by assuming that $S_h + S_w = 1$.

Equation (1.2) was developed using clean sands, but is widely used for marine

sediments, which contain a significant amount of clay. Archie's parameters a, m and n can be calibrated with logging resistivities and gas hydrate estimates from chlorinity measurements [*e.g.,* Serra, 1984; Malinverno et al., 2008]. Ignoring calibration may lead to over- or under-estimation of gas hydrate concentration. The effect of clay on the resistivity in marine sediments is also studied with alternative approaches [*e.g.,* Ellis et al., 2010] based on the Hashin-Shtrikman (HS) bounds [Schmeling, 1986; Hashin and Shtrikman, 1963]. The conductive bounds (HS+) correspond to resistive spherical inclusions within a conductive matrix, and the resistive bounds (HS−) correspond to conductive spherical inclusions within a resistive matrix. Figure 1.4 shows the formation resistivity as a function of porosity for the HS bounds and Archie's law for fully water-saturated sand with ρ_w=0.31 Ωm and ρ_s=10000 Ωm (for glacial sands [Palacky, 1988]) for a=1 and m=2. Figure 1.4 illustrates the exponential increase in resistivity for decreasing porosities < 0.2, while resistivities for a large porosity range > 0.2 differ only by a few Ωm. According to these relationships, a large amount of free gas is required to significantly increase sediment resistivity by replacing conductive pore fluid. In contrast, only a small amount of gas is required to significantly reduce seismic impedance, which produces a strong seismic signal [*e.g.,* Constable and Srnka, 2007]. Hence, seismic and EM methods together yield a better estimate of the amount of free gas and gas hydrate in the sediment.

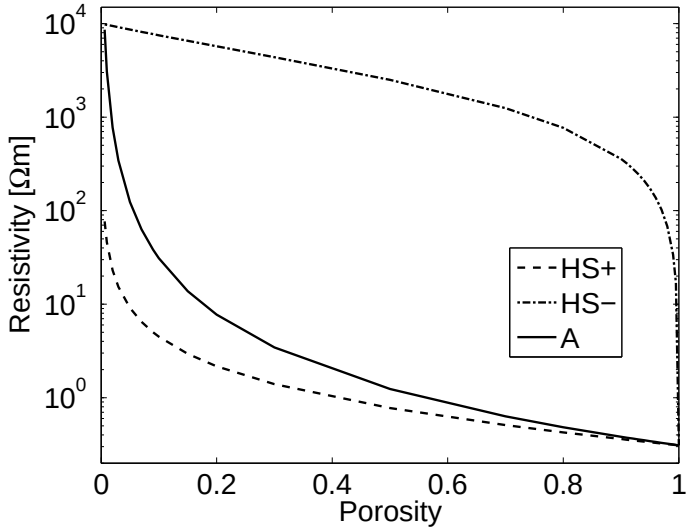

Figure 1.4: Hashin-Shtrikman conductive (HS+) and resistive (HS-) bounds and Archie's equation (A) relating formation resistivity and porosity.

1.3 Introduction to inversion methods

Inversion methods are mathematical algorithms to estimate model parameters and their uncertainties from geophysical data. This requires the definition and solution of the forward problem, the physical theory that describes the system of interest (*e.g.,* electric current flow in a resistive seabed). The forward problem predicts geophysical data for a given set of model parameters and has one unique solution. However, the solution to the inverse problem is typically non-unique: Different models may predict data that fit the observed data equally well [*e.g.,* Tarantola, 2005]. Reasons for this are that the observed data are limited to a finite number of observations which inevitably include measurement errors due to ambient noise (competing sources of signal in the environment) and imperfect instrumentation. Another reason is that the solution to the forward problem may involve approximations which are not perfectly satisfied and introduce theory error. Additionally, the choice of parametrization (discretization) plays an important role. It describes the discretization of the model space (for example, one-dimensional or three-dimensional, with layers or cells) that might only be accurate to a certain degree. Finally, the solution to the inverse problem is mathematical and might produce models which are physically unreasonable. To overcome these difficulties, prior knowledge about the physical system is considered carefully before defining the parametrization and the inverse problem, and generally the simplest parametrization is preferred over complex solutions if it explains the observed data sufficiently and agrees with prior information [*e.g.,* Constable et al., 1987; Menke, 2012].

Linear inversion theory for Gaussian error distributions and priors is fully described in the literature [*e.g.,* Tarantola, 2005], but, unfortunately, physical systems often do not behave linearly. However, in some cases a linearized approximation for local behaviour is adequate. The solution to the inverse problem is often one optimal model, whose predicted data fit the observed data best depending on data error assumptions and parametrization. Not knowing the parametrization properly can be countered with regularization, which restricts the inversion search, for example, to stay close to a starting model or sustain a smooth model if the data information does not indicate otherwise. However, linearization and regularization degrade uncertainty estimation. Non-linear methods based on numerical sampling of the parameter space avoid linearization and regularization approximations, but are often computationally expensive.

To avoid considering only a single optimal model which might be just one of many equally likely solutions, probabilistic approaches are developed that sample the parameter space for all possible solutions. Bayesian methods, named in honor of Rev. Thomas Bayes (1701-1761), are based on probability theory, where a posterior probability density for all unknown quantities of interest is estimated from observed data and prior knowledge. Bayesian probability is understood as a degree of belief. The subjective choice of parametrization influences the inversion results, and the subsurface model and uncertainty estimate need to be understood as the most appropriate solution for the observed data given the specific parametrization [*e.g.,* Gelman et al., 2000].

In this study, parametrization concerns the number of layers of a one-dimensional subsurface model. Estimating the number of layers is addressed with two methods, the Bayesian information criterion (BIC) and trans-dimensional Bayesian inversion, which are described in Sec. 5.2. While the BIC provides a fixed estimate of the number of layers, trans-dimensional inversion treats the number of layers as another unknown which is sampled in the inversion [*e.g.,* Malinverno, 2002; Sambridge et al., 2006].

1.4 Objectives and outline of the thesis

The overall objective of this thesis is to apply methods of progressive sophistication to simulated and observed CSEM data to investigate the sub-seafloor resistivity distribution and uncertainties. This is carried out in a series of studies. The first study investigates the sensitivity of the CSEM data to permafrost thickness with forward modelling and estimates model parameter uncertainties with a linearized technique. The second study applies non-linear Bayesian inversion to observed CSEM data on the Northern Cascadia margin to estimate parameter uncertainties and to investigate gas hydrate occurrences. The final study applies a trans-dimensional Bayesian inversion to observed data in the German North Sea to estimate parameter uncertainties considering an unknown parametrization and to investigate possible shallow gas occurrences. The results from CSEM inversion are compared to reflection seismic data to provide a more complete geological interpretation.

The thesis is organized as follows. Chapter 1 is a general introduction to the CSEM method, gas hydrates and inverse theory. The CSEM method and theory to solve the forward problem for a 1-D, layered subsurface model are described in detail

in Chapter 2. Chapter 3 introduces linear and linearized inversion theory and describes methods which are often applied to invert CSEM data. Chapter 3 also covers uncertainty estimation with linearized methods which are applied in Chapter 4 in a simulation study on the Canadian Beaufort Sea shelf to estimate the sensitivity of the CSEM method to permafrost thickness. Chapter 5 introduces non-linear inversion methods focusing on Bayesian inversion which is applied to simulated and measured data in Section 5.4 and Chapters 6 and 7 to estimate model parameters and uncertainties. In Chapter 6, measured data from the Northern Cascadia margin are analyzed with respect to gas hydrate and free gas occurrences at the landward edge of the gas hydrate stability zone and at a cold vent site. Chapter 6 is based on the paper (to be submitted) *"Bayesian inversion of marine controlled source electromagnetic data offshore Vancouver Island"* by R. A. S. Gehrmann, K. Schwalenberg, M. Riedel, S. E. Dosso and G. D. Spence. In Chapter 7, simulated and measured data from the German North Sea are analyzed with a trans-dimensional Bayesian inversion to evaluate possible shallow gas occurrences. Chapter 7 is based on the paper (to be submitted) *"Trans-dimensional Bayesian inversion of controlled source electromagnetic data in the German North Sea"* by R. A. S. Gehrmann, J. Dettmer, K. Schwalenberg, M. Engels, S. E. Dosso and H. Keil. Chapter 8 contains the summary and conclusion of the thesis.

Chapter 2

Controlled source electromagnetic theory

The controlled source electromagnetic (CSEM) method is based on electromagnetic diffusion, and is sensitive to the electrical resistivity, which in common marine sediments is particularly related to ionic conductance of pore fluids. The marine CSEM data in this study were acquired with the horizontal inline electric dipole-dipole technique (see Fig. 1.1). The horizontal electric dipole (HED) was first proposed by Bannister [1968] and later described by Chave and Cox [1982], and the inline source configuration (transmitter electrode parallel to the profile direction) is generally preferred to broadside (transmitter electrode perpendicular to the profile direction) in marine CSEM for its better vertical resolution and sensitivity to resistive layers (*e.g.*, hydrocarbon bearing sediments) [Cox, 1980; Cox et al., 1986; Key, 2009].

Figure 2.1 shows current diffusion in terms of the stream function of the current density (derived from Ampere's law) in a halfspace model with conductive seawater above the source dipole and resistive seafloor below. The electric current is injected at the transmitter dipole at time zero. After 10 ms it can be observed that the signal diffuses faster in the resistive seafloor, and after a few seconds the steady state of the electric field is reached. The latter is also referred to as the static limit controlled by direct current (DC) when alternating currents (AC) are absent.

Typical continuous waveforms injected at the transmitter dipole for time-domain are square or tristate waveforms for 100% and 50% duty cycle (the percentage when the signal is non-zero within one cycle) respectively. More elaborate doubly symmetric waveforms are used in the frequency domain to improve the signal-to-noise ratio for

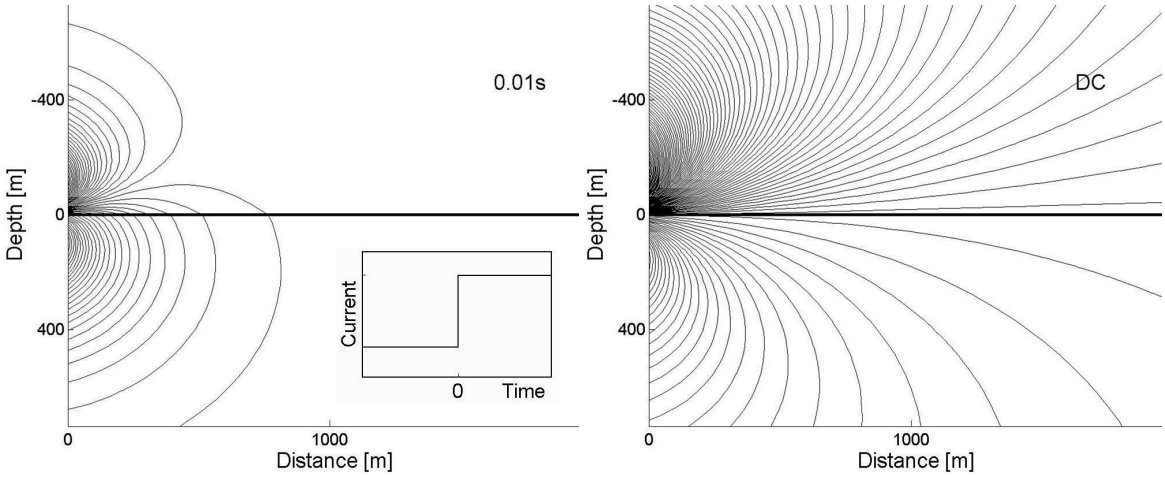

Figure 2.1: Stream functions of electric current density at 0.01 s (left) after current step on (see inlay), and after reaching steady state after a few seconds (DC) on the right. The horizontal electric dipole source on the seafloor is located 100 m to the left of the y-axis. The seawater halfspace has a resistivity of ρ_w=0.33 Ωm and the sediment halfspace of ρ_s=1.33 Ωm. Figure after Edwards et al. [2013] and Edwards [1988].

higher frequencies [Myer et al., 2011]. The square wave function used in this study (see Fig. 2.2) switches from negative to positive and vice versa within ∼1 ms, which is called a "step on". It remains at maximum current for a few seconds. A receiver in the same horizontal plane as the source measures the step-on response of the signal. The arrival time and amplitude of the response depend on the resistivity contrast between seawater and sub-seafloor sediments. The part of the signal that travels through the resistive seafloor arrives first (in greater water depth than a few hundred meters). However, the step-on response is dominated by the signal that travels through the conductive seawater when the static limit is reached [Edwards, 2005]. The electromagnetic field in a layered medium can be separated into two modes

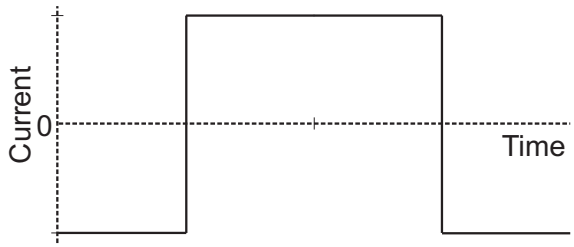

Figure 2.2: One cycle of a continuous square waveform.

characterized by the absence of a vertical magnetic field (transverse magnetic (TM) mode) and the absence of a vertical electric field (transverse electric (TE) mode). The TE mode is defined by horizontal current loops around the depth axis that are coupled by electromagnetic induction, while the TM mode defines current loops perpendicular to the latter that cut across vertically changing media. The TE mode only exists when the electric field is changing, when, according to Faraday's law of induction, a current is induced in the medium to counter changes in the primary field. The TM mode also exists when the static limit is reached, but is absent in highly resistive media (like air). Therefore, the step-on response is a composite of TE and TM modes at early times, when AC currents control the electromagnetic field, but is only made up of TM at late times, after the static limit is reached [Chave and Cox, 1982].

This chapter outlines the electromagnetic theory and the one-dimensional depth-dependent forward problem for the CSEM method.

2.1 Maxwell's equations

Maxwell's equations relate time varying electric and magnetic fields, electric charges and currents. An electric current I corresponds to the transport of electric charges within a conductive medium over time and its amplitude is given in Ampere (A). The density of electric current $\mathbf{j}$ ($[\mathbf{j}]$=A/m^2) depends on the amount of current flow through an area. The electric field $\mathbf{E}$ is linearly related to the current density by Ohm's law

$$\mathbf{E} = \rho\mathbf{j}, \tag{2.1}$$

where ρ is the electrical resistivity with units of Ohm meter (Ωm), and its inverse is the electrical conductivity σ (S/m). The unit of the electric field is given in Volt per meter (V/m), where Volt is the unit for the potential between electric charges. In magnetostatics the analog to electric charges are magnetic pole strengths and the magnetic field strength $\mathbf{H}$ in Ampere per meter (A/m) depends on the attractive or repulsive force between magnetic poles and the magnetic permeability $\mu = \mu_r\mu_0$, the product of relative permeability and permeability of free space $\mu_0 = 4\pi 10^{-7}$ Vs/Am. The magnetic induction is given with

$$\mathbf{B} = \mu\mathbf{H}, \tag{2.2}$$

and its unit is given in Tesla (T=Vs/m^2). More detail can be found, *e.g.,* in Griffiths [2012].

In time domain (quantities are indicated by lower-case letters) Maxwell's equation are described by the following partial differential equations [Ward and Hohmann, 1988].

1. Faraday's law of induction: Time varying magnetic induction creates an electric vortex field
$$\nabla \times \mathbf{e} + \frac{\partial \mathbf{b}}{\partial t} = 0. \tag{2.3}$$

2. Ampere's law with Maxwell's correction: Electrical current and changing electric fields create a magnetic vortex field
$$\nabla \times \mathbf{h} - \frac{\partial \mathbf{d}}{\partial t} = \mathbf{j}, \tag{2.4}$$
where $\mathbf{j}$ represents the contribution from conduction currents and $\mathbf{d}$ the contribution from displacement currents. The dielectric displacement is given by $\mathbf{d} = \epsilon\mathbf{e}$, where $\epsilon = \epsilon_r\epsilon_0$, the product of the relative permittivity and permittivity of free space $\epsilon_0 = 1/(c_0\mu_0)$, where c_0 is the speed of light in free space.

3. Gauss' law for magnetism: Magnetic monopoles do not exist
$$\nabla \cdot \mathbf{b} = 0. \tag{2.5}$$

4. Gauss' law: Relationship between the static electric field and electric charges causing it
$$\nabla \cdot \mathbf{d} = \rho_q, \tag{2.6}$$
where ρ_q is the volume charge density for free charges in a volume ($[\rho_q]$=C/m^3). In homogenous media without electric sources or sinks Eq. (2.6) simplifies to $\nabla \cdot \mathbf{e} = 0$.

2.2 The electromagnetic wave equation

Equation (2.3) and (2.4) can be combined to yield the damped wave equation for the electric field (there is an analogous equation for the magnetic field)

$$\nabla \times \nabla \times \mathbf{e} + \mu\sigma\frac{\partial \mathbf{e}}{\partial t} + \mu\epsilon\frac{\partial^2 \mathbf{e}}{\partial t^2} = 0. \tag{2.7}$$

The vector identity $\nabla \times \nabla \times \mathbf{a} = \nabla(\nabla \cdot \mathbf{a}) - \Delta\mathbf{a}$ in Cartesian coordinates and the Laplace operator $\Delta = \frac{\partial}{\partial x^2} + \frac{\partial}{\partial y^2} + \frac{\partial}{\partial z^2}$ are substituted in Eq. (2.7), and the result transformed into frequency domain to yield

$$\Delta\mathbf{E} - i\omega\mu\sigma\mathbf{E} - \omega^2\mu\epsilon\mathbf{E} = 0, \tag{2.8}$$

where frequency-domain quantities are denoted in capital letters. The notation in Eq. (2.8) helps to understand the following concepts. Electromagnetic fields in free space ($\sigma = 0$) sustain themselves over time and space, as displacement currents govern [Ward and Hohmann, 1988]. However, the conductivity of common rock types lies between 10 and 10^{-6} S/m and the electric permittivity varies between 10^{-9} to 10^{-11} F/m depending on water content. The magnetic permeability is reduced to μ_0 as long as amounts of magnetic minerals in the rock are minor. Marine CSEM utilizes frequencies in the range of 0.1-10 Hz. The low frequencies cause the second term in Eq. (2.8), the attenuation term, to dominate as $\sigma >> \epsilon\omega$ [*e.g.,* Constable, 2010]. Conductive currents govern over displacement currents and Eq. (2.8) reduces to the diffusion equation [Ward and Hohmann, 1988]:

$$\Delta\mathbf{E} = i\omega\mu\sigma\mathbf{E}. \tag{2.9}$$

2.3 The forward problem

In this study the model is a layered one-dimensional subsurface (see Fig. 2.3). Considered are the permittivity of an infinite air layer, the finite sea water thickness, its resistivity and the resistivity of k layers with depths for $k - 1$ layers. The electric dipole source and electric dipole receivers are horizontally aligned on the seafloor. At time $t = 0$ s a current is induced at the source and held constant. The Laplace-

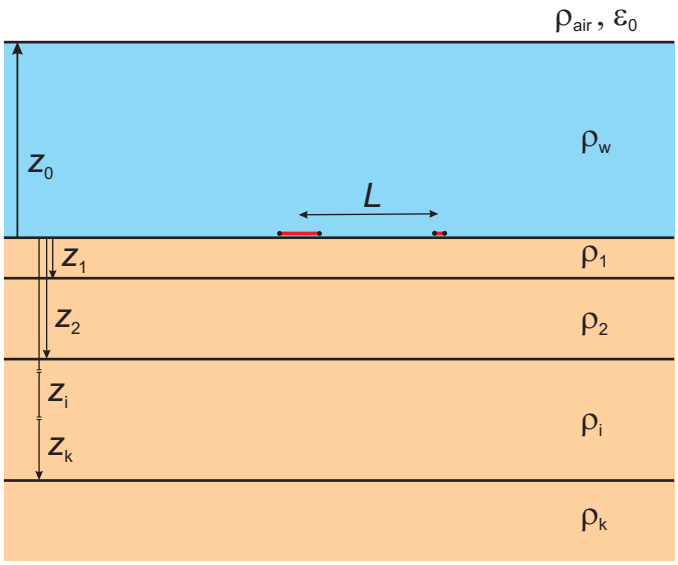

Figure 2.3: One-dimensional model with layered sub-seafloor and homogeneous water layer with transmitter and receiver bipoles at $z = 0$ (seafloor) and distance L from each other.

transformed electric field measured at a receiver dipole a distance L is given

$$E(s) = \frac{j(s)}{2\pi} \left[F(s) + G(s) \right], \tag{2.10}$$

where $s = i\omega$ is the Laplace variable, $j(s) = I\Delta l/s$ the current dipole moment, I is the maximum current and Δl the dipole length. The field is divided into $F(s)$ and $G(s)$ which are Laplace transformations of the TM and TE mode respectively [Edwards and Chave, 1986].

The TM mode is derived from Eq. (2.9), considering an active source, for the z component of the electric field, while the TE mode is derived for the z component of the magnetic field. The derivations require a two-dimensional Fourier transform from x, y into wavenumber domain and back which can be written in terms of the Hankel transform [*e.g.,* Ward and Hohmann, 1988; Scholl and Edwards, 2007] and $F(s)$ and $G(s)$ according to Edwards [2005] become

$$F(s) = -\int_0^\infty \frac{Y_0 Y_1}{Y_0 + Y_1} \lambda J_1'(\lambda L) \mathrm{d}\lambda, \tag{2.11}$$

$$G(s) = -\frac{s}{L} \int_0^\infty \frac{Q_0 Q_1}{Q_0 + Q_1} J_1(\lambda L) \mathrm{d}\lambda, \tag{2.12}$$

where Y_0 for the medium above the source (here, conductive seawater) and Y_1 for the medium below the source (here, seabed) relate the horizontal and vertical electric fields in the layered medium for the TM mode, and Q_0 and Q_1 analogous relate the horizontal and vertical magnetic fields for the TE mode. The Bessel function of first order J_1 and its derivative J_1' oscillate with increasing frequency and amplitude in regions of λL, where the kernel (*e.g.*, $(Y_0 Y_1)/(Y_0 + Y_1)$) decays and Eq. (2.11) and (2.12) are numerically realized by eliminating high-frequency, high-amplitude terms with a low-pass filter. The upward and downward recursion relationship in TM mode for the i^{th} layer is

$$Y_i = \theta_i \rho_i \left[\frac{Y_{i+1} + \theta_i \rho_i \tanh(\theta_i d_i)}{\theta_i \rho_i + Y_{i+1} \tanh(\theta_i d_i)} \right], \tag{2.13}$$

where d_i is the layer thickness and the electromagnetic wavenumber in the ground is $\theta_i = \lambda^2 + s\mu/\rho_i$ and in the air $\theta_{\text{air}} = \lambda^2 + s^2 \mu_0 \epsilon_0$ (as conductive currents are negligible compared to displacement currents in air). The starting layer for the downward recursion relationship is air with $Y_{\text{air}} = \theta_{\text{air}}/(s\epsilon_0)$. For homogeneous seawater the value above the source dipole becomes

$$Y_0 = \theta_0 \rho_0 \left[\frac{\theta_{\text{air}}/\rho_0 + s\epsilon\theta_0 \tanh(\theta_0 d_0)}{s\epsilon\theta_0 + \theta_{\text{air}}/\rho_0 \tanh(\theta_0 d_0)} \right], \tag{2.14}$$

The upwards recursion relationship starts at the bottom layer N with $Y_N = \rho_N \theta_N$ and Y_1 is calculated with Eq. (2.13), where the $(i+1)^{\text{th}}$ layer is below the i^{th} layer as shown in Fig. 2.3. Analogously, the upward and downward recursion relationship in TE mode for the i^{th} layer is

$$Q_i = \frac{\mu_0}{\theta_i} \left[\frac{\theta_i Q_{i+1} + \mu_0 \tanh(\theta_i d_i)}{\mu_0 + \theta_i Q_{i+1} \tanh(\theta_i d_i)} \right], \tag{2.15}$$

where $Q_N = \mu_0/\theta_N$ for the N^{th} layer, and Q_0 for a homogeneous sea becomes

$$Q_0 = \frac{\mu_0}{\theta_0} \left[\frac{\theta_0 + \theta_{\text{air}} \tanh(\theta_0 d_0)}{\theta_{\text{air}} + \theta_0 \tanh(\theta_0 d_0)} \right]. \tag{2.16}$$

Equation (2.10) is transformed into time domain with a discrete, inverse Laplace transform to yield the electromagnetic response, which for this study is the predicted horizontal electric field step-on response at the receivers.

In this thesis I apply the forward code in "Marine transient electromagnetic inversion program (MARTIN)" by Carsten Scholl [Scholl, 2010] written in the computing

language Fortran 90 (except for Sec. 2.4). The code approximates a finite bipole length by summing up the response of several mathematically infinitesimal dipoles. Streich and Becken [2011] have shown that approximating a bipole yields uncertainties especially for receivers close to the source. However, the uncertainty decreases rapidly with distance. The shape of the electronically imperfect step-on signal injected at the transmitter is accounted for by convolving the predicted exact step-on response at each receiver with the measured source signal.

2.4 Step-on response for 3-layer model

The three major characteristics of the horizontal electric step-on response to determine the resistivity of the subsurface are the late-time variation in amplitude (1), the early-time variation in amplitude (2), and the arrival time (3) of the signal [Edwards, 2005]. The arrival time of the signal can be estimated from the maximum of the impulse response, the time derivative of the step-on response. Edwards [2005] demonstrates step-on responses for a double halfspace model as presented in Fig. 2.1, where a halfspace of seawater above the source is less resistive than a homogenous seabed below (see step-on responses in Fig. 2.4). According to Edwards [2005], the arrival time and early-time amplitudes depend mostly on seabed resistivity (compare to left panel of Fig. 2.1). Late-time amplitudes depend on the resistivity contrast between the seawater and seabed resistivity and become less sensitive with increasing contrast. They are mainly controlled by the current flow through the seawater (compare to right panel of Fig. 2.1).

To understand the behavior of the step-on response for a layered sub-seafloor, including a resistive layer that represents, *e.g.*, gas hydrate occurrences, step-on responses are predicted with a simplified forward code from Mir [2011] (used in this section only) that is based on the theory introduced in Sec. 2.3. The sub-seafloor models consist of different combinations of three layers with varying thicknesses. The transmitter is a point dipole on the seafloor which induces a maximum current of 10 A. The seawater resistivity is set to 0.31 Ωm, its thickness to 1000 m, and the receiver-transmitter offset is 176 m similar to the offset used by Yuan and Edwards [2000]. The resistivities ρ for the three layers are chosen to be 0.8 and 1 Ωm representing common resistivities of marine sediments and 20 Ωm for a more resistive target (*e.g.*, sediments containing free gas or gas hydrate). The thickness of the middle layer th_2 is chosen to be 5, 20 and 50 m.

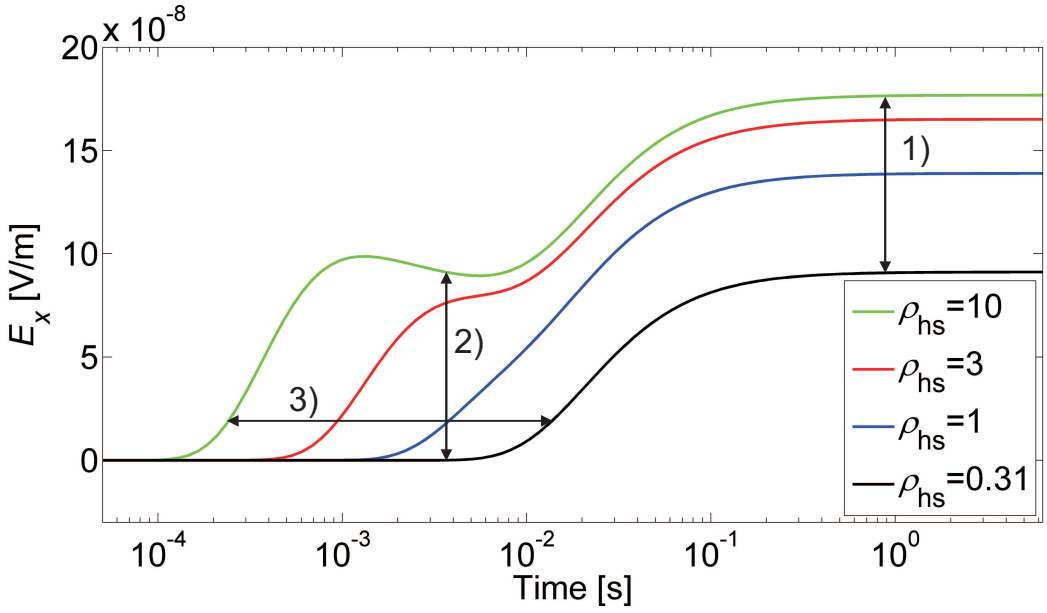

Figure 2.4: Step-on responses for halfspace models, where the horizontal electric source and receiver dipoles are located in line at the interface. The resistivity of the sea water is ρ_w=0.31 Ωm and the halfspace resistivity for the sub-seafloor is ρ_{hs} = 0.31, 1, 3 and 10 Ωm. The transmitter-receiver spacing is 176 m. The difference in sub-seafloor resistivity shows in 1) late-time amplitudes, 2) early-time amplitudes and 3) arrival time. Figure is modified from Edwards [2005].

Increasing resistivity with depth

In the scenario of increasing resistivity with depth, the subsurface resistivity increases from 0.8 Ωm on top, 1 Ωm in the middle to 20 Ωm on the bottom. Figure 2.5 shows the step-on responses for three 3-layer models with an overburden thickness th_1=5 m and varying thicknesses for the middle layer (th_2=5, 20 and 50 m), and step on responses for simple halfspace models ρ_{hs}=0.8, 1 and 20 Ωm for comparison.

The step-on response for a resistive halfspace model with ρ_{hs}=20 Ωm arrives earliest and has the highest early-time and late-time amplitudes. The step-on response for the 3-layer model with the smallest thickness of the middle layer (th_2=5 m) is closest to the resistive halfspace response. However, the two relatively conductive layers with a combined thickness of 10 m above the resistive bottom layer, cause the step-on response to arrive later and with smaller early-time amplitudes, making it easily distinguishable from the resistive halfspace model.

Increasing the thickness of the relatively conductive middle layer most strongly

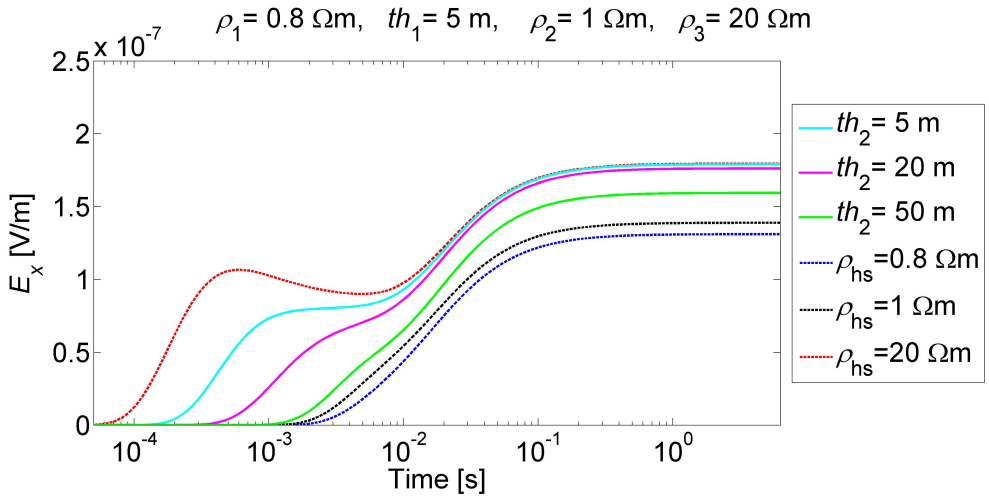

Figure 2.5: Step-on response for three 3-layer models (th_1=5 m) with increasing resistivities with depth and varying thicknesses for the middle layer and three halfspace models.

affects the early-time amplitudes (decrease) and the arrival times (signal arrives later). The late-time amplitudes, in contrary, seem to be governed by the resistive layer on the bottom as the step-on response for th_2=5 and 20 m converge towards the step-on response for the resistive halfspace model.

Figure 2.6 shows the variation in step-on responses for variations in the middle layer thickness, given a first layer thickness of th_1=50 m to evaluate the impact of a thick surface layer as well as the penetration depth of the configuration. Compared to the thin surface layer (Fig. 2.5), all curves arrive much later and early-time amplitudes are relatively small. The step-on response for a thick middle layer is between the responses of conductive halfspace models (close to ρ_{hs}=0.8 at early times and close to 1 Ωm at late times) showing that a contrast towards a resistive layer at 100 m depth is difficult to resolve ($> 0.5 \times L$), which represents the penetration limit.

Resistive middle layer

The next scenario is a conductive layer $\rho_1 = 0.8$ Ωm on top of a resistive layer ($\rho_2 = 20$ Ωm) with a conductive layer ($\rho_3 = 1$ Ωm) at the bottom to represent a simplified (1-D) vent scenario with a gas-free sediment layer on top. The step-on responses for a thin (th_1=5 m) surface layer are shown in Fig. 2.7. The step-on response for the resistive halfspace ($\rho_{\text{hs}} = 20$ Ωm) arrives earliest and has highest late-time amplitudes, but the early-time amplitudes are higher for the 3-layer model

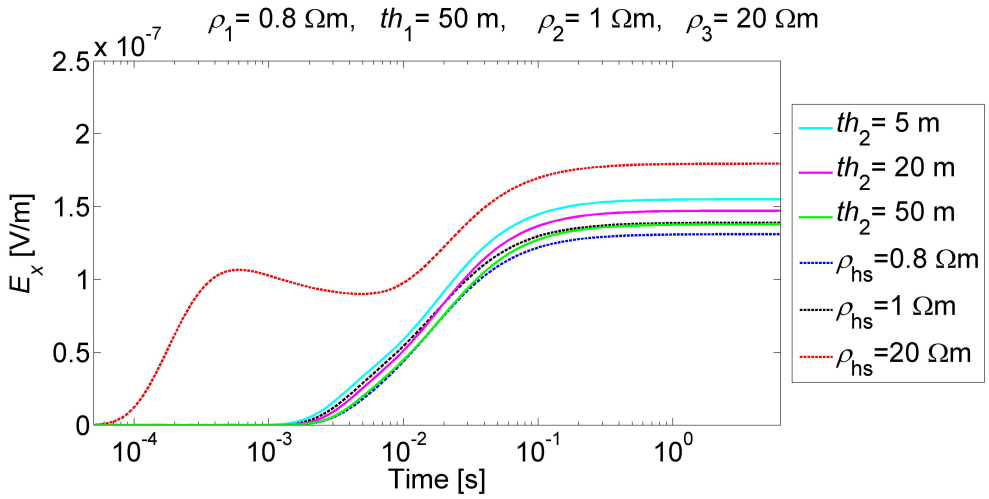

Figure 2.6: Step-on response for three 3-layer models (th_1=50 m) with increasing resistivities with depth and varying thicknesses for the middle layer and three halfspace models.

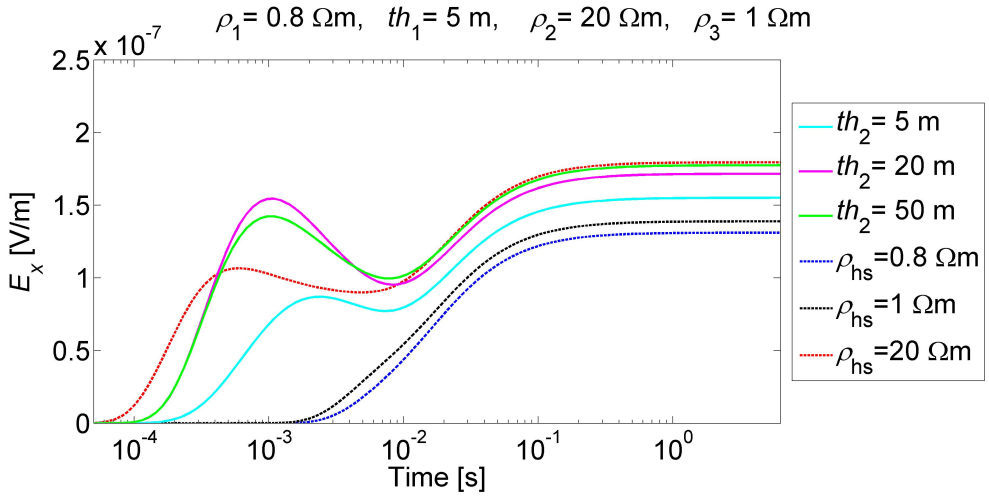

Figure 2.7: Step-on response for three 3-layer models (th_1=5 m) with resistive middle layer and varying thicknesses for the middle layer and three halfspace models.

with the resistive middle layer being 20 or 50 m thick suggesting that the early-time amplitudes are strongly enhanced by the contrast between the resistive middle layer and the more conductive layers above and below. The 20 m thick resistive middle layer results in the highest early-time amplitudes compared to a 5 m or 50 m thick layer indicating a trade-off between a relatively large layer thickness and sensitivity to the bottom layer (penetration depth).

The late-time amplitudes for the model with a 50 m thick resistive middle layer

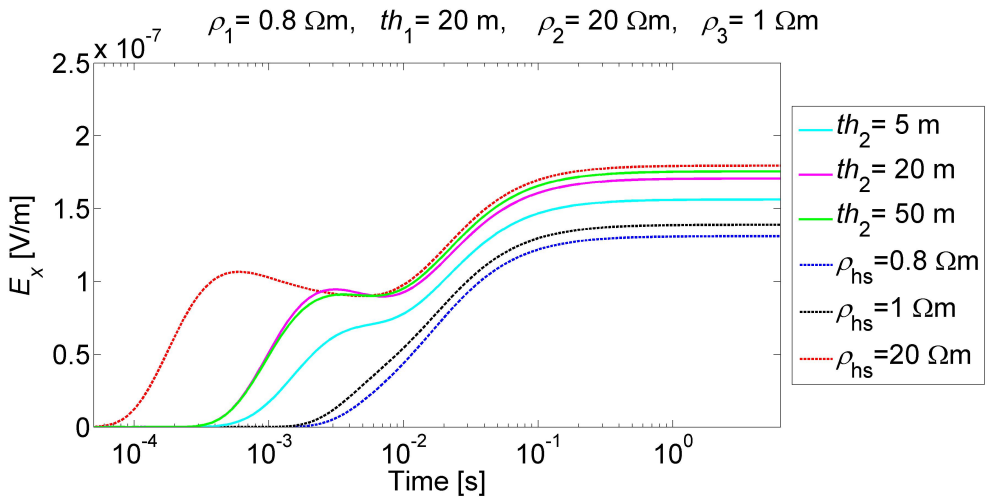

Figure 2.8: Step-on response for three 3-layer models (th_1=20 m) with resistive middle layer and varying thicknesses for the middle layer and three halfspace models.

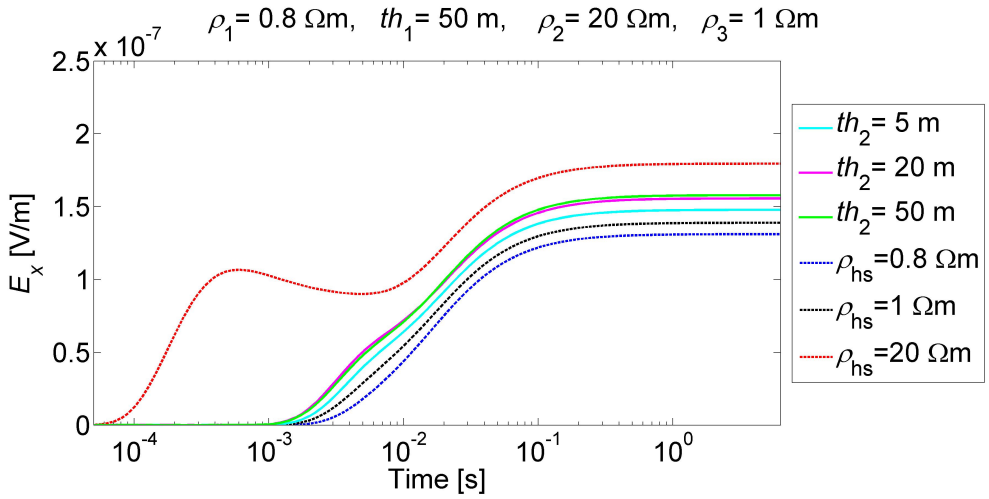

Figure 2.9: Step-on response for three 3-layer models (th_1=50 m) with resistive middle layer and varying thicknesses for the middle layer and three halfspace models.

are closest to the resistive halfspace model. However, the conductive surface layer seems to regulate the arrival times as they are the same for the step-on responses for th_2=20 and 50 m (thick resistive layer), but distinguishably later than for the resistive halfspace. A thicker surface layer of th_1=20 and 50 m causes the early-time amplitudes to decrease as shown in Figs. 2.8 and 2.9. For a 50 m thick surface layer, the response for a 3-layer model with th_2=20 and 50 m become more difficult to distinguish, probably because the penetration depth is limited to ∼100 m.

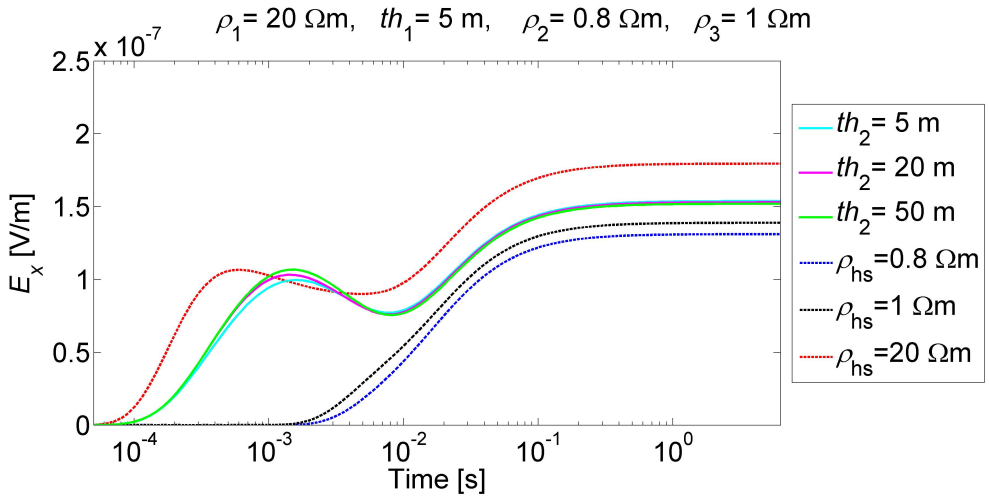

Figure 2.10: Step-on response for three 3-layer models (th_1=5 m) with resistive surface layer and varying thicknesses for the middle layer and three halfspace models.

Resistive surface layer

The last example examines a resistive surface layer (ρ_1= 20 Ωm), which represents resistive material directly underneath the seafloor (*e.g.*, gas hydrates may occur close to the seafloor at vent sites as discussed in Chapter 6). Step-on responses for a thin surface layer (th_1=5 m) are shown in Fig. 2.10. The step-on response for a resistive halfspace model (ρ_{hs}= 20 Ωm) arrives earliest and has the highest late-time amplitudes. The responses for different thicknesses of the middle layer are very similar, resulting in the two conductive sediment layers being hardly distinguishable. The arrival time is mostly controlled by the resistive overburden. Late-time amplitudes are between the more conductive and the resistive halfspace responses. A thicker surface layer (th_1=20 m in Fig. 2.11) results in late-time amplitudes that are closer to the resistive halfspace response. Arrival times are completely controlled by the resistive overburden. The 3-layer models show that the resistive surface layer has a strong impact on the early-time amplitudes as well. Early-time amplitudes are even higher than late-time amplitudes.

Conclusions

The observations for a 3-layer model containing one resistive layer give the following additional insights on information content in controlled source electromagnetic time-domain data: Arrival times are largely controlled by surface layer resistivity.

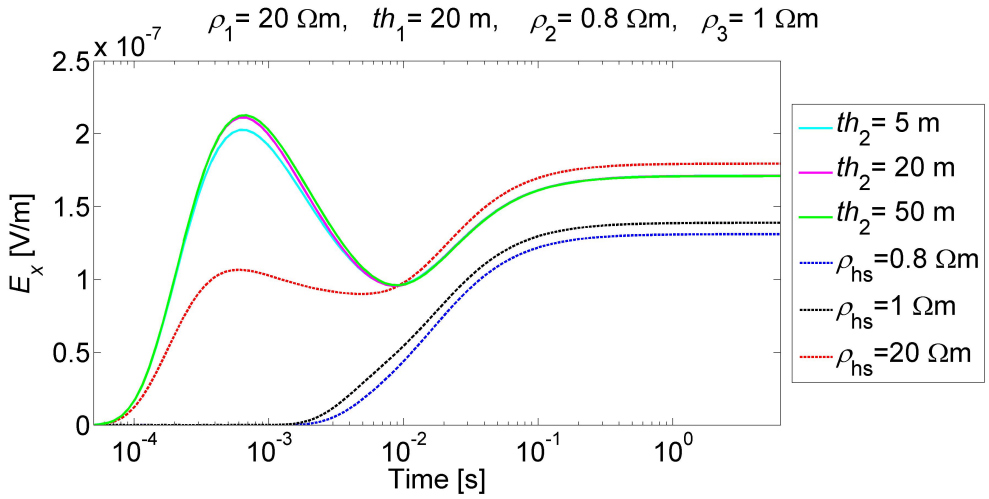

Figure 2.11: Step-on response for three 3-layer models (th_1=20 m) with resistive surface layer and varying thicknesses for the middle layer and three halfspace models.

Electromagnetic fields arrive fastest for a resistive halfspace model and may arrive at the same time for a 3-layer model with a relatively thin (here, th_1/L >0.1) resistive surface layer. However, an even thinner (here, th_1/L >0.05) conductive surface layer limits the arrival of the field to later times than for the resistive halfspace model.

Early-time amplitudes are controlled by the resistivity contrast between the sub-surface layers. A large contrast above and below a resistive layer within the penetration depth of the instrument produces large early-time amplitudes. These can even be higher than late-time amplitudes when the resistive layer is the surface layer and relatively thick (here, th_1/L >0.1).

Late-time amplitudes are largest for a resistive halfspace model. They are controlled by a combination of the sub-surface layers within the penetration depth of the instrument and approach the resistive halfspace model response for relatively thin resistive layers even in greater depth (here th_1/L >0.1 in <20 m depth).

The forward modelling study above has shown the strong sensitivity of the CSEM method with HED transmitter and receivers to a resistive layer, which represents sediments carrying hydrocarbons (*e.g.*, gas hydrates). The sensitivity is especially increased with increasing resistivity contrast between the material above and below the resistive layer. The penetration depth of the instrument for the specific cases above is below $\sim 0.57 \times L$, which is important to consider when designing a CSEM experiment.

Chapter 3

Linear inverse theory

Solving the geophysical inverse problem requires mathematical algorithms to estimate a subsurface model so that the predicted data match the observed data $\mathbf{d}$ within the data error assumptions. Solving the inverse problem requires solving the forward problem first. Data $\mathbf{d}(\mathbf{m})$ is predicted given knowledge of the physical theory and assumptions about the parametrization of the subsurface and its model parameters $\mathbf{m}$ with

$$\mathbf{d}(\mathbf{m}) = f(\mathbf{m}), \tag{3.1}$$

where $f(\mathbf{m})$ is a function based on the the physical theory. Many geophysical methods require solving the inverse problem to infer the subsurface model when non-linearity inhibits direct solutions. Solutions to inverse problems are often non-unique and unstable depending on model parametrization and parameter choice, partly because observed data only cover a finite number of samples of a continuous function and have an unknown data error due to instrumentation limits and ambient noise. Linear inversion theory is well known and solutions to the linear problem can be obtained using linear algebra (*e.g.*, Tarantola [2005], Meju [1994], Menke [2012]). If observed data and model parameters are linearly related the relationship can be written as

$$\mathbf{d} = \mathbf{J}\mathbf{m}, \tag{3.2}$$

where $\mathbf{J}$ is the sensitivity or Jacobian matrix. The following sections introduce selected algorithms which are often applied to invert controlled source electromagnetic data sets for a one-dimensional subsurface and will be referred to in this thesis.

3.1 Linearized inversion

Linearized inversions solve non-linear problems by assuming local linear behavior. Equation 3.1 is expanded in a Taylor series about a starting model $\mathbf{m}_0$, with higher order terms neglected, for observed data $\mathbf{d}$:

$$\mathbf{d} = f(\mathbf{m}_0 + \delta\mathbf{m}) = f(\mathbf{m}_0) + \mathbf{J}\delta\mathbf{m}, \tag{3.3}$$

where $\mathbf{d} - f(\mathbf{m}_0) = \delta\mathbf{d}$, and Eq. (3.3) can be rewritten as

$$\delta\mathbf{d} = \mathbf{J}\delta\mathbf{m}. \tag{3.4}$$

The sensitivity matrix is evaluated about $\mathbf{m}_0$ as $J_{ij} = \partial f_i(\mathbf{m}_0)/\partial m_j$. If J_{ij} is small, the i^{th} data sample is insensitive to a change in model parameter m_j and vice versa. The least-squares solution for $\delta\mathbf{m}$ can be estimated by minimizing the data misfit

$$X^2 = (\delta\mathbf{d} - \mathbf{J}\delta\mathbf{m})^T\mathbf{C}_d^{-1}(\delta\mathbf{d} - \mathbf{J}\delta\mathbf{m}) \tag{3.5}$$

with respect to $\delta\mathbf{m}$, where $\mathbf{C}_d$ is the data covariance matrix describing the data error statistics and ^{T} indicates transpose. The model change becomes

$$\delta\mathbf{m} = (\mathbf{J}^T\mathbf{C}_d^{-1}\mathbf{J})^{-1}\mathbf{J}\mathbf{C}_d^{-1}\delta\mathbf{d}, \tag{3.6}$$

and the updated model is given by $\mathbf{m}_1 = \mathbf{m}_0 + \delta\mathbf{m}$. Since higher-order terms were neglected in the linearization this procedure generally needs to be repeated iteratively ($\mathbf{m}_0 \leftarrow \mathbf{m}_1$) until convergence.

To solve Eq. (3.6) requires $(\mathbf{J}^T\mathbf{C}_d^{-1}\mathbf{J})$ to be nonsingular (the determinant is non zero), which is provided if the problem is even- or over-determined (data provide enough or even more information to solve for all model parameters). However, even- and over-determined problems can be ill-conditioned (close to singular) and under-determined problems (data do not provide enough information for all model parameters) are generally singular. Linearized inversions that are based on the data misfit alone may not yield physically meaningful results, especially when the inverse problem is ill-conditioned. Therefore, a regularization can be introduced that stabilizes the inversion by incorporating geologic constraints and prior assumptions about the model.

3.1.1 Marquardt inversion

The Marquardt optimization technique [Marquardt, 1963] is an extension to the general Gauss-Newton linearization approach that minimizes a least-square function of the data misfit (3.5). The Marquardt algorithm implements a regularization parameter μ to control the deviation of the new model from the old model by minimizing the objective function

$$\Psi^2 = (\delta\mathbf{d} - \mathbf{J}\delta\mathbf{m})^T\mathbf{C}_d^{-1}(\delta\mathbf{d} - \mathbf{J}\delta\mathbf{m}) + \mu\delta\mathbf{m}^T\delta\mathbf{m}. \tag{3.7}$$

The model change becomes

$$\delta\mathbf{m} = (\mathbf{J}^T\mathbf{C}_d^{-1}\mathbf{J} + \mu\mathbf{I})^{-1}\mathbf{J}^T\mathbf{C}_d^{-1}\delta\mathbf{d}, \tag{3.8}$$

where $\mathbf{I}$ is the identity matrix.

The regularization parameter μ controls the step size, that decreases with increasing μ. The choices are not completely subjective as they are often based on statistical requirements. For example, μ can be estimated for $X^2 \to N$, where N is the number of data samples and X^2 the expected misfit for Gaussian distributed errors.

The inversion algorithm that will be referred to as Marquardt inversion in this thesis is based on the Marquardt algorithm as described in Jupp and Vozoff [1975]. It computes the singular value decomposition of $\mathbf{J}^T\mathbf{C}_d^{-1}\mathbf{J} = \mathbf{USV}^T$ (see details in Sec. 3.2), then computes the generalized inverse $\mathbf{B}^g$ such that

$$\delta\mathbf{m} = \mathbf{B}^g\delta\mathbf{d}, \tag{3.9}$$

according to $\mathbf{B}^g = \mathbf{VTS}^{-1}\mathbf{U}^T$, where $\mathbf{T}$ contains damping factors t_i along its main diagonal. The damping factors for the Marquardt method implemented in this thesis are

$$t_i = \begin{cases} \frac{s_i^2}{s_i^2+\mu} & \text{for} \quad 1 \le i \le P \\ 0 & \qquad\quad i > P, \end{cases} \tag{3.10}$$

where P is the maximum number of linearly independent rows or columns of $\mathbf{J}$ and s_i are the singular values on the main diagonal of $\mathbf{S}$. A singular value threshold (computational limit) is defined to estimate P, so that $s_P/s_1 >\sim 2\cdot 10^{-16} > s_{P+1}/s_1$. The Marquardt method stabilizes the iterations and provides a robust solution to the inverse problem. However, difficulties may occur if the initial model is far from the

optimal model, if data errors are large or include outliers and if the parametrization is not well chosen. In practice, the threshold is adjusted throughout the inversion and a starting model with only few layers are chosen to avoid over-parametrization.

3.1.2 Occam's inversion

"It is vain to do with more what can be done with fewer"
William of Occam, early 14^{th} Century

Occam's inversion [Constable et al., 1987] aims for a minimum-structure solution following the principle that the true model might be more complex, but the solution of Occam's inversion represents what the data can actually resolve. It parametrizes the model using a large number of interfaces at fixed depths such that thicknesses of layers are below the resolution of the data, and introduces a regularization term minimizing the second depth derivative of the model parameters to constrain the result to a minimum-structure model. The objective function becomes

$$\Psi^2 = (\mathbf{d} - \mathbf{Jm})^T \mathbf{C}_d^{-1} (\mathbf{d} - \mathbf{Jm}) + \mu \mathbf{m}^T \mathbf{R}^T \mathbf{Rm} \tag{3.11}$$

where $\mathbf{R}$ is a discrete second derivative operator for the model change with depth z

$$\mathbf{m}^T \mathbf{R}^T \mathbf{Rm} \approx \sum_{i=1}^{M-2} \frac{\mathrm{d}^2 m_i}{\mathrm{d}z_i^2} \tag{3.12}$$

The trade-off parameter μ is optimized at every iteration, but objective estimation of the trade-off parameter can be challenging. Occam's inversion addresses geophysical data by smoothest-model regularization and avoids over-fitting the data, but regularization does not adapt locally to the structure supported by the data, which can result in over and/or under smoothing of parameters in various depth regions. Regularization also discriminates against abrupt changes and precludes rigorous uncertainty estimation.

3.2 Singular Value Decomposition

Another method to estimate an effective inverse of an ill-conditioned or singular matrix and therefore to provide stable solutions to the inverse problem is through singular value decomposition (SVD). In this thesis, however, the SVD is carried out

to study model parameter intercorrelation and to estimate parameter uncertainties after Edwards [1997]. Equation (3.4) shows the linear relationship of data changes to a combination of model parameter changes through the sensitivity matrix $\mathbf{J}$. The solution for the model parameters is ambiguous if $\mathbf{J}$ is ill-conditioned or singular. Therefore, the SVD decomposes the sensitivity matrix into three components:

$$\mathbf{J} = \mathbf{ULV}^T, \tag{3.13}$$

where $\mathbf{U}$ contains the column eigenvectors of $\mathbf{JJ}^T$ and can be used to transform the data into eigendata space, $\delta\mathbf{d}^* = \mathbf{U}^T\delta\mathbf{d}$. The diagonal matrix $\mathbf{L}$ consists of the singular values of $\mathbf{J}$ (square root of eigenvalues of $\mathbf{JJ}^T$ or $\mathbf{J}^T\mathbf{J}$). The matrix $\mathbf{V}$ contains the column eigenvectors of $\mathbf{J}^T\mathbf{J}$ and can be used to transform the model into eigenparameter space (also known as the principle axes system) with

$$\delta\mathbf{m}^* = \mathbf{V}^T\delta\mathbf{m}. \tag{3.14}$$

The eigenvectors are orthonormal and have the property that $\mathbf{U}^T\mathbf{U} = \mathbf{I}$ and $\mathbf{V}^T\mathbf{V} = \mathbf{VV}^T = \mathbf{I}$, where $\mathbf{I}$ is the identity matrix of the appropriate dimension ($N \times N$ for the number of data and $M \times M$ for the number of parameters respectively). Eigendata and eigenparameters are linearly related through singular values, which are generally ordered to decrease along the main diagonal of $\mathbf{L}$ (corresponding to a decrease in sensitivity), with

$$\delta\mathbf{d}^* = \mathbf{L}\delta\mathbf{m}^*. \tag{3.15}$$

To estimate the parameter resolution with the SVD according to Edwards [1997], $\mathbf{J}$ is scaled in the following way. It is divided by the data error, so that the standard deviation of the data becomes unity. Additionally J_{ij} is multiplied by m_j to transform it into $m_j J_{ij} = \partial d_i / \partial \ln(m_j)$. The logarithmic scaling is helpful for the physical interpretation and Eq. (3.14) becomes

$$\delta\ln(m_i)^* = \sum_{j=1}^{M} V_{ji}\delta\ln(m_j). \tag{3.16}$$

The eigenparameters δm_i^* are therefore linearly related to the product of the parameters $\prod_{j=1}^{M} m_j^{V_{ji}}$, which Edwards [1997] uses to describe a well known relationship between the resistivity and the thickness, which as a product (also called transverse

resistance) is often well resolved. The physical interpretation of the SVD results becomes complicated for more than a few parameters as it is mostly a mathematical approach. The model parameters (logarithmically scaled) can be estimated combining Eq. (3.16) and Eq. (3.15) to

$$\delta \ln(\mathbf{m}) = \mathbf{V}\mathbf{L}^{-1}\delta\mathbf{d}^{*}. \tag{3.17}$$

Edwards [1997] shows that the standard deviation for the eigendata is unity if the standard deviation of the data is unity. Therefore, the eigenparameter uncertainty is estimated from the inverse of the singular values (derived from Eq. (3.15)) as a function of the fractional measurement error ϵ (in percent) of the step-on response, and the standard deviation on the model parameters can be estimated with $\mathbf{V}\mathbf{L}^{-1}$ from Eq. (3.17). Edwards [1997] defines a coarse upper bound estimate (valid for small errors) with

$$\hat{\sigma}_{\ln(m_i)} = \sum_{j=1}^{M} |V_{ij}/L_{jj}|. \tag{3.18}$$

If $\mathbf{J}$ is ill-conditioned or singular, some values of $\mathbf{L}$ are vanishingly small compared to the maximum value and parameter errors become large (the solution to Eq. (3.4) is unstable) and a non-linear approach is needed to address parameter uncertainties instead. In this study the SVD is based on the work of Golub and Reinsch [1970] and implemented with the "Marine transient electromagnetic inversion program (MARTIN)" by Carsten Scholl.

3.2.1 SVD example

The chosen example is a three-layer model with a resistive layer 10 m below the seafloor, 20 m thick and with a resistivity of 10 Ωm representing potential gas hydrate or free gas accumulations. Resistivities above and below the resistive layer are 1 and 2 Ωm respectively. The simulated data for two receivers at 175 and 292 m offset with Gaussian random noise (2% standard deviation) and SVD results are obtained with MARTIN. Figure 3.1 illustrates the SVD results. The matrix $\mathbf{V}^{T}$ represents how the logarithm of the model parameters make up the eigenparameters. The eigenparameters resemble a combination of parameters with weights towards certain parameters. For example, the first eigenparameter with the smallest uncertainty is the dot product of the first row of $\mathbf{V}^{T}$ and $\delta\ln(\mathbf{m})$, and is mainly represented by ρ_2

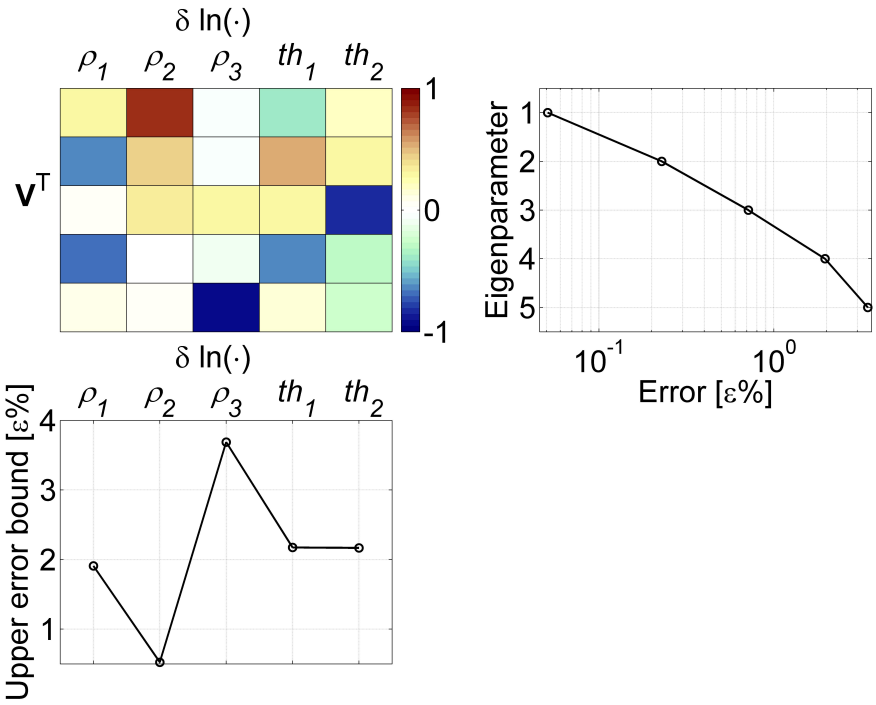

Figure 3.1: SVD analysis of a 3-layer model with resistive middle layer. Top left: $\mathbf{V}^T$ matrix (colourbar refers to V-values). Top right: Standard deviation of eigenparameters as a function of the fractional data error $\epsilon\%$. Bottom: Upper error bound estimate for model parameters. The $\cdot$ in $\delta\ln(\cdot)$ stands for the parameters (which are logarithmically scaled), *e.g.*, $\delta\ln(\rho_1)$.

and to a smaller fraction by ρ_1 and th_1. Therefore, ρ_2 has the lowest upper error bound and can be resolved best. Conversely, ρ_3 is almost only represented by the last eigenparameter with the highest uncertainty, and therefore has the highest upper error bound. The second eigenparameter is dominated by ρ_1 and a smaller fraction of th_1, similar to the fourth eigenparameter (but the sign of the $\mathbf{V}^T$-component for th_1 is opposite), and both values can be resolved well. The third eigenparameter is dominated by the thickness of the resistive layer and can also be resolved well. The resistivity of the resistive layer is resolved best demonstrating the sensitivity of the in-line electric dipole-dipole CSEM instrument to resistive structure.

Chapter 4

Permafrost at the Canadian Beaufort Sea shelf

The Beaufort Sea is a marginal sea of the Arctic Ocean north of Alaska (USA) and of the Yukon and Northwest Territories (Canada). In the Northwest Territories, the Mackenzie River empties into the Beaufort Sea, and forms the world's second largest arctic delta ($\sim$13000 km^2). The Mackenzie Delta is an active delta plain <4 m above sea level that contains several meandering channels and lakes. The deltaic sediments consist of interbedded silts and silty sands. The neighboring Tuktoyaktuk Coastland is an elevated terrain (up to 30 m above sea level) that has been modified (mostly eroded) in the late Pleistocene (glacial) and periglacial Holocene periods and contains glacial till or glaciofluvial sand and gravel [*e.g.,* Pelletier et al., 1987; Emmerton et al., 2007]).

The region is abundant in permafrost at varying depths with varying thicknesses from <100 m to >700 m. It reaches its maximum thickness in the northern Tuktoyaktuk Coastlands beneath Richards Island [Todd and Dallimore, 1998]. Permafrost is a volume of constantly frozen (<0°C for more than two years) sediment. A seasonally-thawed active layer on top of the permafrost is usually about 0.5 to 1 m (coast to inland) thick. The permafrost thickness is controlled by the mean temperature at the base of the active layer, the thermal conductivity of the sediments and the local heat flow. Water bodies that do not freeze in the winter cause the average ground temperature to be locally higher and therefore the permafrost to be thinner. The permafrost may contain sections of partially ice-bounded to non-ice-bounded sediment that may contain free gas, called taliks [Todd and Dallimore, 1998]. Thawing permafrost due

to climate change can have severe effects on the sustainability of coastal settlements and integrity of infrastructure and industry [Nelson et al., 2003].

The Beaufort-Mackenzie basin is abundant in natural gas (255×10^9 m^3) and recoverable crude oil (173×10^6 m^3) [Osadetz et al., 2005]. Gas hydrate has been observed in 20% of all exploration wells. Saturation varies from 50 to 90% and sediments are estimated to contain 2.4×10^{12} to 87×10^{12} m^3 of natural gas [Dallimore and Collett, 2005]. However, extraction implies great risks due to engineering hazards such as ice-scouring, permafrost, gas blowouts and soil failure. To estimate risks, the Federal Government and a segment of the Canadian petroleum industry formed the Beaufort Sea Project in the 1980s. Several research projects were funded to estimate the balance between commercial exploitation of natural resources, protection of the sensitive environment with a unique and versatile collection of animal species, and the preservation of the native culture [Pelletier et al., 1987].

The shelf regions in the Beaufort Sea vary in depth from zero at the delta to ∼100 m water depth after which the water depth increases rapidly and the permafrost pinches out due to warmer waters of ∼1°C at ∼300 m water depth. Free gas from gas-hydrate dissociation can cause the sediments to locally extend and form widely observed pingo-like features, which are characterized by a surface bulge and gas venting [Paull et al., 2007]. The permafrost offshore the Beaufort Sea coast degrades from Tuktoyaktuk Peninsula to northern Yukon due to sea-level rise and ongoing erosion of the shore. During the summer the warm discharge of the Mackenzie River thaws the upper permafrost that is submerged under seawater. The thawing takes place as long as the river outflow reaches the area through coastal water circulation and is supported by slow sea level rise and sediment accumulation. However, steady sea level rise result in larger water depths so that river discharge no longer reaches the seafloor and thawing stops [Dyke, 1991]. Thermal modelling of ocean-bottom temperature increase and the resulting temperature changes in the sub-seafloor suggest possible gas hydrate dissociation at the top and at the bottom of the GHSZ and permafrost thawing that may cause degassing at the seafloor. The vulnerable areas are shown in Fig. 4.1. Seafloor temperature is constantly increasing since 13.5 ka before present (BP) and the temperature subsequentially increases in the sub-seafloor changing the thickness of the stability zone of permafrost which was accumulated in the Pleistocene [Dallimore et al., 2011, 2012].

Seismic data are sensitive to the impedance contrast at boundaries of non-hydrate-bearing to hydrate-bearing sediments, but BSR occurrence is only patchy due to the

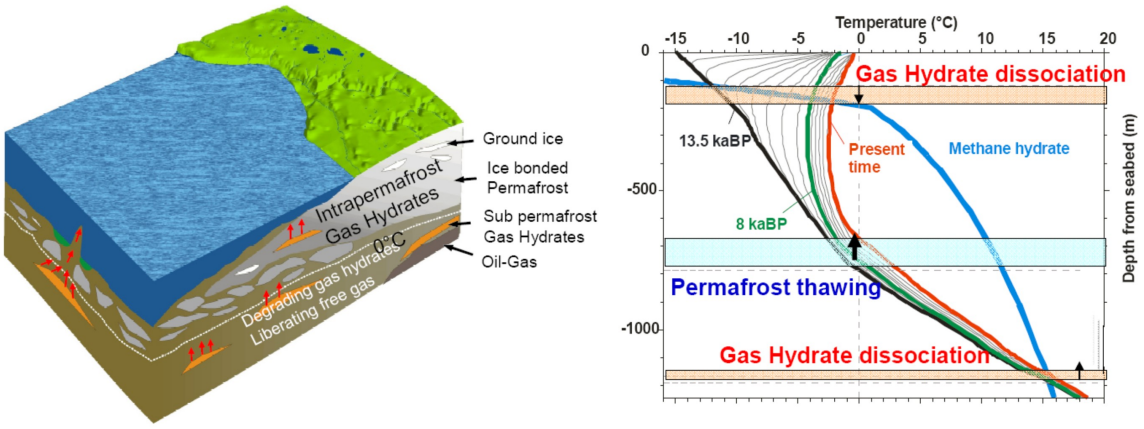

Figure 4.1: Left: Schematic drawing of the Beaufort shelf and coast with permafrost zones and gas hydrate both in the permafrost and below, as well as zones of gas hydrate degradation and pingo development. Right: Temperature over depth diagram for temperature curves 13.5 kaBP (black) to present time (red) and methane hydrate stability curve (blue), as well as resulting gas hydrate dissociation and permafrost thawing, courtesy S. R. Dallimore and C. K. Paull [Dallimore et al., 2012].

lack of free gas underneath the gas hydrate stability zone, as modelled by Andreassen et al. [1995]. Electromagnetic methods have been shown to be sensitive to permafrost as the electrical resistivity increases drastically for frozen sediments [Sartorelli and Frenc, 1982]. Todd and Dallimore [1998] conducted a transient time-domain electromagnetic (TDEM) experiment along a 30 km long transect across the Mackenzie Delta and correlated the results with resistivity and geological information from three boreholes (up to 451 m deep). TDEM measures the secondary electromagnetic field after the current in a transmitter loop has been switched off. The diffusing currents deepen and widen with time. The voltage measured at a central receiver loop over time contains information about the resistivity structure of the subsurface. The interpretation from this study for the central delta is a ∼50 m thick layer of permafrost (40 to 300 Ωm) overlying 100-150 m unfrozen sediments (2 to 3 Ωm) at temperatures $> -1.2°C$ and bedrock (siltstones and shales of the Richards Sequence with 5 to 15 Ωm). The main permafrost body (> 100 Ωm) further to the northeast extents to a depth of 600 to 750 m, but is nerved by a thin talik section (2 to 30 Ωm) at about 100 m depth.

Scholl [2010] presents a simulation study to examine the sensitivity of the long-offset transient electromagnetic (LOTEM) method above the Mallik test site to a gas

hydrate layer at 800 m depth. He simulated synthetic data for two horizontal electric fields and all three magnetic field components for broadside and inline configurations. Scholl [2010] implements a Marquardt inversion [Marquardt, 1963; Jupp and Vozoff, 1975] with varying starting models for a known number of layers with separate and combined inversions for the electric and magnetic fields. A few 10s of models, which fit the data within the error estimates, are obtained from inversions with different starting models. The results for separate inversions (broadside or inline, electric or magnetic fields separately) show significant ambiguity, but a joint inversion seems to improve the model resolution. The gas hydrate layer can be resolved with a joint inversion of H_z (broadside configuration) and E_x (inline configuration) and Tx-Rx offsets >2 km. In all cases small-scale inhomogeneities (a 100 m thick layer with 10 Ωm in a 60 Ωm gas hydrate layer at 1 km depth) within the hydrate layer are not detectable. Forward modelling of LOTEM inline and broadside configurations [Scholl, 2010] show that the gas hydrate layer can only be resolved in special cases, but the permafrost closer to the surface seems to be well resolved.

4.1 CSEM modelling study

The following study models permafrost scenarios on the Beaufort Sea shelf to estimate the sensitivity of the CSEM HED system to the top and bottom of the permafrost, to variations within the permafrost (*e.g.*, ice-bonded to non-ice bonded sediment) and to gas hydrate occurrences underneath the permafrost.

A special challenge for marine CSEM methods in relatively shallow water (compared to the maximum offset of the array) is the resulting sensitivity of the instrument response to the strong resistivity contrast between the conductive seawater and the insulating air above. The electric field is "guided" along this resistivity contrast producing an "airwave" which dominates the initial arrival of the electric field observed at the receivers in the time domain and masks most of the measured data at typical frequencies in the frequency domain [Weiss, 2007; Weidelt, 2007]. While handling data in the time or frequency domain theoretically yields the same information, practical differences exist due to collection and processing of a selected number of data with different sources and noise levels. For example, frequency-domain data are often displayed in terms of real and quadrature components of the recorded electrical field as a function of transmitter-receiver offsets for a limited number of frequencies, while time-domain data are given by a step-on response of the electric field amplitude as

a function of time (logarithmically spaced) for each transmitter-receiver offset [*e.g.,* Cheesman et al., 1987]. Therefore, time-domain data are preferred in shallow water as a broader frequency range is available and the static limit (DC part) is included. The static limit contains most of the seabed response similar to DC resistivity measurements on land [Weiss, 2007; Weidelt, 2007]. Weiss [2007] models the impulse response, the derivative of the step-on response, that corresponds to the arrival of the electromagnetic field, and points out that the airwave signature arrives earliest and almost synchronously at several receiver locations in shallow water depth. In intermediate water depth the airwave signature is eventually superimposed on the geologic signatures of interest. Both the airwave and the signature of resistive structure cause the electric field to arrive earlier and also increase the amplitude at the static limit because of diminished ohmic losses.

Scott [1992] measured Beauford Sea water resistivites of 2 Ωm in 1985 and higher variations in 1990 (1-8 Ωm) depending on the discharge of the MacKenzie River. River discharge can cause semi-fresh water bodies to float within the shelf waters [Carmack and Macdonald, 2002]. However, wind stress promotes upwelling of ocean water onto the shelf, which causes the salinity to be relatively high in some regions on the shelf [Williams and Carmack, 2008]. Therefore, resistivity varies laterally and vertically along the shelf. An average value far from the river delta is 0.38 Ωm estimated with the equations of Fofonoff [1985]. Therefore I choose to model "conductive" and "resistive" seawater of 0.38 and 2 Ωm, accordingly.

Different subsurface models were chosen for the Beaufort Sea permafrost scenario. Models 1 to 3 (Fig. 4.2) are 3-layer models with different depths to the permafrost and different overburden and permafrost resistivities. They are based on the subsurface models inferred by Scott [1992], who conducted an experiment with the ship-towed MICRO-WIP (Waterborne Induced Polarization) system in 1985. Scott [1992] concluded that overburden resistivity varies from 1.6 to 2.6 Ωm. Resistivities in permafrost depth vary from 10 to >500 Ωm and have been correlated with ice-bounded sediments in one borehole. The data interpretation also revealed one intermediate layer with a lower resistivity (between 0.5 to 1.5 Ωm). There is no direct geological correlation to explain this, but Scott [1992] suggests a pronounced increase in salinity above the degrading permafrost.

Depth to permafrost

To analyze the sensitivity to the depth of the permafrost z_P, model 1A and 1B are compared with z_P=40 and 20 metres below seafloor (mbsf) respectively. Figures 4.3 and 4.4 show the difference of the step-on responses for a dipole-dipole CSEM array with 10 receivers in 100 m intervals for conductive and resistive seawater. The grey scale in the left panel is normalized with the absolute standard deviation (2% on half of the maximum value of the step-on response). The arrival time is estimated from the maximum of the impulse response, the time derivative of the step-on response, which is estimated by dividing the difference of neighboring data samples by their associated time difference. The effect of the strong resistivity contrast at the water-air interface on the arrival time can be seen, for example, in Fig. 4.3 when comparing the step-on response for model 1B for 10 m water depth and 1000 m water depth. In 10 m water depth the signal arrives later and only one major increase in amplitude can be observed, while in 1000 m water depth (almost no airwave distortion) the early-time amplitudes are larger and indicate the presence of resistive material in the subsurface.

The difference between the step-on responses of models 1A and 1B is significant, and even larger for resistive seawater (Fig. 4.4). Here, the signal arrives earlier and

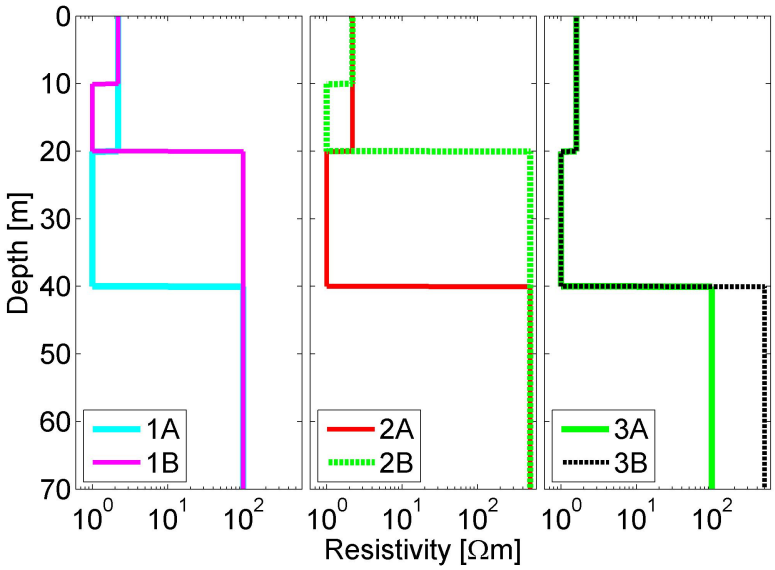

Figure 4.2: Models 1 to 3 with conductive layer of unfrozen sediment above permafrost and different depths to the permafrost as well as different resistivities for the permafrost layer.

the field strength is larger than for the conductive seawater case, but the early-time amplitudes are not as pronounced as for the conductive seawater case. For 1000 m water depth the late-time amplitudes in conductive seawater are the same for both models as they are probably governed by the field diffusing through seawater. However, a difference in late-time amplitudes exist for resistive seawater.

The step-on responses shown in Fig. 4.3 suggest that there is a transition depending on water depth between the time where the step-on responses differ most. The major difference of the step-on response for shallow water is most pronounced in

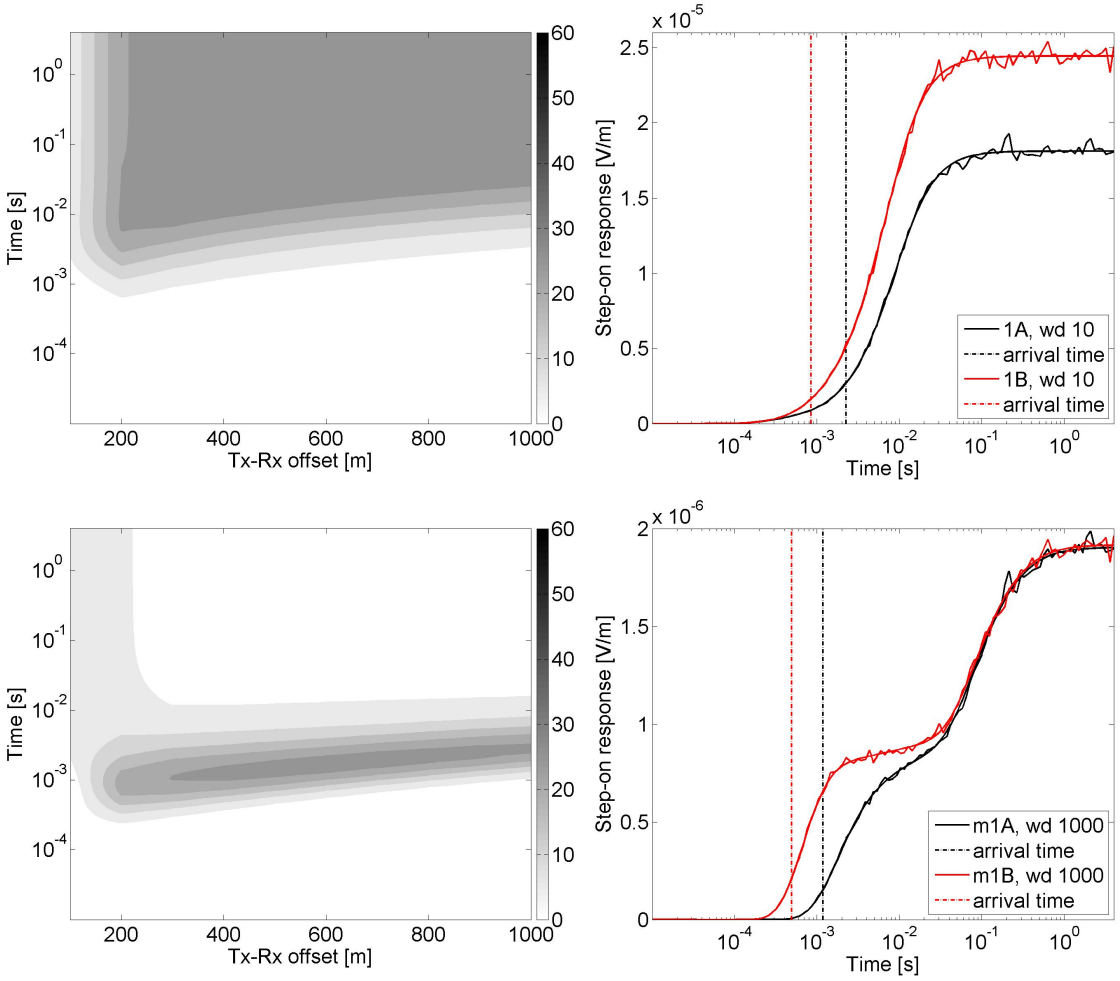

Figure 4.3: Right: Predicted step-on responses for model 1A and model 1B with and without Gaussian random noise for Tx-Rx offset 400 m in 10 m (top) and 1000 m (bottom) water depth (wd). Left: Normalized deviation (colour bar) of the two responses for Tx-Rx offset of 100 to 1000 m and time. Water resistivity is ρ_w=0.38 Ωm.

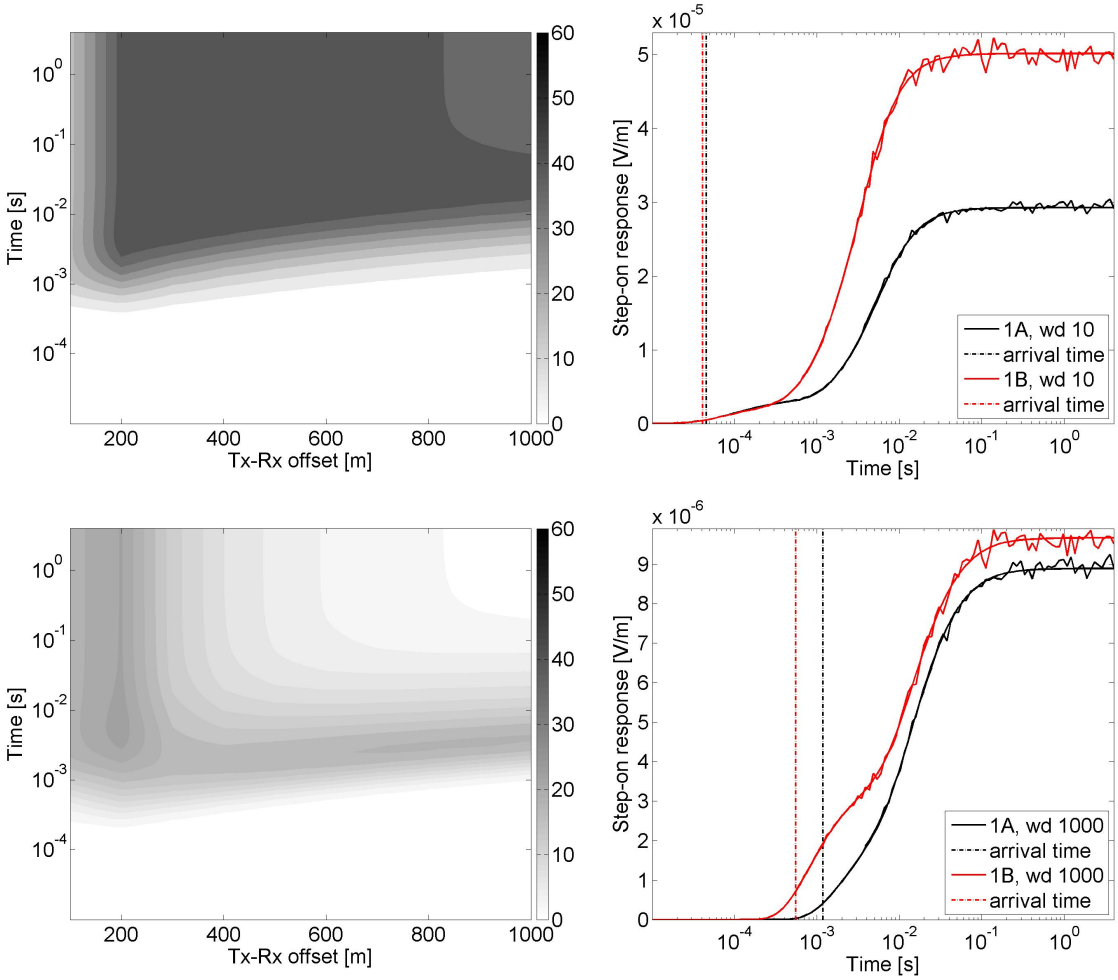

Figure 4.4: Right: Predicted step-on responses for model 1A and model 1B with and without Gaussian random noise for Tx-Rx offset 400 m in 10 m (top) and 1000 m (bottom) water depth (wd). Left: Normalized deviation (colour bar) of the two responses for Tx-Rx offset of 100 to 1000 m and time. Water resistivity is ρ_w=2 Ωm.

late-time amplitudes, while for deep water depth the difference is more pronounced in early-time amplitudes. This is related to the superposition of the airwave signature onto the response of the geological structure demonstrated by Weiss [2007] and depends on the depth and resistivity of the subsurface structure of interest. Figure 4.5 shows the scaled data misfit of the step-on response for water depths up to 300 m and Tx-Rx offsets of 100 to 1000 m for conductive seawater. The scaled data misfit for each receiver Rx_j at increasing offsets to the source dipole is defined for the

permafrost study by

$$X_j^2 = \frac{1}{N_j} \sum_{i=1}^{N_j} ((d_i(\mathbf{m}_p) - d_i(\mathbf{m}_q))/\hat{\sigma}_{\mathbf{d}_j})^2, \tag{4.1}$$

where $\mathbf{d}(\mathbf{m}_{p/q})$ is the predicted data for model p and q respectively (for example, p=1A and q=1B), $\hat{\sigma}_{\mathbf{d}_j}$ is the estimated standard deviation (2% of the step-on response at half maximum) and N_j is the number of data for the j^{th} receiver, which scales the misfit for readability in this section only. If $X^2 < 1$ the data curves do not differ beyond the data error threshold and can hardly be distinguished.

The transition in Fig. 4.5 lies between 70 and 120 m water depth and is characterized by a low data misfit between the two step-on responses. It can be called a blind window if the data misfit falls below the threshold, where the CSEM array is not sensitive to the difference between the two models. Model 1A and 1B can easily be distinguished with a CSEM array with offsets >200 m for water depths <70 m and with an increasing range around 400 m offset at water depths >120 m.

To analyze the resolution of the models individually the SVD analysis is applied.

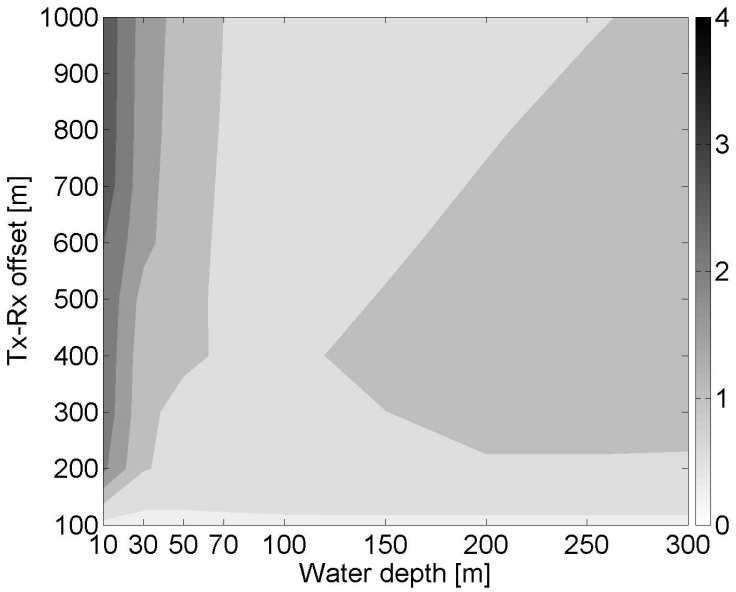

Figure 4.5: Data misfit (colour bar) between step-on response for model 1A and 1B at 10 to 300 m water depth for Tx-Rx offsets of 100 to 1000 m. A blind window (step-on responses cannot be distinguished) can be identified between ∼60 and 150 m water depth.

Figure 4.6 shows the results for models 1A and 1B for the conductive seawater case (estimated for a CSEM array with four receivers at 150 m, 250 m, 450 m and 750 m offset similar to an existing CSEM array [Schwalenberg and Engels, 2012a]) and 10 m water depth. Model 1B with the shallower depth to the permafrost can be resolved better than model 1A (the upper error bound for model 1A is almost double compared to 1B). The resistivity of the overburden can be resolved best (upper error bounds are small) as it is equal to the second eigenparameter (second row of $\mathbf{V}^T$). The resistivity of the permafrost layer can also be resolved well with an upper error bound of $5\epsilon\%$ (fractional errors depend on the fractional measurement error ϵ). The resistivity of the middle layer can only be resolved in combination with its thickness (see first and last row of $\mathbf{V}^T$) and the parameters individually have the highest upper error bounds.

Overburden and permafrost resistivity

When comparing models 1, 2 and 3 the sensitivity of the CSEM array (with HED transmitter and receivers) to overburden and permafrost resistivity can be analyzed. Overburden resistivities for models 2A and 3B are 2.2 Ωm and 1.6 Ωm respectively. The deviation of the step-on responses for models 2A and 3B, shown in Fig. 4.7, for 10 m water depth show that Tx-Rx offsets <200 m are more sensitive to the overburden resistivity than larger offsets. The deviation is strongest for late-time amplitudes.

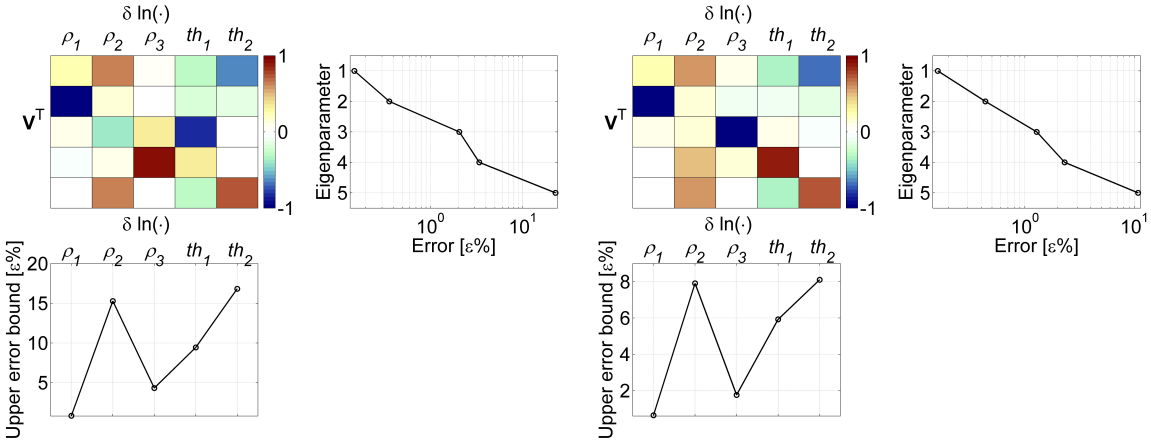

Figure 4.6: SVD analysis of model 1A (left) and 1B (right) for 10 m water depth and ρ_w=0.38 Ωm showing the V-values (colour bar), the eigenparameter standard error and the upper error bounds are fractional errors depending on the fractional measurement error ϵ. The $\cdot$ in $\delta\ln(\cdot)$ stands for the parameters (which are logarithmically scaled), *e.g.*, $\delta\ln(\rho_1)$.

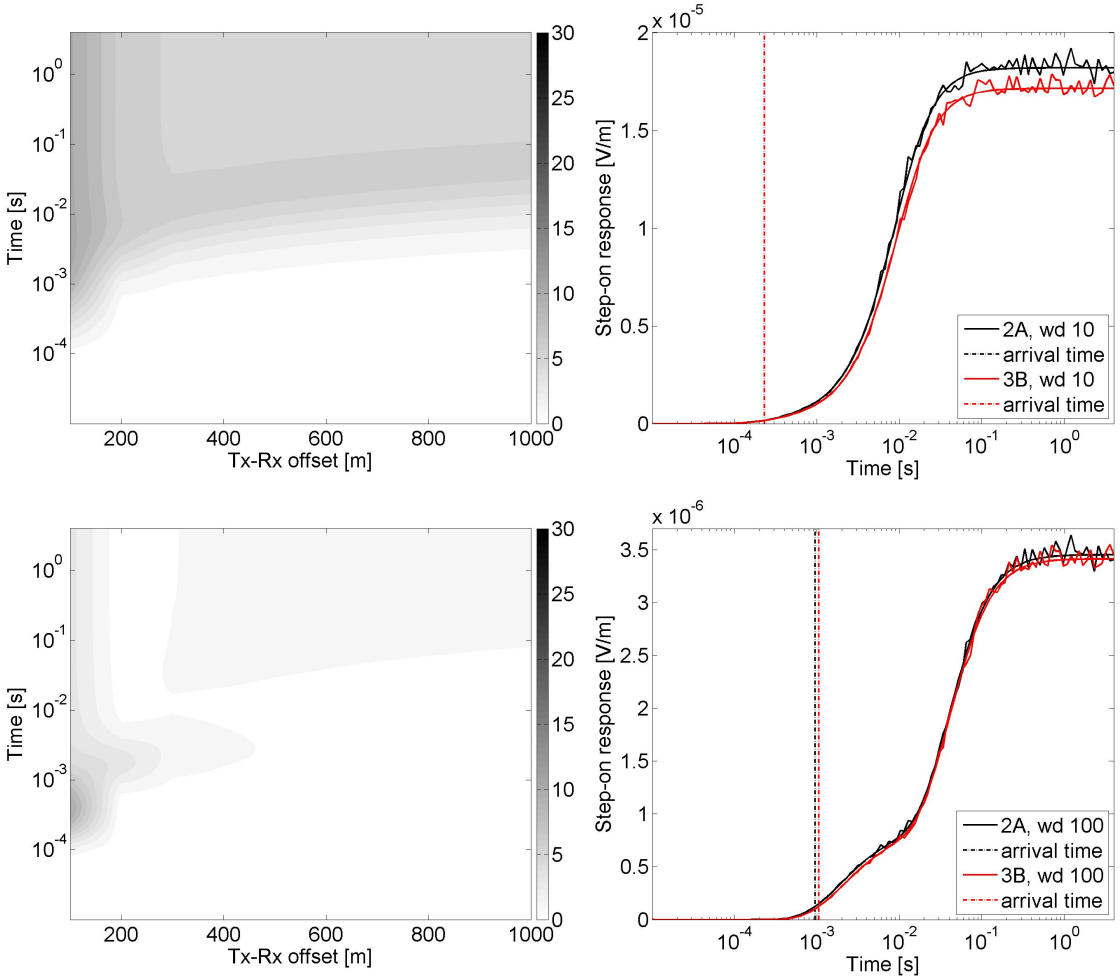

Figure 4.7: Right: Predicted step-on responses for model 2A to model 3B with and without Gaussian random noise for Tx-Rx offset 400 m in 10 m (top) and 100 m (bottom) water depth (wd). Left: Normalized deviation (colour bar) of the two responses for Tx-Rx offset of 100 to 1000 m and time. Water resistivity is ρ_w=0.38 Ωm.

The larger the water depth becomes the smaller the effect on the late-time amplitudes and the greater the response of the sub-seafloor on the early-time amplitudes becomes. The difference between the responses is larger for resistive seawater, and late-time amplitudes still deviate at 100 m water depth as shown in Fig. 4.8. Figures 4.7 and 4.8 show that the step-on response for a higher overburden resistivity arrives slightly earlier and has higher amplitudes. In summary, the overburden resistivity can be resolved best in shallow water depth for Tx-Rx offsets <200 m and resistive seawater.

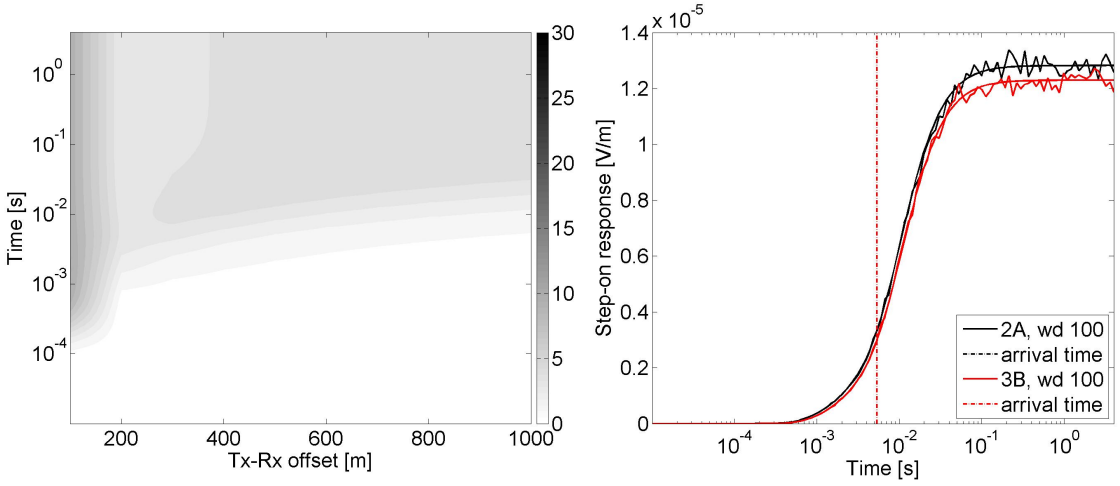

Figure 4.8: Right: Predicted step-on responses for model 2A to model 3B with and without Gaussian random noise for Tx-Rx offset 400 m in 100 m water depth (wd). Left: Normalized deviation (colour bar) of the two responses for Tx-Rx offset of 100 to 1000 m and time. Water resistivity is ρ_w=2 Ωm.

The sensitivity of the CSEM array to different permafrost resisitivities is analyzed by comparing step-on responses for models 1B and 2B (thin overburden on top of permafrost layer with 100 Ωm and 500 Ωm respectively) which are shown in Fig. 4.9. The step-on responses for 30 m water depth are almost identical, except for the arrival time. Deeper water depth of about 100 m or more resistive water (see Fig. A.1 in App. A.2) would be necessary to distinguish between different permafrost resistivities. The misfit of the responses at different water depth is shown in Fig. 4.10, where a blind window can be identified between 30 and 70 m water depth. Comparing the step-on responses for conductive seawater and resistive seawater in Figs. 4.9 and A.1 suggests that the blind window is at greater water depths for resistive seawater. In summary, the difference of the step-on responses for models with different permafrost resistivity shows largely in the arrival time and is generally greater for longer Tx-Rx offsets. A transition window for shallow water depths (here, between ∼30 and 70 m) and a blind window that extends up to ∼200 m water depth makes it difficult to distinguish the responses. The blind window shifts to deeper water depths for more resistive seawater.

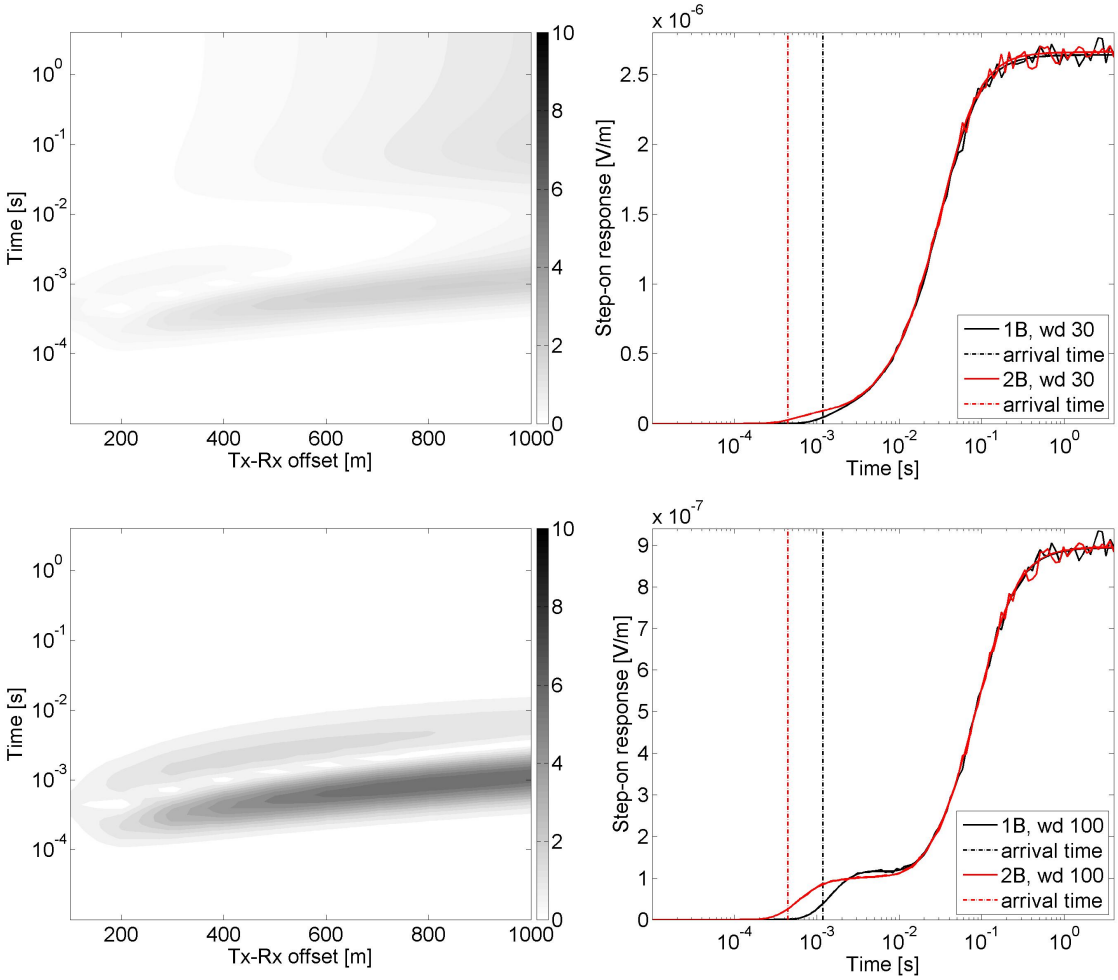

Figure 4.9: Right: Predicted step-on responses for model 1B and model 2B with and without Gaussian random noise for Tx-Rx offset 800 m in 30 m (top) and 100 m (bottom) water depth (wd). Left: Normalized deviation (colour bar) of the two responses for Tx-Rx offset of 100 to 1000 m and time. Water resistivity is ρ_w=0.38 Ωm.

Conductive layer underneath the permafrost

Models 4 (see Fig. 4.11) are 6-layer models that include an unfrozen sediment (conductive) and a gas hydrate layer underneath the permafrost based on the model of Scholl [2010]. The SVD analysis for models 4A and 4B (bottom of the permafrost in 440 and 240 mbsf respectively) in Fig. 4.12 reveals high upper error bounds for structure below the permafrost section. However, the CSEM array is sensitive to the bottom of the permafrost and the upper error bounds for the resistivity of the conductive layer and the thickness of the permafrost are considerably smaller for model 4B

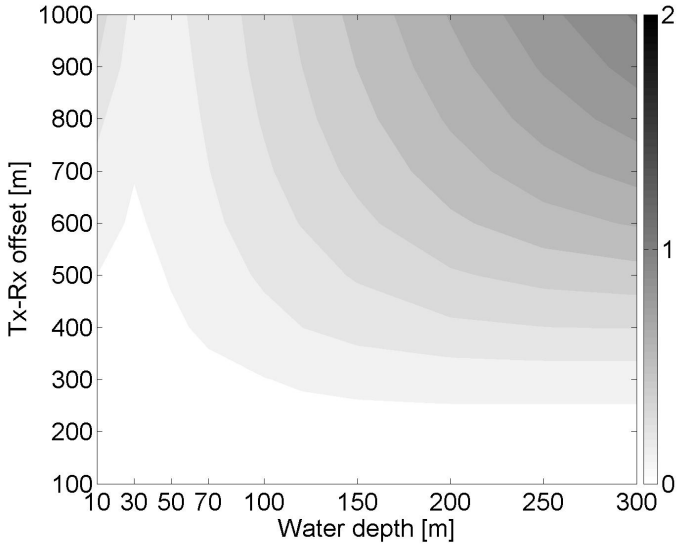

Figure 4.10: Data misfit between step-on response for model 1B and 2B at 10 to 300 m water depth for Tx-Rx offsets of 100 to 1000 m for conductive seawater. The transition window is between ∼30 to 70 m water depth, but the blind window extends wider (data misfit required to be above the threshold of 1) to ∼200 m water depth.

(thinner permafrost) compared to model 4A. Additionally, larger Tx-Rx offsets (than the chosen 750 m for the SVD study) are more sensitive to the difference between models 4A and 4B as shown in Fig. 4.13. For intermediate water depth (here, 50 m) the difference between the step-on responses is shown in the early-time amplitudes for large Tx-Rx offsets (>800 m) and also slightly in the late-time amplitudes for intermediate Tx-Rx offsets (here, 400 to 800 m).

To analyze if one can distinguish between a permafrost halfspace and a thick permafrost layer underlain by a conductive layer interrupted by a “thin” resistive gas hydrate layer, models 1A and 4A are compared. Figure 4.14 shows step-on responses for 10 and 1000 m water depth for conductive and resistive seawater. For 10 m water depth, the airwave masks the early-time amplitudes. The arrival times differ for the resistive and conductive seawater, but the major arrival occurs at about the same time and is the same for the two models. The difference between the step-on responses shows mostly in the late-time amplitudes for Tx-Rx offsets >800 m (chosen spacing for step-on responses shown in Fig. 4.14). The step-on responses for greater water depth (here, 1000 m) differ mostly for early-time amplitudes. The early-time amplitudes for model 4A are larger than for model 1A (especially for conductive seawater) which is

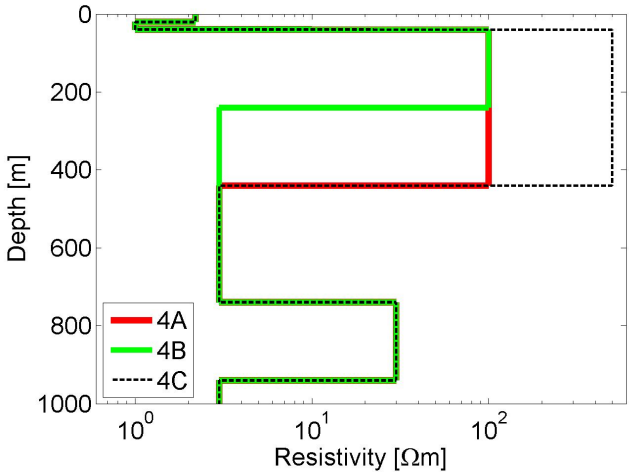

Figure 4.11: Models 4 A, B and C with unfrozen sediment and gas hydrate layer in ∼800 mbsf below the resistive permafrost layer.

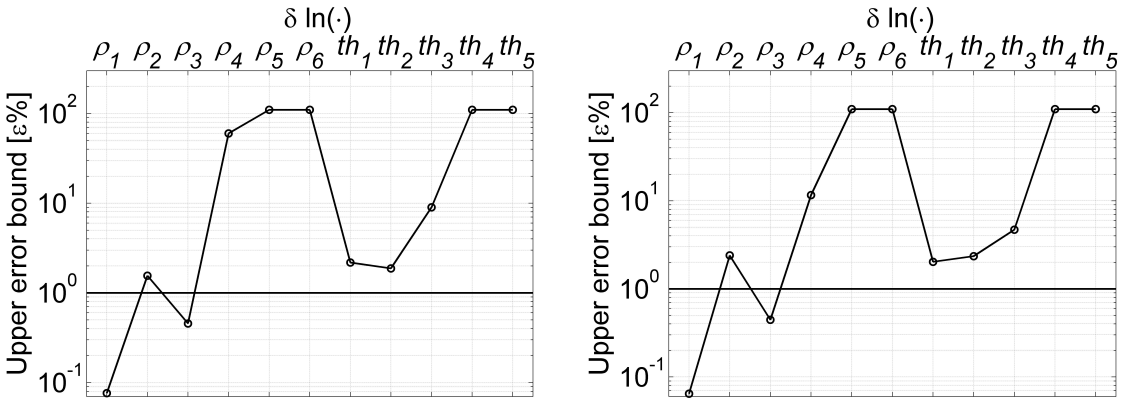

Figure 4.12: Upper error bounds on model parameter resolution from SVD analysis for model 4A (left) and 4B (right) for 30 m water depth and 4 receivers with a maximum Tx-Rx offset of 750 m.

likely due to the sensitivity of the CSEM array to the resistivity contrast above and below the permafrost layer (as discussed in Sec. 2.4). The difference in early-time amplitudes is also the major difference between the step-on responses of models 4A and 4B, which are shown for 50 m water depth in Fig. 4.13, but early-time amplitudes are masked by the airwave for shallower water depth (<50 m).

The data misfit between models 1A and 4A is displayed as a function of Tx-Rx spacing and water depth for conductive seawater in Fig. 4.15. Note that there is no blind window, but the data misfit is larger for deeper water depth.

In summary, the depth to the permafrost can be resolved best for Tx-Rx offsets

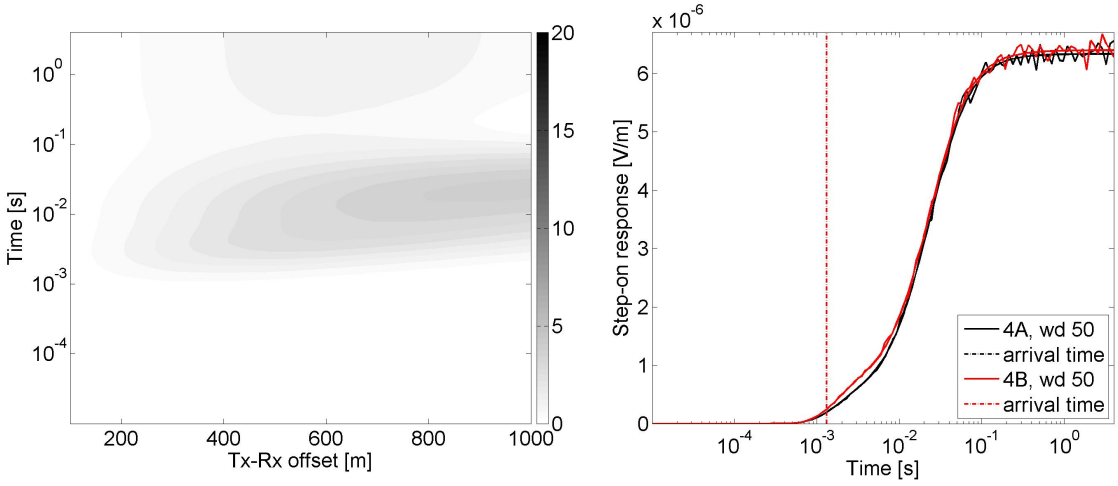

Figure 4.13: Right: Predicted step-on responses for model 4A and model 4B with and without Gaussian random noise for Tx-Rx offset 400 m in 50 m water depth (wd). Left: Normalized deviation (colour bar) of the two responses for Tx-Rx offset of 100 to 1000 m and time. Water resistivity is ρ_w=0.38 Ωm.

>400 m, and the thickness of the permafrost as well as the resistivity of the conductive layer beneath the permafrost are resolved better for a thinner permafrost layer. The transition between differences in late-time amplitudes for shallow water depth to early-time amplitudes for deeper water depth is smooth and no blind window with low misfits is found. However, the step-on responses for models 1A, 4A and 4B are better to distinguish in case of intermediate (here, 50 m) to deep water, conductive seawater and large Tx-Rx offsets. The SVD analysis in Fig. 4.12 shows that the deep gas hydrate layer cannot be resolved with the chosen CSEM array where the depth to the gas hydrate layer is about the same as the maximum Tx-Rx offset.

Talik layer

Models 5 and 6 (see Fig. 4.16) are similar to model 1A, but include a talik section in the permafrost, similar to what Todd and Dallimore [1998] found in the Mackenzie Delta. The resistivity for the talik section is chosen to be 30 Ωm as inferred by Todd and Dallimore [1998]. For models 5A, B and C the top of the talik layer is in 60 mbsf and it is 20, 50 and 100 m thick respectively. Upper error bounds from SVD analysis are shown in Fig. 4.17. It is difficult to determine the talik layer as the upper error bounds are rather high. The resistivity of a thicker talik layer is easier to resolve, but the upper error bound for the resistivity of the permafrost underneath increases

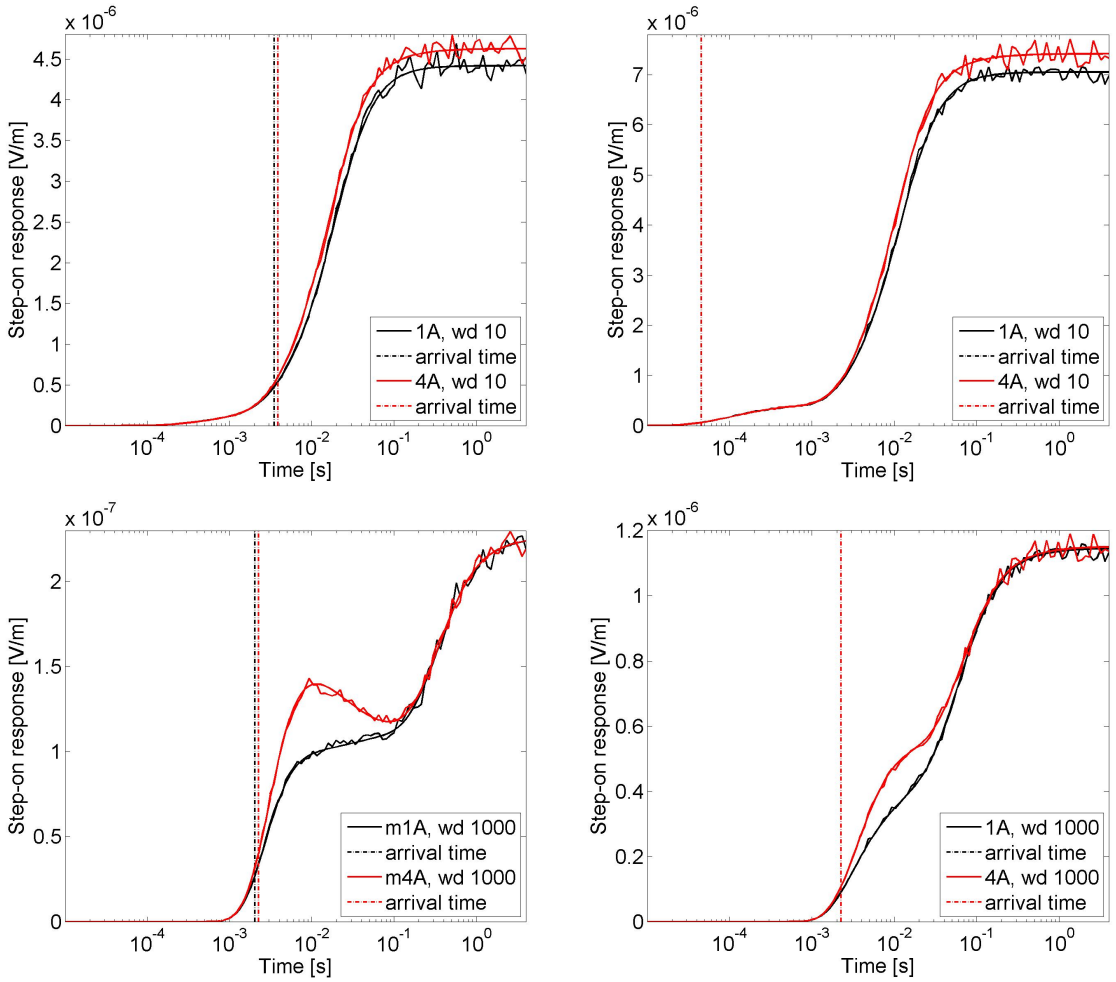

Figure 4.14: Predicted step-on responses for model 1A and model 4A with and without Gaussian random noise for Tx-Rx offset 800 m in 10 m (top) and 1000 m (bottom) water depth (wd). Seawater resistivities: ρ_w=0.38 Ωm (left) and 2 Ωm (right). Tx-Rx offset: 800 m.

with increasing talik thickness. Step-on responses for models 1A and 5C are shown in App. A.3. Similar to analyses above, the differences between the step-on responses for higher water resistivities are larger for late-time amplitudes. Generally, the largest deviation for shallow water depth is in the late-time amplitudes, while deeper water causes the arrival time to deviate stronger.

A transition window is located between 70 to 150 m water depth for conductive seawater as seen on the left panel of Fig. 4.18, but the data misfit is generally below the threshold of 1 and the step-on responses can hardly be distinguished. Step-on responses for more conductive seawater or thinner talik sections are not displayed, but

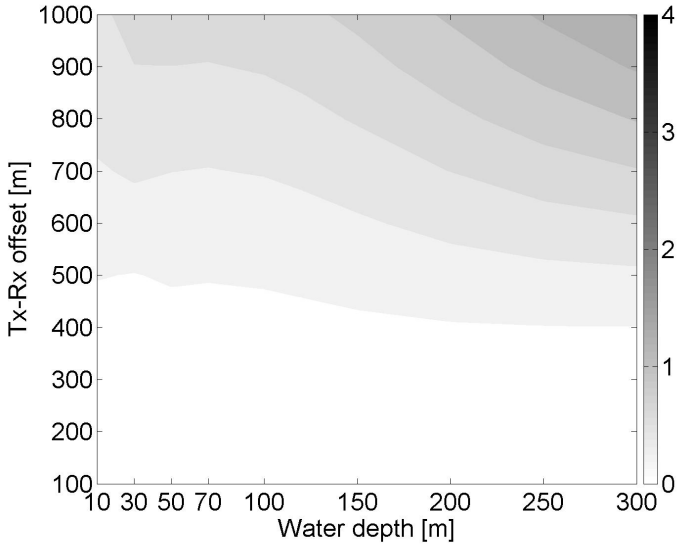

Figure 4.15: Data misfit between step-on response for model 1A and 4A at 10 to 300 m water depth for Tx-Rx offsets of 100 to 1000 m for conductive seawater. No transition window can be identified, but the responses can only be distinguished for large Tx-Rx offsets or deeper water depth (data misfit required to be above the threshold of 1).

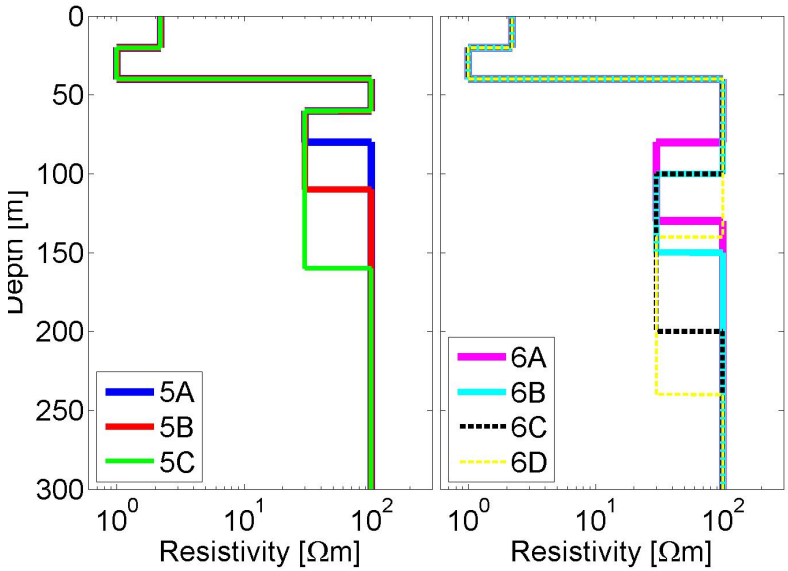

Figure 4.16: Models 5 and 6 are similar to models 1–3 but include a less resistive talik section within the permafrost layer.

they follow the same trend with a smaller deviation. Therefore, it is better to detect relatively thick talik sections (here, 100 m) in shallow (<∼70 m) or deep (>∼200 m)

water depth for more resistive seawater.

Models 6 differ mostly in depth to the talik layer within the permafrost. Model 6C and 5C have a 50 m thick talik layer in different depths. The step-on responses, shown in Fig. 4.19, are very similar and differ only in the late-time amplitudes for shallow water depth and in the arrival times and early-time amplitudes for deeper water depth. Small data misfits shown in the right panel of Fig. 4.18 suggest that the depth to the talik layer can hardly be resolved, but it would be easier in greater water depth and with intermediate Tx-Rx offsets.

Summary

The synthetic modelling study for different permafrost models has shown that resistivity of the overburden as well as the depth to the permafrost can be resolved with relatively small uncertainty. If a more conductive layer exists above the permafrost, as inferred by Scott [1992], it would be more difficult to constrain resistivity or thickness separately. The resistivity of the permafrost is difficult to determine if it is >100 Ωm as used in this study.

More resistive seawater generally improves differentiability between the step-on responses for different models and shallow water depth which is significant for detecting deeper targets like talik layers within the permafrost and non-ice bound and hydrate layers beneath the permafrost. The difference in the step-on response of models with shallow water depth is mainly found in late-time amplitudes. However, for deeper water depth the difference is more pronounced for arrival times and early-time

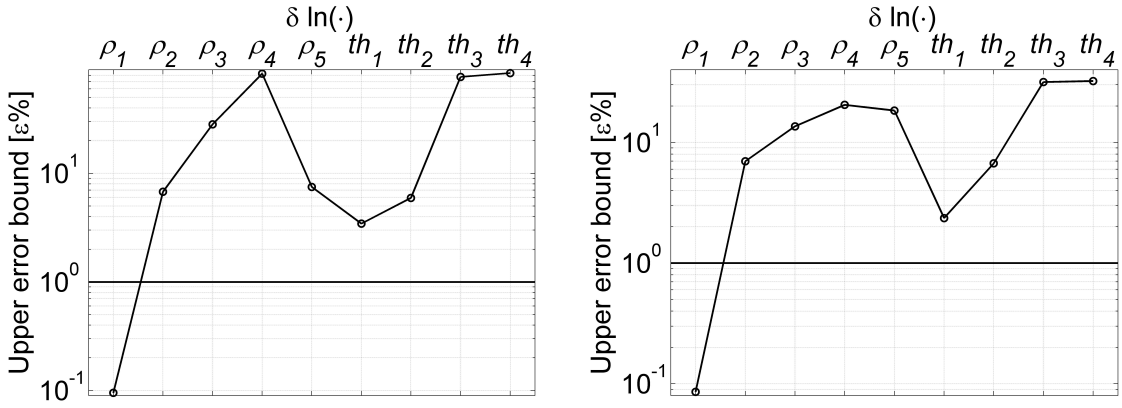

Figure 4.17: Upper error bound on model parameter resolution from SVD analysis for model 5A and 5C for 30 m water depth and 4 receivers with a maximum Tx-Rx offset of 750 m.

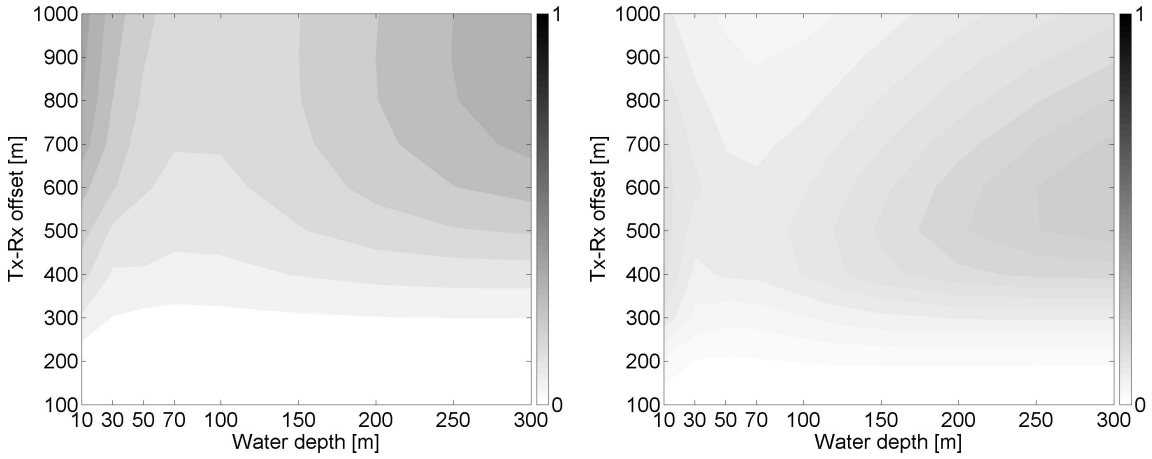

Figure 4.18: Data misfit between step-on response for model 1A and 5C (left) and 5C and 6C (right) at 10 to 300 m water depth for Tx-Rx offsets of 100 to 1000 m for conductive seawater.

amplitudes, which are larger for conductive seawater. A transition as a function of water depth between the differences shown at late times to early times causes a blind window in intermediate water depths depending on the depth and resistivity of the target layer and seawater (here, between ∼30 to 200 m). The transition window is located at deeper water depths for resisitive seawater compared to conductive seawater. While it is easier to distinguish if a talik layer is present it is more difficult to estimate its depth or thickness and it is required to be quite thick and relatively close to the seafloor (here, ∼100 m, centred in ∼150 mbsf). A conductive halfspace beneath the permafrost is easier to detect, likely due to the strong resistivity contrast, but the depth to the bottom of the permafrost has high uncertainties. Gas hydrate occurrences below the permafrost can likely not be resolved with the HED CSEM system. Using a broadside configuration as well as inline as demonstrated by Scholl [2010] and measuring magnetic and electric components in more than one direction has been shown to improve the detectability for gas hydrate layers as well as talik sections for measurements on land and would be worth modelling in the future for experiments on the shelf.

It has also been recommended to measure the E_z component in shallow water depths, as it is not sensitive to the airwave but only to resistive structures in the subsurface [Weidelt, 2007] as, for example, demonstrated by Edwards et al. [1988].

It is important to know the resistivity profile of the water layer exactly as demon-

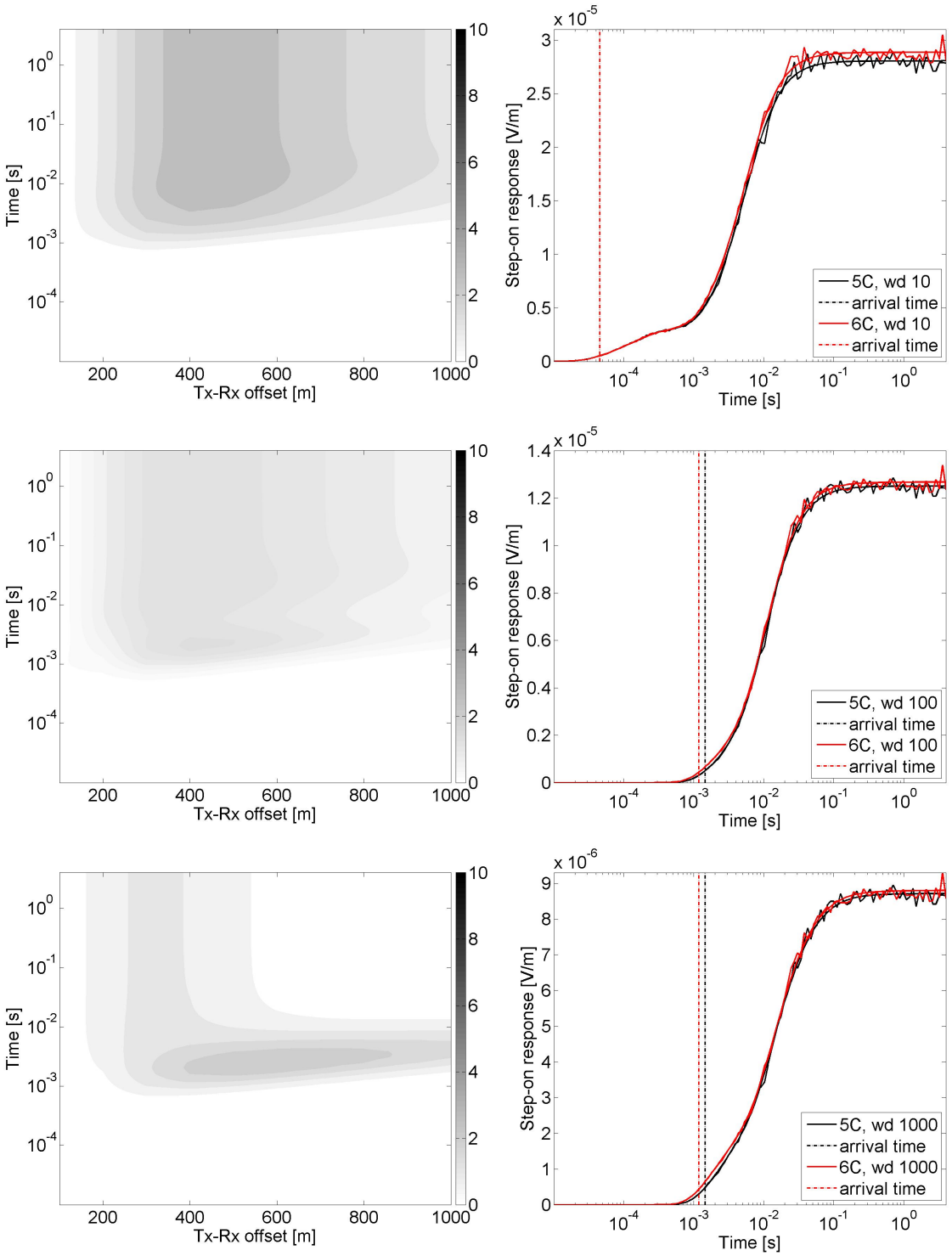

Figure 4.19: Right: Predicted step-on responses for model 5C and model 6C with and without Gaussian random noise for Tx-Rx offset 400 m in 10, 100 and 1000 m water depth (wd). Left: Normalized deviation (colour bar) of the two responses for Tx-Rx offset of 100 to 1000 m and time. $\rho_w = 2$ Ωm.

strated by Key [2009] and shown in this study, because the salinity changes vertically and laterally along the slope [Williams and Carmack, 2008]. It would be necessary to take closely spaced measurements of the conductivity, temperature and pressure of the water column with a CTD instrument.

Chapter 5

Non-linear inverse theory and simulation study on gas hydrate occurrences

Linearized inversions are applicable if problems are linear or weakly non-linear. Chapter 3 discusses how to stabilize linearized inversions in case of ill-conditioned or singular problems by introducing regularization. Section 3.2 shows one approach (singular value decomposition) to estimate uncertainties for model parameters assuming local linear behaviour. However, regularization or truncation of singular values lead to a reduction in model resolution and degrade the uncertainty estimation. A non-linear optimization technique that does not require regularization and numerically minimizes the data misfit over the model parameters is introduced in Sec. 5.1 (called adaptive simplex simulated annealing). A more rigorous approach to estimate uncertainties is Bayesian inversion, which provides a fully non-linear estimate of model parameters and uncertainties. Bayesian inversion is introduced in Sec. 5.2. In this section, the posterior probability density of the model parameters, given the data and prior information, is defined and estimated via numerical sampling. The model parametrization (here, a one-dimensional layered subsurface model with varying numbers of layers) is addressed in two ways in this thesis. One way is to apply the Bayesian information criterion (in Sec. 5.3.1), which estimates the number of layers that the data can resolve and requires the estimation of a global-minimum-misfit model by non-linear optimization. Another way is a trans-dimensional inversion (described in Sec. 5.5) that enables transitions between parametrizations and results in a more complete

uncertainty estimation.

5.1 Adaptive simplex simulated annealing

Adaptive simplex simulated annealing (ASSA) is a hybrid algorithm which combines a global search (simulated annealing) and a local method (downhill simplex optimization) to estimate an optimal model by minimizing the data misfit over a large, non-linear parameter space, combining a stochastic component (for a wide search) with gradient-based information (for efficiency). ASSA is an efficient method for problems with multiple local minima, correlated parameters and a wide range of parameter sensitivities [Dosso et al., 2001].

Simulated Annealing

Simulated annealing (SA) is a global search that randomly perturbs the parameters to minimize an objective function which, in geophysical inversion, can be taken to be the data misfit function

$$X^2 = (\mathbf{d} - f(\mathbf{m}))^T \mathbf{C}_d^{-1} (\mathbf{d} - f(\mathbf{m})), \tag{5.1}$$

where $\mathbf{d}$ are the observed data with their error covariance matrix $\mathbf{C}_d$ and $f(\mathbf{m})$ are the predicted data. The data misfit is estimated from the likelihood of the model parameters $L(\mathbf{m})$ for Gaussian distributed errors with $X^2 = -\ln L(\mathbf{m})$ (Sec. 5.3.3 will discuss likelihood in more detail).

SA is named after the physical process of growing crystals (annealing). When a hot medium is cooled slowly, a single crystal can grow so that the energy end state is at a global minimum. When the medium is cooled too fast, the end state might not reach the global minimum, but become trapped in a local minimum. The algorithm is based on perturbing a current model state $\mathbf{m}$ to obtain a state $\mathbf{m}'$, which is accepted or rejected according to the Metropolis criterion [Metropolis et al., 1953]

$$\alpha = \min \left[1, \left(\frac{L(\mathbf{m}')}{L(\mathbf{m})} \right)^{1/T} \right], \tag{5.2}$$

where T is referred to as the temperature. The new model is accepted if a uniform random number $\xi \in [0, 1]$ satisfies $\xi < \alpha$.

The temperature T is decreased slowly over the iterations. This process is called "cooling". The cooling ensures the algorithm accepts fewer perturbations with higher misfits. In our implementation, the parameter perturbations are randomly drawn from a Cauchy distribution about the current values and the distribution width is controlled by temperature (described below). The advantage of the algorithm is that it accepts some increases in misfit and therefore can escape from local minima. One disadvantage of the method is that it does not remember past models. Another disadvantage is that it is insensitive to local gradients which indicate the downhill direction. A method called "quenching", where T is set to zero, is usually applied when cooling is completed to accept lower misfits only and converge to the nearest minimum (local or global) [Kirkpatrick et al., 1983; Dosso et al., 2001; Dosso, 2009].

Downhill simplex

The downhill simplex (DHS) method is a local method based on a set of $M+1$ models which construct a simplex in an M-dimensional space, where M is the number of model parameters [Fallat and Dosso, 1999]. The goal is to use the relative information from the misfit values at the various models to provide a rough indication of the downhill direction (without calculating derivatives), and to make geometric steps that favour this direction. To do so, the model with the highest misfit in the simplex is altered in the following ways (shown for $M = 2$ on Fig. 5.1):

1. Reflection through the face of the simplex by a factor -1
2. Extension through the face of the simplex by a factor -2
3. Contraction towards face of simplex by a factor 0.5
4. Multiple contraction of all high misfit models towards the best fit model by a factor 0.5

If the reflection results in a better model than the second highest misfit model then the latter becomes the worst misfit model and the algorithm restarts with the reflection. If the reflection results in a model with a better misfit than the former best model, the direction is assumed to be particularly promising and an extension is executed. If the misfit of the model is not less than the second highest misfit after the reflection, a contraction is executed. If the contraction does not work a multiple contraction

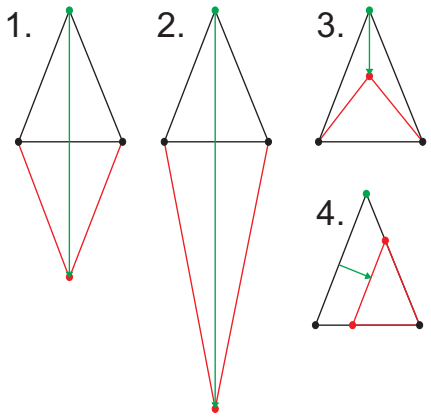

Figure 5.1: DHS realization of reflection (1), extension (2), contraction (3) and multiple contraction (4) of a model simplex with 2 parameters. The green dot represents the model with the highest misfit and the green arrow the direction of model alternation. The multiple contraction (4) is directed towards the model with the lowest misfit in the right bottom corner. The red dots are the updated models.

is executed. The convergence criterion takes the difference of the highest and lowest misfit of the models and evaluates

$$\frac{2(X^2_{\text{high}} - X^2_{\text{low}})}{(X^2_{\text{high}} + X^2_{\text{low}})} < \epsilon, \tag{5.3}$$

where ϵ is the tolerance defined by the user.

ASSA combines DHS and SA to balance between random and gradient-controlled perturbations. The perturbation steps consist of a DHS step (gradient based) with a random component added. The perturbation is accepted or rejected according to the Metropolis criterion. The method is initiated at high temperature so that all perturbations are initially accepted. As the temperature is reduced uphill steps are rejected at an increasing rate. A key element is that the trade-off between the gradient-based and random components of the perturbations is controlled adaptively by adjusting the random step size for each parameter according to a running average of the size of recently accepted perturbations. In this procedure, randomness dominates at high temperatures and gradient-based steps at low temperatures. Further, the optimization retains a memory of good models within the simplex, where all but the current highest misfit model represent the M best models encountered in the search [Dosso et al., 2001].

5.2 Bayesian inversion

The inversion methods described in Chapters 3 (Marquardt, Occam and SVD) and 5.1 (ASSA) are based on the assumption that the problem is deterministic (a true model exists). In Bayesian inversion the model is a random variable that can be described probabilistically. It is a general and scientifically rigorous solution to an inverse problem and is described by a probability density over the model parameters. In geophysical problems, Bayesian inversion can provide quantitative parameter and uncertainty estimates and rigorous error treatment, and is the preferred method if the problem is highly non-linear (*e.g.*, Denison et al. [2002]). The distribution of the model parameters $\mathbf{m}$ are given by the posterior probability density (PPD), which combines prior knowledge about the parameters and information from the observed data $\mathbf{d}$. Bayes' rule can be written as

$$P(\mathbf{m}|\mathbf{d}, H) = \frac{P(\mathbf{d}|\mathbf{m}, H)P(\mathbf{m}|H)}{P(\mathbf{d}|H)}, \tag{5.4}$$

where H is the model parametrization (here, indicating the number of sub-seafloor layers). The left side of Eq. (5.4) represents the PPD, $P(\mathbf{m}|\mathbf{d}, H)$. The term $P(\mathbf{d}|\mathbf{m}, H)$ is the conditional probability of the data given $\mathbf{m}$ and H. However, for fixed observed data this term is interpreted as the likelihood of the model parameters $L(\mathbf{m}, H)$. The term $P(\mathbf{m}|H)$ is the prior density of the model parameters given H independent from the observed data. In Bayesian inversion, probability is interpreted as "degree of belief", which can be somewhat subjective. In this thesis, the priors are designed to be relatively non-informative (so that the data primarily determine the solution), and are taken to be uniform densities between physically-realistic lower and upper bounds for each parameter. The conditional probability for the observed data $P(\mathbf{d}|H)$ can be considered the likelihood of the parametrization H given the observed data and is called the Bayesian evidence. Since the evidence represents a normalizing factor, it can be written as

$$P(\mathbf{d}|H) = \int_{\mathcal{M}} P(\mathbf{m}')P(\mathbf{d}|\mathbf{m}')\,\mathrm{d}\mathbf{m}', \tag{5.5}$$

where the integration is over the M-dimensional parameter space $\mathcal{M}$. However, Eq. (5.5) is particularly difficult to compute, and in some cases the role of evidence in comparing different parametrization can be approximated with the Bayesian information criterion (BIC), as described in Sec. 5.3.1. When different parametrizations

are not being considered H can be omitted and Bayes rule can be written as

$$P(\mathbf{m}|\mathbf{d}) \propto L(\mathbf{m})P(\mathbf{m}). \tag{5.6}$$

Since the PPD is a multi-dimensional distribution, it is generally interpreted in terms of properties representing parameter estimates, uncertainties, and inter-relationships. Parameter estimates include the maximum *a posteriori* (MAP) $\mathbf{m}_{\text{MAP}}$, the mean model $\bar{\mathbf{m}}$ and the median model, all of which are identical for unimodal and symmetric distributions, but not in general (*e.g.*, Gelman et al. [2000]). The MAP model is estimated for the highest probability in the PPD,

$$\mathbf{m}_{\text{MAP}} = \text{Arg}_{\text{max}} \left\{ P(\mathbf{m}|\mathbf{d}) \right\}, \tag{5.7}$$

while the mean model is the average

$$\bar{\mathbf{m}} = \int_{\mathcal{M}} \mathbf{m} P(\mathbf{m}'|\mathbf{d}) \, \mathrm{d}\mathbf{m}', \tag{5.8}$$

and the median model divides the integrated probability density so that half lies above and half below the median with

$$\int_{-\infty}^{m_i^{\text{median}}} P(m_i'|\mathbf{d}) \, \mathrm{d}m_i' = \frac{1}{2}. \tag{5.9}$$

Uncertainties can be expressed as the model covariance matrix, marginal probability distributions, and credibility intervals. The model covariance matrix contains parameter variances on the main diagonal and covariances on the off-diagonal and is estimated with

$$\mathbf{C}_m = \int_{\mathcal{M}} (\mathbf{m}' - \bar{\mathbf{m}})(\mathbf{m}' - \bar{\mathbf{m}})^T P(\mathbf{m}'|\mathbf{d}) \, \mathrm{d}\mathbf{m}'. \tag{5.10}$$

The marginal probability densities for model parameter m_i are estimated with

$$P(m_i|\mathbf{d}) = \int \delta(m_i - m_i') P(\mathbf{m}'|\mathbf{d}) \, \mathrm{d}\mathbf{m}', \tag{5.11}$$

and the credibility intervals (CI), in this thesis, are defined as the intervals with the highest probability density on the smallest parameter range with 95% probability.

5.3 Fixed-dimensional Bayesian inversion

When the parametrization does not change during the inversion it is called fixed-dimensional inversion. It is crucial to determine the appropriate model parametrization beforehand. Too many model parameters result in over-parametrization. Not all of the model parameters are constrained and the inversion might introduce spurious model structure and overestimate uncertainties. Too few model parameters result in under-parametrization. Model structure can be unresolved, and parameters may be biased and uncertainties underestimated. In this study the model parametrization is related to the number of layers of a one-dimensional subsurface model, and, in this section, the appropriate number of model parameters (i.e., the number of parameters that can be resolved by the data) is estimated with the BIC [Dettmer et al., 2009; Dosso and Dettmer, 2011].

5.3.1 Bayesian information criterion

The BIC is derived from Bayes' rule (5.4) and can be used to estimate the most appropriate number of model parameters (here, resistivities and thicknesses for subseafloor layers) that can be resolved by the data. The misfit $X^2(\hat{\mathbf{m}}) = -\ln L(\hat{\mathbf{m}})$ of the maximum-likelihood model $\hat{\mathbf{m}}$ decreases when additional layers are added but at some point the model becomes over-parametrized with unconstrained structure which can be geologically meaningless (an artifact of fitting the noise on the data). The BIC balances a data misfit term with a penalty term which increases linearly with the number of parameters:

$$\mathrm{BIC} = 2X^2(\hat{\mathbf{m}}) + M\ln(N), \tag{5.12}$$

where M is the number of parameters and N the number of data [Schwarz, 1978; Kass and Raftery, 1995; Dettmer et al., 2009].

To compute the maximum-likelihood model for different parametrization, the data misfit is minimized over the parameter space using, *e.g.*, ASSA (described in Sec. 5.1).

5.3.2 Metropolis-Hastings sampling

To apply Bayesian inversion to nonlinear problems, Markov-chain Monte Carlo (MCMC) methods are typically employed to sample the parameter space in a random walk that

converges in the long-run to sample the PPD. Here, Metropolis-Hastings sampling (MHS) is applied [Hastings, 1970; Metropolis et al., 1953]. In this process the parameters of the current model are perturbed from $\mathbf{m} \rightarrow \mathbf{m}'$ using a proposal density $Q(\mathbf{m}'|\mathbf{m})$ and the proposed model is accepted with probability

$$\alpha = \min\left[1, \frac{P(\mathbf{m}')}{P(\mathbf{m})}\left(\frac{L(\mathbf{m}')}{L(\mathbf{m})}\right)^{1/T}\frac{Q(\mathbf{m}|\mathbf{m}')}{Q(\mathbf{m}'|\mathbf{m})}\right], \tag{5.13}$$

where T (referred to as the sampling temperature) is a relaxation term, taken to be unity for unbiased sampling, but non-unity for parallel tempering (described below). For uniform bounded priors and a symmetric proposal density ($Q(\mathbf{m}'|\mathbf{m}) = Q(\mathbf{m}|\mathbf{m}')$), Eq. (5.13) simplifies to the Metropolis criterion (5.2).

To ensure wide and efficient sampling of the parameter space, including isolated regions (modes) of high probability in the PPD, parallel tempering is applied here. Parallel tempering runs a series of Markov chains at an increasing sequence of sampling temperatures $T \geq 1$, which relax the likelihood term in Eq. (5.2) and allow lower-probability models to be accepted [Earl and Deem, 2005; Dosso et al., 2012]. To combine the wide sampling of high temperature chains with the concentrated local sampling of low temperature chains, the chains interact, probabilistically exchanging (swapping) models. The Metropolis-Hastings acceptance criterion is evaluated for the joint probability of model $\mathbf{m}_i$ of the chain with temperature T_i to swap with model $\mathbf{m}_j$ of the chain with temperature T_j and becomes [Dettmer and Dosso, 2012]

$$\alpha = \min\left[1, \left(\frac{L(\mathbf{m}_j)}{L(\mathbf{m}_i)}\right)^{1/T_i}\left(\frac{L(\mathbf{m}_i)}{L(\mathbf{m}_j)}\right)^{1/T_j}\right] \tag{5.14}$$

$$= \min\left[1, \left(\frac{L(\mathbf{m}_j)}{L(\mathbf{m}_i)}\right)^{1/T_i - 1/T_j}\right]. \tag{5.15}$$

The chain(s) sampled at $T = 1$ provide unbiased sampling of the PPD. However, interchange with higher-temperature chains provides efficient wide sampling.

Fixed-dimensional inversions are carried out for simulated data in Sec. 5.4 and for measured data in Chapter 6. Here, MHS initially draws from a proposal distribution based on a linearized approximation to the PPD initiated at an optimal model that was earlier computed with ASSA. The covariance matrix of the linearized PPD estimate is updated throughout the sampling. The parameters are perturbed in principal component space [Dosso and Dettmer, 2011] to sample more efficiently as there are

often strong relationships between parameters (*e.g.*, thickness and resistivity).

5.3.3 Likelihood function

In this thesis, the likelihood function is based on the assumption that the data errors are zero-mean and Gaussian distributed with an unknown covariance matrix $\mathbf{C}_d$ which is estimated from the data. These assumptions are verified *a posteriori* by applying statistical tests [Dosso et al., 2006; Montgomery et al., 2012]. The joint likelihood function for a number of independent data sets with different covariance matrices (in this thesis, data sets for each receiver), becomes

$$L(\mathbf{m}, \mathbf{C}_{d_i}, i = 1, N_{\mathrm{Rx}}) = \prod_{i=1}^{N_{\mathrm{Rx}}} \left\{ \frac{1}{(2\pi)^{N_i/2} \left|\mathbf{C}_{d_i}\right|^{1/2}} \cdot \exp\left[-\frac{1}{2} (\mathbf{d}_i - \mathbf{d}_i(\mathbf{m}))^T \mathbf{C}_{d_i}^{-1} (\mathbf{d}_i - \mathbf{d}_i(\mathbf{m})) \right] \right\}, \tag{5.16}$$

where N_{Rx} is the number of receivers, and N_i is the number of data for the i^{th} receiver. The measured data presented in this thesis require the inclusion of an unknown calibration factor (CF) in the inversion, which is multiplied to the predicted data and described in more detail in Chapter 6 and 7. The likelihood function (5.16) is expanded to

$$L(\mathbf{m}, \mathbf{C}_{d_i}, cf_i, i = 1, N_{\mathrm{Rx}}) = \prod_{i=1}^{N_{Rx}} \left\{ \frac{1}{(2\pi)^{N_i/2} \left|\mathbf{C}_{d_i}\right|^{1/2}} \cdot \exp\left[-\frac{1}{2} (\mathbf{d}_i - cf_i \mathbf{d}_i(\mathbf{m}))^T \mathbf{C}_{d_i}^{-1} (\mathbf{d}_i - cf_i \mathbf{d}_i(\mathbf{m})) \right] \right\}, \tag{5.17}$$

where cf_i represents the CF for the i^{th} receiver. The CF is sampled implicitly within the fixed-dimensional inversion by maximizing the likelihood with respect to cf_i. For readability the i will be dropped in the following description. Setting $\partial L(\mathbf{m}, \mathbf{C}_d, cf)/\partial cf = 0$ leads to

$$cf = \frac{\mathbf{d}^T \mathbf{C}_d^{-1} \mathbf{d}(\mathbf{m})}{\mathbf{d}^T(\mathbf{m}) \mathbf{C}_d^{-1} \mathbf{d}(\mathbf{m})}, \tag{5.18}$$

which provides a closed form expression for the maximum-likelihood cf estimate in terms of the model parameters $\mathbf{m}$ which are sampled explicitly [Dosso et al., 2006].

5.3.4 Data covariance matrix

The fixed-dimensional inversion approach, in this thesis, estimates both the optimal number of layers, using the BIC, and the data covariance matrix from residual analysis. The difficulty is that the BIC requires an estimate of the covariance matrix, while estimating the covariance matrix requires knowledge of the number of layers. The approach applied here cycles twice through a set of inversions. The first inversion cycle implements the standard deviations of the mean obtained from stacking the raw CSEM data. The data covariance matrix consists of variable variances (squared data standard deviations) along its main diagonal and zero covariances. The stacking error, however, is only one part of the actual error in the inversion. It does not cover deviations from model assumptions (*e.g.*, 1-D parametrization), physical theory and CSEM array geometry. Therefore, a scale factor δ_i^2 is included as an unknown in the inversion that multiplies $\mathbf{C}_{d_i}$ from the stacking process of the i^{th} receiver. This factor is sampled implicitly by maximizing the likelihood with respect to δ_i^2 ($\partial L(\mathbf{m}, \mathbf{C}_{d_i}, cf_i, \delta_i^2, i = 1, N_{\text{Rx}})/\partial\delta_i^2 = 0$), where L is rewritten as

$$\begin{aligned} L(\mathbf{m}, \mathbf{C}_{d_i}, cf_i, \delta_i^2, i = 1, N_{\text{Rx}}) = & \frac{1}{\prod_{i=1}^{N_{\text{Rx}}}(2\pi)^{N_i/2}} \\ & \cdot \exp\left[-\frac{1}{2}\sum_{i=1}^{N_{\text{Rx}}}\left\{(\mathbf{d}_i - cf_i\mathbf{d}_i(\mathbf{m}))^T(\delta_i^2\mathbf{C}_{d_i})^{-1}(\mathbf{d}_i - cf_i\mathbf{d}_i(\mathbf{m}))\right\}\right. \\ & \left. -\frac{1}{2}\sum_{i=1}^{N_{\text{Rx}}}\left\{\ln\left|\delta_i^2\mathbf{C}_{d_i}\right|\right\}\right], \end{aligned} \tag{5.19}$$

leading to (i is dropped for readability)

$$\delta^2 = \frac{1}{N}\left(\mathbf{d}^T\mathbf{C}_d^{-1}\mathbf{d} - \frac{(\mathbf{d}^T\mathbf{C}_d^{-1}\mathbf{d}(\mathbf{m}))^2}{\mathbf{d}^T(\mathbf{m})\mathbf{C}_d^{-1}\mathbf{d}(\mathbf{m})}\right), \tag{5.20}$$

which is substituted back into Eq. (5.19).

One method to estimate a full covariance matrix with non-zero covariances (a non-diagonal matrix) requires an approximation of the ensemble average from one data set using an iterative, nonparametric procedure following the assumption that the error process is stationary and ergodic [Montgomery et al., 2012; Dosso et al., 2006]. The residual errors for an optimal model estimate $\hat{\mathbf{m}}$, defined as

$$\mathbf{r}_i = \mathbf{d}_i - cf_i\mathbf{d}_i(\hat{\mathbf{m}}), \tag{5.21}$$

are considered one realization of the underlying error process (representing data and theory errors), and a non-diagonal data covariance matrix $\mathbf{C}_{d_i}$ for the i^{th} receiver can be obtained from the residual errors (see below). For fixed-dimensional inversions, in this thesis, several high-likelihood models with increasing number of layers are obtained with ASSA (see Sec. 5.1), and $\hat{\mathbf{m}}$ is estimated by selecting the model with the smallest BIC value.

Variances from the stacking process are not constant along the main diagonal (*e.g.*, standard deviations from stacking have been shown to be higher when the electric field response is close to zero) and error correlation is especially large for early, closely-spaced data samples, but declines quickly. Therefore, I estimate a non-diagonally constant matrix, or non-Toeplitz matrix, from standardized residuals. Residuals are standardized by their estimated standard deviation to $\tilde{\mathbf{r}}_i = \mathbf{r}_i / \hat{\boldsymbol{\sigma}}_i$ with (i is dropped for readability)

$$\hat{\sigma}_j^2 = \frac{1}{n} \sum_{l=j-n/2}^{j+n/2} r_l^2 \tag{5.22}$$

for a window of data samples of width n centred at the current data point j to accommodate standard deviations which vary slowly across the data set. The non-Toeplitz data covariance matrix is estimated by computing the autocorrelation of the residuals for each receiver, analogously to Dosso et al. [2006], with (i is dropped for readability)

$$\hat{C}_{d\,jl} = \frac{1}{N} \sum_{k=1}^{N-|j-l|} (\tilde{r}_k - \bar{\tilde{\mathbf{r}}})(\tilde{r}_{k+|j-l|} - \bar{\tilde{\mathbf{r}}}) \cos^p \frac{\pi |j-l|}{2(N-1)}, \tag{5.23}$$

where $j = 1, N$, $l = 1, N$, $\bar{\tilde{\mathbf{r}}}$ is the mean of the standardized residuals, and $\cos^p \frac{\pi|j-l|}{2(N-1)}$ is a damping function which drops off more sharply for higher p values (here, $p = 16$). Damping is applied to suppress correlation values for widely spaced data samples as these covariances are expected to be small and the available number of samples ($N - |j - l|$) may be insufficient to meaningfully estimate the covariance values.

The updated non-Toeplitz covariance matrix is implemented into ASSA for a second inversion cycle. The final estimate for the most probable number of layers is determined by minimizing the BIC using this covariance matrix. Metropolis-Hastings sampling is then carried out applying this number of layers and set of covariance matrices, and starting at a good (*e.g.* from ASSA) model [Dosso et al., 2006].

5.4 Ulleung Basin gas hydrate modelling

This section provides a simulation study which uses the fixed-dimensional Bayesian inversion algorithm outlined in Sec. 5.3 to target gas hydrate occurrences in the Ulleung Basin offshore southeast Korea. The Ulleung Basin is part of the East Sea between Korea, Russia and Japan, a backarc basin that developed in the early Miocene. It consists of a thick oceanic crust and ∼6 km of sediment. The Ulleung Basin underwent periods of tectonic extension, subsidence and compression that is ongoing in the present (*e.g.*, Uyeda and Kanamori [1979], Yoon and Chough [1995], Gardner et al. [1998]).

The republic of Korea started a "10-year Korean National Gas Hydrate Program" in 2005 to explore new energy resources in the form of offshore gas hydrate accumulations that would decrease the country's dependence on imported energy. Several 2-D and 3-D seismic surveys as well as drilling expeditions have been completed to study possible gas hydrate extraction sites [Ryu et al., 2013b]. Gas hydrates were recovered from piston cores in seismic blank zones in 2007 containing 99% methane [Park, 2008]. Gas hydrates occur disseminated in silts, but in large amounts locally controlled by an enhanced methane flux in fracture systems. However, coarse grained sediments like silty sands are preferred for large-scale gas hydrate formation in pore spaces [Bahk et al., 2013].

For this study five sub-seafloor resistivity models were chosen to represent different possible scenarios in the Ulleung Basin in 2150 m water depth similar to Site UBGH2.6, which has been chosen for a possible gas hydrate production test. Model 1 consists of a small increase in resistivity with depth for marine sediments without gas hydrates. Models 2 to 4 contain an additional sand layer at 130 m depth carrying gas hydrate. The thickness of the layer is 45 m and the porosity is 60%. The sand layer in model 2 contains ∼15 % gas hydrate (of the total volume), in model 3 ∼42 % and in model 4 ∼55 %. Archie's law (Sec. 1.2.2) was used to convert gas hydrate content to formation resistivity, and the Archie coefficients were chosen $a = 1$, $m = 2$ and $n = 2$ [Edwards, 1997]. Formation resistivities become 1.6, 10 and 100 Ωm based on the given porosity and gas hydrate saturations. Model 5 represents a site with massive shallow gas hydrate occurrences with a resistive layer (10 Ωm) close to the surface (30 m thick at 5 m depth). Model parameters are listed in Tab. 5.1.

The synthetic data are calculated for four dipole receivers at 150, 300, 450 and 600 m offsets from the source dipole. Gaussian-distributed noise (2% of the average step-

Layer\ Model	1	2	3	4	5
1	0.7 Ωm	0.7 Ωm	0.7 Ωm	0.7 Ωm	0.7 Ωm
	220 mbsf	130 mbsf	130 mbsf	130 mbsf	5 mbsf
2	1.2 Ωm	1.6 Ωm	10 Ωm	100 Ωm	10 Ωm
	400 mbsf	175 mbsf	175 mbsf	175 mbsf	35 mbsf
3	2 Ωm	1.2 Ωm	1.2 Ωm	1.2 Ωm	0.7 Ωm
	∞	400 mbsf	400 mbsf	400 mbsf	130 mbsf
4	-	2 Ωm	2 Ωm	2 Ωm	1.2 Ωm
	-	∞	∞	∞	220 mbsf
5	-	-	-	-	4 Ωm
	-	-	-	-	270 mbsf
6	-	-	-	-	1.2 Ωm
	-	-	-	-	400 mbsf
7	-	-	-	-	2 Ωm
	-	-	-	-	∞

Table 5.1: Five models used in the simulation study of the Ulleung Basin. Model 1 is a background model and does not contain gas hydrate. Models 2–4 contain a sand layer in 130 mbsf with a gas hydrate saturation of 15%, 42% and 55% of the total volume (porosity = 60%). Model 5 contains a shallow resistive layer.

on response amplitude) is added to the data. Fixed-dimensional Bayesian inversion is implemented according to Sec. 5.3, but the procedure for estimating non-diagonal covariance matrices outlined in Sec. 5.3.4 is not applied to this simulation study. The data covariance matrix is a diagonal matrix with non-varying (known) variances for each receiver instead. Results for the number of sub-seafloor layers estimated using the BIC and marginal probability density profiles are shown in Figs. 5.2 to 5.4.

For model 1 (see Fig. 5.2) two layers are estimated given the data, which is one less than the true model. However, the true model lies well within the credibility intervals (CI) down to 400 mbsf. The CIs envelop the true model closely down to 220 mbsf, while at depths >400 mbsf the true model is outside the CIs, which are relatively narrow ($\sim$1 Ωm wide). The resistivity increase at 400 mbsf cannot be resolved with these data for the chosen offsets of 150, 300, 450 and 600 m.

Two layers can be resolved for model 2 (Fig. 5.3). The small increase in resistivity in the sand layer (130 mbsf) cannot be detected. However, the data can be explained with a simpler model that averages the subsurface structure below 100 mbsf.

Four layers (the true parametrization) can be resolved for model 3. CIs are generally wider than for the other models and the true depth to the sand layer lies within the CIs. However, the thickness and resistivity of the sand layer are difficult to es-

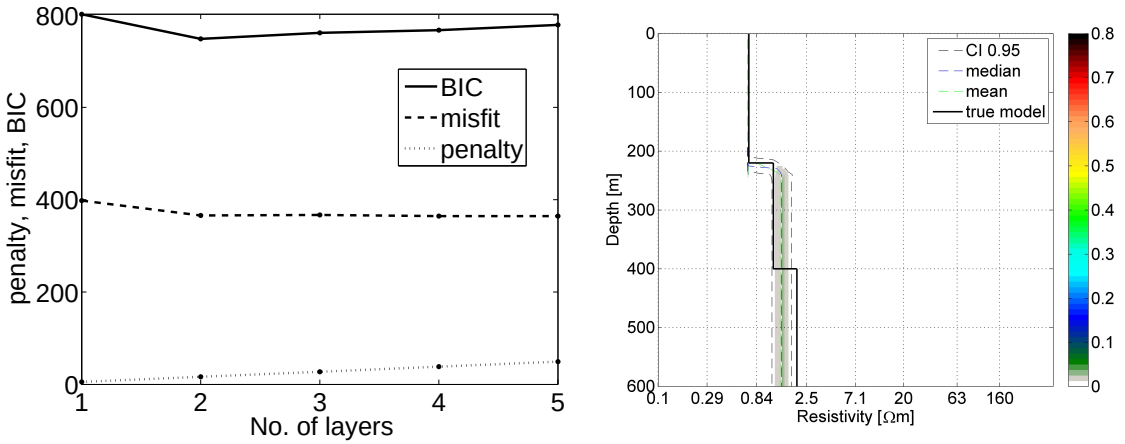

Figure 5.2: Bayesian inversion results for model 1. Left: Two layers can be resolved with the data (estimated with BIC from Eq. (5.12)). Right: Marginal probability density (colour bar) profile for resistivity with depth with credibility intervals (CI), posterior median and mean models as well as the true model.

timate independently. The probabilities for the second layer are higher for smaller resistivity values and larger thicknesses than the true model. It is probable that only a combination of the two can be resolved from the data. The marginal probability profile below 200 mbsf suggests a decrease in resistivity beyond the true model and beyond the values for the first layer. Additionally, the CIs are wide, which suggests that the resistivity below the resistive layer is difficult to estimate from the data. The resistivity increase at 400 mbsf can be resolved, but with a high uncertainty (>100 m) on the depth to the layer.

For model 4 the resistivities above and below the highly resistive layer can be very well resolved, while the resistivity of the resistive layer is overestimated by ∼60 Ωm. It seems that after reaching a certain high resistivity value, changes in this value do not change the predicted data much. Converted into gas hydrate amounts, 100 to 160 Ωm correspond to only a few additional percent in gas hydrate as the pore space is almost completely filled with gas hydrate. The resistivity increase at 400 mbsf cannot be resolved.

The appropriate number of layers for model 5 is five layers as shown on the left panel in Fig. 5.4. However, the BIC results could be misinterpreted if ASSA did not converge to the most likely model in one or more cases. Looking at the marginal probability distribution for three, four and five layers (Figs. 5.4 and 5.5) it seems more probable that four is the optimal number of layers that can be resolved from the data. The marginal probability density for four layers shows a steady increase in resistivity

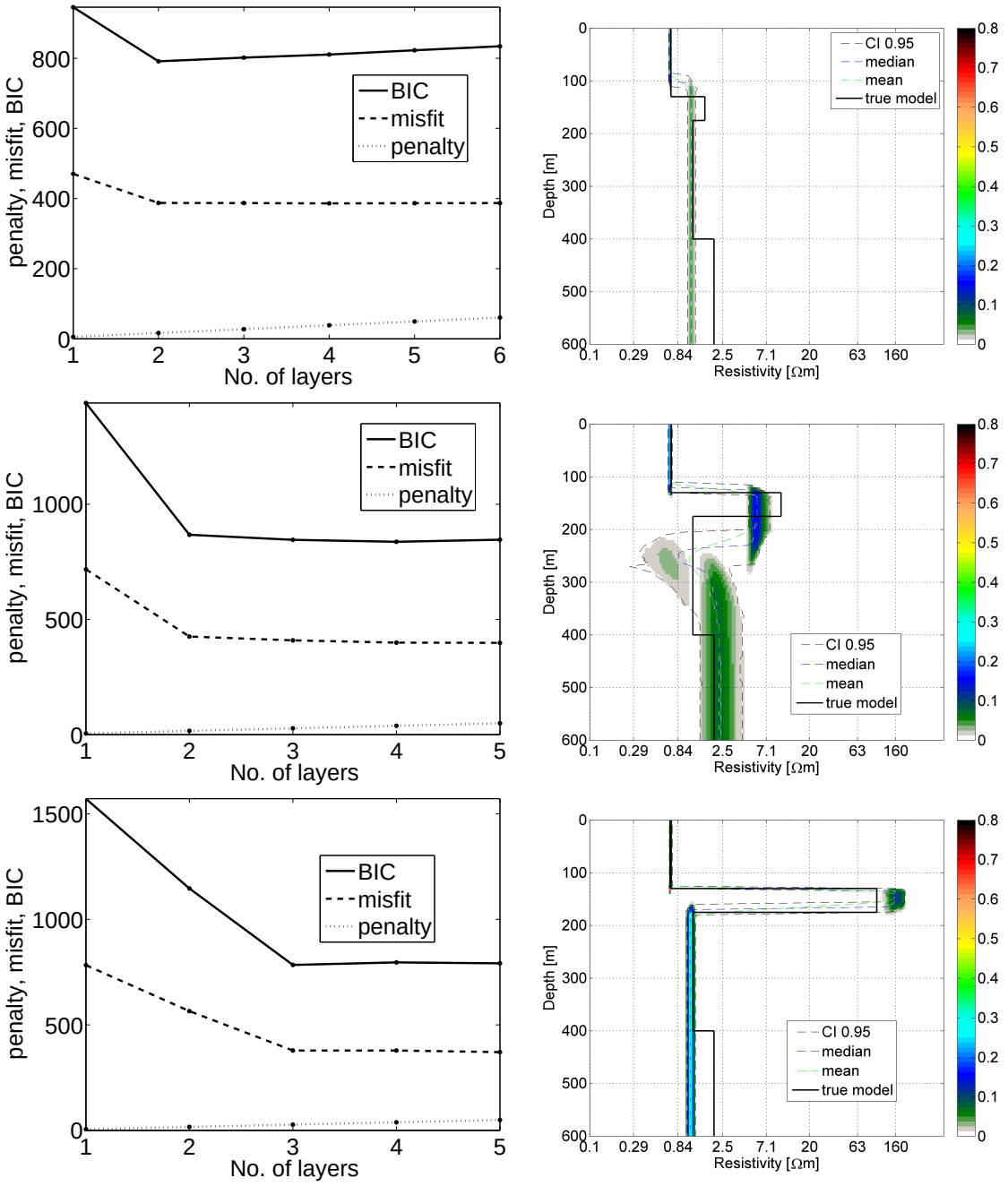

Figure 5.3: Bayesian inversion results for models 2 to 4. Left: Two to four layers can be resolved with the data (estimated with BIC). Right: Marginal probability density (colour bar) profile for resistivity with depth with credibility intervals (CI), posterior median and mean models as well as the true model.

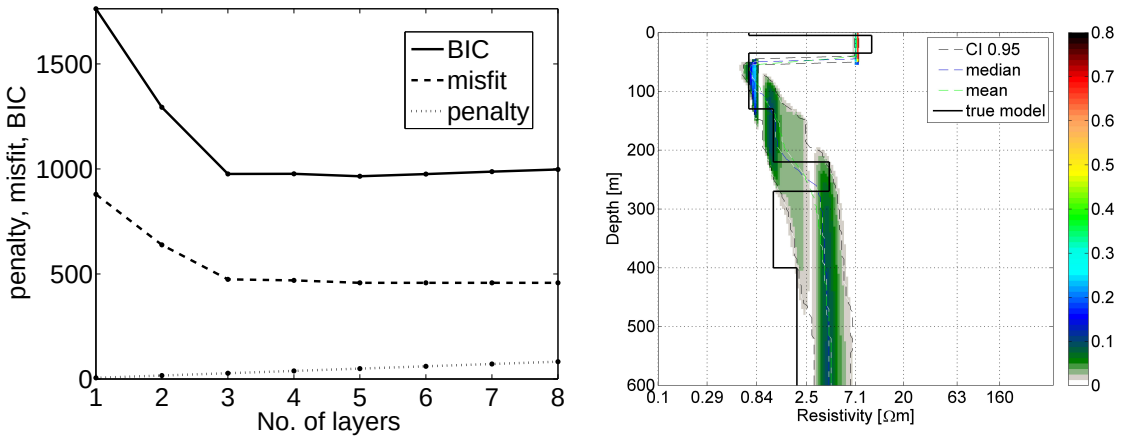

Figure 5.4: Bayesian inversion results for model 5. Left: Three to five layers can be resolved with the data (estimated with BIC). Right: Marginal probability (colour bar) density profile for four layers for resistivity with depth with credibility intervals (CI), posterior median and mean models as well as the true model..

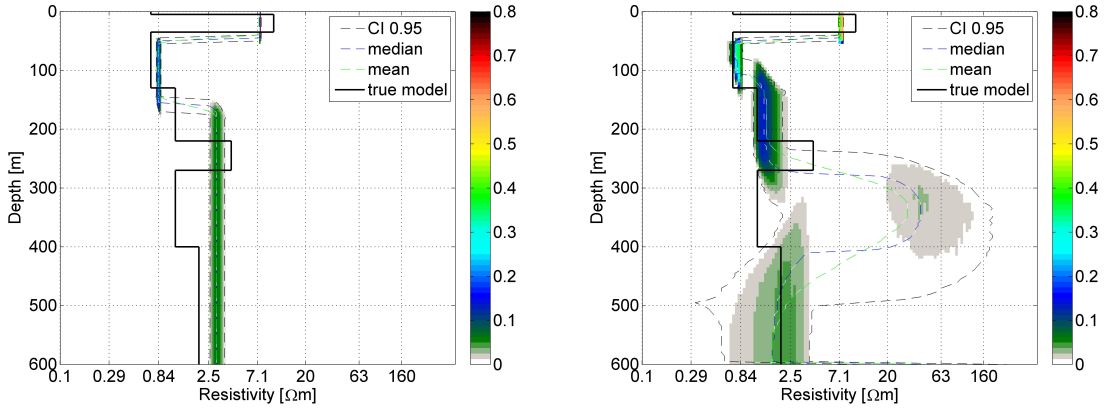

Figure 5.5: Marginal probability density (colour bar) profile for model 5 with three (left) and five (right) layers for resistivity with depth with credibility intervals (CI), posterior median and mean models as well as the true model..

with depth, which fits the true model well down to 270 mbsf. The number of layers is underestimated if only three layers are chosen as demonstrated in Fig. 5.5. The CI widths are narrow and the true model does not lay within them. The PPD represents an average solution over the true subsurface model that explains the data well. The inversion result for five layers is closer to the true model down to 220 mbsf. Below 220 mbsf the inversion introduces a high resistive layer with a high uncertainty (wide CIs). Therefore including five layers into the inversion might be overestimated. The data and residuals for the ASSA solutions for three, four and five layers are shown in

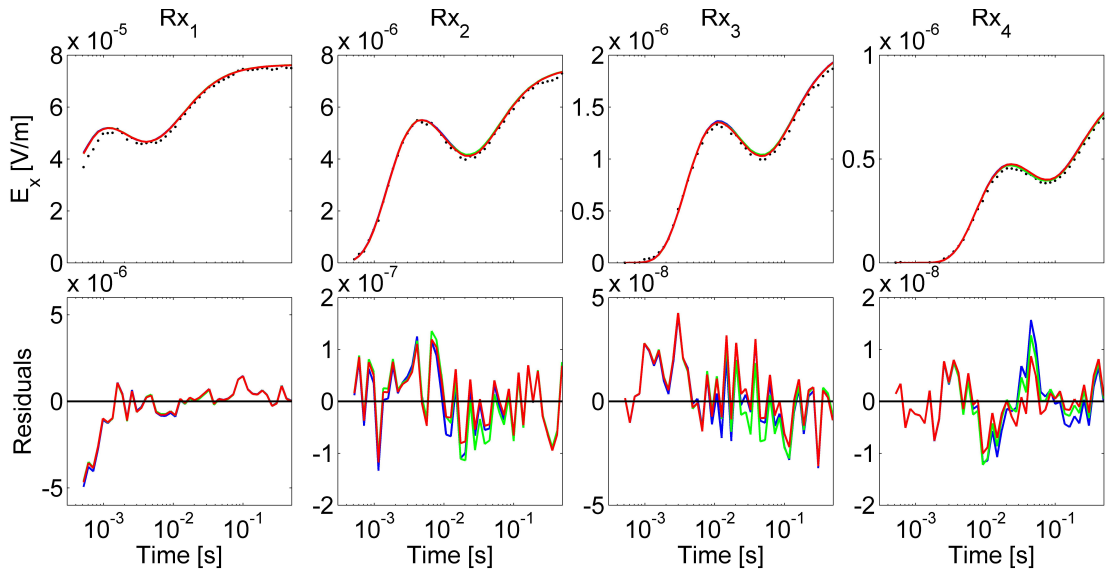

Figure 5.6: Data and residuals (units: V/m) of four receivers (at offsets of 150, 300, 450 and 600 m) for WP 5. Simulated data (black dotted line), predicted data for optimal model with three (blue), four (green) and five layers (red solid line).

Fig. 5.6 and the differences between the step-on responses are relatively small. The greatest difference to the observed data can be observed for early times of receiver 1 data, which is due to the thin conductive overburden (true model) which cannot be resolved in the inversion. The example for model 5 demonstrates the difficulty in estimating the appropriate number of layers.

Summary

The simulation study for five sub-seafloor models similar to the Ulleung Basin resistivity structure yields the following results. Resistivities above 400 mbsf are well resolved for most of the subsurface models. Resistivities below 400 mbsf are not well resolved probably due to the penetration limit of the CSEM array with 600 m maximum Tx-Rx offset. Small to intermediate resistivity contrasts (here, 0.6 to 9 Ωm) cannot be estimated correctly when considering the resistivity or thickness of the resistive layer alone, but rather in combination. The parametrization estimated with the BIC is simpler than the true model and model parameters, especially at greater depths, are averaged. Depth to and thickness of a sand layer with a high resistivity (here, 100 Ωm) and resistivities above and below are very well estimated, but the resistivity of the resistive layer itself is not. In this case the resistivity difference relates

to a few percent of gas hydrate. However, it may be relevant for production tests to estimate the amount of gas hydrate more accurately. Another approach for smaller amounts of gas hydrate might be to fix the depth to the gas hydrate-bearing sand layer to reduce the number of unknown in the problem.

5.5 Trans-dimensional Bayesian inversion

This section describes a trans-dimensional Bayesian inversion to infer parameter and uncertainty estimates in the presence of unknown layering [Green, 1995]. The approach does not require regularization or linearization, but samples probabilistically over the parameter space based on the information content of the data. Fixed-dimensional Bayesian inversion presented in Sec. 5.3.1 and 5.4 demonstrates how to estimate the number of layers that can be resolved with the data with the BIC. Other implementations of Bayesian algorithms for CSEM in fixed dimensions either constrain the subsurface resistivity structure with seismic inferred structure like hydrocarbon reservoir depth [Chen et al., 2007], or constrain the prior parameter width [Buland and Kolbjørnsen, 2012]. However, underestimating the number of parameters over-determines the inversion, and results in averaging the true model with too few parameters and underestimating uncertainties. On the other hand, overestimating the number of parameters under-determines the inversion and additional structure may be introduced by the inversion to fit the data error or create structural excess in areas that the data are insensitive to. Additionally, CI widths are often underestimated due to leaving out the uncertainty of the unknown parametrization. Trans-dimensional inversion is a good alternative and is becoming popular for various geophysical techniques [Malinverno, 2002; Sambridge et al., 2006; Bodin and Sambridge, 2009; Dettmer et al., 2010; Bodin et al., 2012]. Ray and Key [2012] have implemented a trans-dimensional inversion for frequency-domain CSEM data to estimate the resolution of different field components of the electromagnetic response and illustrated the challenges for CSEM data when targeting deep-situated, thin hydrocarbon reservoirs in anisotropic environments.

Our approach implements an algorithm similar to that described in Dettmer et al. [2010] and addresses the unknown layering of the earth model by introducing a hyperparameter which indexes models with various numbers of interfaces. Transitions (jumps) between models with differing numbers of layers are implemented by creating a new interface (birth step) or deleting an existing interface (death step). Jumps are

probabilistically accepted according to the Metropolis-Hastings-Green criterion. Additionally, parallel tempering [Dosso et al., 2012; Dettmer and Dosso, 2012] is applied to improve the acceptance rate of dimension jumps and the efficiency of parameter-space exploration for multi-modal solutions. Ray et al. [2013] show that parallel tempering can significantly speed up convergence to the posterior model distribution.

While Ray and Key [2012] work with diagonal data covariance matrices, in this thesis, correlated errors are accounted for with a non-Toeplitz data covariance matrix estimated from residual errors independent of the stacking standard deviation, and verify inversion results by testing standardized residual errors of the posterior median model for Gaussianity and randomness.

5.5.1 Reversible-jump MCMC sampling

Reversible-jump MCMC (RJMCMC) sampling enables transitions between dimensions $H \rightarrow H'$, where H represents a 1-D subsurface model with the number of interfaces k, and ensures reversibility for each transition [Green, 1995, 2003]. The methodology is based on partition modelling (Denison et al. [2002], page 177) and trans-dimensional jumps of the birth-death form [Geyer and Møller, 1994; Malinverno, 2002; Dettmer et al., 2010]. The acceptance criterion in Eq. (5.13) is extended to

$$\alpha = \min\left[1, \frac{P(k')P(\mathbf{m}'_{k'}|k')}{P(k)P(\mathbf{m}_k|k)}\left(\frac{L(k',\mathbf{m}'_{k'})}{L(k,\mathbf{m}_k)}\right)^{1/T}\frac{Q(k,\mathbf{m}_k|k',\mathbf{m}'_{k'})}{Q(k'\mathbf{m}'_{k'}|k,\mathbf{m}_k)}|\mathbf{J}|\right], \tag{5.24}$$

where k is a hyper-parameter that indexes the model choices and $|\mathbf{J}|$ is the determinant of the Jacobian for the transition function [Green, 2003]. If changes in k are limited to ± 1 for each dimension transition and parameter values within a new layer depend only on the values of the originating layer, $|\mathbf{J}|$ is unity [Agostinetti and Malinverno, 2010]. The prior probability in Eq. (5.24) is the product of the interface probability $P(k)$ and the parameter probability for interface k, $P(\mathbf{m}_k|k) = P(\mathbf{z}|k)P(\log_{10}\boldsymbol{\rho}|k)P(\boldsymbol{\sigma})$ for depth partition $\mathbf{z}$, layer resistivities $\boldsymbol{\rho}$ (sampled in the logarithmic domain) and the data error model, here, represented by standard deviation $\boldsymbol{\sigma}$ for simplicity. The prior probability for k is taken to be uniform in $[k^-, k^+]$:

$$P(k) = \begin{cases} \frac{1}{k^+ - k^-} \text{ if } k^- \leq k \leq k^+ \\ 0 \quad \text{otherwise.} \end{cases} \tag{5.25}$$

Likewise the prior distribution for resistivity $\boldsymbol{\rho}$ in the logarithmic domain is a bounded uniform distribution:

$$P(\log_{10}\boldsymbol{\rho}|k) = \begin{cases} \prod_{i=1}^{k+1} \frac{1}{\log_{10}\rho_i^+ - \log_{10}\rho_i^-} & \text{if } \log_{10}\rho^- \leq \log_{10}\rho_i \leq \log_{10}\rho^+ \\ 0 & \text{otherwise.} \end{cases} \tag{5.26}$$

Likewise the prior densities for the data-error model and for additional parameters that will be introduced (for example, cf) are bounded uniform distributions, and illustrated for a constant standard deviation $\boldsymbol{\sigma}$ for each receiver with

$$P(\boldsymbol{\sigma}) = \begin{cases} \prod_{i=1}^{N_{\mathrm{Rx}}} \frac{1}{\sigma^+ - \sigma^-} & \text{if } \sigma^- \leq \sigma_i \leq \sigma^+ \\ 0 & \text{otherwise,} \end{cases} \tag{5.27}$$

where N_{Rx} is the number of receivers. The prior distribution for the set of interface depths $\mathbf{z}$ can be written by initially introducing a fictitious grid with G depth points:

$$P(\mathbf{z}|k) = \frac{k!(G-k)!}{G!}, \tag{5.28}$$

as the chance of all combinations possible of k out of G, $\binom{G}{k}$. The advantage for choosing a fictitious grid is that it will cancel out in the final acceptance ratio.

5.5.2 Interface birth and death criteria

A birth step introduces a new interface at a random position drawn from a uniform prior over $[z_0, z_{\max}]$, where z_0=0 mbsf and the maximum depth $z_{\max}$ is chosen to be deeper than the penetration limit of the instrument. The parameters of the old layer (which is being sub-divided) are transcribed into the two new layers and one layer is randomly chosen and its parameters perturbed with a Gaussian proposal distribution. A death step reduces the model by one randomly-chosen interface. The parameter of the new layer is one (random draw) of the two layers that were divided by the deleted interface. Here, the chance for a birth or death proposal is between 1/4 and 1/3. All other times depth and resistivity parameters are perturbed for fixed dimensions. The general form of the proposal ratio for a transition from $k \to k'$ is

$$\begin{aligned} \frac{Q(k, \mathbf{m}_k|k', \mathbf{m}'_{k'})}{Q(k', \mathbf{m}'_{k'}|k, \mathbf{m}_k)} = & \frac{Q(k|k', \mathbf{m}'_{k'})}{Q(k'|k, \mathbf{m}_k)} \frac{Q(\mathbf{z}|k', \mathbf{m}'_{k'})}{Q(\mathbf{z}'|k, \mathbf{m}_k)} \\ & \cdot \frac{Q(\log_{10}\boldsymbol{\rho}|k', \mathbf{m}'_{k'})}{Q(\log_{10}\boldsymbol{\rho}'|k, \mathbf{m}_k)} \frac{Q(\boldsymbol{\sigma}|k', \mathbf{m}'_{k'})}{Q(\boldsymbol{\sigma}'|k, \mathbf{m}_k)}, \end{aligned} \tag{5.29}$$

where the proposal ratio for k is unity and cancels out for the error parameters (here, represented by $\boldsymbol{\sigma}$) because a symmetric Gaussian proposal distribution is applied.

When proposing the birth of an interface, where $k'{=}k+1$, the new interface can appear at any of the G fictitious grid points except at points that are already taken. The proposal for the depth of the interface becomes

$$Q(\mathbf{z}'|k,\mathbf{m}_k) = \frac{1}{G-k}. \tag{5.30}$$

The resistivity for the new layer is Gaussian distributed around the old value in this study and the proposal becomes

$$Q(\log_{10}\rho'|k,\mathbf{m}_k) = \frac{1}{\sqrt{(2\pi)\hat{\sigma}_\rho^2}} \exp\left(-\frac{1}{2}\frac{(\log_{10}\rho' - \log_{10}\rho)^2}{\hat{\sigma}_\rho^2}\right), \tag{5.31}$$

which is simplified from Dettmer et al. [2010] as every layer has only one physical parameter. The standard deviation of the Gaussian proposal $\hat{\sigma}_\rho$ is estimated by the prior boundaries $(\log_{10}\rho^+ - \log_{10}\rho^-)^2/int_\rho$, where int_ρ is a constant (chosen to be 30 here). The proposal density for the depths and resistivity of the reverse move is

$$Q(\mathbf{z}|k',\mathbf{m}'_{k'}) = \frac{1}{k+1}, \tag{5.32}$$

and $Q(\log_{10}\rho|k',\mathbf{m}'_{k'}) = 1$. The expressions for the proposal of a death move can be analogously derived with $k' = k-1$ and the proposal ratio (5.29) for birth and death become

$$\left[\frac{Q(k,\mathbf{m}_k|k',\mathbf{m}'_{k'})}{Q(k',\mathbf{m}'_{k'}|k,\mathbf{m}_k)}\right]_{\text{birth}} = \frac{G-k}{k+1}\sqrt{(2\pi)\hat{\sigma}_\rho^2}\exp(\frac{1}{2}\frac{(\log_{10}\rho' - \log_{10}\rho)^2}{\hat{\sigma}_\rho^2}), \tag{5.33}$$

$$\left[\frac{Q(k,\mathbf{m}_k|k',\mathbf{m}'_{k'})}{Q(k',\mathbf{m}'_{k'}|k,\mathbf{m}_k)}\right]_{\text{death}} = \frac{k}{G-k+1}\frac{\exp(-\frac{1}{2}(\log_{10}\rho' - \log_{10}\rho)^2/\hat{\sigma}_\rho^2)}{\sqrt{(2\pi)\hat{\sigma}_\rho^2}}. \tag{5.34}$$

From Eq. (5.25)-(5.28) it follows that the prior ratio for the acceptance criterion of birth or death becomes

$$\left[\frac{P(k',\mathbf{m}'_{k'})}{P(k,\mathbf{m}_k)}\right]_{\text{birth}} = \frac{k+1}{G-k}\frac{1}{(\log_{10}\rho^+ - \log_{10}\rho^-)} \tag{5.35}$$

$$\left[\frac{P(k',\mathbf{m}'_{k'})}{P(k,\mathbf{m}_k)}\right]_{\text{death}} = \frac{G-k+1}{k}\left(\log_{10}\rho^{+} - \log_{10}\rho^{-}\right) \tag{5.36}$$

The acceptance ratio in Eq. (5.24) can now be calculated with Eq. (5.33-5.36). The fictitious grid G conveniently cancels out and the acceptance ratios become

$$\alpha_{\text{birth}} = \min\Bigg[1, \frac{1}{(\log_{10}\rho^{+} - \log_{10}\rho^{-})} \cdot\sqrt{(2\pi)\hat{\sigma}_{\rho}^{2}}\exp\left(\frac{1}{2}\frac{(\log_{10}\rho' - \log_{10}\rho)^2}{\hat{\sigma}_{\rho}^{2}}\right)\frac{P(\mathbf{d}|k',\mathbf{m}'_{k'})}{P(\mathbf{d}|k,\mathbf{m}_k)}\Bigg], \tag{5.37}$$

$$\alpha_{\text{death}} = \min\Bigg[1, (\log_{10}\rho^{+} - \log_{10}\rho^{-}) \cdot\frac{1}{\sqrt{(2\pi)\hat{\sigma}_{\rho}^{2}}}\exp\left(-\frac{1}{2}\frac{(\log_{10}\rho' - \log_{10}\rho)^2}{\hat{\sigma}_{\rho}^{2}}\right)\frac{P(\mathbf{d}|k',\mathbf{m}'_{k'})}{P(\mathbf{d}|k,\mathbf{m}_k)}\Bigg]. \tag{5.38}$$

The likelihood function is evaluated with Eq. (5.17), but in the trans-dimensional implementation *cf* is sampled explicitly and perturbed with a Gaussian distribution. The data covariance matrix $\mathbf{C}_d$ is addressed in two ways for the observed data which will be considered in Chapter 7. A preliminary PPD is obtained when sampling with a diagonal covariance matrix with standard deviations from the stacking process of the data and a multiplicative factor analogous to Eq. (5.19). A non-Toeplitz covariance matrix is subsequently estimated with Eq. (5.23) from the residual errors of a median model of the preliminary PPD. A second inversion cycle (MHS sampling) with the non-Toeplitz covariance matrix samples the PPD to obtain parameter and uncertainty estimates.

A simulation study was carried out to demonstrate the trans-dimensional inversion for a model simulating the German North Sea environment. It is presented in Sec. 7.3 where it forms an important part of the planned publication that the chapter represents.

Another approach, which has not been used to estimate the sub-seafloor model, but was examined for simulated data and North Sea data in App. B, uses an auto-regressive (AR) error model to address correlated errors for CSEM data following Dettmer et al. [2012]. In this case, $\mathbf{C}_d$ is a diagonal matrix, that consists of constant variances along the main diagonal and error correlations are represented by a first-

order AR(1) process (equivalent to an exponentially-decaying covariance function). The unknown variance and AR coefficient for each receiver are perturbed during the inversion. The reason why this approach has been examined is because $\mathbf{C}_d$ is not fixed but calculated for every evaluation of the likelihood. A simulation study in App. B shows that the auto-regressive model accounts for error correlation if the acquisition parameters are well known. However, if acquisition parameters are unknown the problem becomes under-determined (the data cannot resolve the AR parameters, the acquisition parameters and the sub-seafloor parameters) and too much subsurface structure is introduced.

Chapter 6

Northern Cascadia Margin CSEM experiment

The Northern Cascadia margin, is an active subduction zone, where the oceanic Juan de Fuca plate subducts beneath the North American plate. Most of the oceanic sediments are accreted onto the continental margin, pressurized, and faulted [Davis and Hyndman, 1989]. Ongoing fluid flow and localized cold vents have been observed via heat flow, seismic, and borehole data [Davis et al., 1990; Hyndman et al., 1993; Riedel et al., 2009]. Gas hydrate occurrences have been detected during various expeditions with geophysical and geochemical techniques [Riedel et al., 2006b; Hyndman et al., 2007; Dash and Spence, 2011]. Seismic surveys and deep sea drilling have provided greater insights into the gas hydrate distributions in marine sediments, from gas hydrate recycling at the base of the gas hydrate stability zone (GHSZ) to fracture filling and laterally-variable hydrate accumulations along major fluid conduits [Riedel et al., 2006a; Haacke et al., 2007; Zühlsdorff and Spiess, 2004]. While drilling provides very localized, fine-scaled information and seismic data are usually sensitive to impedance contrasts associated with velocity and/or density changes, electromagnetic studies allow the evaluation of bulk volumes of sediments containing gas hydrates and/or free gas [Edwards et al., 2010]. Controlled source electromagnetic (CSEM) surveys have been conducted previously to study gas hydrate accumulations and cold vent systems on the Northern Cascadia margin [Yuan and Edwards, 2000; Schwalenberg et al., 2005; Willoughby et al., 2008]. The CSEM data analyzed in this study were acquired in the late summers of 2005 and 2006. The two survey areas are located on the middle and upper slope of the continental margin off Vancouver Island, Canada

(see Fig. 6.1).

This chapter is based on the paper (to be submitted) *"Bayesian inversion of marine controlled source electromagnetic data offshore Vancouver Island"* by R. A. S. Gehrmann, K. Schwalenberg, M. Riedel, S. E. Dosso and G. D. Spence. The dissertation author is the primary investigator and author of this paper. Schwalenberg provided the CSEM data and helped with the development of processing codes (written in MATLAB). Riedel and Spence provided the seismic data (upper slope) and knowledge on tectonics and gas hydrate distribution on the Northern Cascadia margin. Dosso helped with the development of the non-linear optimization and Bayesian inversion codes (written in Fortran 77/90).

6.1 Geology of the survey areas

A geological interpretation of the survey areas is drawn from the Integrated Ocean Drilling Program (IODP) Expedition 311 (X311) by Expedition 311 Scientists [2005] and Riedel et al. [2006a]. A transect of five drill sites was carried out on the continental margin offshore Vancouver Island in 2005 along multi-channel seismic (MCS) line 89-08, which runs from the abyssal plain to the upper slope basin (Fig. 6.1). An additional site (U1328) was drilled at Bullseye vent, an active cold vent 5 km southeast of the transect. The main objective of the drilling expedition was to constrain geological models for the formation of gas hydrates in an active subduction zone. The two CSEM survey areas are located on the upper slope around Site U1329 (area 1), and on the middle slope, around the Bullseye vent and Site U1328 (area 2).

6.1.1 Area 1: Upper slope near U1329

Site U1329 is situated 65 km from the coast of Vancouver Island, Canada, at the edge of the gas hydrate stability field. The area is marked with multiple canyons and topographic changes from 500 to 1300 m water depth along a 7.5 km track with an average slope of 6°. Reflection seismic data reveal turbidite sequences and erosional surfaces [Expedition 311 Scientists, 2005; Scherwath et al., 2006].

The detailed analysis of five boreholes from logging-while-drilling (LWD), wireline, and core data at Site U1329 (drilled to ∼220 mbsf) reveal three main lithostratigraphic units [Riedel et al., 2006a]. Unit 1 consists of Holocene to Pleistocene clay to silty clay to ∼40 mbsf. Unit 2 consists of Pleistocene silty clay with diatoms (>0.3 to

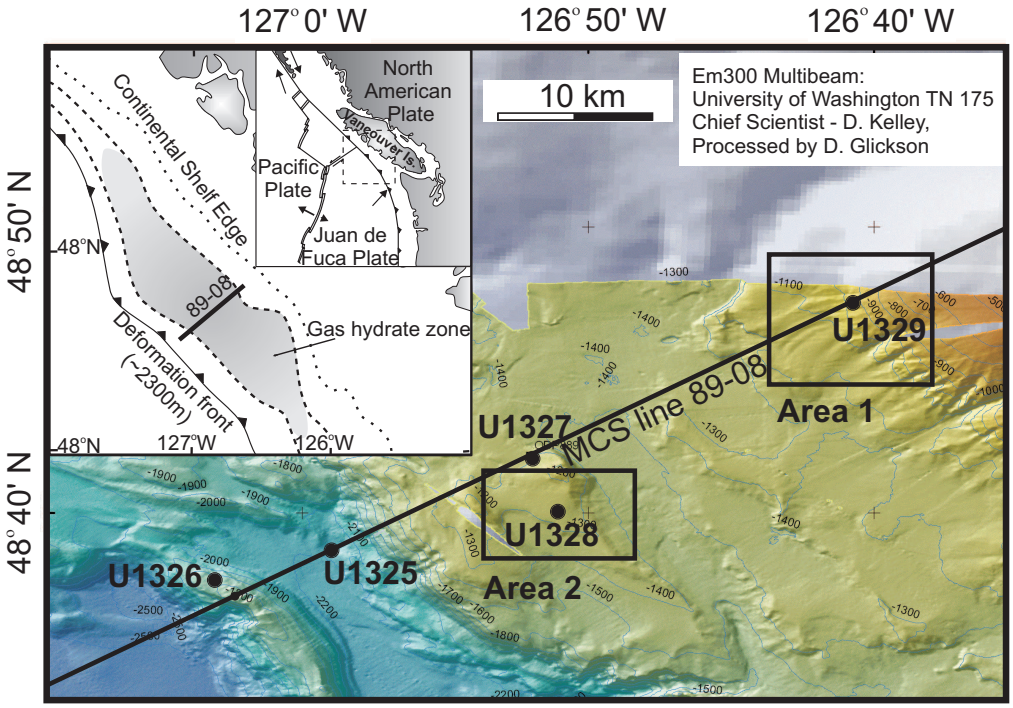

Figure 6.1: Overview of the Northern Cascadia margin offshore Vancouver Island with multi-channel seismic line 89-08 (black line), CSEM survey areas (black rectangles) and location of IODP X311 Sites.

2 Ma) from ∼40 to 140 mbsf, and Unit 3 consists of late Miocene material (>6.7 Ma). Sediment age increases from 2 to 6.7 Ma at the boundary between Unit 2 and 3, marking this as an erosional unconformity [Expedition 311 Scientists, 2006a], which can be observed on MCS line 89-08 (see Sec. 6.4.3). Resistivities (measured downhole with the *in-situ* GeoVISION high-resolution button deep averaging tool) increase from ∼1 Ωm above ∼170 mbsf to >4 Ωm due to a reduction in sediment porosity.

A bottom simulating reflector (BSR) is observed on MCS line 89-08 and on single channel seismic (SCS) line CAS05C-3 which runs perpendicular to MCS line 89-08, but does not continue upslope of X311 Site U1329. BSR's generally result from an impedance contrast at the base of the GHSZ caused by either sediments containing gas hydrate above the GHSZ or free gas beneath the GHSZ [Hyndman and Spence, 1992]. Boreholes through the GHSZ suggest only a few accumulations of gas hydrates at the base of the GHSZ at Site U1329 in 126 mbsf. Estimates of gas hydrate saturation based on biogenic gas production incorporating paleo-sedimentation rates also suggest a thin gas hydrate occurrence zone (GHOZ) at the bottom of the GHSZ [Malinverno

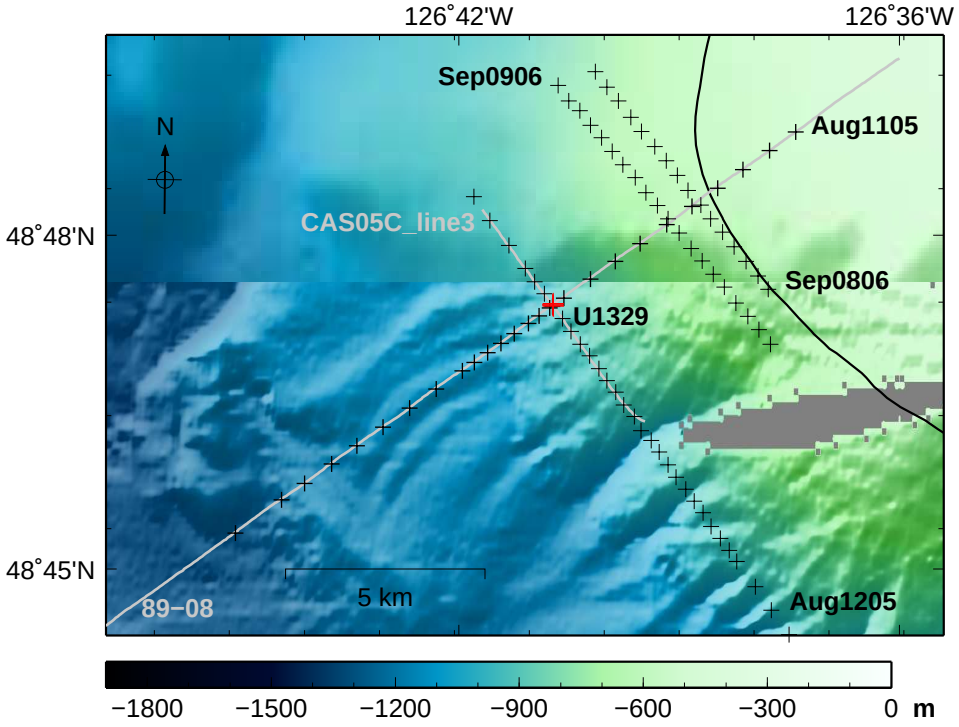

Figure 6.2: Bathymetry of Area 1 with data gap (gray area), CSEM way points (black crosses with annotations for those mentioned in the article), IODP X311 Site U1329 (red cross), MCS line PGC89-08 and SCS line CAS05C-line3 (gray lines), and estimated landward edge of the GHSZ (black curved line).

et al., 2008]. Four CSEM lines have been collected around U1329 (see Fig. 6.2), one line perpendicular to the slope and across the drill site, and three lines parallel to slope. One slope-parallel line intersects at U1329 and two further up the slope at the edge of the gas hydrate stability field.

6.1.2 Area 2: Middle slope, Bullseye vent

Bullseye vent is an extensively studied cold vent site on the middle slope of the northern Cascadia margin. Massive gas hydrate was recovered in piston cores in the upper 8 mbsf [Riedel et al., 2006b]. The vent site, one out of a series of blank zones observed in reflection seismic data over a wide range of frequencies [Riedel et al., 2002], is characterized by a prominent seismic diffraction produced by a shallow gas hydrate cap. CSEM data collected in 2004 prior to X311 revealed highly anomalous electrical resistivities over Bullseye vent which have been interpreted as sediments with high gas hydrate concentrations [Schwalenberg et al., 2005]. Local gas plumes were observed

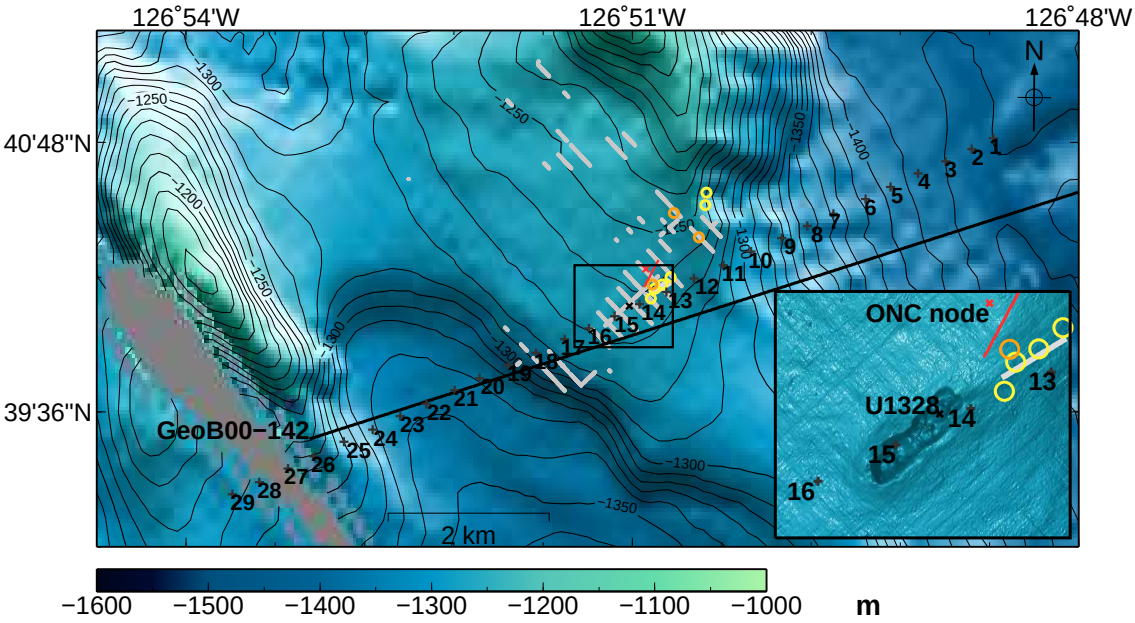

Figure 6.3: Overview of area 2 with Bullseye vent (black rectangle with enlarged detail by Paull et al. [2009], grey areas represent data gap), X311 Site U1328 (black cross), MCS line GeoB00-142 (black line), CSEM WPs (black plus signs), Ocean Networks Canada (ONC) platform at Clayoquot Slope (red cross), fixed CSEM system (red line), observed blanking on high-frequency AUV data from Paull et al. [2009] (gray lines), observed gas plumes in 2006 on CCGS *John P. Tully* (dark red circles) and in 2013 on RV *Falkor* (blue circles) and bacterial mats observed in 2013 on RV *Falkor* (light gray line on detail).

in 2006 in the water columns with a 18 kHz echo sounder on Canadian Coast Guard Ship (CCGS) *John P. Tully* during cruise 20060012PGC [Willoughby et al., 2008] and in 2013 with the multibeam system EM710 on research vessel (RV) *Falkor* during Neptune Canada cruise "Wiring the Abyss" [Römer, 2014, private communication]. The borehole analysis of U1328 revealed three major lithostratigraphic units: Unit 1 (0 to 130 m thick) contains Pleistocene sediments (<1 Ma) that consist of clay and silty clay interbedded with thin sand layers, with few microfossils. The transition to Unit 2 (130 to 200 mbsf) is characterized by a decrease in sand and silt content, while diatoms and other microfossils become more abundant. Unit 3 (200 to 300 mbsf) is 0.3 to 1.6 Ma old and contains far fewer microfossils than Unit 2, but also consists of similar clay to silty clay.

Observations of pore-water chlorinity provide information about hydrate formation within the sediment column. Between 5 and 20 mbsf, high chlorinity values

indicate a recent and rapid formation of gas hydrates, faster than the assumed diffusion rate of 5×10^{-6} cm^2/s [Riedel et al., 2006a]. Rapid gas hydrate formation is possible in scenarios of high methane supply, *e.g.*, along fractures. Accumulations of gas hydrates are also supported by LWD-deep button average resistivities from 1 to 20 Ωm between 5 to 50 mbsf [Expedition 311 Scientists, 2006b]. A strong reflector, possibly related to the top of a solid hydrate cap, is observed on seismic lines just below the seafloor reflection. Chlorinity values and on-board infrared thermal imaging (IR) suggest little to no gas hydrate between 60 and 150 mbsf. The lack of gas hydrate at intermediate depths is also supported by low resistivities, which increase with depth from 1 to 2 Ωm between 50 and 150 mbsf. One exception is a thin interval with elevated resistivity of up to 3 Ωm between 90 and 100 mbsf. Hydrates were discovered at 92 mbsf in one core (0.7 to 38%), but do not seem to be laterally continuous suggesting hydrate formation along fractures. However, low chlorinity values between 150 and 220 mbsf indicate an increased gas hydrate content just above the base of the GHSZ, especially in the 10 m above the assumed base of the GHSZ at 220 mbsf, which is also supported by strong IR anomalies. Free gas concentrations of 58% below the GHSZ were found in one pressure core, but could not be confirmed by wireline acoustic logging or by vertical seismic profiles [Riedel et al., 2006a].

Four CSEM lines were collected across Bullseye vent in 2004 and 2005 [Schwalenberg et al., 2005; Schwalenberg, 2007]. The line analyzed here is shown in Fig. 6.3 and runs in a NE to SW direction intersecting the Bullseye vent. The insert map in Fig. 6.3 also shows the location of the CSEM experiment that was installed at the Ocean Networks Canada (ONC) node at Bullseye vent. Analysis of CSEM data collected here predicts a resistivity of ∼5 Ωm in a ∼40-m thick overburden layer underlain by a less resistive halfspace of ∼0.7 Ωm, and this supports shallow gas hydrate and/or free gas occurrences [Mir, 2011].

6.2 Marine CSEM method and instrumentation

Marine CSEM measurements presented here were carried out with the time-domain electrical dipole-dipole system shown in Fig. 6.4. The system was developed at the University of Toronto and was particularly designed for the investigation of marine gas hydrates [Edwards, 1997; Yuan and Edwards, 2000]. On the seafloor it consists of a ∼123 m long electrical transmitter dipole (Tx) followed by two electrical receiving dipoles with a length of ∼14 m at offsets of ∼174 m and 292 m from Tx measuring

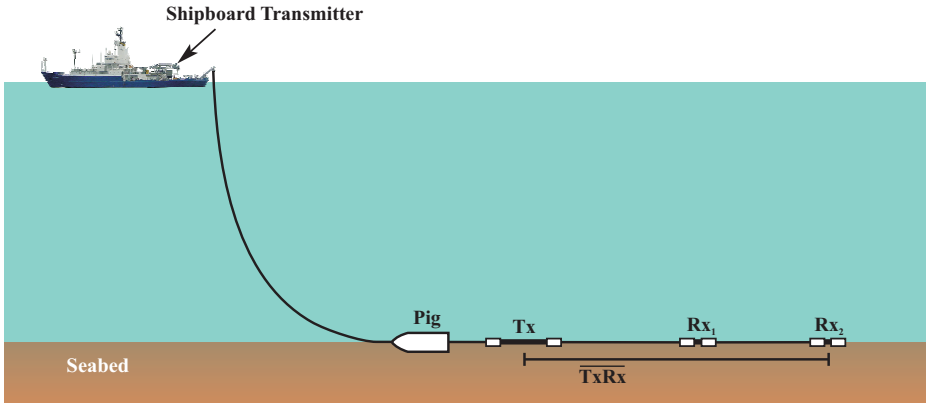

Figure 6.4: Configuration of the seafloor-towed horizontal dipole-dipole CSEM instrument which consists of a heavy weight (pig), a transmitter (Tx) and two receivers (Rx), where $\overline{\text{TxRx}}$ is the offset between them [Schwalenberg et al., 2005; Yuan and Edwards, 2000]. Figure not to scale.

the inline-component of the ambient electrical fields with silver chloride electrodes from Woods Hole Oceanographic Institution. A heavy, plough-shaped weight, called a "pig", is attached to the front end of the array to keep it on the seafloor. The array is connected to the vessel through a coaxial tow cable. The current signal has a square waveform with a peak-to-peak amplitude of 20 A and a period of 6.6 s that is generated by a custom-made current transverter situated on board the research vessel. The signal is sent to the transmitter dipole on the seafloor via the coaxial tow cable. The autonomous receiver units are equipped with a data logger, a high-precision clock board, analog electronics and battery packs inside aluminum pressure cylinders. An identical unit was used on the ship to record the source signal. CSEM data are collected by aligning the CSEM system on the seafloor where it is towed along lines making stops to record data at each way point (WP). Due to limited data storage at the time of the experiments, data processing was carried out in two steps. The first processing step was carried out during data recording. The analog raw time series recorded with both receiver units and the unit recording the source current were band-pass filtered to remove high-frequency noise and low-frequency electrode drifts, stacked during recording and stored in equal-length data sets. The second processing step was carried out after the experiment. The step-on response and its standard deviation, which are used as input in the inversion described in Sec. 6.3, were obtained when stacking periodic half periods. Figure 6.5 shows a set of step-on responses and source signals (inset) measured on August 11$^{\text{th}}$ 2005. The data

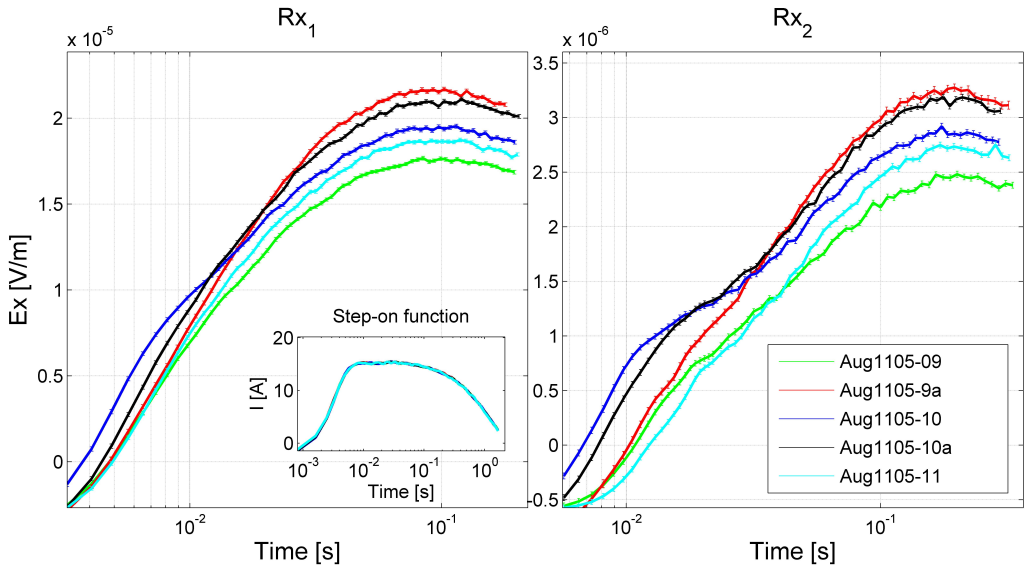

Figure 6.5: Observed data of two receivers with error bars (stacking standard deviation) and source signal (step on) for five adjacent WPs (9-11) of CSEM line Aug1105.

generally have a moderate data quality. Differences in the electrical field responses may indicate variations in the seafloor resistivity along the profile, *e.g.*, earlier arrival of the step-on response is related to a higher resistivity in the subsurface. Table 6.1 gives an overview of the lines analyzed in this study.

Profile	Date	Comments
Area 1		
Aug1105	11th Aug. 2005	parallel to slope Tx electrode corroded
Aug1205	12th Aug. 2005	perpendicular to slope Rx_1 electrode cable torn
Sep0806	8th Sept. 2006	perpendicular to slope
Sep0906	9th Sept. 2006	perpendicular to slope
Area 2		
Jul3105	31st July 2005	across Bullseye vent

Table 6.1: List of CSEM data from the Northern Cascadia margin which was analyzed in this study.

6.3 Inversion methods

Preliminary apparent resistivities, based on a simple model of seawater above a homogenous sediment halfspace, are obtained using a linearized Marquardt inversion technique [Meju, 1994; Scholl, 2010]. Linearized inversion is a local method that moves down the data misfit gradient from an initial model and converges to a global or local minimum. When carrying out multi-layer inversions, a fundamental issue is that the amount of vertical structure resolved by the data is not known *a priori*. One approach to multi-layer linearized inversions for CSEM data is to over-parametrize the model with many layers below the resolution of the data and include a regularization (smoothing) term to avoid unconstrained resistivity structure in the model. The most widely used algorithm is Occam's inversion [Constable et al., 1987], which minimizes an L_2-norm of the second depth-derivative of the resistivity to fit the data with minimal structure as introduced in Sec. 3.1.2. However, linearized inversion algorithms utilizing regularization are not well suited to quantitatively estimate model uncertainties. This section addresses the question of how much vertical structure can be resolved with CSEM data and a 1-D non-linear Bayesian inversion technique. I first implement a non-linear hybrid optimization (described in Sec. 5.1), which combines simulated annealing, a global search, with a downhill simplex optimization [Dosso et al., 2001]. The BIC is used to determine the optimal number of layers resolved by the data, and subsequently Metropolis-Hastings sampling (MHS) with parallel tempering is used to sample the parameter space and obtain parameter uncertainty estimates following Dosso and Dettmer [2011] and Dosso et al. [2012] as described in Sec. 5.3.1. The non-linear, numerical approach allows additional experimental parameters to be included in the inversion. Marginalizing over such parameters includes the effect of their uncertainties in the total uncertainty of the resistivity model. Here, a multiplicative calibration factor (CF) is included that scales the predicted step-on response [Scholl, 2005]. Amplifiers and electrode calibration values are already incorporated in the processing. However, the CF is implemented here to compensate for possible errors of survey parameters such as the measured source amplitude and array geometry. Another unknown included in the inversion is a small time delay representing drift of the Tx/Rx oven-heated crystal clocks that were synchronized on board but found to have drifted by up to 3 ms after instrument recovery (after $\sim$12 hours).

In this study, the likelihood function is based on the assumption that the data

errors are zero-mean and Gaussian distributed with an unknown covariance matrix $\mathbf{C}_d$ estimated from the data according to Eq. 5.17. These assumptions are verified *a posteriori* by applying statistical tests [Dosso et al., 2006; Montgomery et al., 2012]. The CF is sampled implicitly within the inversion and a non-Toeplitz data covariance matrix is estimated as described in Sec. 5.3.4. The inversion procedure is illustrated in Fig. 6.6.

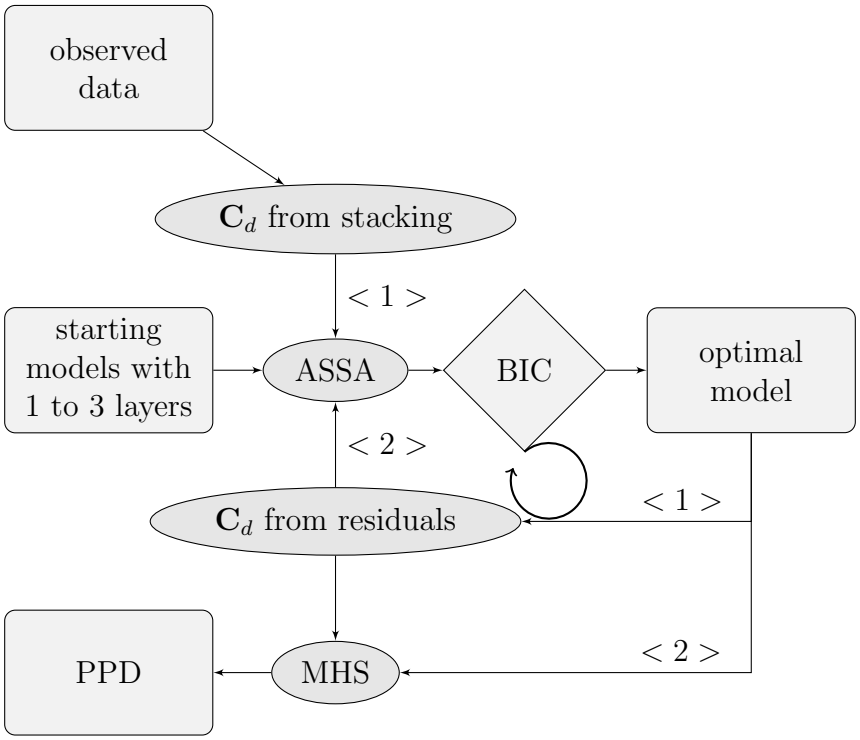

Figure 6.6: Inversion flow: $< 1 >$ ASSA inversion for three models with 1 to 3 subsurface layers and a diagonal data covariance matrix from data stacking. Number of subsurface layers that can be resolved with the data is selected with BIC. A full non-Toeplitz data covariance matrix is estimated from residual error analysis. $< 2 >$ ASSA inversion for three models with 1 to 3 subsurface layers and non-Toeplitz data covariance matrix. Number of subsurface layers that can be resolved with the data is selected with BIC. MHS samples the parameter space to obtain the PPD.

6.4 Inversion results and discussion

6.4.1 Number of sediment layers

As mentioned previously, the optimal number of sub-seafloor layers is estimated by minimizing the BIC, which requires minimizing the data misfit for different numbers of layers using ASSA. A representative example of this procedure is given in Fig. 6.7 for WP 11 from CSEM line Aug1105 where two layers are resolved. The number of layers that can be resolved generally varies between WPs and between CSEM lines. Over 50% of the WPs are interpreted with halfspace (1-layer) models, while about 40% of the WPs can be represented by 2-layer models according to the information in the data, and the remaining ∼10% are made up of 3-layer models. The relatively small number of layers is due to the lack of resolution inherent to diffusion methods, the lack of strong resistivity contrast in the shallow penetration depth of the CSEM array (to ∼200 m depth), and the relatively low signal-to-noise ratio of the survey [compared to more recently developed instruments by Schwalenberg and Engels, 2012a].

6.4.2 Marginal probability profiles

After the number of layers is determined, MHS is applied to sample the parameter space. The resulting PPD of WP 11 from line Aug1105 at X311 Site U1329 are shown in Fig. 6.8 in form of marginal probability densities, joint-marginal probability densities and a marginal probability profile. One-dimensional marginal densities

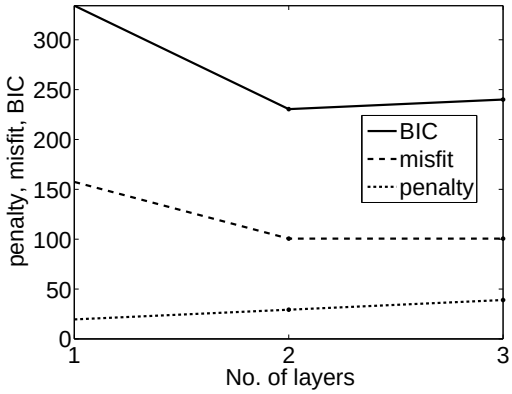

Figure 6.7: Bayesian information criterion (BIC) to evaluate the number of layers that are resolved with the data for WP 11 from line Aug1105. Here, two layers are resolved.

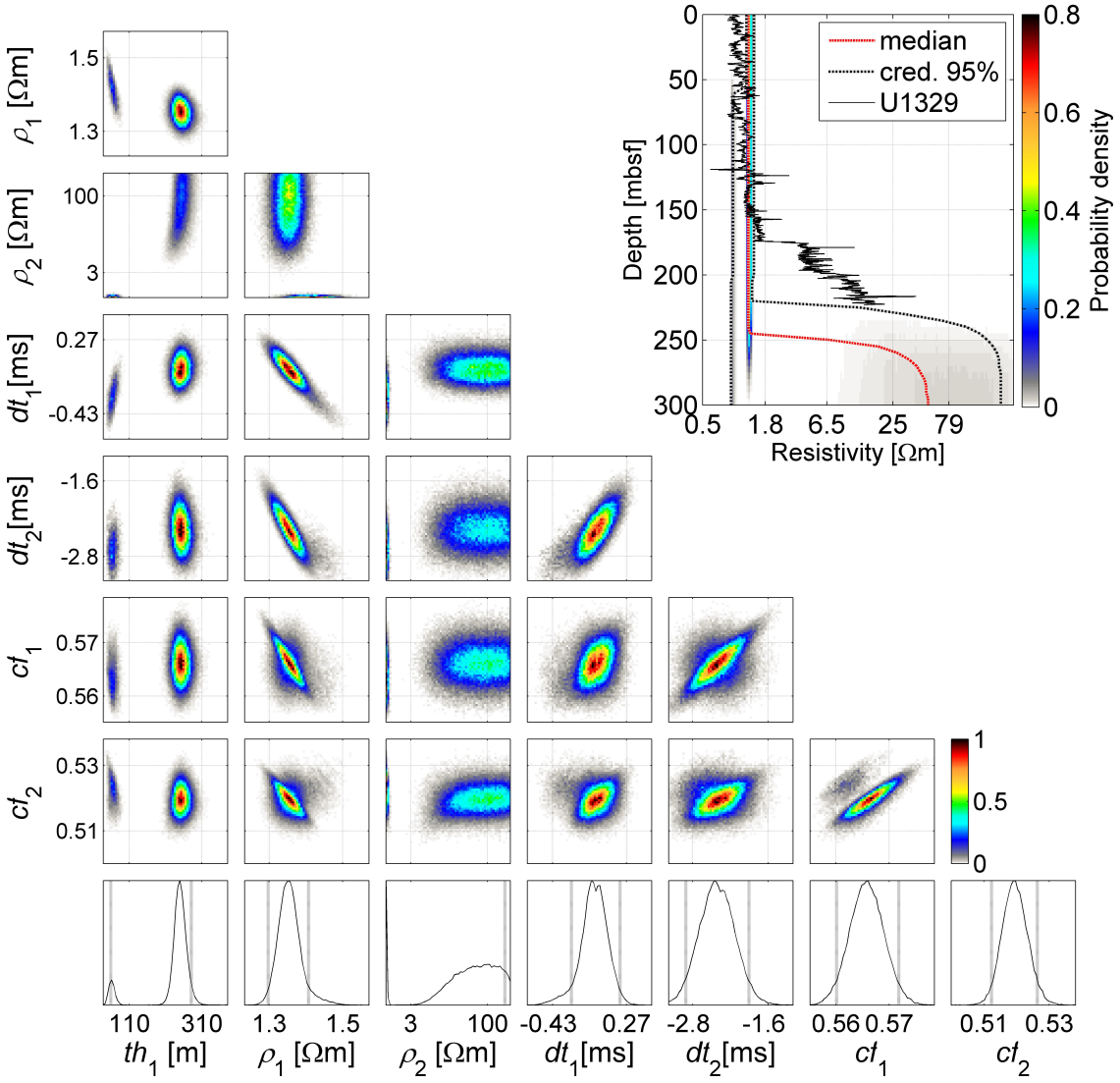

Figure 6.8: Inversion results for WP 11 from line Aug1105 in Area 1 close to X311 Site U1329. Bottom: Marginal probability densities for each parameter (thickness th_l and resistivity ρ_l for the l^{th} layer, as well as calibration factor cf_i and time delay dt_i for the i^{th} receiver) with 95%-credibility intervals shown as dotted lines. Middle: Joint marginals (normalized to unit maximum) showing relationships between parameters. Top right corner: Marginal probability density profile with posterior median model estimate, 95% credibility interval, and deep button average resistivities from U1329A.

represent uncertainty distributions for individual parameters, while joint marginals indicate relationships between parameters (all distributions in Fig. 6.8 are normalized independently for display purposes). Parameter relationships show some non-linear behavior and parameters are both positively and negatively correlated. For instance, ρ_2 increases as th_1 increases, indicating the data are sensitive to a resistivity increase with depth, but cannot resolve the depth or the resistivity individually. Critical are the relationships between instrument parameters such as cf and dt to the sub-seafloor parameters, which increase ambiguity and model uncertainty. For instance, ρ_1 is negatively correlated with dt_1 and dt_2; hence, not knowing the time delays exactly increases the uncertainty for ρ_1. Uncertainties are quantified with 95%-credibility intervals (CI), which contain 95% of all model samples evaluated for every depth interval. CIs are shown for marginals densities (bottom panels of Fig. 6.8) and on the resistivity marginal probability density profile that represents the PPD as a function of depth (top left of Fig. 6.8). The CI width for ρ_1 is two orders of magnitudes narrower than for ρ_2 as the resolution of the data is limited for greater depths. The CIs for ρ_1 are by two orders of magnitudes smaller than for ρ_2 as the resolution of the data is limited for greater depths. The probability density as a function of depth for WP 11 indicates an increase in resistivity between 220 to 250 mbsf. Within the first 150 m depth the inversion results match well with the measured LWD-resistivity (deep button average) at X311 Site U1329. The LWD measurements show an increase in resistivity starting at about 175 m depth due to the lower porosity of lithological Unit 3; this depth is not well resolved in the inversion results. The width of the CIs for the 2-layer model may underestimate the actual range of resistivities in the sub-seafloor, because the uncertainty on the number of layers is not included. The posterior median model in Fig. 6.8 is represented by a similar 2-layer model with a high likelihood to evaluate residual error statistics. Standardized residuals are estimated by $\tilde{\mathbf{r}} = \mathbf{S}(\mathbf{d} - cf\mathbf{d}(\mathbf{m}))$, where $\mathbf{S}$ is the Cholesky decomposition of $\mathbf{C}_d^{-1}$, and are shown on Fig. 6.9. Residual errors are calculated with predicted data from one 2-layer model that is similar to the posterior median model in Fig. 6.8 and has a high likelihood. Observed and predicted data for this model as well as standardized residuals are shown in Fig. 6.9. The standardized residual errors generally pass statistical tests [Dosso et al., 2006] for Gaussianity (Kolmogorov-Smirnov test) and randomness (runs test). Standardized residual errors pass statistical tests if resulting p-values are larger than a significance level of 0.025. Histograms for standardized residuals at WP 11 compared to a standard Gaussian are shown in the bottom row of Fig. 6.9.

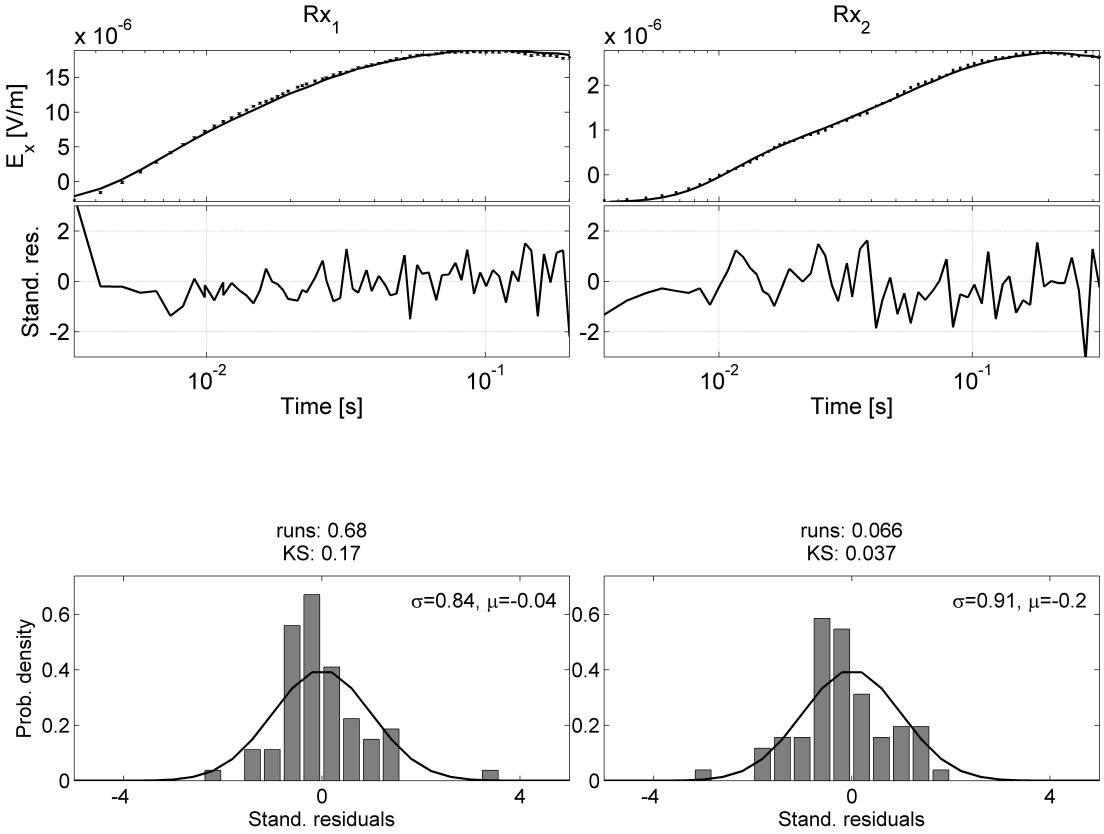

Figure 6.9: Top: Step-on response for WP 11 from Aug1105 with observed data with standard deviations from $\mathbf{C}_d$ (crosses with error bars) and predicted data (black line) and standardized residuals. Bottom: Histograms of standardized residuals with p-values for runs and KS test compared to a standard Gaussian distribution.

6.4.3 Area 1: Inversion results and implications

Three CSEM lines around X311 Site U1329 were inverted with the Bayesian algorithm. Line Aug1105 (Fig. 6.10) along MCS line 89-08 is perpendicular to line Aug1205 (Fig. 6.11) along SCS line CAS05C-3, and perpendicular to line Sep0806 (Fig. 6.13) that intersects with line Aug1105 on the upper slope (see Fig. 6.2). Median posterior models for each WP are plotted in Figs. 6.10 and 6.11 (upper panel) as coloured bars to represent the resistivity values. The bar widths correspond to the Tx-Rx_2 offset and the WP locations are approximately (max. 200 m apart) merged with the seismic lines. The coloured bars overlap where WPs are close (generally $\sim$500 m apart with exception of the central part around X311 Site U1329 where they are $\sim$250 m apart). At each WP the credibility intervals are plotted as black lines

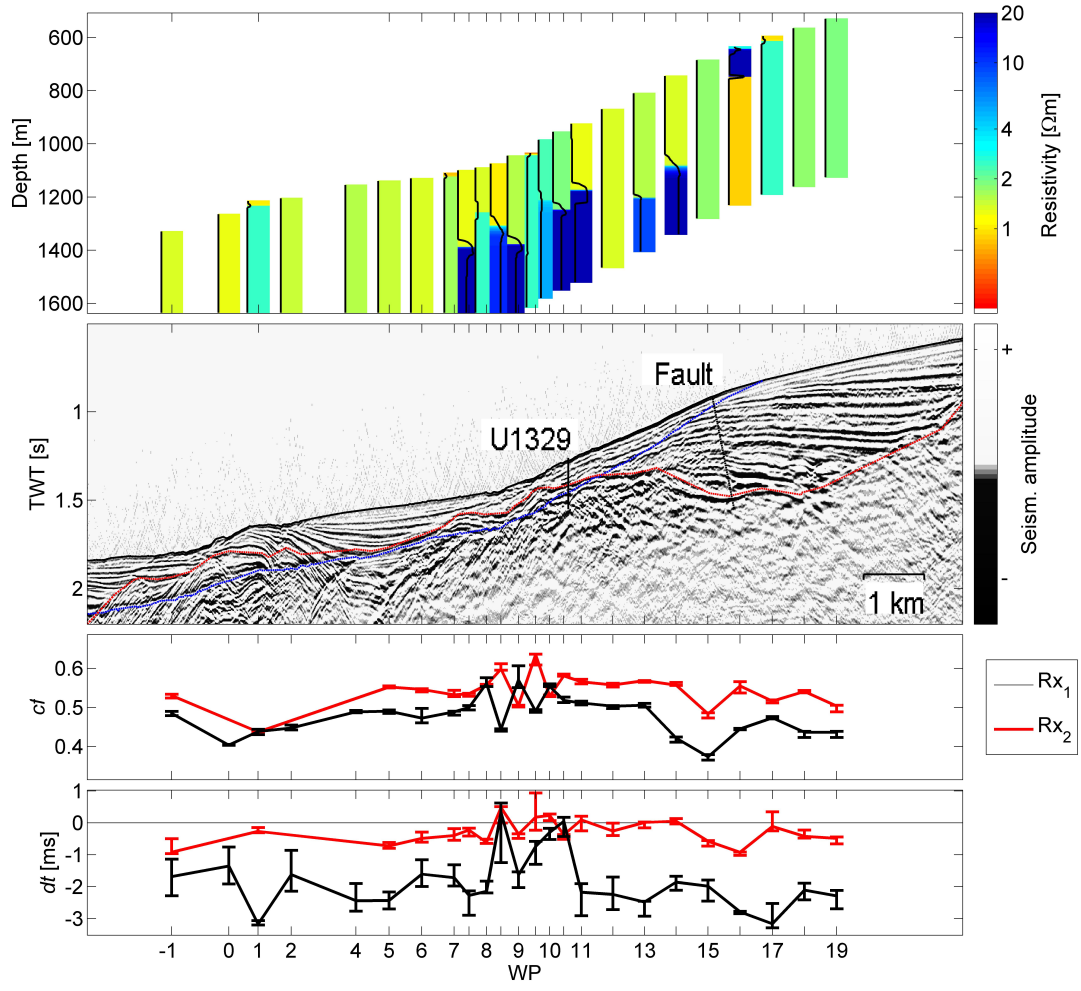

Figure 6.10: Top: CSEM median resistivity models for line Aug1105 with CI width (black line) normalized so that the maximum width equates to the width of the colored bars. Middle: MCS line 89-08 with X311 Site U1329, observed and extrapolated BSR (blue line) and sediment unconformity (red line). Bottom: calibration factor (CF) and time delay (dt) for each receiver, error bars represent 95%-credibility intervals.

at the left edge of the coloured bars. The right edge corresponds to the prior resistivity bound width. Additional inversion parameters shown in the bottom panels of Fig. 6.10 and 6.11, are *cf*, which accounts for unknown source amplitude, and *dt*, which accounts for time drift after synchronization of the transmitter and receiver clocks.

Figure 6.10 shows results for CSEM line Aug1105 along MCS line 89-08. The seismic data (middle panel) acquired in 1989 by the Geological Survey of Canada [see

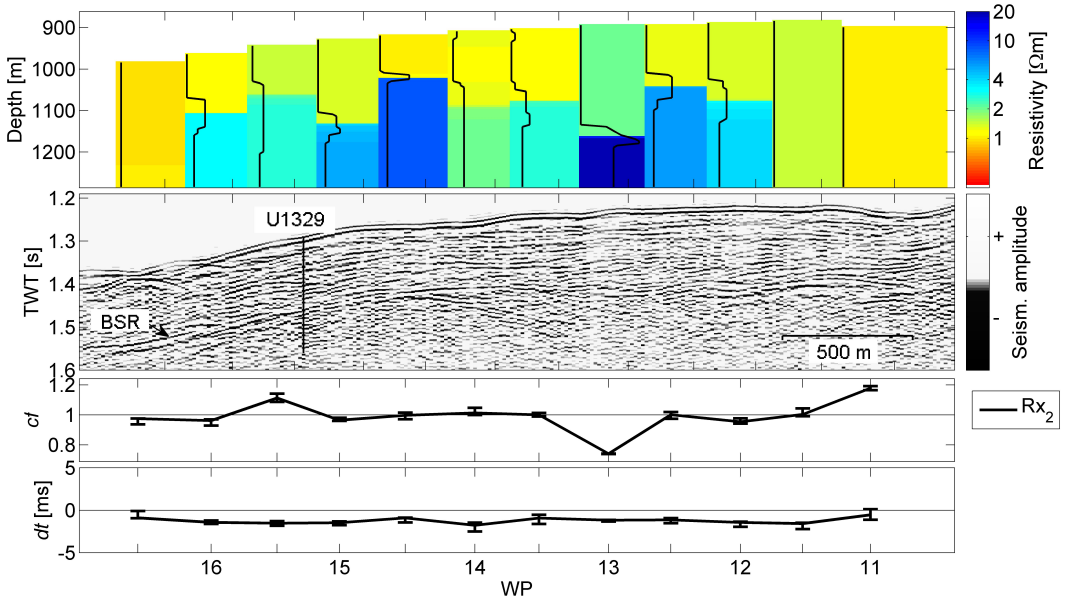

Figure 6.11: Top: CSEM median resistivity models with 95%-credibility interval width (black lines) for line Aug1205. Middle: SCS line Cas05C-3 with Site U1329 (black line). Bottom: CF and time delay between Tx and Rx (error bars represent 95%-credibility intervals).

e.g., Hyndman et al., 1993] show parallel layering of marine sediments representing Units 1 and 2 that lay on top of highly disturbed, accreted sediments with a rugged surface (Unit 3). A BSR is observed on the middle slope, as far landward as Site U1329, but it cannot be observed further up slope. The base of the GHSZ is calculated from the observed BSR depths and extrapolated landward of U1329 [Gehrmann et al., 2009].

The Bayesian inversion reveals that halfspace interpretations are adequate for the data at most of the measurement sites. Exceptions on line Aug1105 are WP 16 (possible venting site) and WP 7a to 14, where 2 layers with a resistive deeper layer are more probable. This layer may relate to the sediment unconformity seen on MCS line 89-08, which is characterized by a decrease in porosity and increase in resistivity, as seen in the borehole log data of X311 Site U1329. The second layer resistivity has wide CIs, which reflects the penetration limit of the CSEM array. The same unconformity lies relatively close to the seafloor between WP -1 and 2, but only WP 1 resolves two layers with an elevated resistivity below $\sim$20 mbsf.

The very pronounced resistivity anomaly at WP 16 on line Aug1105 is located at the landward edge of the GHSZ. This might be related to gas hydrate or free gas

accumulations. MCS line 89-08 reveals a normal fault which may support upward migrating fluids transporting gases. There are no indications (*e.g.*, diffractions, seismic blanking) of gas hydrate or free gas in the seismic data at this location. However, several localized venting sites have been detected along the upper slope of the margin [Riedel et al., 2006b]. The main frequencies of MCS 89-08 were chosen to penetrate the deep subsurface structure and may not resolve the upper 100 m in detail. To detect small gas hydrate lenses or along-fault rising gases may require higher frequencies. The resistivity anomaly at WP 16 is localized but consistent, it was observed on two consecutive days (the profile was repeated due to technical reasons) and also on the perpendicular line Sep0906 where it intersects with line Aug1105 (shown on Fig. 6.2).

The CF for Aug1105 reveals that the current induced into the seafloor might have been about half of the expected value (which was measured with a Hall sensor on the ship). This might be due to a corroded connection to the transmitter electrode (observed on board). The time delay is between 0 to -1 ms for Rx_1 and less consistent for Rx_2 with a mean value between -1 to -3 ms. The rugged trend likely relates to correlation between the sub-seafloor parameters and dt. However, the measured total drift on board after the instrument was recovered was -0.2 ms for Rx_1 and -1.2 ms for Rx_2 which fall within the inferred time delay range. I infer from the inversion results that most of the drift happened during deployment, likely due to pronounced pressure and temperature changes, and not between WPs.

CSEM line Aug1205 is perpendicular to line Aug1105 and coincident with the SCS line CAS05C-3. Only one part has been inverted with the Bayesian inversion, WP 11 to 16a, and the results are shown in Fig. 6.11. The seismic data (middle panel) show a strong BSR that might also coincide with the unconformity observed on MCS line 89-08. At WP 13 slight seismic blanking is observed and the CSEM inversion indicates elevated resistivity that might be related to gas venting or hydrate accumulations. Other WPs have lower resistivities at shallow depths, but higher resistivities at depth of $\sim$150 to 200 mbsf might be related to the resistive material of geological Unit 3. The inferred time delay for Rx_2 is between -1 and -2 ms.

The southeastern part of Aug1205, WP 3 to 11, has only been inverted with a linarized Marquardt inversion [Scholl, 2010] for halfspace resistivities due to the rough topography, and is shown with 3.5-kHz sub-bottom profiler data on Fig. 6.12. A pronounced resistivity anomaly is found at WP 6 which is located on the edge of a shell-shaped topographic depression. The anomaly could be caused by free gas

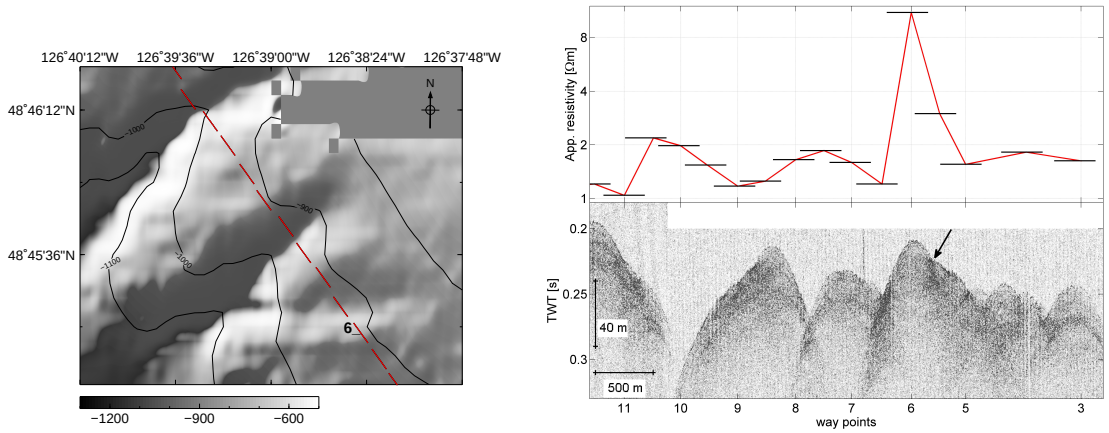

Figure 6.12: Left: Bathymetry at the south-east end of line Aug1205. Right, top: Apparent resistivities, black solid lines represent the length of the instrument and position (assuming a flat seafloor). Right, bottom: 3.5-kHz sub-bottom profiler data, arrow pointing to erosional surface.

rising along a fault plane that might also have caused the depression to form during a slide. If this is the case, this feature would be of interest for further studies of the stability of the upper slope. The 3.5-kHz sub-bottom (chirp) profiler data show elevated amplitudes and a reflector that might relate to an erosional surface that was refilled (south of the anomaly itself). The resistivity anomaly at WP 6 is significantly larger than others in this area, and is unlikely caused by the topographic effects, whereas elevated apparent resistivities between WP 7 and 11a are difficult to interpret due to the strong seafloor topography changes relative to the length of the CSEM array (which may introduce large theory errors for an unknown geometry that is not accounted for in the inversion).

Bayesian inversion results for line Sep0806 (see Fig. 6.13) reveal that at most WPs only a single layer is resolved with generally higher resistivities on the upper slope compared to resistivities down the slope on lines Aug1105 and Aug1205. The mean values for the CF for Rx_1 are around 1, while mean values for Rx_2 are around 0.8. The inferred time delay is only about -1 ms for the data set collected in 2006.

6.4.4 Area 2: Inversion results and implications

Resistivity median models from the Bayesian inversion are shown in Fig. 6.14 along MCS line GeoB00-142. The CSEM WPs are projected to the seismic line with a maximum projection distance of 1 km at WP 1 (see Fig. 6.3). The seismic section

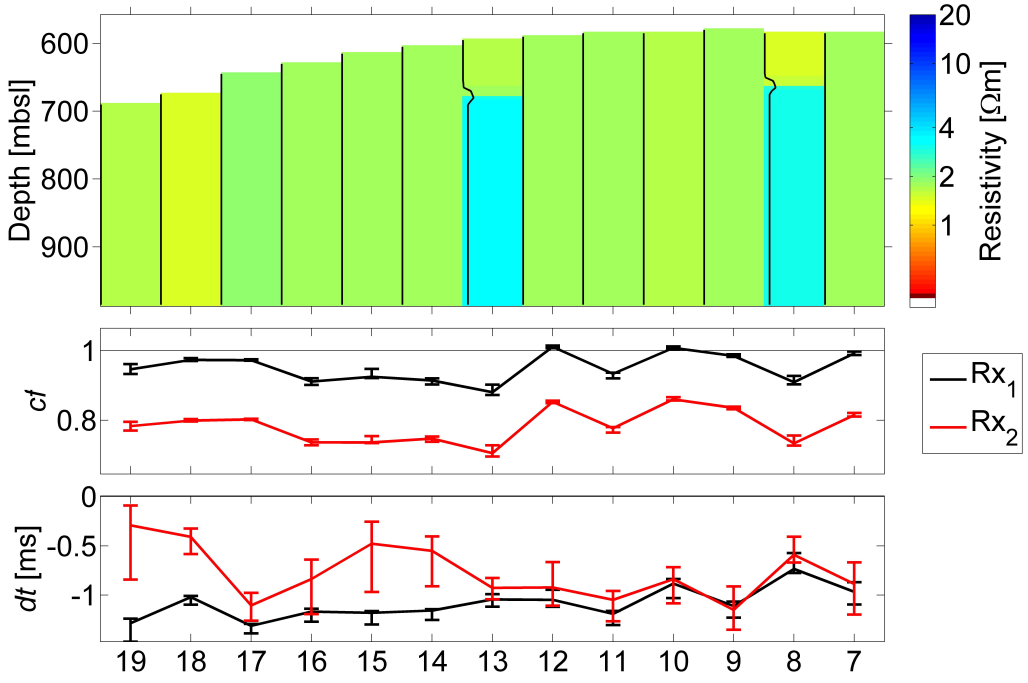

Figure 6.13: Line Sep0806. Top: Median models along the line. Middle: Calibration factor (CF). Bottom: time shift, error bars represent 95%-credibility intervals

(middle panel on Fig. 7.10) shows several high amplitude reflections, and seismic blanking at X311 Site U1328 which may relate to gas hydrates or free gas in the sediment. Sediment reflectors at U1329 are seemingly distorted, which might be caused by a shorter travel time through sediments containing massive gas hydrates or by faulting. Seismic amplitudes increase west of Site U1328 at 1.92 to 1.98 s two-way travel time (twt) close to the base of the GHSZ. Older, distorted, accretionary-wedge sediments are uplifted on both sites of U1328 and are overlain with younger, stratified slope deposits. Bullseye vent is the most dominant feature, centred on CSEM line Jul3105 at WPs 14 and 15 (see Fig. 6.3). Inversion results at WPs 13 and 14 reveal high resistivities around ∼25 Ωm within the first 70 to 100 mbsf. Observed gas plumes and bacterial mats (see Fig. 6.3) at the same location support the presence of shallow gas hydrate or free gas. WP 14 is close to Site U1328 and inversion results match with the high resistivities observed during drilling (see Fig. 6.15). The high resistivities may be caused by the massive gas hydrates, which were found during piston coring [Riedel et al., 2006b]. The inversion at WP 15 introduces a deeper resistive layer, which might relate to resistive material at greater depth. The seismic reflector on

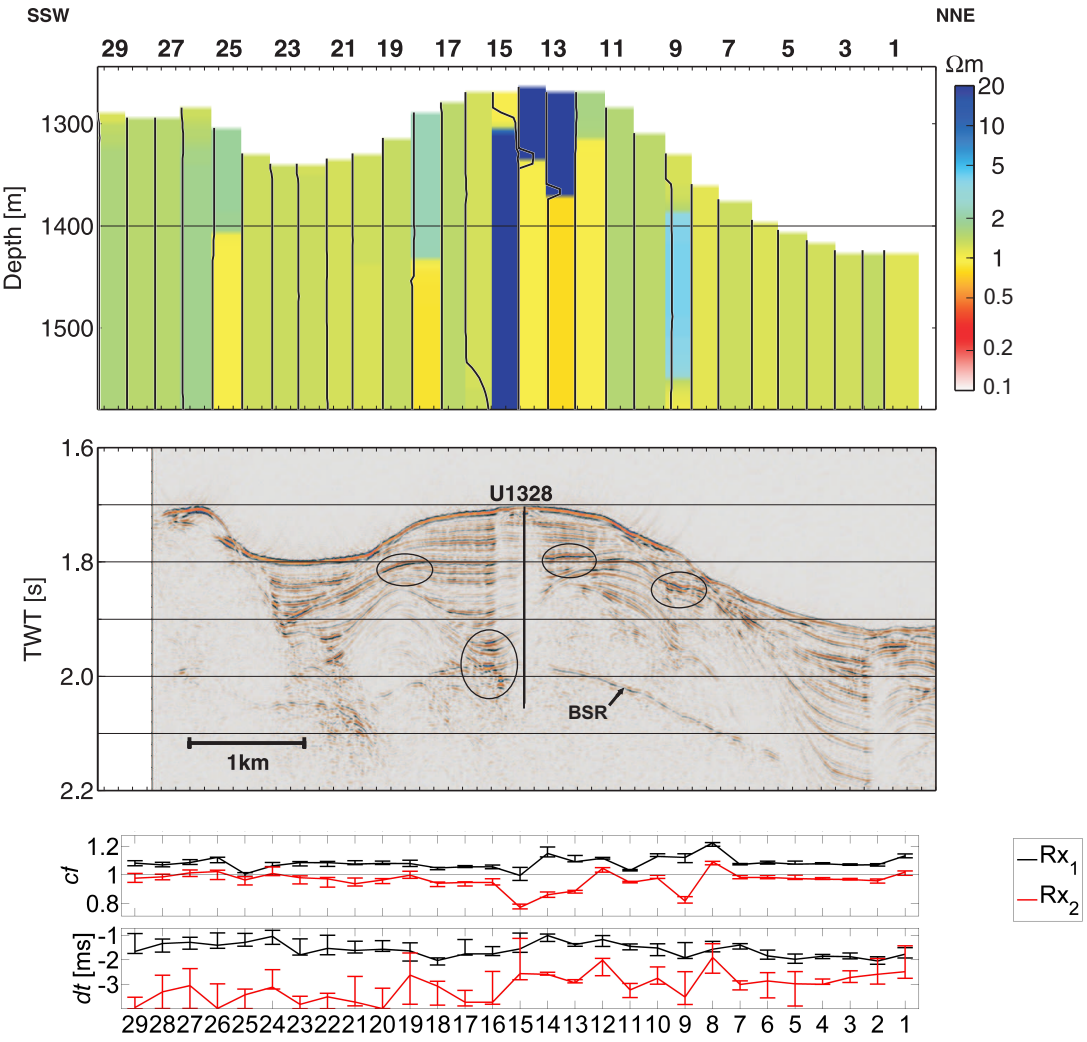

Figure 6.14: Top: CSEM median model with uncertainties (black lines) for line Jul3105. Middle: MCS line GeoB00-142 with X311 Site U1328, where black ellipses mark high-amplitude reflections. Bottom: CF (cf) and time delay (dt).

MCS line GeoB00-142, that may relate to a gas hydrate cap, is also deeper at WP 15 than at WP 14. However, 3-D effects that are likely present at the vent site, but are not accounted for, and therefore the inversion results need to be interpreted with caution. Uncertainties at greater depths are likely higher than illustrated. The inversion of data from WP 13 and 14 introduce low resistivities in the halfspace below the shallow high resistivities. The geologically unreasonable trend is countered by setting the resistivity lower bound for the second layer to 0.9 Ωm. This also applies for WP 18 and 25 where resistivities of ∼2.5 Ωm at <150 mbsf were inferred that may be related to the presence of free gas or gas hydrate underlain by a less resistive

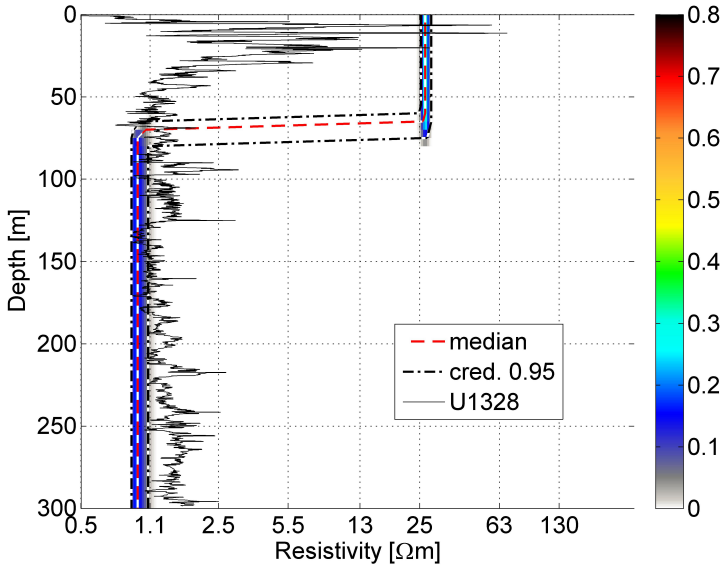

Figure 6.15: Marginal probability density profile with posterior median model estimate and deep button average resistivities from U1328A.

halfspace. Comparing the vertical position of elevated resistivities to seismic data at WP 18 suggests that the resistive material is in the shallow, younger sediments, rather than in the older, accreted sediments. Additionally, sub-bottom profiler data obtained with an autonomous underwater vehicle [Paull et al., 2009] show seismic blank zones at WP 18 that may indicate the presence of fluid venting and/or gas hydrate occurrences. WP 11 to 12 are on the eastern flank of Bullseye vent and show elevated halfspace resistivities (1 to 2 Ωm), which are ∼500 m south and east of a region, where high backscatter and bubble plumes were observed on sonar data from an remotely operated vehicle [Paull et al., 2009; Furlong, 2013] that likely relate to authigenic carbonate surfaces and free gas venting (see Fig. 6.3).

At WP 9 an interval of ∼4 Ωm at depths of 90 to 200 mbsf is inferred that might be related to elevated seismic amplitudes and faults seen on the projected seismic reflection line GeoB00-142. Both might be caused by the presence of free gas or gas hydrate. The CF is around 1 which indicates only small deviations from the assumed geometry of the CSEM array. The time delay is between −1 and −2 ms for Rx_1 and between −3 and −4 ms for Rx_2.

6.5 Conclusions

Time-domain marine CSEM data were acquired in 2005 and 2006 in two survey areas on the middle and upper continental slope of the northern Cascadia margin in the vicinity of IODP Expedition 311 Sites U1328 and U1329. A seafloor-towed electric dipole-dipole system was used which records the inline electric field components with two receivers at offsets of 174 m and 292 m from the source dipole respectively. A one-dimensional non-linear Bayesian inversion is implemented to estimate model parameters and uncertainties. Survey parameters, *i.e.* time drift of the receiver clocks and a calibration factor have been included as unknown parameters in the inversion. The Bayesian information criterion was applied to select the number of subsurface layers that can be resolved with the data, which was generally found to be one or two (sometimes three) layers. The parameters were sampled in principle-component space with Metropolis-Hastings sampling and the resulting posterior probability density contains information about model parameter uncertainties and relationships. Parameter uncertainties increase significantly for deeper structure, but might be generally underestimated due to the assumption that the number of sub-surface layers is determined exactly. For example, LWD resistivities from drilling extend the inferred CSEM resistivity range (see Figs. 6.8 and 6.15) but they match the inferred resistivity trend with depth. The following geological interpretation can be drawn.

A major resistivity contrast found by CSEM inversion is caused by a sediment unconformity around Site U1329. The sediment unconformity divides younger marine sediments from denser accreted sediments ($\sim$5 Ma older). Resistivities of the deeper layer are higher and have wider credibility intervals with widths of $\sim$10 to 100 Ωm. On the upper slope on the landward edge of the gas hydrate stability zone, inversion results for two sites (WP 16 on line Aug1105 and WP 6 on line Aug1205) show anomalously high resistivities that might be caused by gas hydrate or free gas occurrences at possible cold vents (although, gas hydrate nor gas plumes have been observed at these locations, yet). Generally elevated resistivity values on the upper slope along line Aug1105 are probably due to sediment erosion that exposes deeper, more compacted sediments. At Site U1328 on the middle slope of the margin, elevated sub-seafloor resistivity values were determined associated with massive gas hydrates at Bullseye vent. Additional gas venting sites on both flanks around the main vent also cause elevated resistivity values.

Overall, the 1-D non-linear statistical inversion revealed that the data sets contain

limited information on the vertical resistivity structure. This may be due to the lack of strong resistivity contrasts within the penetration depth of the instrument (maximum offset 272 m), the 1-D assumption in modeling vent structures which are likely 2-D or 3-D, the relatively low signal-to-noise ratio compared to recently built instruments [Schwalenberg and Engels, 2012a], and erroneous survey parameters including array geometry, source current amplitude and clock drift. Joint marginal probability densities additionally reveal significant parameter correlations between instrument unknowns and sub-seafloor parameters. However, the non-linear Bayesian inversion defines a range for unknown acquisition parameters that agree with presumptions (*e.g.,* measured total time drift after instrument recovery). The Bayesian inversion also reveals well constrained, one layer models with typical seafloor resistivities between 1 and 1.5 Ωm at most sites along the lines. Other sites where the resistivity structure correlates with seismically inferred vent structures, seismic amplitude anomalies and a sediment unconformity are more likely to be explained with a two- (sometimes three-) layer model. Parameters and uncertainties agree at adjacent way points and with local resistivity data from drilling during the IODP Expedition 311.

Chapter 7

North Sea CSEM experiment

The marine controlled source electromagnetic (CSEM) method has become a popular tool to detect electrical resistivity contrasts in the seabed that may relate to potential hydrocarbon reservoirs [*e.g.,* Constable and Srnka, 2007]. The conductivity of marine sediments is mainly controlled by conductive pore water, and resistivity contrasts relate to changes in porosity, permeability and hydrocarbon content among other factors. CSEM is a diffusion method, sensitive to volume resistivity changes, and the solution to the sub-seafloor resistivity structure is generally non-unique [Edwards, 2005; Constable, 2010]. To evaluate the 1-D structural resolution a trans-dimensional Bayesian inversion approach is applied which samples probabilistically over the number of sub-seafloor resistivity layers. Furthermore, trans-dimensional Bayesian inversion estimates the layering structures from the data and is consistent with the local resolving power of the data (i.e., adapts model complexity locally as required by the data). In addition, probabilistic sampling approaches, unlike linearized inversions, can provide rigorous estimates of model parameter uncertainties. The CSEM instrument used in this study is a seafloor-towed array consisting of a horizontal current source dipole and four electric receiver dipoles developed recently at the German Federal Institute for Geosciences and Natural Resources [BGR; Schwalenberg and Engels, 2011]. This instrument targets shallow resistivity structure (to a few hundred meters depth) and is particularly sensitive to lateral resistivity changes such as could be caused by cold vents [Schwalenberg and Engels, 2012a] or high vertical resistivity contrasts due to gas hydrate accumulations in sandy sediments [Schwalenberg and Engels, 2012b].

While many multi-channel seismic profiles have been collected in the North Sea, only a small number of CSEM surveys have been conducted there, mostly targeting

deep natural gas reservoirs in the British and Norwegian sectors [*e.g.,* MacGregor et al., 2006; Ziolkowski et al., 2010]. A special challenge for marine CSEM methods in the North Sea is the relatively shallow water (compared to the maximum offset of the array) and the resulting sensitivity of the instrument response to the strong resistivity contrast between the conductive seawater and the insulating air above [*e.g.,* Weiss, 2007; Weidelt, 2007], as discussed in Chapter 4.

The time-domain CSEM data presented here were acquired in September 2012 about 30 km NWW from Heligoland in the North Sea on the rim of the Pleistocene channel of the Elbe River (see Fig. 7.1). The time-domain CSEM data presented

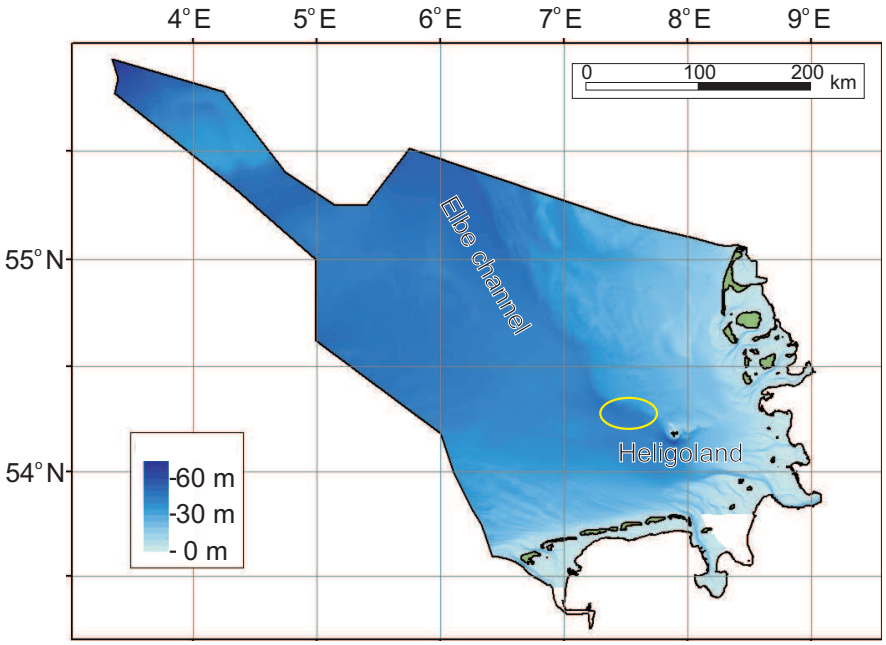

Figure 7.1: Bathymetry of the German sector of the North Sea [(courtesy of BGR) Schwalenberg et al., 2012]. The target area (yellow ellipse) of the CSEM survey is northwest of Heligoland.

here were acquired in September 2012 about 30 km NWW from Heligoland in the North Sea on the rim of the Pleistocene channel of the Elbe River (see Figure 7.1). The CSEM survey targeted a shallow, phase-reversed reflector observed on multi-channel seismic (MCS) line Aur03-23a acquired by the BGR in 2003 [Kudraß et al., 2003]. This reflector may be due to shallow gas occurrences or significant lithological changes. The experiment was part of a joint project to study the geological evolution, stratigraphy and potential for energy resources (hydrocarbon reservoirs, locations for wind and water power plants) of the German North Sea [Schwalenberg et al., 2012;

Arfai et al., 2011].

The geological history of the North Sea goes back to the Permian when two large basin systems opened up. A number of phases of stretching, subsidence, and uplift have caused several kilometres of sediment deposition (and erosion) since then. Several layers of salt deposits within the sediments uplifted and deformed the upper sediment layers, causing widely abundant diapir formations during the late Permian [Arfai et al., 2011]. Northern Germany was below sea level until the late Tertiary, when the sea retreated westward. While sedimentation during the Paleogene was dominated by marine clays, a great influx of sediments during the Miocene was dominated by river deposits and was followed by large sea level changes during the Pleistocene. Several protruding glaciers deformed the landscape and deposited glacial tills, and meltwater cut into older sediments to form tunnel valleys [*e.g.,* Hepp et al., 2012]. After the last ice age, sea levels rose again and supported moor and swamp development, leading to the formation of thin layers of peat within marine Holocene sediments [Kirsch et al., 2012]. The present bathymetry of the German sector of the North Sea, which is shaped like a duck's bill extending towards Great Britain, is relatively shallow with a maximum depth of ∼65 m (see Fig. 7.1).

This chapter is based on the paper (to be submitted) *"Trans-dimensional Bayesian inversion of controlled source electromagnetic data in the German North Sea"* by R. A. S. Gehrmann, J. Dettmer, K. Schwalenberg, M. Engels, S. E. Dosso and A. Özmaral. The dissertation author is the primary investigator and author of this paper. Schwalenberg and Engels provided pre-processed CSEM data and helped with the development of processing codes (written in MATLAB). Dettmer provided the trans-dimensional Bayesian inversion codes and Dosso provided knowledge about Bayesian theory. Özmaral processed the high-frequency seismic data from the University of Bremen and shared her knowledge on the geology of the German North Sea. In this chapter, active seismic reflection profiles are compared with interface probabilities estimated with trans-dimensional Bayesian inversion (described in Sec. 5.5) of CSEM data to draw a combined geological interpretation of the sub-seafloor.

7.1 Instrumentation and processing

The CSEM array used here (see Figure 7.2) is a seafloor-towed system with four receiver dipoles (Rx) at offsets of 150 m, 252 m, 453 m and 754 m developed at the BGR [Schwalenberg and Engels, 2012a] with silver-chloride electrodes (Silvion

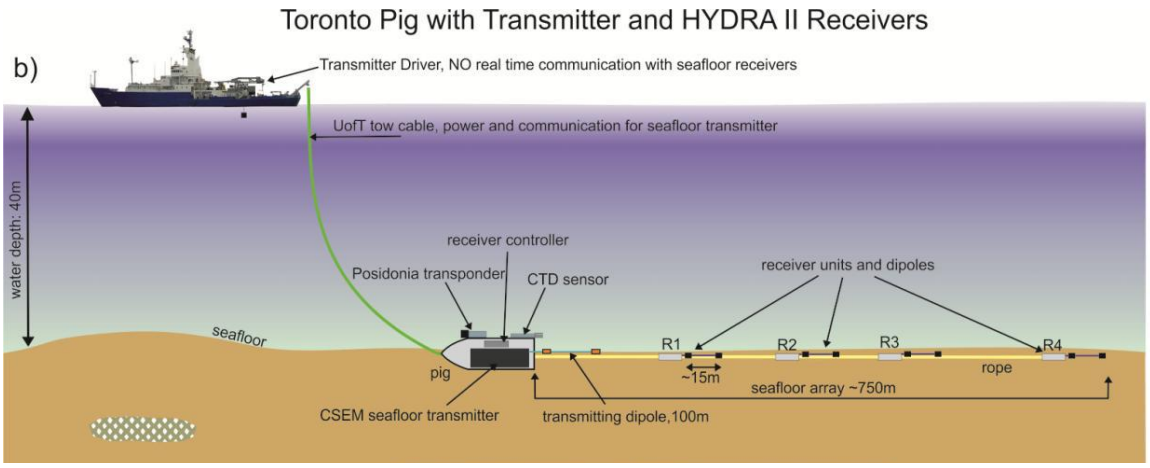

Figure 7.2: Sketch of the CSEM array during data acquisition. The array is held on the ground by a heavy weight (pig) which contains the transmitter and receiver controllers as well as the Posidonia transponder and a CTD sensor. The transmitter unit and the cable were developed at the University of Toronto (UofT). The four receivers were developed at the BGR as part of the bottom-towed electric multi-receiver system HYDRA II [Schwalenberg et al., 2012].

and Castle type). The array uses a high sampling rate (10 kHz) and precise timing, a CTD to measure water resistivities, and an ultra-sound locator device (Posidonia transponder). The observed data has a high signal-to-noise ratio due to minimal electronic noise (signal resolution below 10 nV). A square wave signal with a maximum amplitude of ±50 A and 6 s period is injected at the ∼100 m transmitter dipole (Tx) that was developed at the University of Toronto. During the measurement at each way point (WP) the horizontal electric field is recorded while the array is held stationary for ∼5 minutes. Data processing includes the identification of stationary half periods, timing correction, DC correction, electrode drift correction for each half period, and an iterative scheme for the selection of accepted half periods for stacking. Figure 7.3 shows half periods for Rx_1–Rx_4. About 64 half periods (green) are accepted for stacking, other half periods with erratic noise are discarded. The mean step-on response and the standard deviation of the mean are derived from stacking of the accepted preprocessed data. The stacked data show only a small amount of high-frequency electronic noise; however, the electrode-drift effect cannot be completely eliminated and imprints systematic errors onto the step-on response. Systematic data errors (*e.g.,* from electronics, electrodes, timing errors, geometry errors, uncertainty in water depth) are believed to be larger for the present data set than stacking errors and have been addressed in preliminary analyses by introducing error factors and a

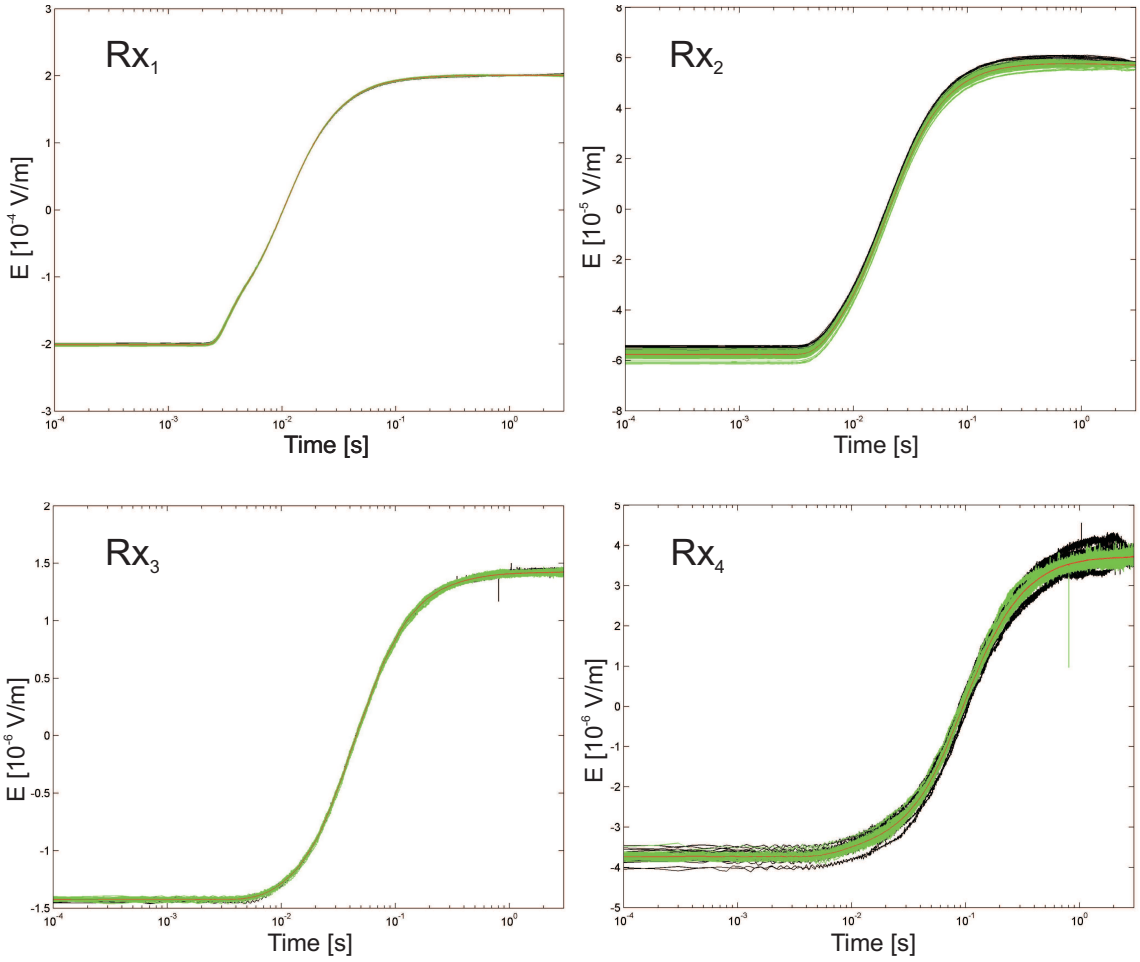

Figure 7.3: Half periods for Rx_1–Rx_4. About 64 half periods (green) are selected for stacking, while others are rejected due to erratic noise (black).

minimum error floor [Schwalenberg et al., 2012].

7.2 Inversion sequence

Inversions are carried out in a two stage process. A preliminary inversion with diagonal data covariance matrices based on the estimated variance from data stacking is carried out to obtain a preliminary PPD and median model estimate. Data residual errors are computed for the preliminary median model and used to estimate a non-Toeplitz data covariance matrix with Eq. (5.23) which accounts for correlated errors and is then applied in a second inversion to infer the PPD used for interpretation. Individual parameters from the PPD are inferred by marginalization (integrating over all

parameters but the parameter(s) of interest). The seabed depth profile is partitioned for plotting purposes and marginal probability densities are evaluated at each depth interval. Highest-probability density credibility intervals (CI) displayed throughout this work represent the narrowest interval which contains 95% of the model samples. The new median model estimate is examined with statistical tests as the formulation of the likelihood in equation (5.17) is based on the assumption of Gaussian-distributed residual errors with zero mean and data covariance $\mathbf{C}_d$. If assumptions are reasonably met, the standardized residuals should be random (uncorrelated) and Gaussian distributed with unit standard deviation. These assumptions are tested with the Kolmogorov-Smirnov (KS) test for Gaussianity [Massey, 1951], which is based on the maximum difference between the cumulative marginal distributions of the residual errors and the standard Gaussian, and the runs test (median-delta test) which tests if the residual errors are random or serially correlated by counting the number of runs of the residual errors on either side of the median value [Dosso et al., 2006].

7.2.1 Calibration factor

The CSEM data at the first receiver for all WPs generally exhibit a high signal-to-noise ratio (see Figure 7.3). The standard deviation of the mean from stacking seems to mainly result from a slight bias of the individual pre-stack data due to an electrode drift. However, in the inversion the amplitudes of the first receiver cannot be matched by a 1-D subsurface model within the estimated error bounds (standard deviation of the mean). Amplitudes of the predicted data are a few percent smaller than the observed. Deviations in amplitudes can be accounted for with a multiplicative calibration factor (CF) [Scholl, 2005]. The CF was originally named after the calibration of each electrode pair before deployment. However, receiver electronics (offset and scale factor) were calibrated precisely during the cruise and the CF in this inversion is implemented to account for effects of a conductive target close to the source, 3-D structure, unknown time shift of the data, geometry variations or topography changes. Preliminary inversions have shown that the CF at all WPs generally lies close to 1 with a higher value for the first receiver and higher uncertainties for the other receivers (probably due to the larger distance and therefore smaller signal-to-noise ratio). Possible causes were analyzed and the following conclusions drawn:

- Highly conductive bodies close to the transmitter (*e.g.*, metallic ship wrecks)

would have been observed on images from the echo sounder EM710 and PARASOUND P70 system on board and can be excluded.

- 2.5-D multi-channel seismic data indicate only very small changes in the layered structure perpendicular to the CSEM-profile [Damm et al., 2012] and I assume that 2-D and/or 3-D structure likely does not affect our data.
- A time shift between the transmitter and the receiver clocks was measured on board and corrected for in the laboratory. The transmitter uses a Seascan clock, while all receivers have chip-sized highly-precise atomic clocks installed. Hence, I inverted for a single time shift which applies to all four receivers but did not improve the overall data fit. I conclude that a time shift can be at most a small part of the problem.
- A slight error in the system geometry, *e.g.*, a deviation of only 30 cm from the assumed receiver dipole length, can explain 2% deviations of step-on response amplitudes. This might explain different CFs for each receiver. Values also differ slightly from WP to WP.
- Water depth uncertainties could be another factor. The water depth is just ∼40 m and the data are strongly affected by the airwave. Water depths in the region were found to range from ∼39 to 42 m along the whole profile. The instrument array is ∼750 m long and small changes in topography may cause varying CFs. Additionally, the observed water depth suffers from variable ship draft and might deviate up to a metre from the estimated value.

Initial inversions indicated that marginal densities for CF for Rx_2–Rx_4 are wider than for Rx_1 and usually overlap with a value of 1. Hence, I conclude that including an unknown CF for Rx_2–Rx_4 is not necessary to fit the data. Preliminary inversions also indicate additional (unnecessary) parameters in the inversion have a detrimental effect on the recovery of subsurface parameters: the problem becomes under-determined and unreasonable subsurface structure can be introduced. Therefore, the inversion results shown in this paper are based on inverting for CF at Rx_1 (cf_1) only.

7.3 Simulation study

This section applies the Bayesian inversion to simulated data for a subsurface model similar to the model estimate for WP 19 (see Sec. 7.4). The model consists of four

layers including a halfspace (see Table 7.1), and is chosen to examine if a thin resistive layer at a shallow depth and a very deep resistivity contrast (relative to the maximum offset at Rx_4 of 750 m) can be resolved with the data. Random correlated errors are added, which are generated from the data covariance matrix derived while inverting WP 19 (see Sec. 7.4). Standard deviations are on average ∼2% of the predicted data. A new non-Toeplitz data covariance matrix to sample the PPD for the synthetic data is estimated with the sequence outlined in Sec. 7.2. Figure 7.4 shows Bayesian inversion results for the simulated data in terms of interface probabilities and the marginal probability density profile of the resistivity. Marginal probability densities are normalized to unit area for plotting purposes. Interface probabilities as a function of depth indicate two distinct interfaces at 20- and 60-m depth. Both interfaces are well estimated with low uncertainty (a few metres) and are in excellent agreement with the true model. The third interface is highly uncertain with probability extending from ∼450 to 800 m. The 95% CIs for resistivity exhibit characteristics typical of the resolution of EM diffusion methods and demonstrate decreasing sensitivity of the data with depth: CIs at shallow depth (up to 400 mbsf) are narrow (<1 Ωm in width), and widen to a maximum of 14 Ωm at about 700 mbsf. However, the trend of the resistivity distribution follows the true model by indicating another contrast to a halfspace with larger resistivities. Figure 7.4 also shows marginal probability density for cf_1 which is well determined at 1 (true value), and the marginal probability distribution for the number of interfaces k has a peak at 3 interfaces (true value) although the distribution extends to the upper bound of 10.

To examine the impact of additional unknowns, two further simulations are carried out. First, data were generated for different water depths for different receivers: the water depths for Rx_1, $Rx_{2,3}$ and Rx_4 are 40, 42 and 41.1 m respectively. However, the assumed water depth in the inversion is taken to be 41.1 m for all receivers, and an unknown cf_1 is included. Inversion results in Figure 7.5 show wider credibility

Layer	Resistivity [Ωm]	Depth [mbsf]
1	0.8	20
2	3	60
3	1	600
Halfspace	4	-

Table 7.1: Synthetic model similar to inversion results for WP 19. Sea water conductivity is 0.232 Ωm and water depth is 41.1 m.

intervals at depths >350 mbsf. The third interface of the true model is hardly resolved. The resistivity of the overburden is estimated higher than the true model, and cf_1 is slightly above 1 to compensate for the water depth discrepancy.

The second test addresses a possible time shift between transmitter and receiver clocks. The time of the receivers is shifted by 0.3 ms, and the inversion is run twice, once with an unknown cf_1 and once with an unknown time delay dt. Inversion results are shown in Fig. 7.6. The inversion scheme resolves the structure of the true model when inverting for cf_1 with cf_1 slightly above 1 or dt where dt is well estimated at -0.3 ms.

The synthetic modelling suggests that the inversion algorithm with cf_1 for the first receiver efficiently resolves the model even in case of deviating water depth or time shift. However, model uncertainties increase with additional systematic uncertainties and CIs below ∼400 m become increasingly wider with depth, while a qualitative

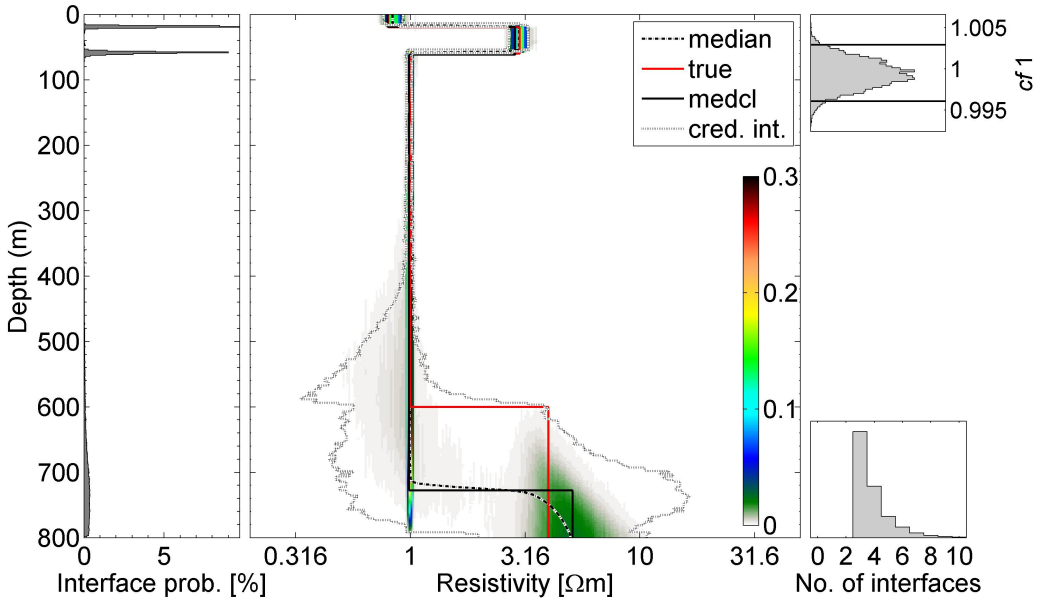

Figure 7.4: Left: Interface probability as a function of depth. Middle: Resistivity marginal probability profile. Colour indicates probability density for 10^5 samples from the inversion of synthetic data (model in Table 7.1) with correlated errors. A model with 4 layers closest to the posterior median model profile is chosen to evaluated residual error statistics and is referred to as"medcl". Credibility intervals contain 95% of the model samples evaluated at each depth interval. Right: Marginal probability density for cf_1 on top and for number of interfaces (bottom). Three interfaces (four layers) are most probable.

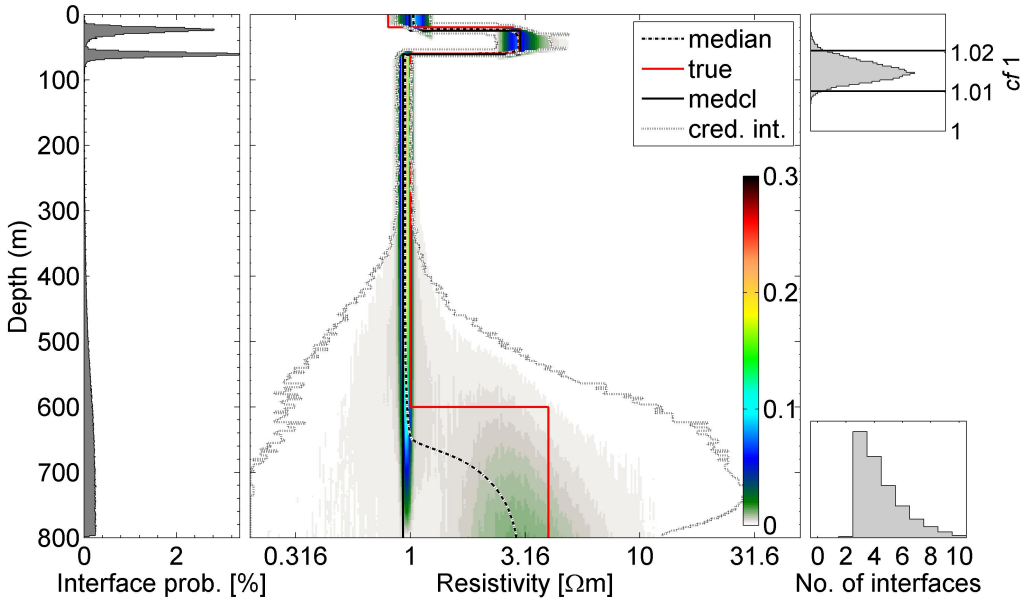

Figure 7.5: Interface probability and marginal probability depth profile for synthetic data (model in Tab. 7.1) with different water depth for different receivers and with correlated errors.

resistivity contrast similar to the true model is preserved.

7.4 German North Sea inversion results

Way point 19 has been chosen to demonstrate the trans-dimensional Bayesian algorithm and results for measured CSEM data in detail. It lies in the centre west of the profile and is representative of other WPs.

Interface probabilities and marginal probability densities are shown in Fig. 7.7. The first two interfaces are well defined at ∼20 and 50 mbsf. The interface probability is also increased between 180 and 520 mbsf indicating an interface with large position uncertainty. Marginal probability profiles exhibit narrow credibility intervals down to ∼200 mbsf of width of <1 Ωm, while below this depth they extend to widths of ∼10 Ωm. The number of interfaces with the highest probability is four, while the median model estimate has three interfaces. The CF for the first receiver is well determined and slightly over 1 that may be related to unknown parameters such as water depth and time shift as outlined in Sec. 7.2.1 and 7.3.

Figure 7.8 shows observed and predicted data for the median model estimate and standardized residuals for WP 19. The runs test and KS test are applied to the stan-

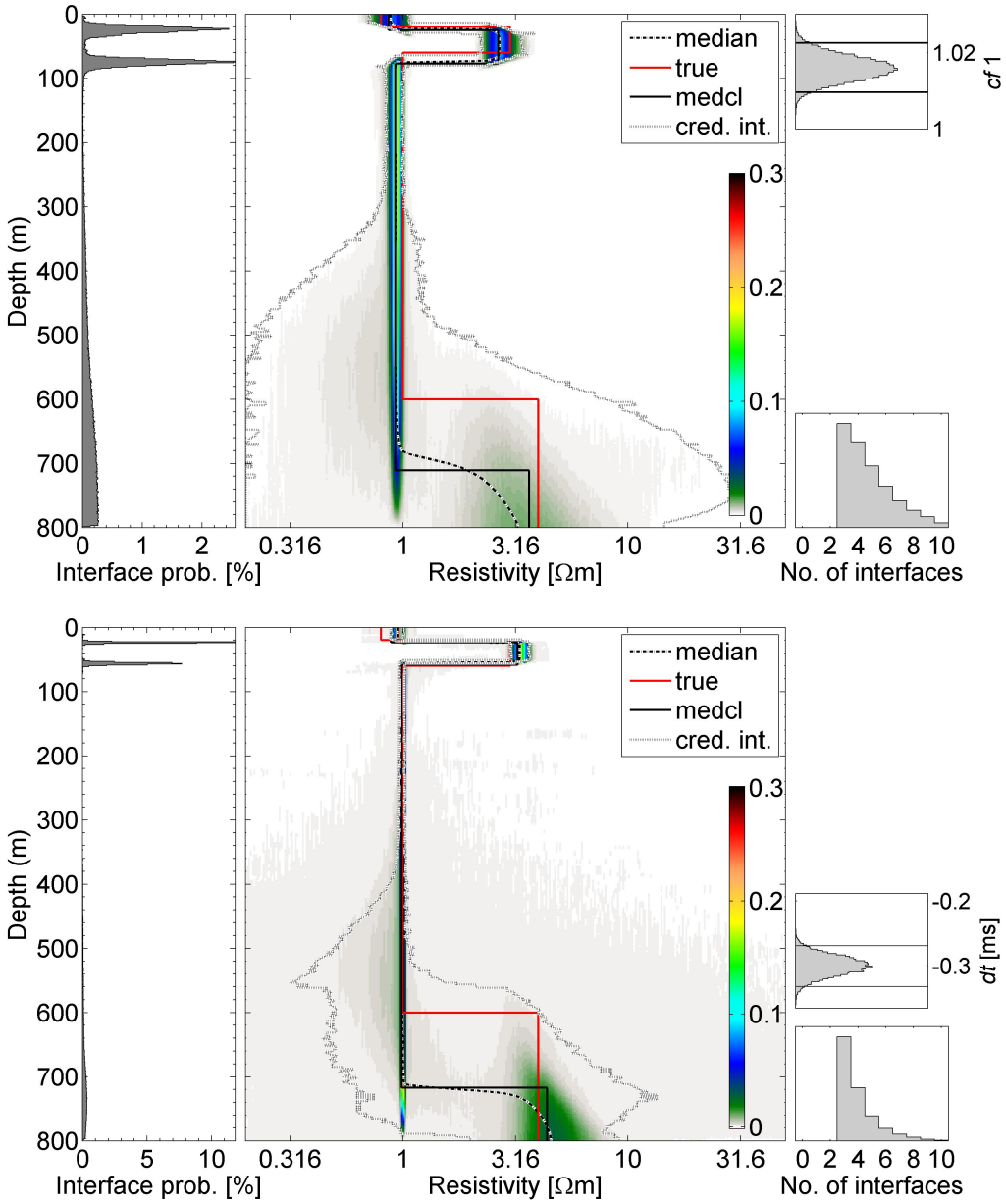

Figure 7.6: Interface probabilities and marginal probability depth profile from inversion results for unknown cf_1 (top) and dt (bottom) for the same synthetic data (model in Tab. 7.1) with 0.3 ms time shift and correlated errors.

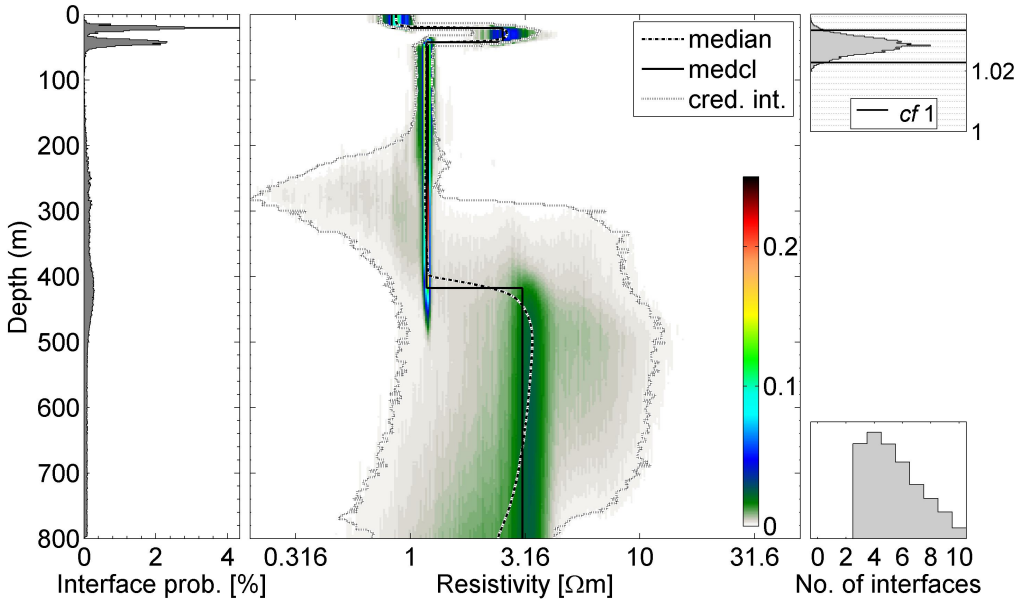

Figure 7.7: Interface probability (left) and marginal probability density (middle) as a function of depth for WP 19, where "median" refers to the posterior median profile, and "medcl" to the median model estimate, and credibility intervals contain 95% of all model samples evaluated at each depth interval; right: marginal probability densities for cf_1 and number of interfaces k.

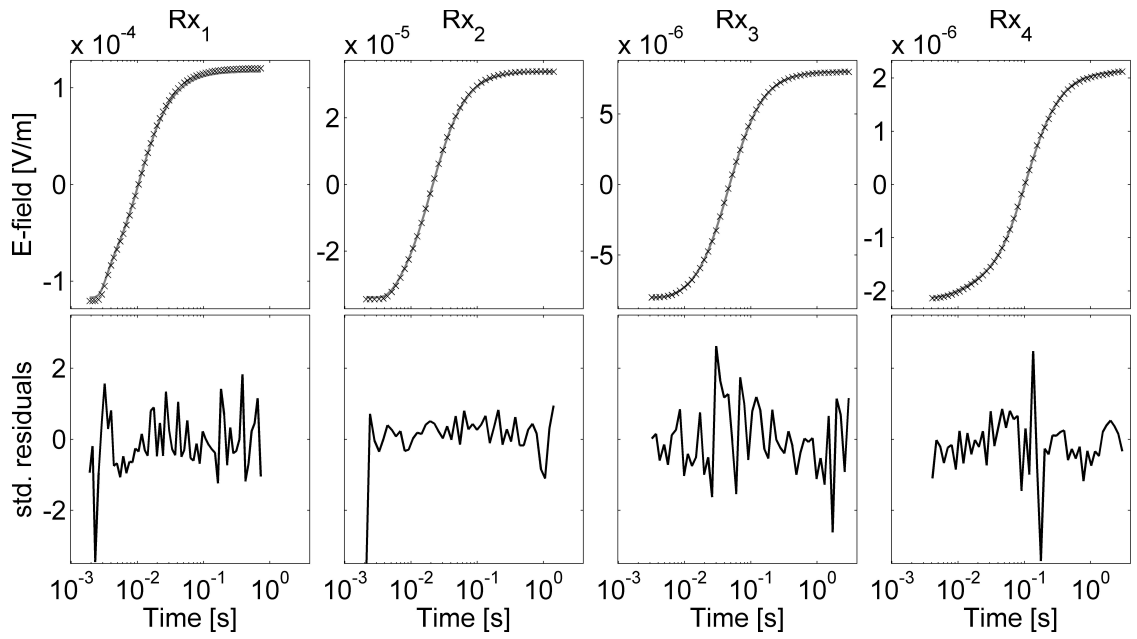

Figure 7.8: Top: predicted (black line) and observed data (crosses with error bars) for WP 19. Bottom: standardized residuals over time.

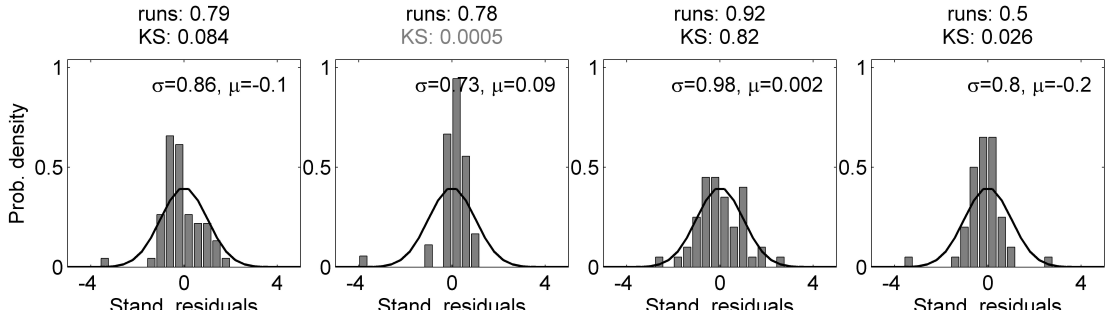

Figure 7.9: Histograms of standardized residuals for Rx_1 to Rx_4 shown in Fig. 7.8 compared to a standard Gaussian distribution (black curve); Titles: p-values from the runs and KS test, which are black for passing and grey for failing; Textboxes: standard deviation σ and mean μ for stand. residuals.

dardized residuals [Dosso et al., 2006] of the median model estimate. Standardized residuals pass tests if p-values for a two-sided test are larger than a significance level of 0.025, and test results are shown in the bottom row of Fig. 7.8. Standard deviation and mean value of the standardized residuals as well as p-values are shown in the text box, and in the title (for runs and KS test) respectively. Statistical tests result in general acceptance of the assumption of Gaussian distributed errors and the process of addressing correlated errors.

The posterior median model profiles for all 22 WPs are shown in Figure 7.10 as coloured bars, which are stitched together to approximately represent 2-D structure along the CSEM line. The width of the bars corresponds to the spacing between Tx and Rx_4, and the bars are overlain with the resistivity standard deviation profile (black line) which is normalized so that the maximum standard deviation is equal to the width of the coloured bars. Inversion results for all WPs agree on a ∼5 to 20 m thick surface layer with resistivities of ∼0.7 to 1 Ωm. Below the surface layer is a second layer with increased resistivity of ∼1.8 to 3.5 Ωm. The maximum thickness of the second layer is ∼200 m at WP 1–9, and this layer thins to the west where neighbouring resistivities become more heterogeneous. Inversions of WP 9, 11, 16, 18 and 20 include a thin conductive layer which is geologically unlikely, but improves the fit to the observed data. Resistivities below ∼200 m decrease to ∼1 Ωm, with increased uncertainties due to the limited penetration depth of the array. The inversion results suggest an increase in resistivity for the deepest layer (>400 mbsf) of ∼3 Ωm, but the CIs for the resistivity are [∼0.5 10] Ωm.

The bottom panel in Figure 7.10 shows MCS line AUR03-23a [Kudraß et al., 2003]

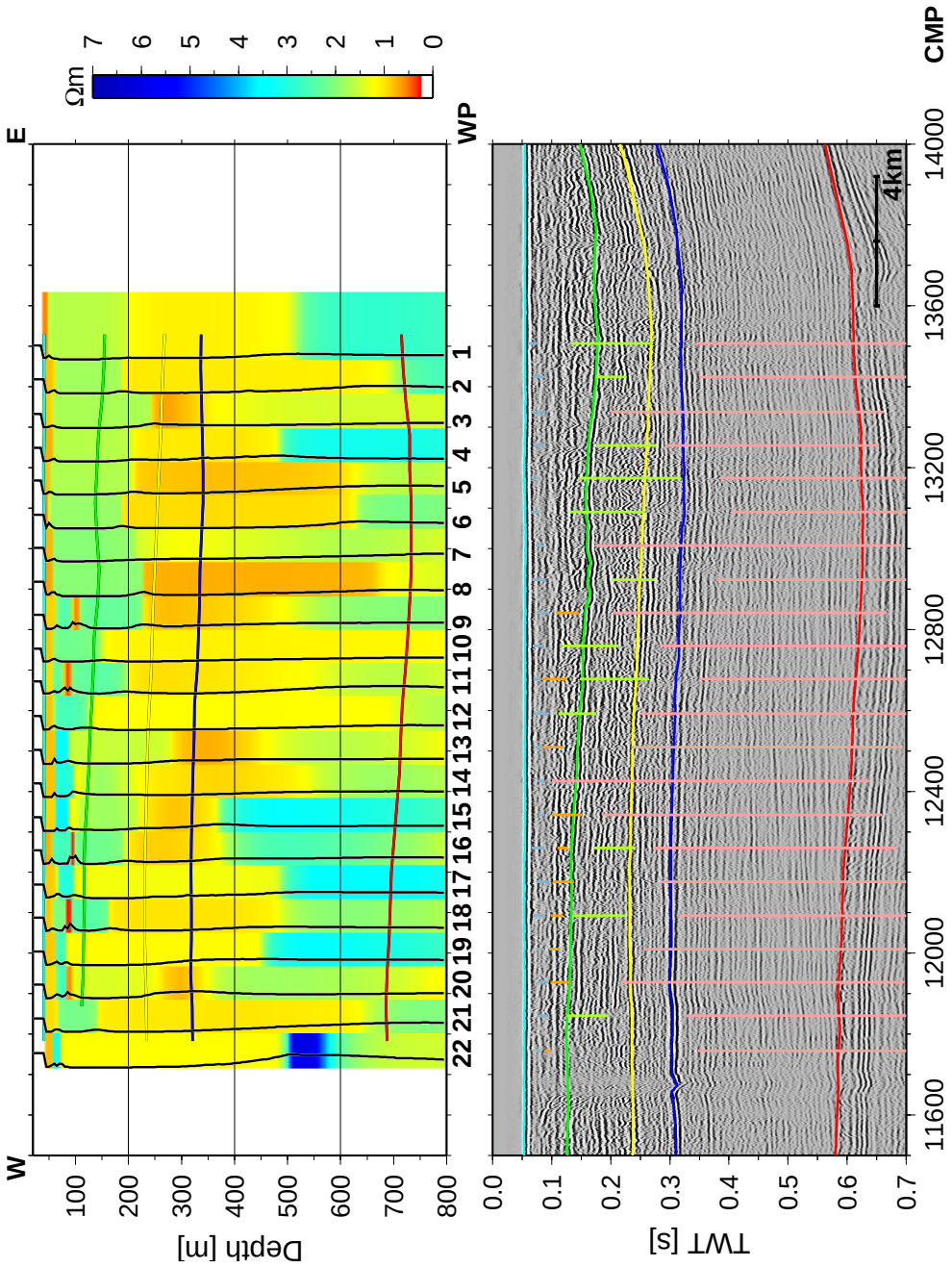

Figure 7.10: Top: Posterior median profiles from CSEM inversion shown as coloured bars that represent the Tx-Rx_4 offset and whose location corresponds to the location of the CMP of the MCS line below. Black lines: Standard deviations of the marginal probability density profile for resistivity over depth which are normalized to width of coloured bars. Coloured horizontal lines: Seismic horizons converted from TWT to depth; cyan - seafloor, green - Pleistocene basin, blue/yellow - late Tortonian sediments, red - MMU. Bottom: MCS line AUR03-23a with seismic horizons. Coloured vertical lines: Credibility interval widths for interface depths from CSEM inversion (colour coding is subjectively chosen to match with seismic horizons).

which was acquired along the same line as the CSEM data. The location of the WPs in respect to the common mid point (CMP) of the MCS line may deviate by a few metres. Three major reflectors can be traced on the seismic profile: The red reflector at 0.6 s two-way travel time (TWT) is related to the Mid Miocene Unconformity (MMU). The MMU is interpreted as the base of the downlap sequence, a result of the Eridanos Delta (Baltic river system). It has a distinct wavy structure related to rapid dewatering of clayey sediments and is highly recognizable in gamma-ray (GR) logs due to a high content of organic material in the clay [Arfai et al., 2011]. The blue reflector at 0.3 s TWT is defined to be of late Tortonian age. Horizontally layered sediments above the blue reflector are also defined as late Miocene origin. GR logs indicate an increasing content of fine-grained sediments from the MMU towards the blue reflector marking it as a maximum flooding surface, while the GR count decreases above the blue reflector [Thöle et al., 2014]. Other strong reflectors also correlate with sharp GR-count increases over thin depth intervals. The horizontally layered sediments in the late Miocene are alternating layers of sand, silt and clay due to world-wide sea-level changes, high basin subsidence rates, uplift and erosion of Paleogene clays, sandy river deposits, and massive flooding events [Rasmussen, 2004; Sørensen et al., 1997]. The green reflector is a phase-reversed dipping reflector between 0.1 to 0.2 s TWT from Pleistocene origin that was targeted by the survey because of enhanced, phase-reversed amplitudes between CMP 12500 and 13500 which are caused by a negative impedance contrast related to shallow gas or a boundary from course- to fine-grained sediments. A Pleistocene valley likely filled with unsorted glacial deposits is identified between CMP 11600 and 11800.

The reflectors are converted to depth with an average rms-velocity/twt profile and superimposed onto the resistivity posterior median profiles. Approximated 95%-credibility intervals for interface probabilities from CSEM inversion were converted to twt and plotted on the seismic section with a colour coding that is chosen to correspond to the interpreted relationship between the interfaces at adjacent WPs and the seismic reflectors. For example, the first interface is blue for all WPs because it is interpreted to match with the blue seismic reflector on Fig. 7.11. However, interface probabilities from CSEM inversion are more difficult to match with seismic reflectors at greater depth and the colour choice becomes highly subjective.

While the seismic method is highly sensitive to small-scale impedance changes, the CSEM method has a depth-averaging character. Hence, I do not expect the seismic reflectors to match with the median profiles perfectly. However, large-scale changes

in sediment properties which effect both seismic impedance and resistivity should be observed on both seismic and CSEM results. Figure 7.11 is analogous to Fig. 7.10 but focuses on the first 300 m and shows MCS line GeoB13-170 which was acquired by the University of Bremen with a high-frequency seismic system [Keil and Hepp, 2013]. The main seismic reflectors above the green reflector (target of the CSEM survey) are the base of the Holocene sediments (dark blue), two small and one large tunnel valley (pink) and a reflector within the Pleistocene sediments (orange).

7.5 Discussion

This section presents a geologic interpretation of the sub-seafloor resistivity model from CSEM inversion together with the MCS reflection data and logs from two boreholes (one 130 m deep with grain size information, the other several hundred metres deep with GR information). The first 5 m of sediments below the seafloor are fine-grained Holocene deposits observed in borehole J-14-1/2/3 (close to WP 20). The Holocene deposits in this borehole are followed by 5 m of fine-grained Pleistocene deposits and 120 m of middle to coarse-grained sandy Pleistocene sediments. The CSEM inversion results support ∼10–20 m of fine-grained, highly-porous sediments with typically low resistivities for marine sediments around 0.8–1 Ωm. The credibility intervals for interface depths overlain on the MCS line in Figure 7.11 match the dark blue seismic reflector which represents the transition from fine-grained overburden sediments to course-grained, unsorted Pleistocene sediments.

The second interface from CSEM inversion is more difficult to match with a single seismic reflector. Between WP 16 and 22 the interface correlates with the orange reflector on Figure 7.11, and between WP 13 to 15 it correlates with irregular seismic reflections at the same depth for the orange reflector. Uncertainties in matching CSEM and seismic features increase with depth due to the approximate conversion from TWT to depth (and vice versa) and due to the increase in CSEM uncertainties with depth.

The observed elevated resistivities (2–4 Ωm) below the marine Holocene surface layer (below ∼20 mbsf) may result from decreased porosity in sand-dominated sediments. The traceable phase-reversed (green) reflector in Fig. 7.10 only partially matches probability distributions for interface depths from CSEM inversion and the inferred resistivities do not support the free gas hypothesis underneath the reflector. The reflector might instead be caused by a lithological change within the Pleistocene

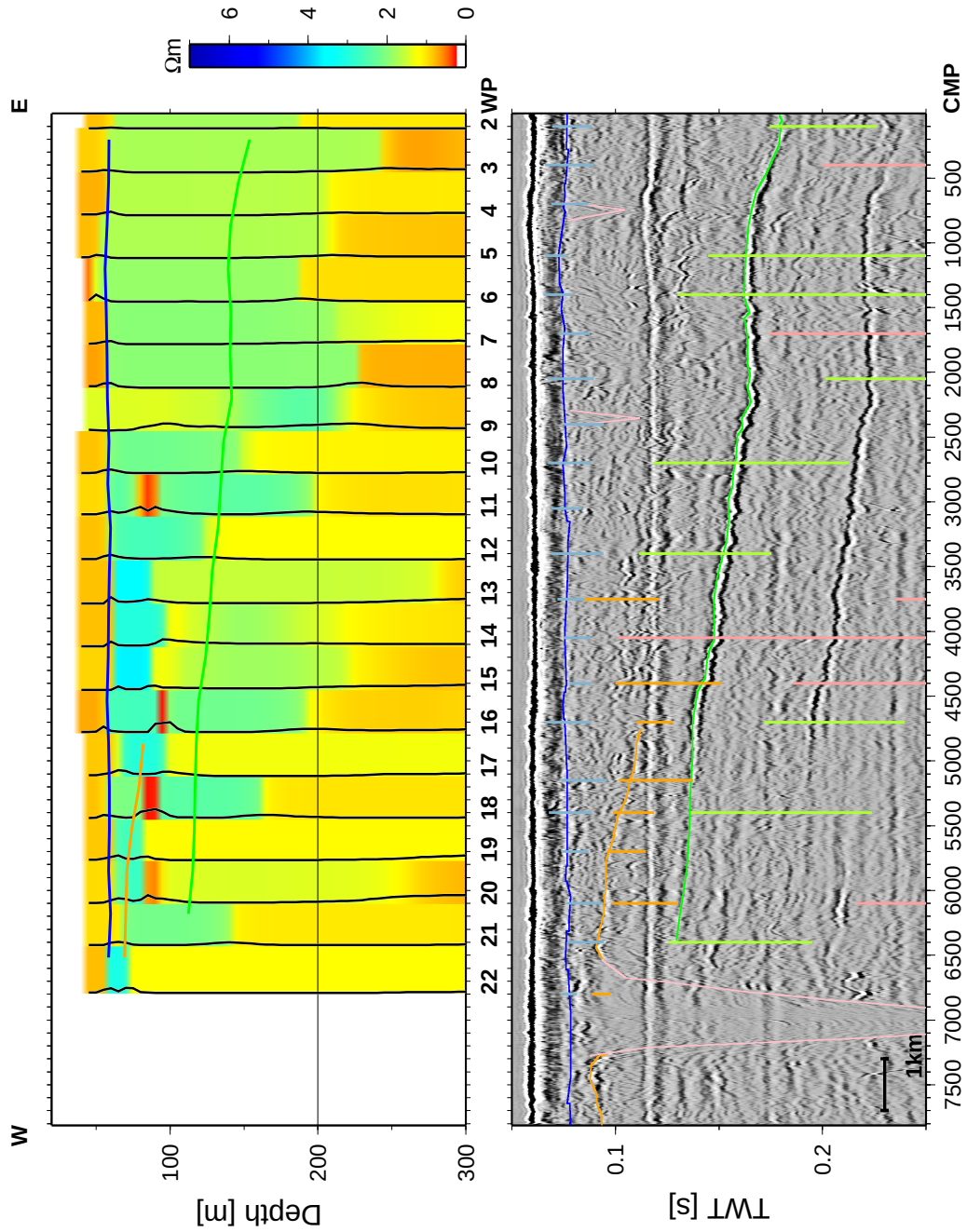

Figure 7.11: Posterior median profiles from CSEM inversion overlying MCS line GeoB13-170. Black lines on the median models represent model standard deviations normalized to the Tx-Rx offset. Vertical coloured lines on the seismic profile represent interface probability widths from CSEM inversion.

sediments, and the phase reversal might be due to a transition from sands to a layer rich in clayey sediment, as large amount of clays typically result in lower velocities. A similar phase-reversed reflections can be observed in the depth of the MMU (red reflector) which is caused by a transition of sandy river deposits to marine clays [Arfai et al., 2011].

The boundary between Pleistocene glacial sediments and Pliocene river deposits (kaolinitic sands) is difficult to distinguish with seismic or CSEM data, which might be due to the similar physical characteristics of the two sediment types. The sediment units between the yellow and red reflectors in Fig. 7.10 are dated to be of Messinian to late Tortonian age by Thöle et al. [2014]. The GR count in borehole R-1 (see App. C), drilled in the same geological units ∼100 km northwest of this site increases with depth from the yellow to the blue reflector and then decreases toward the MMU. A high GR count can be related to an increase in fine-grained silts and clays. The increased clay content might cause larger porosities as clay minerals in sea water form thin double layers and deposit in a flocculated (edge to face) manner. The flocculant structure collapses under pressure to a denser dispersed structure. Erchul [1972] infers that marine sediments with a higher percentage of clay are stable at higher porosities. If this relationship holds at ∼300 m depth (the depth of the blue reflector shown in Fig. 7.10), the lower resistivities of around 1 Ωm could be caused by increased porosity. Further measurements are necessary, preferably logging-while-drilling, to investigate the effect of clay content and composition, porosity, permeability and resistivity of the pore water on the bulk resistivity at this location. The overall interpretation of the grain size distribution up to 300 mbsf is summarized in Fig. 7.12.

Posterior median model resistivities tend to increase below the blue reflector towards the red reflector (MMU), but interface probabilities are wide (>400 m) which makes it difficult to relate the seismic reflector with CSEM interface depths. Resistivities from CSEM inversion beneath the blue reflector exhibit high uncertainties, and synthetic studies (Sec. 7.3) also showed that interfaces below 500 m depth may not be resolved. However, deep marine Paleogene clays are known to have resistivities of 1–5 Ωm [Jørgensen et al., 2003] and the Oligocene sediments are dominated by silts and clays [Arfai et al., 2011], so that one explanation for elevated resistivities in greater depth might be sediment compaction.

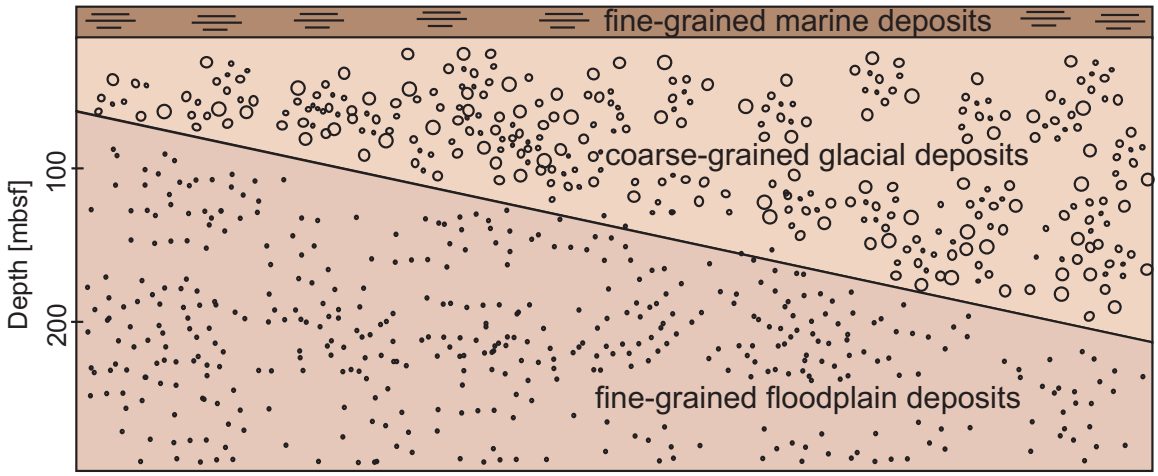

Figure 7.12: Sketch of the geological interpretation of CSEM inversion results. Depth scale is only approximate.

7.6 Conclusion

This chapter examined the information content of CSEM data with trans-dimensional Bayesian inversion where the number of sub-seafloor layers resolved by the data is treated as an unknown in the inverse problem. Time-domain CSEM data were acquired in the German North Sea with a seafloor-towed dipole-dipole array with four receivers and a maximum offset of 750 m. The survey was carried out to study the sub-seafloor resistivity structure and to interpret a shallow, phase-reversed reflector observed on multi-channel seismic data which could indicate gas occurrences in the sediments.

Simulation studies with realistic correlated errors were carried out to investigate the ability of trans-dimensional Bayesian inversion to estimate model parameters and uncertainties. Inversion results of simulated data show that slight biases in water depth or time synchronization increase uncertainties and decrease the resolution of resistivity structure with depth. Including additional unknowns such as water depth and clock drift tend to over-parametrize the inverse problem and unreasonable structure can be introduced into the subsurface model. Therefore, the number of additional parameters is limited to the calibration factor for the first receiver for observed CSEM data in the German North Sea. A non-Toeplitz (non-stationary) data covariance matrix is estimated from residual errors to account for correlated

errors and varying variance with time and standardized residual errors generally pass posterior statistical test for Gaussianity and randomness. Interface probabilities from trans-dimensional inversion demonstrate the decreasing resolution of the CSEM data with depth, which are a few hundred metres wide below 400 mbsf. However, an average of four layers with different resistivities to a depth of 800 m can be identified, although the last layer has high uncertainties for depth position and resistivity, and is probably below the penetration depth of the CSEM array. The following geological interpretation was drawn from the CSEM inversion results together with borehole and reflection seismic data. A thin ($\sim$20 m) overburden layer of fine-grained Holocene (to late Pleistocene) sediments is well encased by relatively low resistivities (0.8–1 Ωm) as delineated by high interface probabilities in the Bayesian inversion results. Pleistocene sediments underneath show elevated resistivities (2–4 Ωm) that may be related to the unsorted, sand-dominated composition. Higher amounts of fine-grained materials in Miocene sediments, again, correlate with lower resistivities ($\sim$1 Ωm). The geological interpretation excludes the possibility of free gas and relates the targeted seismic reflector to a thin layer of fine grained sediments which was likely deposited upon an erosional unconformity.

Chapter 8

Summary and conclusions

The main goal of this thesis was to develop and apply CSEM inversions to estimate sub-seafloor resistivity models and uncertainties and compare the results to reflection seismic data to provide a more complete geological interpretation. The thesis focuses on three major studies to investigate the ability of CSEM to detect subsurface resistivity anomalies related to hydrocarbon accumulations (specifically, gas hydrates and free gas).

1. A simulation was carried out for a case study of Beaufort Sea permafrost environments with a horizontal electric dipole (HED) seafloor-towed system and variable offsets to estimate the sensitivity to permafrost and gas hydrate occurrences.

2. CSEM data on the upper and middle slopes of the Northern Cascadia accretionary prism, acquired in 2005 and 2006 with an HED seafloor-towed system with two receivers, were analyzed to study cold vent sites and regional gas hydrates.

3. CSEM data, acquired in the German North Sea in 2012 with an HED seafloor-towed system with four receivers, were analyzed to study possible free gas occurrences.

The various data sets were analyzed with different techniques which progressed in sophistication. The simulation study in the Beaufort Sea is primarily a forward modelling study, and secondly uses linearization and singular value decomposition to evaluate model parameter uncertainties. The CSEM data from the Northern Cascadia margin were analyzed with a probabilistic, non-linear Bayesian inversion in fixed

dimensions, where the number of model parameters (subsurface layers) was estimated in a preliminary inversion step with the Bayesian information criterion. Finally, the CSEM data from the North Sea were analyzed with a trans-dimensional Bayesian inversion to rigorously estimate model parameters and uncertainties by including the number of parameters as an unknown which was sampled probabilistically in the inversion.

The results can be summarized as follows.

1. The simulation study in the Beaufort Sea showed that the HED seafloor-towed CSEM system is sensitive to the top and the bottom of the permafrost. However, the uncertainty for the depth to the top of the permafrost can be up to one order of magnitude smaller than the uncertainty for the depth to the bottom of the permafrost. The uncertainty for the resistivity of the conductive layer (non-ice bounded sediments) underneath the permafrost can even be up to two orders of magnitudes larger than the uncertainty for the resistivity above the permafrost. The resistivity of the permafrost and possible talik sections within the permafrost are also difficult to estimate, and talik sections are required to be relatively thick ($\sim$100 m centred in 150 mbsf). It is even more challenging to estimate gas hydrate occurrences underneath the permafrost. The shallow water depth on the Beaufort shelf causes the step-on response at the receivers to be overlain by the electromagnetic signature of the air-water boundary (airwave). Depending on the sub-seafloor model, the airwave can mask the subsurface signal at certain water depths and specific transmitter-receiver offsets (blind window). More resistive seawater decreases the impact of the airwave, and shifts the blind window to greater water depth. Further modelling studies are needed to evaluate how measuring additional electromagnetic components (especially E_z which is recommended for shallow water studies as it is insensitive to the airwave [Weidelt, 2007]) would improve the sensitivity to the bottom of the permafrost and possible gas hydrate occurrences.

2. The CSEM survey at the Northern Cascadia margin targeted two areas, one of which is located on the upper slope at the landward edge of the gas hydrate stability zone while the other is located at the middle slope which is abundant in cold vent sites with high gas hydrate concentrations.

   (a) The data analysis on the upper slope with a non-linear Bayesian inversion method shows that the data resolve halfspace models where there is either no

significant change in resistivity within the penetration depth of the instrument (penetration depth is limited by the maximum offset of 292 m), or the data error is too large to infer detailed resistivity structure. The data do resolve two layers for some waypoints where the resistivity increase with depth can be related to accreted sediments below younger slope sediments. The resistivity increase can be correlated with an unconformity visible in seismic reflection data and increasing logging resistivities. However, the resistivity of the bottom layer has high uncertainties probably due to the depth of the unconformity, the relatively high noise on the data and additional unknowns about the acquisition. Indications for gas hydrate or free gas were found locally at three sites where high resistivities were inferred. The hypothesis of local fluid venting along fault zones (indicated by seismic reflection data) with abundant free gas needs to be verified by additional studies, for example, with high frequency acoustic data (3.5 kHz echo sounder data for the seabed or multibeam data to detect gas plumes in the water column and bathymetric changes).

(b) The inversion results of the CSEM data on the middle slope reveal locally high resistivities at the Bullseye vent, which can be related to shallow gas hydrates (verified with piston core data, strong seismic amplitudes and matching logging resistivities). High-resistive, shallow layers at other way points can also be correlated with high seismic amplitudes and/or seismic blanking at possible vent sites close to Bullseye vent. Regionally elevated resistivities close to the vent sites might be related to regional gas hydrate or free gas abundance in sediment layers, where gas plumes were observed in the water column.

The non-linear Bayesian inversion has proven advantageous compared to linearized inversions when inverting for additional unknowns such as acquisition parameters (for example, the time delay) as they are simpler to implement in non-linear inversions. Furthermore, a full analysis of their probability is possible with Bayesian inversion to understand the distribution of acquisition as well as the sub-seafloor parameters. The Bayesian inversion also resolves the relationship of acquisition parameters and sub-seafloor parameters, which can be significant (*e.g.*, between the time delay and the overburden resistivity, as both influence the arrival time of the step-on response).

3. The CSEM data in the German North Sea were analyzed with a trans-dimensional Bayesian inversion, where the number of sub-seafloor layers is another

unknown in the inversion. The North Sea data have a higher signal-to-noise ratio than the Northern Cascadia data. Other differences are a source amplitude of 30 to 50 A compared to 10 A and a system with four receivers with a maximum offset of 750 m, instead of two with a maximum offset of 292 m. The challenge in inverting the North Sea data is the shallow water depth. The modelling study for the Beaufort Sea has shown the effect of the shallow water on the misfit between two sub-seafloor models. A blind window results from the airwave overlying subsurface information, which depends on the water depth, the water resistivity and the subsurface model. However, trans-dimensional Bayesian inversion results reveal subsurface resistivity structure that correlates with seismic reflection data in the upper few 10s of metres. The free gas hypothesis at a phase-reversed, high amplitude reflector (which provided the motivation for the CSEM survey) could not be supported by the CSEM inversion results. The layer that causes the high-amplitude reflections may be too thin or the resistivity contrast too weak to be resolved with the CSEM data. Interface probabilities and parameter uncertainties increase with depth, so that they cannot be matched with seismic reflectors. However, relatively low resistivities at $\sim$300 mbsf can be related to a seismic reflector that correlates with an increased gamma-ray count related to an increased amount of fine-grained sediments.

The non-linear Bayesian inversion of CSEM data has successfully resolved model parameters and uncertainties and evaluated parameter relationships, as well as examined unknown acquisition parameters. The probabilistic approach reveals that the geometry of the CSEM array, water resistivity and timing needs to be precisely known to deduct subsurface parameters with sufficient resolution, especially if the target layer of interest is at greater depth. A trans-dimensional Bayesian inversion offers a more rigorous uncertainty estimation and accounts for unknown parametrization. The CSEM inversion results have been shown to successfully detect shallow resistivity anomalies which appear to be related to gas hydrates or free gas venting and major stratigraphic changes to sediments with higher resistivities. Future studies are needed to model cold vents in two or three dimensions to more adequately resolve the resistive structure. Comparing interface probabilities from trans-dimensional CSEM inversion with seismic reflection data helps to identify if, for example, seismic reflectors indicate an actual change of the physical parameters which is large enough to be detected with the CSEM method or if they indicate a thin stratigraphic boundary. The North Sea study was challenged by the shallow water depth and it would be in-

teresting as future research to conduct a trans-dimensional inversion on CSEM data in greater water depth for more resistive targets.

Appendix A

Beaufort Sea permafrost synthetic modelling

A.1 Models

Models 1 to 6 represent possible sub-surface structure below the Beaufort Sea and were used for the simulation study presented in Sec. 4.1 to infer the resolution of permafrost for CSEM data in shallow water depth. Models are shown in Fig. 4.2, 4.11 and 4.16 and are listed in Tab. A.1 to A.3.

Model	Layer 1	2	Halfspace
1A	2.2 Ωm, 20 m	1 Ωm, 20 m	100 Ωm
1B	2.2 Ωm, 10 m	1 Ωm, 10 m	100 Ωm
2A	2.2 Ωm, 20 m	1 Ωm, 20 m	500 Ωm
2B	2.2 Ωm, 10 m	1 Ωm, 10 m	500 Ωm
3A	1.6 Ωm, 20 m	1 Ωm, 20 m	100 Ωm
3B	1.6 Ωm, 20 m	1 Ωm, 20 m	500 Ωm

Table A.1: Chosen permafrost models (resistivity and thickness) based on Scott [1992]

Model	Layer	1	2	3	4	5	Halfspace
4A		2.2 Ωm	1 Ωm	100 Ωm	3 Ωm	30 Ωm	3 Ωm
		20 m	20 m	400 m	300 m	200 m	
4B		2.2 Ωm	1 Ωm	100 Ωm	3 Ωm	30 Ωm	3 Ωm
		20 m	20 m	200 m	500 m	200 m	
4C		2.2 Ωm	1 Ωm	500 Ωm	3 Ωm	30 Ωm	3 Ωm
		20 m	20 m	400 m	300 m	200 m	

Table A.2: Chosen permafrost models (resistivity and thickness) based on Scott [1992] and Scholl [2010]

Model	Layer	1	2	3	4	Halfspace
5A		2.2 Ωm	1 Ωm	100 Ωm	30 Ωm	100 Ωm
		20 m	20 m	20 m	20 m	
5B		2.2 Ωm	1 Ωm	100 Ωm	30 Ωm	100 Ωm
		20 m	20 m	20 m	50 m	
5C		2.2 Ωm	1 Ωm	100 Ωm	30 Ωm	100 Ωm
		20 m	20 m	20 m	100 m	
6A		2.2 Ωm	1 Ωm	100 Ωm	30 Ωm	100 Ωm
		20 m	20 m	40 m	50 m	
6B		2.2 Ωm	1 Ωm	100 Ωm	30 Ωm	100 Ωm
		20 m	20 m	60 m	50 m	
6C		2.2 Ωm	1 Ωm	100 Ωm	30 Ωm	100 Ωm
		20 m	20 m	60 m	100 m	
6D		2.2 Ωm	1 Ωm	100 Ωm	30 Ωm	100 Ωm
		20 m	20 m	100 m	100 m	

Table A.3: Chosen permafrost models (resistivity and thickness) based on Scott [1992] and Todd and Dallimore [1998]

A.2 Misfits for different resistivities of permafrost layer

When comparing model 1B and 2B (thin overburden on top of permafrost layer with 100 Ωm and 500 Ωm respectively), I analyze if the resistivity of the permafrost layer can be discriminated. Figure A.1 shows the deviation of the step-on responses for resistive seawater.

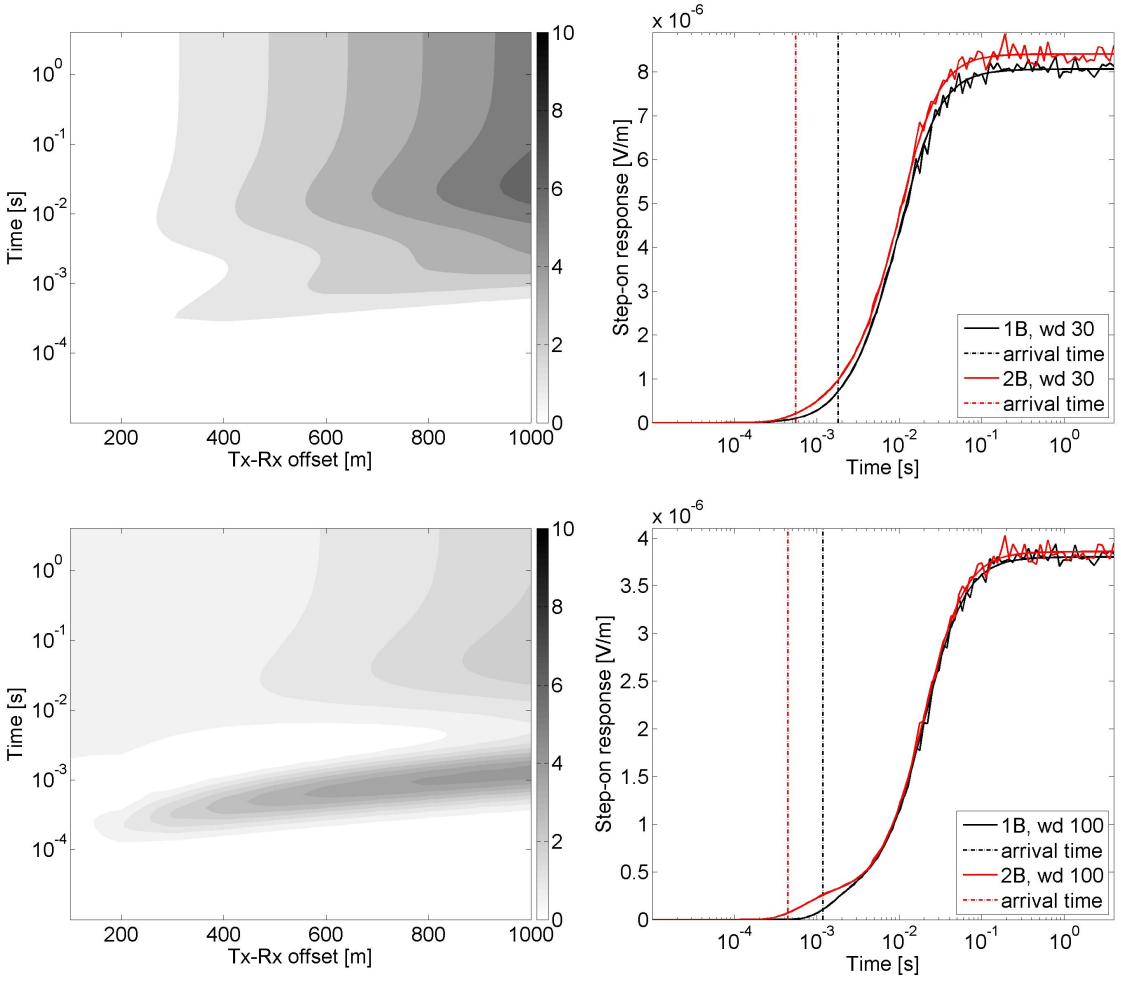

Figure A.1: Right: Predicted step-on responses for model 1B and model 2B with and without Gaussian random noise for Tx-Rx offset 800 m in 30 m (top) and 100 m (bottom) water depth (wd). Left: Normalized deviation (colour bar) of the two responses for Tx-Rx offset of 100 to 1000 m and time. Water resistivity is ρ_w=2 Ωm.

A.3 Talik section in permafrost

Figures A.2 and A.3 show the difference of the step-on response for model 1A and 5C for ρ_w=0.38 and 2 Ωm respectively. Model 1A has no talik section, while model 5C has a relatively thick talik section. The strongest difference between the step-on responses is for large Tx-Rx spacings because of the increasing sensitivity to deeper layers. In shallow water depth, the late-time amplitudes deviate stronger. In 100 m water depth the step-on response for models 1A and 5C for conductive seawater (bottom panel of Fig. A.2) differ mainly in the arrival time, while for resistive seawater

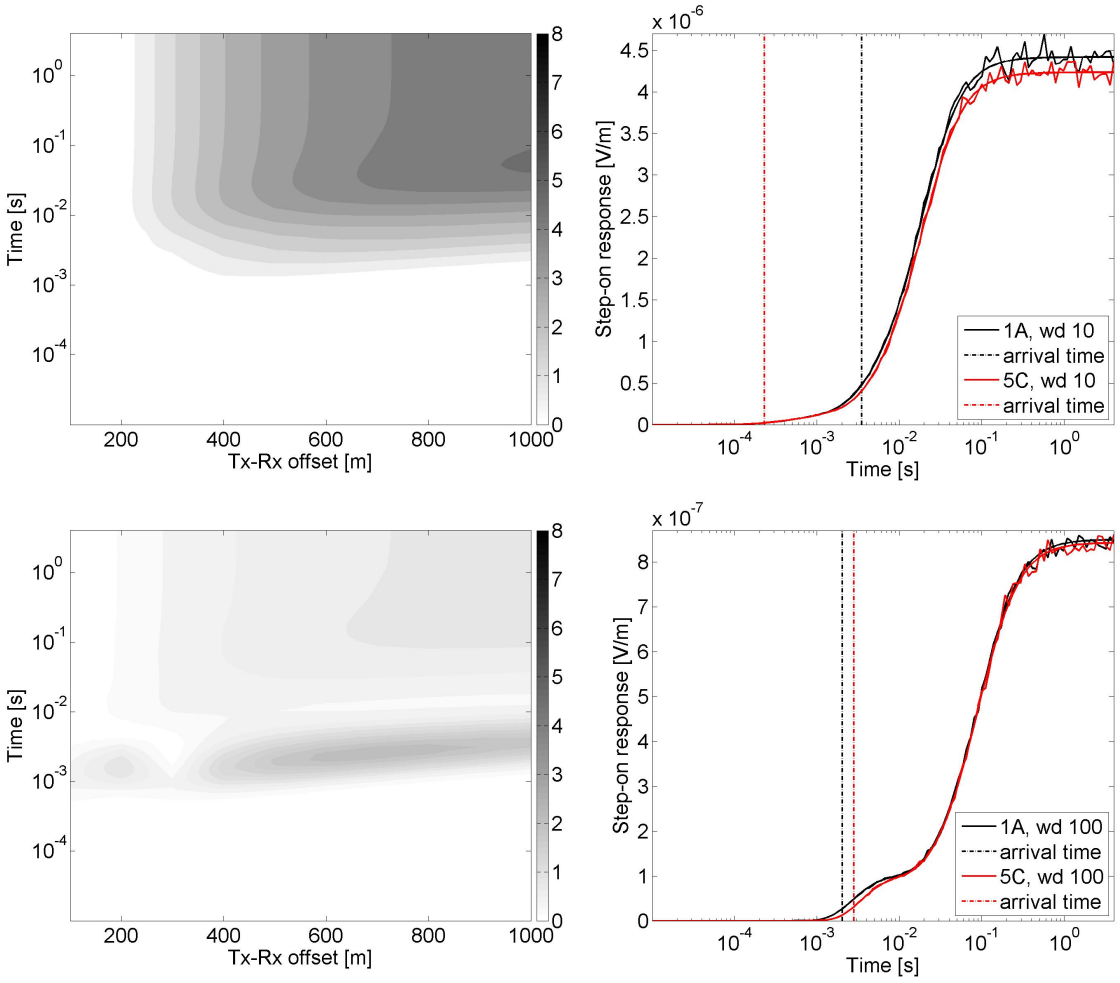

Figure A.2: Right: Predicted step-on responses for model 1A and model 5C with and without Gaussian random noise for Tx-Rx offset 800 m in 10 m (top) and 100 m (bottom) water depth (wd). Left: Normalized deviation (colour bar) of the two responses for Tx-Rx offset of 100 to 1000 m and time. Water resistivity is ρ_w=0.38 Ωm.

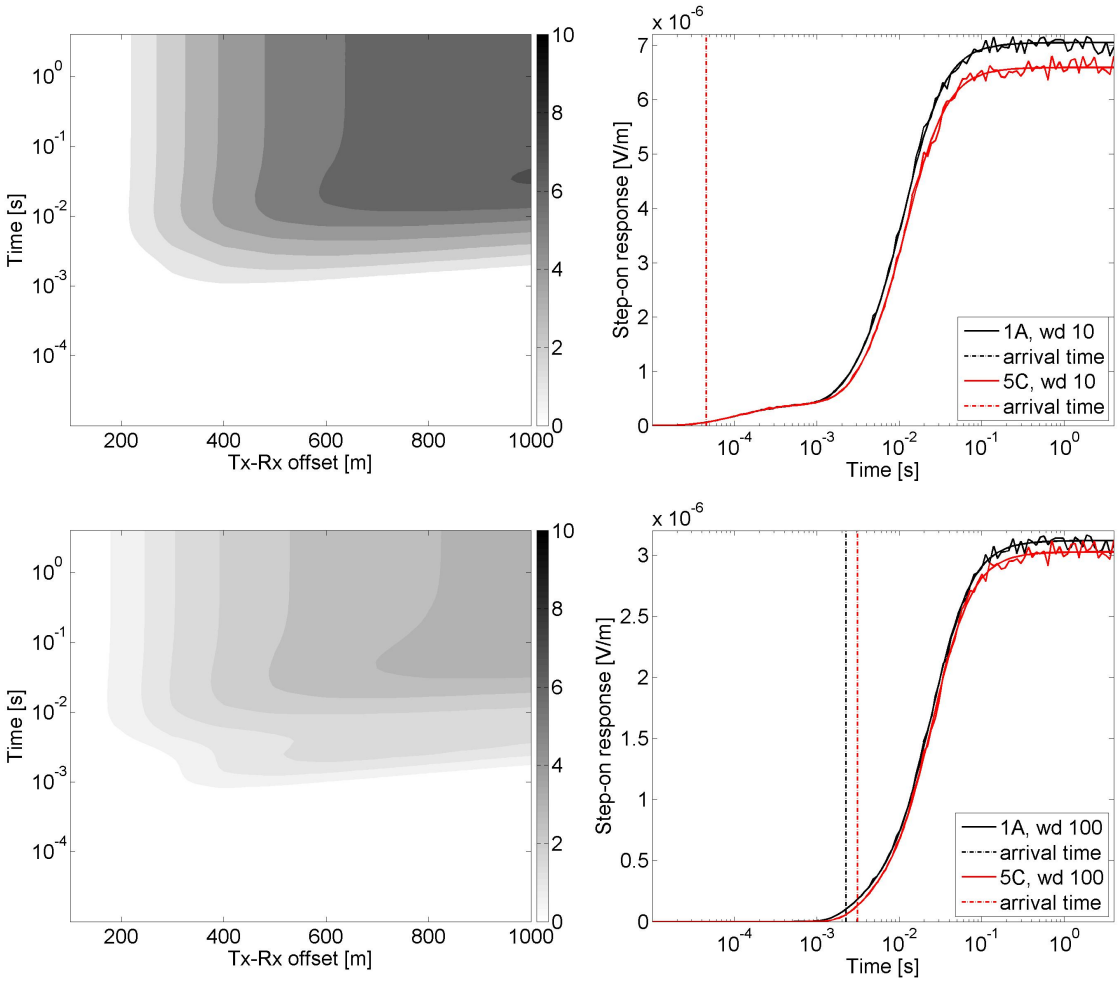

Figure A.3: Right: Predicted step-on responses for model 1A to model 5C with and without Gaussian random noise for Tx-Rx offset 800 m in 10 m (top) and 100 m (bottom) water depth (wd). Left: Normalized deviation (colour bar) of the two responses for Tx-Rx offset of 100 to 1000 m and time. Water resistivity is ρ_w=2 Ωm.

they also differ in their late-time amplitudes (bottom panel of Fig. A.3).

Appendix B

Auto-regressive error model

One way of addressing correlated errors is by computing a non-Toeplitz covariance matrix from the residual errors calculated for an optimal model as explained in Sec. 5.3.3. Another way to address error correlation is by using a first-order auto-regressive (AR(1)) model, which is equivalent to an exponential fall off of the covariances from the variance value (diagonally constant σ^2), where φ^{AR} represents the fall-off rate [Dettmer et al., 2012]. The AR(1) model represents exponentially decaying error covariances. The advantage is that the covariances change according to the model, while a fixed covariance matrices from a point estimate does not.

The likelihood function from Eq. (5.17) becomes

$$L(\mathbf{m}, \mathbf{C}_d, cf) = \prod_{i=1}^{N_{Rx}} \left\{ \frac{1}{(2\pi\sigma_i^2)^{N_i/2}} \exp\left(-\frac{1}{2} \frac{(\mathbf{d}_i - cf_i \mathbf{d}_i(\mathbf{m}) - \mathbf{d}_i^{\mathrm{AR}})^2}{\sigma_i^2} \right) \right\}, \tag{B.1}$$

where $\mathbf{d}^{AR}$ represents the prediction of the AR(1) model given by

$$d_i^{AR} = \varphi_i^{\mathrm{AR}}(d_{i-1} - d(\mathbf{m})_{i-1}), \tag{B.2}$$

for equally-spaced data in logarithmic time. The total residuals $\mathbf{r}_i = \mathbf{d}_i - cf_i \mathbf{d}_i(\mathbf{m}) - \mathbf{d}_i^{\mathrm{AR}}$ are assumed to be uncorrelated Gaussian distributed with a standard deviation σ_i for the i^{th} receiver. The unknown σ_i and φ_i^{AR} are sampled in the inversion, with an additional birth/death procedure for the AR process (to determine if it is actually necessary to explain the data) [Steininger et al., 2013]. The acceptance criterion is similar to the interface birth and death. For the AR birth move (going from a model $\mathbf{m}_0$ which does not include the AR process to a model $\mathbf{m}_1$ which does) the proposal

density is chosen to be equal to the (uniform) prior density: $P(\mathbf{m}_1) = Q(\mathbf{m}_1|\mathbf{m}_0) = 1/(\varphi^{AR+} - \varphi^{AR-})$, where $\varphi^{AR-} = -0.6$ and $\varphi^{AR+} = 0.9999$ are the prior bounds. The prior for the death is unity, but the proposal is $Q(\mathbf{m}_0|\mathbf{m}_1) = 0.5$ as there is 50 % chance that the model is perturbed instead. The acceptance criteria become

$$\begin{aligned} \alpha^{AR}_{birth} &= \min\left[1, \frac{P(\mathbf{m}'_1)}{P(\mathbf{m}_0)}\frac{L(\mathbf{m}'_1)}{L(\mathbf{m}_0)}\frac{Q(\mathbf{m}_0|\mathbf{m}'_1)}{Q(\mathbf{m}'_1|\mathbf{m}_0)}\right] \\ &= \min\left[1, \frac{1}{2}\frac{L(\mathbf{m}'_1)}{L(\mathbf{m}_0)}\right], \end{aligned} \tag{B.3}$$

$$\begin{aligned} \alpha^{AR}_{death} &= \min\left[1, \frac{P(\mathbf{m}'_0)}{P(\mathbf{m}_1)}\frac{L(\mathbf{m}'_0)}{L(\mathbf{m}_1)}\frac{Q(\mathbf{m}_1|\mathbf{m}'_0)}{Q(\mathbf{m}'_0|\mathbf{m}_1)}\right] \\ &= \min\left[1, 2\frac{L(\mathbf{m}'_0)}{L(\mathbf{m}_1)}\right]. \end{aligned} \tag{B.4}$$

After the inversion, the residual errors of the median model are tested with the runs-test for randomness and the Kolmogorov-Smirnov (KS) test for Gaussianity [Massey, 1951].

Preliminary tests with simulated data with an exponentially decaying error correlation have shown that the physical model parameters as well as the error correlation can be well resolved with the AR(1) model. In the following, simulated data with added correlated errors (correlation level inferred from measured data) are inverted with the AR(1) model. The correlated errors are obtained from a non-Toeplitz covariance matrix from residual analysis after evaluating a median model estimate from WP 19 (North Sea data presented in Sec. 7.4). Therefore, the simulation study examines if the AR(1) model can account for correlated errors from measured data which are not necessarily exponentially decaying. Figure B.1 compares inversion results using the AR(1) model (4 AR(1) coefficients and 4 standard deviations for 4 receivers) and an unknown calibration factor for Rx_1 (cf_1) for two cases. In one case the time delay is 0 ms and in the other the time is shifted by 0.3 ms to test the AR(1) model when acquisition parameters are not known precisely. The result is shown in Fig. B.1 and shall be compared to Fig. 7.4 and 7.6. The inversion with the AR(1) model is not as efficient as the inversion with the covariance matrix from residuals in case of unaccounted unknowns. Sampling takes longer due to the additional parameters and the inversion results for the subsurface model are more complicated than needed. Compared to the inversions with a non-Toeplitz data covariance matrix the inversion with the AR(1) model includes 8 more parameters to invert for. The problem

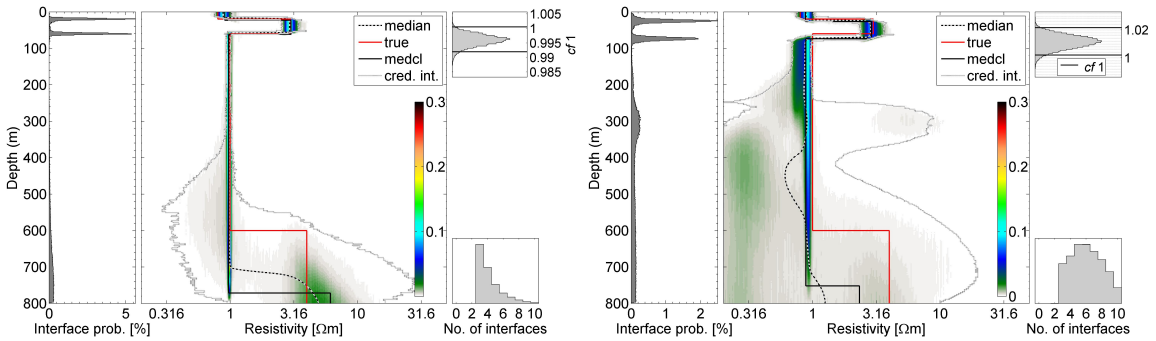

Figure B.1: Interface probability and marginal probability depth profile for inversion with AR(1) model of synthetic data with correlated errors without time shift (left) and a time shift of 0.3 ms (right). Inversion for calibration factor cf_1.

appears to become under-determined. Several layers with high and low resistivities are introduced that are geologically unreasonable. However, inversion results with an AR(1) model pass statistical tests for Gaussian distributed errors and seem to model error correlation well.

Inversions results of measured data at WP 19 are shown in Fig. B.2. The uncertainties are large for model structure below ∼200 mbsf, and when comparing to Fig. 7.7 it seems that the AR(1) model over-parametrizes the inversion and introduces spurious, unconstrained subsurface structure. The synthetic modelling above has shown that if time, instrument geometry or water depth are not known precisely, the problem can become under-determined, which may be the case for the measured data. Therefore the AR model is not used for inversion results in this thesis.

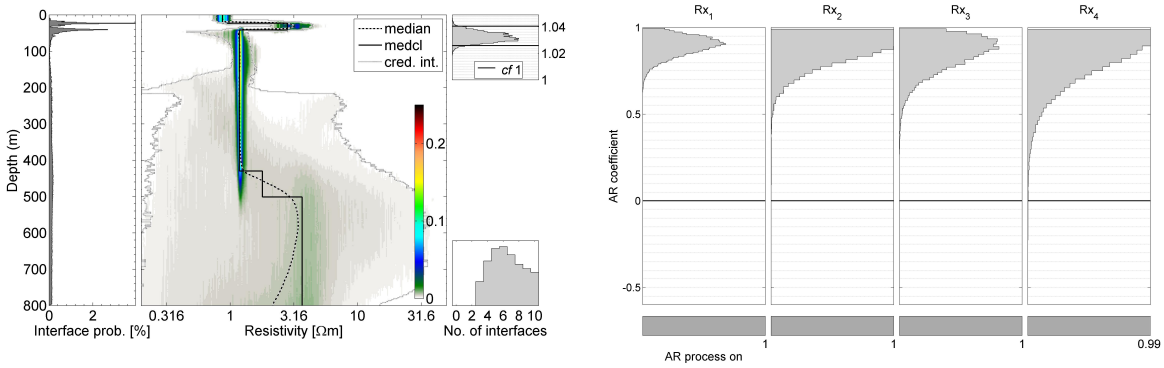

Figure B.2: Left: Interface probability and marginal probability depth profile for resistivity with depth of WP 19 for inversion with AR(1) model and calibration factor cf_1. Right: AR parameter distribution for each receiver and sliding scale to show for how many models the AR process was used (1 refers to 100%).

Appendix C

Selected drilling information for the German North Sea

Several drilling and seismic reflection surveys have been conducted in the German North Sea to evaluate the geologic evolution, hydrocarbon occurrences and the composition of the upper sediments for building purposes. The available seismic data is shown on Fig. C.1. Drill sites in the vicinity of the CSEM survey presented in this thesis (area D on Fig. C.1) cover mostly the upper ∼100 mbsf (shown in Fig. C.2) or greater depths (>600 mbsf). The project "Geopotential in the German North Sea" at the Federal Institute for Geosciences and Natural resources (BGR, Germany) funded the mapping of common seismic reflection surfaces in the German North Sea. Furthermore Thöle et al. [2014] have correlated gamma-ray logs to seismic reflectors north of Heligoland as shown in Fig. C.3. Two seismic reflectors (blue and red) can also be traced on AUR03-23a (shown on Fig. 7.10).

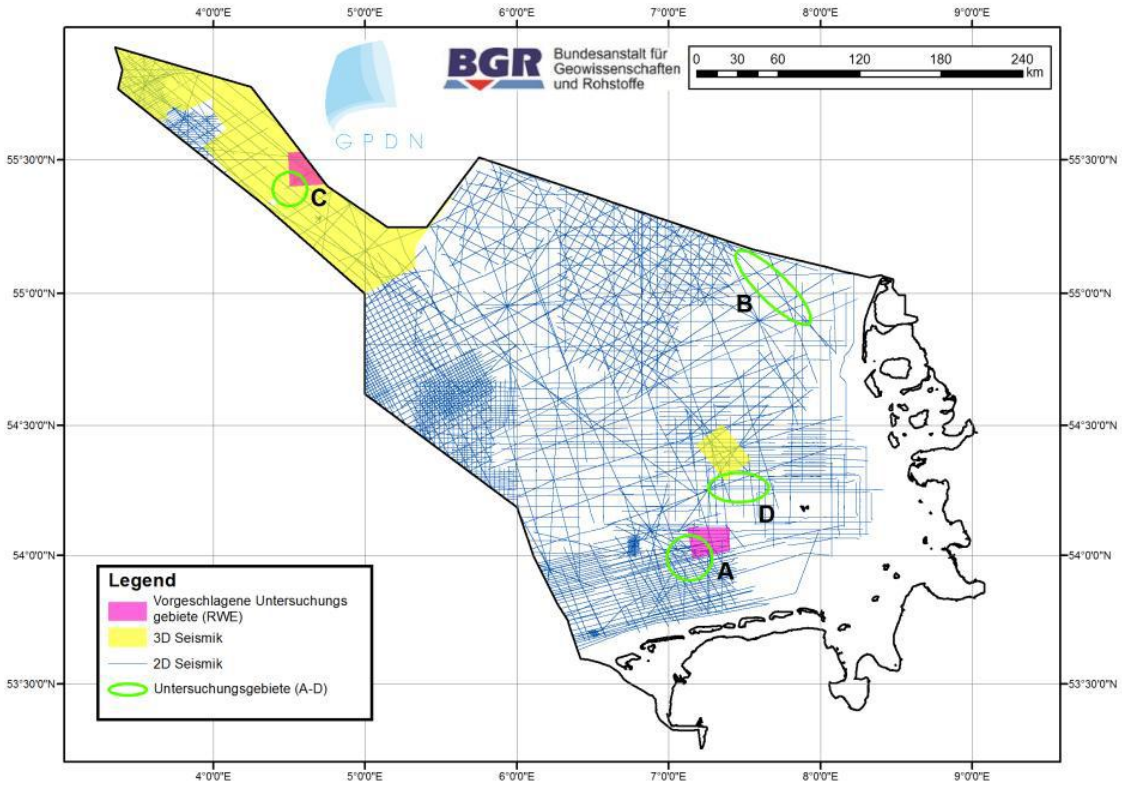

Figure C.1: Coverage of seismic reflection surveys in the German North Sea (yellow patches: 3-D seismic data, grey lines: 2-D seismic data, pink patches: proposed CSEM study areas by RWE). The green ellipses are the planned CSEM survey areas A–D. CSEM data presented in this thesis is located in area D. Courtesy BGR, Germany.

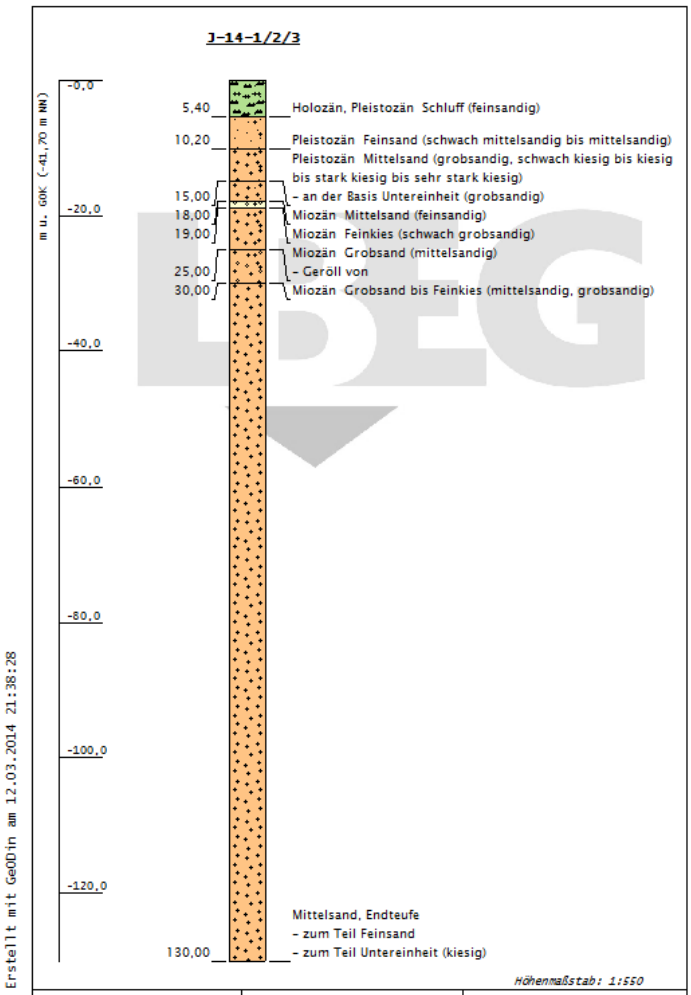

Figure C.2: Sediment grain size from J-14-1/2/3 which is located at WP 20. Grain sizes are silty sand (line with two cross lines in green section) of Holocene origin, fine sand (dots in orange section) of Pleistocene origin, middle sand (crosses) and coarse sand (circles) of Pleistocene origin. Note that the interpretation of Miocene material in 30 m depth is likely not correct (personal communication with Lutz Reinhardt (BGR) [2014]). Courtesy State Authority for Mining, Energy and Geology (LBEG), Germany.

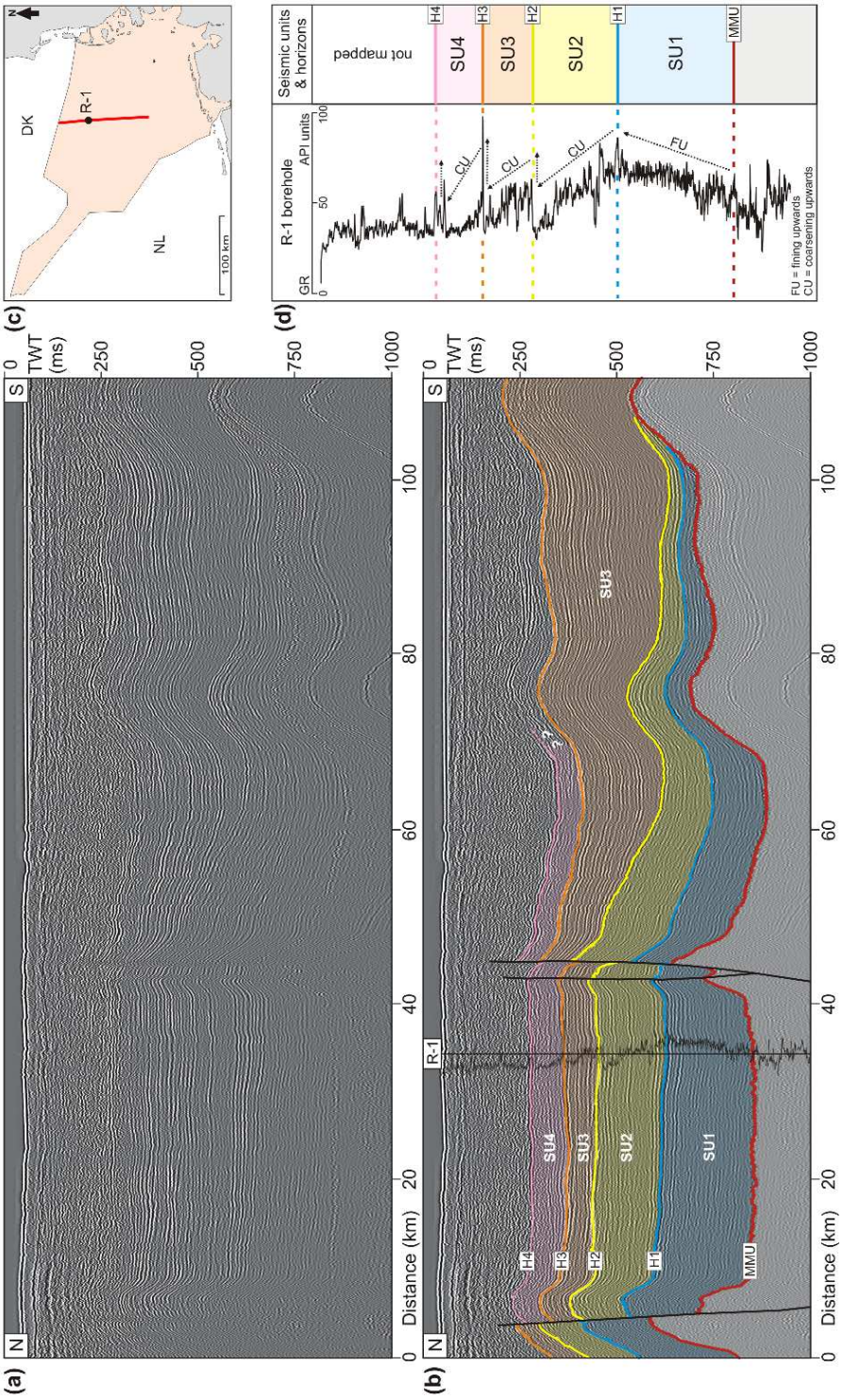

Figure C.3: Seismic interpretation and gamma-ray log by Thöle et al. [2014]. The blue and red seismic reflectors match with the colour coding on Fig. 7.10. Relevant for this thesis is the increased gamma-ray count at the blue reflector between seismic units (SU) 1 and 2 which indicates increased values of fine-grained sediments. Courtesy Hauke Thöle [Fig. 5 in Thöle et al., 2014].

Bibliography

N. P. Agostinetti and A. Malinverno. Receiver function inversion by trans-dimensional Monte Carlo sampling. *Geophys. J. Int.*, 181:858–872, 2010.

K. Andreassen, P. E. Hart, and A. Grantz. Seismic studies of a bottom simulating reflection related to gas hydrate beneath the continental margin of the Beaufort Sea. *Journal of Geophysical Research*, 100(B7):12659–12673, 1995.

D. Archer, M. Eby, V. Brovkin, A. Ridgwell, L. Cao, U. Mikolajewicz, K. Caldeira, K. Matsumoto, G. Munhoven, A. Montenegro, and K. Tokos. Atmospheric lifetime of fossil-fuel carbon dioxide. *Annual Reviews of Earth and Planetary Sciences*, 37: 117–134, 2009.

G. E. Archie. The Electrical Resistivity Log as an Aid in Determining Some Reservoir Characteristics. *Trans. Am. Inst. Min. Metall. Pet. Eng.*, 146:54–62, 1942.

J. Arfai, F. Jaehne, R. Lutz, L. Reinhardt, H. Thöle, and H. Wirth. Datengrundlage, Arbeitskonzepte und erste vorlaeufige Ergebnisse zum Projekt Geopotenzial Deutsche Nordsee (2009-2010), 2011.

J.-J. Bahk, D.-H. Kim, J.-H. Chun, B.-K. Son, J.-H. Kim, B.-J. Ryu, M. E. Torres, M. Riedel, and P. Schultheiss. Gas hydrate occurrences and their relation to host sediment properties: Results from Second Ulleung Basin Gas Hydrate Drilling Expedition, East Sea. *Marine and Petroleum Geology*, 47:21–29, 2013.

P. R. Bannister. Determination of the electrical conductivity of the sea bed in shallow waters. *Geophysics*, 33(6):995–1003, 1968.

C. Bily and J. W. L Dick. Naturally occurring gas hydrates in the Mackenzie Delta. *Bulletin of Canadian Petroleum Geology*, 22:320–352, 1974.

T. Bodin and M. Sambridge. Seismic tomography with the reversible jump algorithm. *Geophys. J. Int.*, 178:1411–1436, 2009.

T. Bodin, M. Sambridge, H. Tkalcic, P. Arroucau, K. Gallagher, and N. Rawlinson. Transdimensional inversion of receiver functions and surface wave dispersion. *Journal of Geophysical Research*, 117:24, 2012.

G. Bohrmann and M. E. Torres. Gas Hydrates in Marine Sediments. In H. D. Schulz and M. Zabel, editors, *Marine Geochemistry*, pages 481–512. Springer, Berlin, Heidelberg, New York, 2 edition, 2006.

H. Brown, W. Holbrook, M. Hornbach, and J. Nealon. Slide structure and role of gas hydrate at the northern boundary of the Storegga Slide, offshore Norway. *Marine Geology*, 229(3-4):179–186, 2006.

B. Buffett and D. Archer. Global inventory of methane clathrate: sensitivity to changes in the deep ocean. *Earth and Planetary Science Letters*, 227:185–199, 2004.

A. Buland and O. Kolbjørnsen. Bayesian inversion of CSEM and magnetotelluric data. *Geophysics*, 77(1):E33–E42, 2012.

E. C. Carmack and R. W. Macdonald. Oceanography of the Canadian shelf of the Beaufort Sea: A setting for marine life. *Arctic*, 55:29–45, 2002.

A. D. Chave and C. S. Cox. Controlled Electromagnetic Sources for Measuring Electrical Conductivity Beneath the Oceans 1. Forward Problem and Model Study. *Journal of Geophysical Research*, 87(B7):5327–5338, 1982.

S. J. Cheesman, R. N. Edwards, and A. D. Chave. On the Theory of Sea Floor Conductivity Mapping using Transient Electromagnetic Systems. *Geophysics*, 52: 204–217, 1987.

J. Chen, G. M. Hoversten, D. Vasco, Y. Rubin, and Z. Hou. A Bayesian model for gas saturation estimation using marine seismic AVA and CSEM data. *Geophysics*, 72(2):WA85–WA95, 2007.

T. S. Collett and J. Ladd. Detection of gas hydrate with downhole logs and assessment of gas hydrate concentrations (saturations) and gas volumes on the Blake Ridge with electrical resistivity log data. In C.K. Paull, R. Matsumoto, P.J. Wallace,

, and W.P Dillon, editors, *Proceedings of the Ocean Drilling Program, Scientific Results*, volume 164, page 179191. TX (Ocean Drilling Program), College Station, 2000.

T. S. Collett, A. H. Johnson, C. C. Knapp, and R. Boswell. Natural Gas Hydrates: A Review. In T. S. Collett, A. H. Johnson, C. C. Knapp, and R. Boswell, editors, *Natural gas hydrates - Energy resource potential and associated geologic hazards*, page 146219. AAPG Memoir 89, 2009.

S. Constable and C. S. Cox. Marine controlled-source electromagnetic sounding 2. The PEGASUS experiment. *Journal of Geophysical Research*, 101(B3):55195530, 1996.

S. Constable and L. J. Srnka. An introduction to marine controlled-source electromagnetic methods for hydrocarbon exploration. *Geophysics*, 72(2):WA3–WA12, 2007.

S. C. Constable. Ten years of marine CSEM for hydrocarbon exploration. *Geophysics*, 75(5):75A67–75A81, 2010.

S. C. Constable, R. L. Parker, and C. G. Constable. Occam's inversion: A practical algorithm for generating smooth models from electromagnetic sounding data. *Geophysics*, 52:289–300, 1987.

C. Cox. Electromagnetic induction in the oceans and inferences on the constitution of the earth. *Geophysical Surveys*, 4:137–156, 1980.

C. Cox, S. Constable, and A. Chave. Controlled-source electromagnetic sounding of the oceanic lithosphere. *Nature*, 320(6):5254, 1986.

J. Dai, H. Xu, F. Snyder, N. Dutta, and Schlumberger Reservoir Services. Detection and estimation of gas hydrates using rock physics and seismic inversion: Examples from the northern deepwater Gulf of Mexico. *The Leading Edge*, pages 60–66, 2004.

J. Dai, N. Banik, D. Gillespie, and N. Dutta. Exploration for gas hydrates in the deepwater, northern Gulf of Mexico: Part 2. Model validation by drilling. *Marine and Petroleum Geology*, 25:845–859, 2008.

S. R. Dallimore and T. S. Collett. Summary and implications of the Mallik 2002 Gas Hydrate Production Research Well Program. In S.R. Dallimore and T.S.

Collett, editors, *Scientific results from the Mallik 2002 Gas Hydrate Production Research Well Program. Mackenzie Delta, Northwest Territories, Canada*, volume 585. Geological Survey of Canada Bulletin, 2005.

S. R. Dallimore, J. F. Wright, F. M. Nixon, M. Kurihara, K. Yamamoto, T. Fujii, K. Fujii, M. Numasawa, M. Yasuda, and Y. Imasato. Geologic and porous media factors affecting the 2007 production response characteristics of the JOGMEC,NRCAN,AURORA Mallik Gas Hydrate Production Research Well, 2008.

S. R. Dallimore, C. K. Paull, and A. E. Taylor. Degrading permafrost and gas hydrate under the Beaufort Shelf and marine gas hydrate on the adjacent continental slope: Geothermal and porous media setting. Abstract GC511-05 presented at 2011 Fall Meeting, AGU, San Francisco, CA, 5-9 Dec, 2011.

S. R. Dallimore, C. K. Paull, T. S. Collett, Y. K. Kim, J. Mienert, B. Horsfield, and M. Riedel. Scientific drilling to investigate methane release and geologic processes associated with warming permafrost and gas hydrate deposits beneath the Beaufort Sea Shelf. Integrated Ocean Drilling Program pre-proposal, 2012.

V. Damm, J. Adam, O. Bargeloh, T. Behrens, M. Block, Ü. Demir, A. Ehrhardt, G. Kallaus, C. Kuhlmann, S. Ladage, R. Lutz, C. Papenberg, M. Schnabel, U. Schrader, B. Schreckenberger, and H. Sonnabend. 3D-Test North Sea, Geopotenzial Deutsche Nordsee (GPDN) - CSEM, Cruise No. 88, Leg 1, Aug. 10 - Sept. 6, Bremerhaven - Bremerhaven. Meteor-Berichte, Leitstelle Deutsche Forschungsschiffe, Institut fuer Meereskunde der Universitaet Hamburg, 2012.

R. Dash and G. Spence. P-wave and S-wave velocity structure of northern Cascadia margin gas hydrates. *Geophys. J. Int.*, pages 1–15, 2011.

E. E. Davis and R. D. Hyndman. Accretion and recent deformation of sediments along the northern Cascadia subduction zone. *Geological Society of America Bulletin*, 101:1465–1480, 1989.

E. E. Davis, R. D. Hyndman, and H. Villinger. Rates of Fluid Expulsion Across the Northern Cascadia Accretionary Prism: Constraints From New Heat Flow and Multichannel Seismic Reflection Data. *Journal of Geophysical Research*, 95(B6): 8869–8889, 1990.

H. Davy. On a combination of oxymuriatic gas and oxygen gas. *Philosophical Transactions of the Royal Society*, page 155, 1811.

A. Demirbas. *Methane Gas Hydrate*. Green Energy and Technology. Springer, Berlin, Heidelberg, New York, 2010.

D. G. T. Denison, C. C. Holmes, B. K. Mallick, and A. F. M. Smith. *Bayesian Methods for Nonlinear Classification and Regression*. Wiley, 1 edition, 2002.

J. Dettmer and S. E. Dosso. Trans-dimensional matched-field geoacoustic inversion with hierarchical error models and interacting Markov chains. *J. Acoust. Soc. Am.*, 132(4), 2012.

J. Dettmer, S. E. Dosso, and C. W. Holland. Model selection and Bayesian inference for high-resolution seabed reflection inversion. *J. Acoust. Soc. Am.*, 125(2):706–719, 2009.

J. Dettmer, S. E. Dosso, and C. W. Holland. Trans-dimensional geoacoustic inversion. *J. Acoust. Soc. Am.*, 128(6):3393–3405, 2010.

J. Dettmer, S. Molnar, G. Steininger, S. E. Dosso, and J. F. Cassidy. Trans-dimensional inversion of microtremor array dispersion data with hierarchical autoregressive error models. *Geophys. J. Int.*, 188:719–734, 2012.

S. E. Dosso. Inverse Theory in Earth and Ocean Sciences - classnotes, 2009.

S. E. Dosso and J. Dettmer. Bayesian matched-field geoacoustic inversion. *Inverse Problems*, 27:23, 2011.

S. E. Dosso, M. J. Wilmut, and A.-L. S. Lapinski. An Adaptive-Hybrid Algorithm for Geoacoustic Inversion. *Journal of Oceanic Engineering*, 26(3), 2001.

S. E. Dosso, P. L. Nielsen, and M. J. Wilmut. Data error covariance in matched-field geoacoustic inversion. *J. Acoust. Soc. Am.*, 119(1), 2006.

S. E. Dosso, C. W. Holland, and M. Sambridge. Parallel tempering for strongly nonlinear geoacoustic inversion. *J. Acoust. Soc. Am.*, 132(5):3030–3040, 2012.

L. D. Dyke. Temperature changes and thaw of permafrost adjacent to Richards Island, Mackenzie Delta, N.W.T. *Can. J. Earth Sci.*, 28:1834–1842, 1991.

D. J. Earl and M. W. Deem. Parallel tempering: Theory, applications, and new perspectives. *Phys. Chem. Chem. Phys.*, 7:3910–3916, 2005.

D. N. Edwards, A. Danesh, and A. Swidinsky. On dynamic electric charge and its relevance in marine CSEM. Presentation at MARELEC, 17$^{\text{th}}$ July, 2013.

R. N. Edwards. Two-dimensional modeling of a towed in-line electric dipole-dipole sea-floor electromagnetic system: The optimum time delay or frequency for target resolution. *Geophysics*, 53(6):846–853, 1988.

R. N. Edwards. On the resource evaluation of marine gas hydrate deposits using sea-floor transient electric dipole-dipole methods. *Geophysics*, 62(1):63–74, 1997.

R. N. Edwards. Marine Controlled Source Electromagnetics: Principles, methodologies, future commercial applications. In *Surveys in Geophysics*, volume 26, pages 675–700. Springer, Berlin, Heidelberg, New York, 2005.

R. N. Edwards and A. D. Chave. A transient electric dipole-dipole method for mapping the conductivity of the sea floor. *Geophysics*, 5(4):984–987, 1986.

R. N. Edwards, P. A. Wolfgram, and A. S. Judge. The ICE-MOSES Experiment: Mapping Permafrost Zones Electrically beneath the Beaufort Sea. *Marine Geophysical Researches*, 9:265–290, 1988.

R. N. Edwards, K. Schwalenberg, E. C. Willoughby, R. Mir, and C. Scholl. Marine Controlled-source Electromagnetics and the Assessment of Seafloor Gas Hydrate. In M. Riedel, E. C. Willoughby, and S. Chopra, editors, *Geophysical Characterization of Gas Hydrates*, pages 149–162. Society of Exploration Geophysicists, 2010.

S. Ellingsrud, T. Eidesmo, S. Johansen, M. C. Sinha, L. M. MacGregor, and S. Constable. Remote sensing of hydrocarbon layers by seabed logging (SBL): Results from a cruise offshore Angola. *The Leading Edge*, 21(10):972–982, 2002.

M. H. Ellis, M. C. Sinha, T. A. Minshull, J. Sothcott, and A. I. Best. An anisotropic model for the electrical resistivity of two-phase geologic materials. *Geophysics*, 75 (6):E161–E170, 2010.

C. A. Emmerton, L. F. W. Lesack, and P. Marsh. Lake abundance, potential water storage, and habitat distribution in the Mackenzie River Delta, western Canadian Arctic. *Water Resour. Res.*, 43(W05419):14, 2007.

R. A. Erchul. Ph.D. thesis at University of Rhode Island, 1972.

R. L. Evans, S. Constable, M. Sinha, and M. Unsworth. On the electrical nature of the axial melt zone at 13N on the East Pacific Rise. *Journal of Geophysical Research*, 99:577–588, 1994.

Expedition 311 Scientists. Cascadia margin gas hydrates. In *IODP Prel. Rept.*, volume 311, page 104. Integrated Ocean Drilling Program Management International, Inc., Washington, DC, 2005.

Expedition 311 Scientists. Site U1329. In M. Riedel, T.S. Collett, M.J. Malone, and the Expedition 311 Scientists, editors, *Proceedings of the Integrated Ocean Drilling Program*, volume 311. Integrated Ocean Drilling Program Management International, Inc., Washington, DC, 2006a.

Expedition 311 Scientists. Site U1328. In M. Riedel, T.S. Collett, M.J. Malone, and the Expedition 311 Scientists, editors, *Proceedings of the Integrated Ocean Drilling Program*, volume 311. Integrated Ocean Drilling Program Management International, Inc., Washington, DC, 2006b.

M. R. Fallat and S. E. Dosso. Geoacoustic inversion via local, global and hybrid algorithms. *J. Acoust. Soc. Amer.*, 105(1/2):3219–3230, 1999.

N. P. Fofonoff. Physical Properties of Seawater: A New Salinity Scale and Equation of State for Seawater. *Journal of Geophysical Research*, 90(C2):3332–3342, 1985.

R. Forster, V. Ramaswamy, P. Artaxo, T. Berntsen, R. Betts, D.W. Fahey, J. Haywood, J. Lean, D. C. Lowe, G. Myhre, J. Nganga, R. Prinn, G. Raga, M. Schulz, and R. Van Dorland. Changes in Atmospheric Constituents and in Radiative Forcing. In S. Solomon, D. Qin, M. Manning, Z. Chen, M. Marquis, K. B. Averyt, M. Tignor, and H. L. Miller, editors, *Climate Change 2007: The Physical Science Basis. Contribution of Working Group I to the Fourth Assessment Report of the Intergovernmental Panel on Climate Change*, page 106. Cambridge University Press, Cambridge, United Kingdom and New York, NY, USA, 2007.

J. Furlong. Characteristic Morphology, Backscatter, and Sub-seafloor Structures of Cold-Vents on the Northern Cascadia Margin from High-Resolution Autonomous Underwater Vehicle Data, 2013.

J. M. Gardner, A. N. Shor, and W. Y. Jung. Acoustic imagery evidence for methane hydrates in the Ulleung Basin. *Marine Geophysical Researches*, 20:495–503, 1998.

R. A. S. Gehrmann, C. Mueller, P. Schikowsky, T. Henke, M. Schnabel, and C. Boennemann. Model-Based Identification of the Base of the Gas Hydrate Stability Zone in Multichannel Reflection Seismic Data, Offshore Costa Rica. *International Journal of Geophysics*, page 12, 2009.

A. Gelman, J.B. Carlin, H.S. Stern, and D.B. Rubin. *Bayesian Data Analysis*. Chapman and Hall/CRC, 2 edition, 2000.

Charles J. Geyer and J. Møller. Simulation Procedures and Likelihood Inference for Spatial Point Processes. *Scandinavian Journal of Statistics*, 21(4):359–373, 1994.

G. H. Golub and C. Reinsch. Singular value decomposition and least squares solutions. *NUM. MATH.*, 14:403–420, 1970.

J. Grace, T. Collett, F. Colwell, P. Englezous, E. Jones, R. Mansell, P. Meekinson, R. Ommer, M. Pooladi-Darwisch, M. Riedel, J. Ripmeester, C. Shipp, and E. Willoughby. Energy from Gas Hydrates: Assessing the opportunities and challenges for Canada, 2008.

P. J. Green. Reversible jump Markov chain Monte Carlo computation and Bayesian model determination. *Biometrika*, pages 711–732, 1995.

P. J. Green. Trans-dimensional markov chain monte carlo. In P. J. Green, N. L. Hjort, and S. Richardson, editors, *Highly Structured Stochastic Systems*, Oxford Statistical Science Series, pages 179–198. Oxford University Press, Oxford, 2003.

D. J. Griffiths. *Introduction to Electrodynamics*. Pearson Education Limited, Essex, 4 edition, 2012.

C. Gutt, B. Asmussen, W. Press, C. Merkl, H. Casalta, J. Greinert, G. Bohrmann, J. Tse, and A. Hüller. Quantum rotations in natural methane-clathrates from the pacific sea-floor. *Europhysics Letters*, 48:269–275, 1999.

R. R. Haacke, G. K. Westbrook, and R. D. Hyndman. Gas hydrate, fluid flow and free gas: Formation of the bottom-simulating reflector. *Earth and Planetary Science Letters*, 261:407–420, 2007.

E. G. Hammerschmidt. Formation of gas hydrates in natural gas transmission lines. *Industrial and Engineering Chemistry*, 26:851, 1934.

J. J. Hance. Submarine slope stability. M.Sc. Thesis, 2003.

Z. Hashin and S. Shtrikman. A variational approach to the theory of the elastic behaviour of multiphase materials. *Journal of Mechanics of Physical Solids*, 11: 127140, 1963.

W. K. Hastings. Monte Carlo sampling methods using Markov chains and their application. *Biometrika*, 57(1), 1970.

J. R. Hearst, P. H. Nelson, and F. L. Paillet. *Well Logging for Physical Properties*. John Wiley, Hoboken, N.J., 2nd edition, 2000.

D. A. Hepp, D. Hebbeln, S. Kreiter, H. Keil, C. Bathmann, and J. Ehlers und T. Mörz. An east-west-trending Quaternary tunnel valley in the south-eastern North Sea and its seismic-sedimentological interpretation. *J. Quaternary Sci.*, 27:844–853, 2012.

W. S. Holbrook, A. R. Gorman, M. Hornbach, K. L. Hackwith, J. Nealon, D. Lizarralde, and I. A. Pecher. Seismic detection of marine methane hydrate. *The Leading Edge*, 21:686–689, 2002.

M. J. Hornback, S. Holbrook, A. R. Gorman, K. L. Hackwith, D. Lizarralde, and I. Pecher. Direct seismic detection of methane hydrate on the Blake ridge. *Geophysics*, 68(1):92100, 2003.

G. M. Hoversten, G. Cassassuce, E. Gasperikova, G. A. Newman, J. CHen, Y. Rubein, Z. Hou, and D. Vasco. Direct reservoir parameter estimation using joint inversion of marine seismic AVA and CSEM data. *Geophysics*, 71(3), 2006.

W. Hu, A. Abubakar, and T. M. Habashy. Joint electromagnetic and seismic inversion using structural constraints. *Geophysics*, 74(6):R99–R109, 2009.

J. Hughes-Clarke, I. W. Church, S. Blasco, J. Muggah, and R. Toodesh. Identification of Active Gas Seeps on the Beaufort Continental Margin : New Multibeam Water Column Imaging Capability of the CCGS Amundsen. Proceedings of the 6th Annual ArcticNet Scientific Meeting, December 8-11, 2009.

R. D. Hyndman and E. E. Davis. A Mechanism for the Formation of Methane Hydrate and Seafloor Bottom-Simulating Reflectors by Vertical Fluid Expulsion. *Journal of Geophysical Research*, 97(B5):7025–7041, 1992.

R. D. Hyndman and G. D. Spence. A Seismic Study of Methane Hydrate Marine Bottom Simulating Reflectors. *Journal of Geophysical Research*, 97(B5):6683–6698, 1992.

R. D. Hyndman, K. Wang, T. Yuan, and G. D. Spence. Tectonic Sediment Thickening, Fluid Expulsion, and the Therman Regime of Subduction Zone Accretionary Prisms: The Cascadia Margin off Vancouver Island. *Journal of Geophysical Research*, 98(B12):21,865–21,876, 1993.

R. D. Hyndman, G. D. Spence, R. Chapman, M. Riedel, and R. N. Edwards. Geophysical studies of marine gas hydrate in Northern Cascadia. *Geological Survey of Canada*, 2007.

F. Jørgensen, P. Sandersen, E. Auken, H. Lykke-Andersen, and K. I. Sørensen. Contributions to the geological mapping of Mors, Denmark: A study based on a large-scale TEM survey. *Bull. Geol. Soc. Den.*, 57:167–178, 2003.

D. L. B. Jupp and K. Vozoff. Stable Iterative Methods for the Inversion of Geophysical Data. *Geophys. J. R. astr. Soc.*, 42:957–976, 1975.

R. E. Kass and A. E. Raftery. Bayes Factors. *Journal of the American Statistical Association*, 90(430):773–795, 1995.

H. Keil and D. A. Hepp. Tracing the Holocene transgression of the North Sea in the German Bight. RV Heincke HE-405, Bremerhaven-Bremerhaven, 27$^{\text{th}}$ June - 13$^{\text{th}}$ July 2013. Marum - Centre for Marine Environmental Sciences, 2013.

J. Kennett, K. Cannariato, I. Hendry, and R. Behl. *Methane Hydrates in Quaternary Climate Change: The Clathrate Gun Hypothesis*. American Geophysical Union, Washington, DC, 2003.

K. Key. 1D inversion of multicomponent, multifrequency marine CSEM data: Methodology and synthetic studies for resolving thin resistive layers. *Geophysics*, 74(2):F9–F20, 2009.

S. Kirkpatrick, C. D. Gelatt, and M. P. Vecchi. Optimization by Simulated Annealing. *Science*, 220(4598):671–680, 1983.

R. Kirsch, T. Burschil, R. Roeloffs, H. Ketelsen, W. Scheer, F. Steinmann, B. König, C. Thomsen, M. Lilienfein, H. Wiederhold, B. Nommensen, and A. Wolf. Der Untergrund von Föhr: Geologie, Grundwasser und Erdwaerme. Ergebnisse des INTERREG-Projektes CLIWAT. Technical report, Leibniz Institute for Applied Geophysics and State Agency for Agriculture, Environment and Rural Areas, Germany, 2012.

H. R. Kudraß, C. Bönnemann, C. Gaedicke, S. Ladage, S. Neben, L. Reinhardt, and C. Rosenkranz. BGR03-AUR Nordsee, MV-Aurelia, 16^{th} Sep. -9^{th} Oct. 2003. Federal Institute for Geoscience and Natural Resources, 2003.

K. A. Kvenvolden. Gas hydrates - Geological Perspective and Global Change. *Reviews of Geophysics*, 31:173–187, 1993.

C. Lopez, G. D. Spence, R. D. Hyndman, and D. Kelley. Frontal ridge slope failure at the northern Cascadia margin: Margin-normal fault and gas hydrate control. *Geology*, 38(11):967–970, 2010.

L. M. MacGregor, D. Andreis, J. Tomilinson, and N. Barker. Controlled-source electromagnetic imaging on the Nuggets-1 reservoir. *The Leading Edge*, 25, 2006.

Y. F. Makogon, F. A. Trebin, A. A. Trofimuk, V. P. Tsarev, and N. V. Cerskiy. Detection of a pool of natural gas in a solid (hydrated gas) state. *Doklady, Akademii Nauk SSSR*, pages 59–66, 1971.

A. Malinverno. Parsimonious Bayesian Markov chain Monte Carlo inversion in a non linear geophysical problem. *Geophys. J. Int.*, 151:675–688, 2002.

A. Malinverno, M. Kastner, M. E. Torres, and U. G. Wortmann. Gas hydrate occurrence from pore water chlorinity and downhole logs in a transect across the Cascadia margin (Integrated Ocean Drilling Program Expedition 311). *Journal of Geophysical Research*, 113(B08103), 2008.

R. G. Markl, G. M. Bryan, and J. I. Ewing. Structure of the Blake-Bahama Outer Ridge. *Journal of Geophysical Research*, 75(24):4539–4555, 1970.

D. W. Marquardt. An Algorithm for Least-Squares Estimation of Nonlinear Parameters. *J. Soc. Indust. Appl. Math.*, 11(2):431–441, 1963.

F. J. Massey. The Kolmogorov-Smirnov Test for Goodness of Fit. *Journal of American Statistical Association*, 46:68–78, 1951.

D. F. McGinnis, J. Greinert, Y. Artemov, S. E. Beaubien, and A. Wuest. Fate of rising methane bubbles in stratified waters: How much methane reaches the atmosphere? *Journal of Geophysical Research*, 111:15, 2006.

R. D. McIver. Role of Naturally Occurring Gas Hydrates in Sediment Transport. *AAPG Bulletin*, 66(6):789–792, 1982.

M. A. Meju. *Geophysical Data Analysis: Understanding Inverse Problem Theory and Practice*. SEG, Tulsa, 1994.

W. Menke. *Geophysical Data Analysis: Discrete Inverse Theory*. Elsevier Inc., New York, 3 edition, 2012.

N. Metropolis, A. Rosenbluth, M. Rosenbluth, and A. E. Teller. Equation of state calculations by fast computing machines. *J. Chem. Phys.*, 21(6):1087–1092, 1953.

A. Micallef, C. Berndt, D. G. Masson, and D. A. Stow. Scale invariant characteristics of the Storegga Slide and implications for large-scale submarine mass movements. *Marine Geology*, 247:4660, 2008.

J. Mienert, M. Vanneste, S. Buenz, K. Andreassen, H. Haflidason, and H. P. Sejrup. Ocean warming and gas hydrate stability on the mid-Norwegian margin at the Storegga Slide. *Marine and Petroleum Geology*, 22:233–244, 2005.

R. A. Mir. Design and Deployment of a Controlled Source EM Instrument on the Neptune Observatory for Long-Term Monitoring of Methane Hydrate Deposits. Ph.D. thesis at University of Toronto, 2011.

D. C. Montgomery, E. A. Peck, and G. G. Vining. *Introduction to linear regression analysis*. Wiley series in probability and statistics, 5 edition, 2012.

D. Myer, S. Constable, and K. Key. Broad-band waveforms and robust processing for marine CSEM surveys. *Geophys. J. Int.*, 184:689–698, 2011.

F. E. Nelson, L. W. Brigham, D. M. Hinkel, W. Parker, V. Romanovsky, O. Smith, W. Tucker, T. Vinson, and N. I. Shiklomanov. *Climate Change, Permafrost, and Impacts on Civil Infrastructure*. U.S. Arctic Research Commission, Permafrost Task Force Report, Special Report 1–3, Arlington, Virginia, 2003.

K. G Osadetz, G. R. Morrell, J. Dixon, J. R. Dietrich, L. R. Snowdon, S. R. Dallimore, and J. A. Majorowicz. Beaufort-Mackenzie Basin: a review of conventional and nonconventional (gas hydrate) petroleum reserves and undiscovered resources. In S.R. Dallimore and T.S. Collett, editors, *Scientific results from the Mallik 2002 Gas Hydrate Production Research Well Program. Mackenzie Delta, Northwest Territories, Canada*, volume 585. Geological Survey of Canada Bulletin, 2005.

G.V. Palacky. Resistivity characteristics of geologic targets. In Misac N. Nabighian, editor, *Electromagnetic Methods in Applied Geophysics*, volume 1, chapter 3, pages 52–129. Society of Exploration Geophysicists, 1988.

K. P. Park. Gas hydrate exploration activities in Korea. *Proceedings of the 6th International Conference on Gas Hydrates*, page 10, 2008.

C. K. Paull, W. Ussler, S. R. Dallimore, S. M. Blasco, T. D. Lorenson, H. Melling, B. E. Medioli, F. M. Nixon, and F. A. McLaughlin. Origin of pingo-like features on the Beaufort Sea shelf and their possible relationship to decomposing methane gas hydrates. *Geophysical Research Letters*, 34, 2007.

C. K. Paull, W. Ussler, W. D. Caress, H. Thomas, E. Lundstein, M. Riedel, and L. Lapham. Seafloor manifestations of gas venting and near seafloor gas hydrate occurences. *AGU, Fall Meeting Suppl., Abstract*, OS23B-05, 2009.

B. R. Pelletier, W. F. Bawden, S. M. Blasco, R. A. Burns, R. L. Coles, J. R. Dietrich, J. Dixon, D. A. Forsyth, R. M. Gagne, R. L. Good, G. V. Haines, P. R. Hill, J. A. M. Hunter, A. S. Judge, C. F. M Lewis, H. A. MacAulay, A. Maisonneuve, D. H. McNeil, L. Meagher, D. Monahan, R. Monroe, P. J. Mudie, I. Norquay, D. K. Norris, M. J. O'Connor, V. K. Prest, R. A. Price, S. Pullan, V. N. Rampton, L. W. Sobczak, R. J. Wetrniller D. Weichert, C. J. Yorath, and F. G. Young. Marine Science Atlas of the Beaufort Sea; Geology and Geophysics. In B. R. Pelletier, editor, *Marine Science Atlas of the Beaufort Sea; Geology and Geophysics*, volume 40, page 53. Geological Survey of Canada, Miscellaneous Report, 1987.

E. S. Rasmussen. Stratigraphy and depositional evolution of the uppermost Oligocene - Miocene succession in western Denmark. *Bulletin of the Geological Society of Denmark*, 51:89–109, 2004.

A. Ray and K. Key. Bayesian inversion of marine CSEM data with a trans-dimensional self parametrizing algorithm. *Geophys. J. Int.*, 191:1135–1151, 2012.

A. Ray, D. L. Alumbaugh, G. M. Hoversten, and K. Key. Robust and accelerated Bayesian inversion of marine controlled-source electromagnetic data using parallel tempering. *Geophysics*, 78(6):E271–E280, 2013.

M. Riedel. 4D seismic time-lapse monitoring of an active cold vent, northern Cascadia margin. *Mar. Geophys. Res.*, 28:355–371, 2007.

M. Riedel, G. D. Spence, N. R. Chapman, and R. D. Hyndman. Seismic investigation of a vent field associated with gas hydrates, offshore Vancouver Island. *Journal of Geophysical Research*, 107(B9), 2002.

M. Riedel, T.S. Collett, and M. Malone. Expedition 311 synthesis: scientific findings. In M. Riedel, T.S. Collett, M.J. Malone, and the Expedition 311 Scientists, editors, *Proceedings of the Integrated Ocean Drilling Program*, volume 311, page 28. Integrated Ocean Drilling Program Management International, Inc., Washington, DC, 2006a.

M. Riedel, I. Novosel, G. D. Spence, R. D. Hyndman, R. N. Chapman, R. C. Solem, and T. Lewis. Geophysical and geochemical signatures associated with gas hydrate-related venting in the northern Cascadia margin. *GSA Bulletin*, 118(1-2):23–38, 2006b.

M. Riedel, A. M. Trehu, and G. D. Spence. Characterizing the thermal regime of cold vents at the northern Cascadia margin from bottom-simulating reflector distributions, heat-probe measurements and borehole temperature data. *Mar. Geophys. Res.*, 31:16, 2009.

M. Römer. personal communication, 2014.

C. Ruppel. Tapping methane hydrates for unconventional natural gas. *Elements*, 3 (3):193–199, 2007.

B.-J. Ryu, J.-H. Chun, and S. McLean. Gas hydrate environmental monitoring program in the Ulleung Basin, East Sea of Korea. European Geoscience Union (EGU), General Assembly, 2013a. Geophysical Research Abstracts, Vol. 15, EGU2013-1853.

B.-J. Ryu, T.S. Collett, M. Riedel, G.-Y. Kim, J.-H. Chun, J.-J. Bahk, J.-Y. Lee, J.-H. Kim, and D.-G. Yoo. Scientific Results of the Second Gas Hydrate Drilling Expedition in the Ulleung Basin (UBGH2). *Journal of Marine and Petroleum Geology*, 47:1–20, 2013b.

M. Sambridge, K. Gallagher, A. Jackson, and P. Rickwood. Trans-dimensional inverse problems, model comparison and the evidence. *Geophys. J. Int.*, 167:528–542, 2006.

A. N. Sartorelli and R. B. Frenc. Electro-magnetic induction methods for mapping permafrost along northern pipeline corridors. *Geophysics and Subsea Permafrost, Proc. 4th Can. Permafrost Conf.*, page 13, 1982.

M. Scherwath, M. Riedel, G.D. Spence, and R.D. Hyndman. Data report. seismic structure beneath the north Cascadia drilling transect of IODP Expedition 311. In M. Riedel, T.S. Collett, M.J. Malone, and the Expedition 311 Scientists, editors, *Proceedings of the Integrated Ocean Drilling Program*, volume 311, page 25. Integrated Ocean Drilling Program Management International, Inc., Washington, DC, 2006.

H. Schmeling. Numerical models on the influence of partial melt on elastic and anelastic and electrical properties of rocks. Part II: electrical conductivity. *Physics of the Earth and Planetary Interiors*, 43:123136, 1986.

D. Schoderbek and R. Boswell. Iġnik Sikumi #1, Gas Hydrate Test Well, Successfully Installed on the Alaska North Slope. *USDOE-NETL Fire in the Ice Newsletter*, 11: 14, 2011.

C. Scholl. The influence of multidimensional structures on the interpretation of LOTEM data with one-dimensional models and the application to data from Israel. Ph.D. thesis at the University of Cologne, 2005.

C. Scholl. Resolving an Onshore Gas-hydrate Layer with Long-offset Transient Electromagnetics (LOTEM). In M. Riedel, E. C. Willoughby, and S. Chopra, editors, *Geophysical Characterization of Gas Hydrates*, pages 149–162. Society of Exploration Geophysicists, 2010.

C. Scholl and R. N. Edwards. Marine downhole to seafloor dipole-dipole electromagnetic methods and the resolution of resistive targets. *Geophysics*, 72(2):WA39–WA49, 2007.

C. A. Scholz and B. R. Rosendahl. Low lake stands in lakes Malawi and Tanganyika, East Africa, delineated with multifold seismic data. *Science*, 240:1645–1648, 1988.

E. A. G. Schuur, J. Bockheim, , J. G. Canadell, E. Euskirchen, C. B. Field, S. V. Goryachkin, S. Hagemann, P. Kuhry, P. M. Lafleur, H. Lee, G. Mazhitova, F. E. Nelson, A. Rinke, V. E. Romanovsky, N. Shiklomanov, C. Tarnocai, S. Venevsky, J. G. Vogel, and S. A. Zimov. Vulnerability of Permafrost Carbon to Climate Change: Implications for the Global Carbon Cycle. *BioScience*, 58(8):701–714, 2008.

K. Schwalenberg. Marine controlled source electromagnetics: Using a bottom-towed system to explore submarine cold vent sites in Cascadia and New Zealand. Presentation at IUGG 14$^{\text{th}}$ General Assembly, 2007.

K. Schwalenberg and M. Engels. HYDRA - A new towed electromagnetic seafloor system. European Geoscience Union (EGU), General Assembly, 2011. Geophysical Research Abstracts, Vol. 13, EGU2011-12525.

K. Schwalenberg and M. Engels. Marine controlled source electromagnetic methods for gas hydrate assessment: Latest results from the Black Sea and the Hikurangi Margin, NZ. Extended Abstract, 21st Workshop on Electromagnetic Induction in the Earth, 2012a.

K. Schwalenberg and M. Engels. Marine controlled source electromagnetic methods for gas hydrate assessment: New instrumentation and first results from the Black Sea test cruise. *Protokoll über das 24. Schmucker-Weidelt-Kolloquium für Elektromagnetische Tiefenforschung*, pages 239–249, 2012b.

K. Schwalenberg, E. Willoughby, R. A. Mir, and R. N. Edwards. Marine gas hydrate electromagnetic signatures in Cascadia and their correlation with seismic blank zones. *First Break*, 23:99, 2005.

K. Schwalenberg, M. Engels, R. A. Mir, and "Scientific Party of M88/2". Geopotenzial Deutsche Nordsee (GPDN) - CSEM, Cruise No. 88, Leg 2, Sept. 08-22, Bre-

merhaven - Bremerhaven. Meteor-Berichte, Leitstelle Deutsche Forschungsschiffe, Institut fuer Meereskunde der Universitaet Hamburg, 2012.

G. Schwarz. Estimating the dimension of a model. *Ann. Stat.*, 6:461–464, 1978.

W. J. Scott. Real-Time Interpretation of Marine Resistivity. Proceedings of the Beaufort Sea Granular Resources Workshop, 1992.

O. Serra. *Fundamentals of well-log interpretation. Developments in Petroleum Science*, volume 1. Elsevier, Amsterdam, the Netherlands, 1984.

N. Shakhova and I. Semiletov. Methane release and coastal environment in the East Siberian Arctic shelf. *Journal of Marine Systems*, 66(14):227243, 2007.

N. Shakhova, I. Semiletov, A. Salyuk, V. Yusupov, D. Kosmach, and Oerjan Gustafsson. Extensive Methane Venting to the Atmosphere from Sediments of the East Siberian Arctic Shelf. *Science*, 327:1246–1250, 2010.

T. H. Shipley, M. H. Houston, R. T. Buffler, F. J. Shaub, K. J. McMillen, J. W. Ladd, and J. Worzel. Seismic evidence for widespread possible gas hydrate horizons on continental slopes and rises. *AAPG Bulletin- American Association of Petroleum Geologists*, 63(12):22042213, 1979.

E.D. Sloan and C.A. Koh. *Clathrate hydrate of natural gases*. Taylor & Francis Group, CRC Press, 3 edition, 2008.

J. C. Sørensen, U. Gregersen, M. Breiner, and O. Michelsen. High-frequency sequence stratigraphy of Upper Cenozoic deposits in the central and sourtheastern North Sea areas. *Marine and Petroleum Geology*, 14(2):99–123, 1997.

E. Spangenberg. Modeling of the influence of gas hydrate content on the electrical properties of porous sediment. *J. Geophys. Res.*, 106:6535–6548, 2001.

G. Steininger, J. Dettmer, S.E. Dosso, and C.W. Holland. Trans-dimensional joint inversion of seabed scattering and reflection data. *J. Acoust. Soc. Am.*, 133(3): 1347–1357, 2013.

R. Streich and M. Becken. Electromagnetic fields generated by finite-length wire sources: comparison with point dipole solutions. *Geophysical Prospecting*, 59: 361374, 2011.

A. Tarantola. *Inverse problem theory and methods for model parameter estimation*. Society for Industrial and Applied Mathematics, Philadelphia, 2005.

H. Thöle, C. Gaedicke, G. Kuhlmann, and L. Reinhardt. Late Cenozoic sedimentary evolution of the German North Sea - A seismic stratigraphic approach. *Newsletters of Stratigraphy, accepted*, 2014.

B. J. Todd and S. R. Dallimore. Electromagnetic and geological transect across permafrost terrain, Mackenzie River delta, Canada. *Geophysics*, 63(6):1914–1924, 1998.

S. Uyeda and H. Kanamori. Back-arc opening and mode of subduction. *J. Geophys. Res.*, 84:10491061, 1979.

K. Wallmann, G. Aloisi, M. Haeckel, A. Obzhirov, G. Pavlova, and P. Tishchenko. Kinetics of organic matter degradation, microbial methane generation, and gas hydrate formation in anoxic marine sediments. *Geochim Cosmochim Ac*, 70:3905–3927, 2006.

S. H. Ward and G. W. Hohmann. Electromagnetic Theory for Geophysical Applications. In Misac N. Nabighian, editor, *Electromagnetic Methods in Applied Geophysics*, volume 1, chapter 4, pages 131–313. Society of Exploration Geophysicists, 1988.

P. Weidelt. Guided waves in marine CSEM. *Geophys. J. Int.*, 171:153–176, 2007.

C. J. Weiss. The fallacy of the "shallow-water problem" in marine CSEM exploration. *Geophysics*, 72(6):A93–A97, 2007.

K. A. Weitemeyer, S. Constable, and A. M. Tréhu. A marine electromagnetic survey to detect gas hydrate at Hydrate Ridge, Oregon. *Geophys. J. Int.*, pages 1–16, 2011.

G. K. Westbrook, K. E. Thatcher, E. J. Rohling, A. M. Piotrowski, H. Paelike, A. H. Osborne, E. G. Nisbet, T. A. Minshull, M. Lanoisellé, R. H. James, V. Huehnerbach, D. Green, R. E. Fisher, A. J. Crocker, A. Chabert, C. Bolton, A. Beszczynska-Moeller, C. Berndt, and A. Aquilina. Escape of methane gas from the seabed along the West Spitsbergen continental margin. *Geophysical Research Letters*, 36:L15608, 2009.

W. J. Williams and E. C. Carmack. Combined effect of wind-forcing and isobath divergence on upwelling at Cape Bathurst, Beaufort Sea. *Journal of Marine Research*, 66:645–663, 2008.

E. C. Willoughby, R. Mir, C. Scholl, and R. N. Edwards. Neptune-Canada based Geophysical Imaging of Gas Hydrate in the Bullseye Vent. *Proceedings of the 6th International Conference on Gas Hydrates*, page 9, 2008.

W. O. Winsauer and H. M. Shearin. Resistivity of brine-saturated sands in relation to pore geometry. *AAPG Bull.*, 36:253–277, 1952.

J. F. Wright, S. R. Dallimore, F. M. Nixon, and C. Duchesne. In situ stability of gas hydrate in reservoir sediments of the JAPEX/JNOC/GCS et al. Mallik 2L-38 gas hydrate production research well. In S. R. Dallimore, T. Uchida, and T. S. Collett, editors, *Scientific Results from Mallik 2002 Gas Hydrate Production Research Well Program*, page 11. Geological Survey of Canada, Bulletin 585, Mackenzie Delta, Northwest Territories, Canada, 2005.

K. Yamamoto, Y. Terao, T. Fujii, I. Terumichi, M. Seki, M. Matsuzawa, and T. Kanno. Operational overview of the first offshore production test of methane hydrates in the Eastern Nankai Trough, 2014.

Ö. Yilmaz. *Seismic Data Analysis: Processing, Inversion and Interpretation of Seismic Data*. Society of Exploration Geophysicists, 2 edition, 2001. ISBN 9781560800941.

S. H. Yoon and S. K. Chough. Regional strike slip in the Eastern continental margin of Korea and its tectonic implications for the evolution of Ulleung Basin, East Sea (Sea of Japan). *Geol. Soc. Am. Bull.*, 107(1):8397, 1995.

J. Yuan and R. N. Edwards. The assessment of marine gas hydrates through electrical remote sounding: Hydrate without a BSR? *Geophysical Research Letters*, 27(16): 2397–2400, 2000.

A. Ziolkowski, R. Parr, D. Wright, V. Nockles, C. Limond, E. Morris, and J. Linfoot. Multi-transient electromagnetic repeatability experiment over the North Sea Harding field. *Geophysical Prospecting*, 58:1159–1176, 2010.

L. Zühlsdorff and V. Spiess. Three-dimentsional seismic characterization of a venting site reveals compelling indications of natural hydraulic fracturing. *Geology*, 32: 101–104, 2004.